Universitat Politècnica de València
Departamento de Máquinas y Motores Térmicos

Doctoral Thesis

Computational study of formation and development of liquid jets in low injection pressure conditions. Focus on urea-water solution injection for exhaust gas aftertreatment.

Presented by:
Mr. Javier Marco Gimeno

Supervised by:
Dr. Pedro Martí Gómez-Aldaraví

Valencia, July 2023

Universitat Politècnica de València
Departamento de Máquinas y Motores Térmicos

Doctoral Thesis

Computational study of formation and development of liquid jets in low injection pressure conditions. Focus on urea-water solution injection for exhaust gas aftertreatment.

Presented by:
Mr. Javier Marco Gimeno

Supervised by:
Dr. Pedro Martí Gómez-Aldaraví

in fulfillment of the requirements for the degree of
Doctor of Philosophy

Valencia, July 2023

Ph.D. Thesis

Computational study of formation and development of liquid jets in low injection pressure conditions. Focus on urea-water solution injection for exhaust gas aftertreatment.

Written by: Mr. Javier Marco Gimeno
Supervised by: Dr. Pedro Martí Gómez-Aldaraví

Thesis committee:

Chairman: Prof. Francisco Javier Salvador
Secretary: Dr. Daniel Rodriguez Álvarez
Member: Dr. Łukasz Jan Kapusta

Reviewing board:

Dr. Günter Brenn
Dr. Roberto Torelli
Dr. Łukasz Jan Kapusta

Valencia, July 2023

Abstract

The increasing awareness of the effect of emitting harmful gases coming from Internal Combustion Engines (ICE) into the atmosphere has driven the governments across the globe to limit the amount of these emissions, particularly in Europe through the EURO norms. The difficulty to meet such limitations has driven the automotive industry to shift from traditional Compression Ignited (CI) or Spark Ignited (SI) engines toward electrification or carbon-free fuels. Nonetheless, this transition will not be easily done in the short and medium time frames, while carbon-free fuels such as Hydrogen (H_2) and Ammonia (NH_3) will keep producing certain pollutants such as Nitrogen Oxides (NO_x) which need taking care of. These emissions can be particularly hazardous for the human being, increasing the risk of developing lung cancer. Selective Catalytic Reduction (SCR) has proven to be an effective technology for the reduction of this specific ICE contaminant. Through an injection of a Urea-Water Solution (UWS), together with the thermal energy of the combustion gases can generate a sufficient amount of NH_3 capable of neutralizing the unwanted NO_x in a reduction catalyst. With the fitting of SCR systems within light-duty applications, in addition to their traditional presence on heavy-duty usage, SCR has been on the focus of the scientific community to further understand their working principle, and improve their efficiency in a legislative environment where emission limits have become really tight. This Thesis tries to become part of that scientific ensemble by characterizing the whole UWS injection process within a computational framework.

The present research aims to provide a better understanding of the atomizing and degradation processes undergone by the UWS sprays. The transient dynamics taking place in the near-field region, added to the great influence of the inner-injector characteristics on the development of the spray make experimental approaches on such sprays challenging in providing such knowledge. On the other hand, Computational Fluid Dynamics (CFD) provide an alternative which has certain advantages. For the purpose of this Thesis they have been adopted as the main methodology on characterizing SCR sprays. Within the computational framework, the Thesis tries to develop and select the appropriate models that best suit low-velocity sprays, and set a proper know-how for subsequent studies performed on the same topic. Once acquired the suitable methods that best predict these sprays, the main jet breakup mechanisms, together with the driving urea-to-ammonia transformation phenomenon will have their behavior analyzed. In that way, the usage of experimental techniques could be avoided for such applications.

The CFD methods are applied and validated both in the near-field and

far-field regions. For the near-field, the treatment of multi-component flows is done through Eulerian-Eulerian such as the Mixture Model or the Volume-Of-Fluid method. Through them, a hydraulic characterization on two reconstructions of the UWS injector is performed, whose results are compared with experimental data. Further analysis is done on the jet-to-droplet dynamics, assessing which mechanisms were driving the process. The far-field analysis uses a Discrete Droplet Model (DDM) for dealing with the gas and liquid phases. In it, the evaporation of water and the thermolysis process of the urea have been considered and again, compared with experimental results to have a faithful methodology for its characterization. All the acquired knowledge has been later applied to a commercial Close-Coupled SCR, in which real-working conditions have been considered. From the results obtained from the several studies, an additional tool called Maximum Entropy Principle (MEP), capable of predicting the UWS spray atomization phenomenon without the need of performing near-field simulations, has been provided.

Accordingly, this Thesis provides a valuable methodology capable of predicting the near-field and far-field dynamics in a accurate way thanks to its validation against experimental results from literature. The mentioned methodology can be applied not only to the CFD software used during this Thesis, but can be extrapolated to the other packages available. Additionally, the MEP tool can be used independently for computational and experimental works to predict the performance of UWS atomizers. In that sense, the work carried out during the present Thesis presents a significant leap in the application of CFD tools in predicting challenging low-velocity sprays such as UWS.

Resumen

La creciente preocupación sobre el efecto de la emisión de gases nocivos provenientes de motores de combustión interna alternativos (ICE) a la atmósfera ha llevado a los gobiernos a lo ancho del planeta a limitar la cantidad de dichas emisiones, particularmente en Europa a través de las normas EURO. La dificultad en cumplir dichas limitaciones ha llevado a la industria automovilística a cambiar el foco de motores de encendido por compresión (CI) o provocado (SI) hacia la electrificación o los combustibles libres de carbono. Sin embargo, esta transición no se puede llevar a cabo de manera sencilla en el corto y medio plazo, mientras que combustibles libres de carbono como el Hidrógeno (H_2) o el Amoniaco (NH_3) siguen produciendo algunos contaminantes como los Óxidos de Nitrógeno (NO_x), con los cuales hay que lidiar. Estas emisiones pueden ser particularmente dañinas para el ser humano ya que incrementan el riesgo de cáncer de pulmón. La Reducción Catalítica Selectiva (SCR) ha demostrado ser una tecnología eficaz para la reducción de este contaminante en particular. A través de una inyección de una Solución de Urea-Agua, junto con la energía térmica de los gases de escape, se genera una cantidad suficiente de NH_3 capaz de neutralizar los indeseados NO_x en un catalizador de reducción. Con la inclusión de los SCR en automóviles ligeros además de su presencia tradicional en automóviles pesados, los SCR han sido el foco de la comunidad científica para mejorar el entendimiento de su principio de actuación, y mejorar su eficiencia en un entorno legislativo en el que los limites de emisión se han estrechado enormemente. Esta Tesis intenta ser parte de ese esfuerzo científico en caracterizar el proceso de inyección de UWS en su totalidad a través de un entorno computacional.

El presente estudio tiene como objetivo proveer de un mejor entendimiento del proceso de atomización y degradación sufrido por los chorros de UWS. Las dinámicas no estacionarias que se dan lugar en la zonas cercana del chorro, añadido a la gran influencia de las características internas del inyector sobre el desarrollo del spray hacen que los métodos experimentales sean complicados para poder entender dicho proceso. Por otro lado, la Mecánica de Fluidos Computacional (CFD) supone una alternativa con ciertas ventajas. Para el propósito de esta Tesis, el CFD ha sido utilizado como la principal metodología para caracterizar los espray de SCR. Mediante dichos métodos, se intenta desarrollar y seleccionar los modelos más apropiados que mejor se adapten a chorros de baja velocidad, y establecer un conocimiento para posteriores estudios desarrollados sobre la misma temática. Una vez adquiridos dichos métodos, los mecanismos principales de rotura del chorro, así como los de degradación de la urea en amoníaco se han analizan. En ese sentido, el

uso de técnicas experimentales podrían ser sustituidos en el futuro para esta aplicación.

Los métodos CFD son aplicados y validados tanto en el campo cercano como en el lejano. Para el campo cercano, el tratamiento multi-fase se lleva a cabo a través de métodos Euleriano-Euleriano, como el Modelo de Mezclas, o el método Volume-Of-Fluid. A través de ellos, la caracterización hidráulica de dos reconstrucciones del inyector de UWS se lleva a cabo, cuyos resultados son comparados con datos experimentales. Subsiguientes análisis se llevan a cabo sobre las dinámicas de rotura de la vena líquida, descubriendo que mecanismos rigen el proceso. El estudio de campo lejano usa un Discrete Droplet Model (DDM) para lidiar con las fases líquidas y gaseosas. En él, la evaporación del agua y el proceso de termólisis de la urea han sido considerados y de nuevo, comparados con resultados experimentales con el fin de obtener una metodología fiel para su caracterización. Todo el conocimiento adquirido se aplica más tarde a un Close-Coupled SCR, en el cual condiciones de trabajo realista han sido consideradas. De los resultados obtenidos de los distintos estudios, una herramienta adicional llamada Maximum Entropy Principle (MEP), capaz de predecir el fenómeno de atomización de los chorros de UWS sin necesidad de realizar simulaciones de campo cercano, es presentada.

Por tanto, esta Tesis aporta una metodología valiosa capaz de predecir tanto el campo cercano como el lejano de una manera precisa por su comparación con los resultados experimentales de la literatura. Dicha metodología puede aplicarse no solo al software CFD usado durante esta Tesis, si no al resto de paquetes disponibles. Adicionalmente, la herramienta MEP puede ser usada de manera independiente para estudios computacionales como experimentales para predecir el rendimiento de inyectores de UWS. En ese sentido, el trabajo realizado presenta un salto adelante significativo en la aplicación de herramientas CFD para la predicción de chorros desafiantes como los de UWS.

Resum

La creixent preocupació sobre l'efecte de l'emissió de gasos nocius provinents de motors de Combustió Interna Alternatius (ICE) a l'atmòsfera ha dut als governs a l'ample del planeta a limitar la quantitat de dites emissions, particularment a Europa mitjant les normes EURO. La dificultat en complir dites limitacions ha dut a l'indústria automovilística a canviar el foc de motors d'encés per compressió (CI) o provocat (SI) cap a l'electrificació o els combustibles lliures de carboni. No obstant, esta transició no es pot portar a terme de manera senzilla en el curt i mig termini, mentres que combustibles lliures de carboni com l'Hidrogen (H_2) o l'Amoníac (NH_3) seguirien produint alguns contaminants com els Òxits de Nitrogen (NO_x), en els quals cal bregar. Estes emissions poden ser particularment nocives per a l'esser humà ja que incrementen el risc de càncer de pulmó. La Reducció Catalítica Selectiva (SCR) ha demostrat ser una tecnologia eficaç per a la reducció d'este contaminant en particular. Mitjançant una injecció d'una Solució D'Urea-Aigua, junt en l'energia tèrmica dels gasos de fuita, es pot generar una quantitat suficient de NH_3 capaç de neutralitzar els indesitjats NO_x a un catalitzador de reducció. Amb l'inclusió dels SCR en automòvils lleugers a més de la seua tradicional presència a automòvils pesats, els SCR han segut el foc de la comunitat científica per a millorar l'enteniment del seu principi d'actuació, i millorar la seua eficiència en un entorn legislatiu en el que els límits d'emissió s'han limitat enormement. Esta Tesi intenta ser part d'eixe esforç científic en caracteritzar el procés d'injecció de UWS en la seua totalitat a través d'un entorn computacional.

El present estudi té como a objectiu proveir d'un millor enteniment del procés d'atomització i degradació patit pels dolls de UWS. Les dinàmiques no estacionàries que es donen lloc en la zona propenca del doll, afegit a la gran influència de les característiques internes de l'injector sobre el desentroll de l'esprai, fan que els métodes experimentals siguen complicats d'aplicar per a poder entendre dit procés. Per un altre costat, la Mecànica de Fluïts Computacional (CFD) supon una alternativa que té certes avantatges. Per al propòsit d'esta Tesi, el CFD ha sigut utilitzat com la principal metodologia per a caracteritzar els esprais de SCR. Per mitjà de dits métodes, la Tesi intenta desentrollar i seleccionar els models més apropiats que millor s'adapten a esprais de baixa velocitat, i establir un coneiximent per a posteriors estudis desentrollats sobre la mateixa temàtica. Una volta adquirits dits métodes, els mecanismes principals de trencament del doll, així com els de degradació de la urea en amoníac s'analitzaran. En eixe sentit, l'us de tècniques experimentals podria no ser utilitzats més en el futur per a esta aplicació.

Els métodes CFD són aplicats i validats tant en el camp propenc com en el llunyà. Per al camp propenc, el tractament multi-component es porta a terme a través de métodes Eulerià-Eulerià, com el Model de Mescles, o el métode Volume-Of-Fluid. A través d'ells, la caracterització hidràulica de dos reconstruccions de l'injector de UWS es porta a terme, els resultats del qual són comparats amb resultats experimentals. Subsegüents anàlisis es porten a terme sobre les dinàmiques de trencament de la vena líquida, descobrint qué mecanismes regixen el procés. L'estudi de camp llunyà usa un Discrete Droplet Model (DDM) per a bregar en la fase líquida i gaseosa. En ell, l'evaporació de l'aigua i el procés de termòlisis de l'urea han sigut considerats i de nou, comparats amb el resultats experimentals amb la finalitat d'obtindre una metodologia fidel per a la seua caracterització. Tot el coneiximent adquirit s'aplica més tard a un Close-Coupled SCR, en el qual, condicions de treball realistes han sigut considerades. Dels resultats obtinguts dels distints estudis, una ferramenta adicional anomenada Maximum Entropy Principle (MEP), capaç de predir el fenomen d'atomització dels doll de UWS sense necessitat de realitzar simulacions de camp propenc, és presentat.

Per tant, esta Tesi aporta una metodologia capaç de predir tant el camp propenc com el llunyà d'una manera precisa per la seua comparació en els resultats experimentals de la literatura. Dita metodologia pot aplicar-se no només al software CFD usat durant esta Tesi, sino a la resta de paquets disponibles. Adicionalment, la ferramenta MEP pot ser usada de manera independent per a estudis computacionals com a experimentals per a predir el rendiment d'injectors de UWS. En eixe sentit, el treball realitzat durant esta Tesi presenta un salt cap avant significatiu en l'aplicació de ferramentes CFD per a la predicció de dolls desafiants com els de UWS.

"No había otro remedio que seguir y seguir, aun después de sentir que no podrían dar un paso más."
— El Hobbit

A mis padres y a mi hermano

Acknowledgements

No quiero perder esta oportunidad para poder agradecer a toda persona que ha contribuido tanto al desarrollo de esta Tesis doctoral como a mi evolución personal en esta etapa. Durante cuatro años he tenido la suerte de coincidir con gente maravillosa, desde compañeros, profesores, técnicos y profesionales que de una u otra manera me han ayudado a seguir adelante un día tras otro. Sin todos ellos esto no habría sido posible.

En primer lugar quiero agradecer su labor a mi tutor y director, Pedro Martí. La culminación de esta Tesis no sería posible si no fuera por su conocimiento y orientación. Quiero agradecerle su optimismo y capacidad de encontrar soluciones en aquellos momentos en los que yo no era capaz de ver la luz al final del túnel. Gracias a tí he conseguido valorar el trabajo realizado durante esta etapa. Has sido un ejemplo de trabajo y como persona. Tras estos cuatro duros años además de director, quiero considerarte como un amigo.

Expresar mi gratitud a CMT-Motores Térmicos y a su dirección por permitirme desarrollar mi Tesis doctoral en tan prestigioso centro de investigación. Particularmente, agradecer a Raúl Payri, mi jefe de línea por siempre ayudarme en lo posible. Ha sido un placer trabajar contigo. También agradecer al resto de profesores de la línea de inyección: Gabriela, Jaime, Marcos y Javi, que no han dudado en ayudarme profesionalmente. No quiero olvidarme del personal que compone la secretaría del departamento por la ayuda prestada, con mención especial a Amparo Cutillas, ya que con su labor, los doctorandos del departamento podemos despreocuparnos de las labores de gestión asociadas al programa.

Asimismo, agradecer a Argonne National Laboratory la oportunidad de conocer y colaborar con un centro de investigación de prestigio global. Especialmente a Sibendu Som por apreciar mi labor y permitirme formar parte del grupo. Así pues, palabras de agradecimiento a Roberto por facilitarme el transporte, Kathy por su amabilidad y colaboración y concretamente a Lorenzo Nocivelli por ayudarme a que mi periodo allí fuera lo más cómodo posible y a considerarme como uno más del equipo.

No quiero continuar sin acordarme de mis compañeros de departamento. A María por su guía y ayuda cuando trabajamos en el mismo despacho y una vez se fue. A Kike, por su ayuda incondicional ante cualquier situación y por su increíble conocimiento de nuestro tema de investigación. Gracias a él y a

Óscar, las risas y buenos momentos pasados en el despacho quedarán siempre en mi memoria. No quiero olvidarme de Lucas, Mario, Víctor, Rami, César, Tomás, Armando, David y Carlos. Hemos formado una pequeña familia. También mencionar a José Enrique y Omar, que me han ayudado en los montajes experimentales.

Mis apoyos no solo han estado dentro del centro de trabajo, y es por ello que he de agradecer enormemente a Enrique las risas, las cenas y las largas horas que hemos hablado por Teams, ya que en los momentos de agobio y estrés, siempre ha conseguido sacarme una sonrisa. Gracias por todo, amigo.

De manera especial, quiero expresar mis agradecimientos a mi familia. Este es el resultado de vuestra guía, camino y compañía. A mi Madre, porque me ha inculcado los valores de trabajo duro y persistencia. A mi Padre, gracias por apoyarme en mis sueños sin importar que ellos pudieran alejarme de vosotros. Tete, gracias por hacerme ser tan curioso, y por estar ahí siempre. Y a mis abuelos, tanto los que están como los que no, por vuestro cariño infinito. Espero que estéis orgullosos, soy lo que soy gracias a vosotros.

Por último, nada de esto habría sido posible sin tí, Cecilia. Tu apoyo diario, cariño y consuelo han permitido que me haya podido levantar cuando me he caído. No puedo expresar con palabras la importancia que has tenido durante esta etapa. Gracias por quererme tanto.

A todos vosotros, de nuevo, gracias.

Funding acknowledgements

Javier Marco Gimeno has been founded through a grant from the Government of Generalitat Valenciana with reference ACIF/2020/259 and financial support from the European Union.

These same institutions, Government of Generalitat Valenciana and The European Union, supported through a grant for pre-doctoral stays out of the Comunitat Valenciana with reference CIBEFP/2021/11 the research carried out during the stay at Energy Systems, Argonne National Laboratory, United States of America.

Special gratitude from the author to both institutions, Government of Generalitat Valenciana and The European Union, for making this dream possible.

Technical acknowledgements

The author would like to special thank "Rigel" from Universitat Politècnica de València, the HPC Cluster from CMT-Motores Térmicos and "Bebop" from Argonne National Laboratory for allowing to use their cluster to perform the simulations carried out in this work and the excellent attention and technical support received.

Last but not least, thanks to the team of CONVERGE™ for allowing the author to use their software to carry out this Thesis and for the attention received from all the members and the technical support.

Contents

List of Figures

List of Tables

Nomenclature

Acronyms

AMG	Algebraic MultiGrid.
AMR	Adaptive Mesh Refinement.
ANL	Argonne National Laboratory.
APS	Advance Photon Source.
ASOI	After Start Of Injection.
BiCGSTAB	BiConjugate Gradient STABilized.
BL	Breakup Length.
CBC	Convective Boundedness Criterion.
CC	Close-Coupled.
CDF	Cumulative Distribution Function.
CDS	Central Differential Schemes.
CFD	Computational Fluid Dynamics.
CFL	Courant-Friedrichs-Lewy.
CICSAM	Compressive Interface Capturing Scheme for Arbitrary Meshes.
CI	Compression Ignited.
CO2	Carbon Dioxide.
CSF	Continuum Surface Force.
CT	Computerized Tomography.
CUC	Clean-Up Catalyst.
DBI	Diffused Backlight Illumination.
DDM	Discrete Droplet Model.

DEF	Diesel Exhaust Fluid.
DL	Diffusion Limited.
DNS	Direct Numerical Simulation.
DOC	Diesel Oxidation Catalyst.
DPF	Diesel Particulate Filter.
EGR	Exhaust Gas Recirculation.
EPA	Environmental Protection Agency.
EU	European Union.
FE	Fixed Embedding.
FTIR	Fourier Transform Infra-Red.
FVM	Finite Volume Method.
GDI	Gasoline Direct Injection.
GHG	Greenhouse Gases.
HCCI	Homogeneous Charge Compression Ignition.
HNCO	Isocyanic Acid.
HPC	High Performance Computing.
HRIC	High Resolution Interface Capturing.
HRLBI	High-Resolution Laser Backlight Imaging.
ICE	Internal Combustion Engines.
IQ	Index Of Quality.
IRT	Infra-Red Thermography.
IR	Infra-Red.
KDE	Kernel Density Estimation.
KH	Kevin-Helmholtz.
LES	Large Eddy Simulation.
LIF	Laser Induced Fluorescence.
MEP	Maximum Entropy Principle.
MM	Mixture Model.
MNCN	Museo Nacional de Ciencias Naturales.
N-S	Navier-Stokes.
NH3	Ammonia.
NOx	Nitrogen Oxides.
NRTL	Non-Random Two-Liquid.
NSC	NOx Storage Catalyst.

NTC	No Time Counter.
PCCI	Premixed Charge Compression Ignition.
PDA	Phase Droplet Anemometry.
PDE	Partial Differential Equations.
PDF	Probability Density Function.
PISO	Pressure Implicit with Splitting of Operators.
PMS	Portable Measuring System.
PM	Particulate Matter.
RANS	Reynolds-Averaged Navier-Stokes.
RDE	Real Driving Emissions.
RM	Rapid Mixing.
RNG	Re-Normalisation Group.
ROI	Rate Of Injection.
ROM	Rate Of Momentum.
RR	Rosin-Rammler.
RSME	Root Square Mean Error.
RSM	Reynolds Stress Model.
RT	Rayleigh-Taylor.
SCR	Selective Catalytic Reduction.
SGS	Sub-grid Scale.
SI	Spark Ignited.
SLIPI	Structured Laser Illumination Planar Imaging.
SMD	Sauter Mean Diameter.
SOR	Succesive Over Relaxation.
TAB	Taylor Analogy Breakup.
TGA	Thermal Gravimetric Analysis.
TIM	Transverse Integrated Mass.
TKE	Turbulent Kinetic Energy.
UDS	Upwind Differential Scheme.
UI	Uniformity Index.
UWS	Urea Water Solution.
VOF	Volume-Of-Fluid.
WALE	Wall-Adapting Local Eddy-Viscosity.
WFD	Wall Film Dynamics.

Dimensionless quantities

α	Void fraction.
δ_{ij}	Kronecker delta function.
$barG$	Gauge pressure in bar units.
C_a	Area coefficient.
C_D	Drag coefficient.
C_d	Discharge coefficient.
C_m	Momentum coefficient.
C_v	Velocity coefficient.
C_{SGS}	Dynamic Smagorinsky constant.
CFL	Courant-Friedrichs-Lewy number.
IQ_ν	Viscosity Index Of Quality.
IQ_k	TKE Index Of Quality.
IQ_{VOF}	VOF Index Of Quality.
K	Kuhnke Impact Parameter.
La	Laplace number.
Nu	Nusselt number.
Oh	Ohnesorge number.
Pr	Prandtl number.
Q	RR probability value.
q	RR spread parameter/Momentum Ratio.
Re	Reynolds number.
Sch	Schmidt number.
T^*	Non dimensional temperature.
Ta	Taylor number.
We	Weber number.
Y	Mass fraction.

Greek symbols

α	Void fraction.
$\boldsymbol{\tau}$	Viscous shear stress [Pa].
Δ	Spatial filter cut-off width in LES [m].
Δp	Pressure Difference [Pa].
γ	Surface tension force [$\mathrm{N\,m^{-1}}$].
μ	Dynamic viscosity [kg/ms].

ν	Kinematic viscosity [m^2/s].
ν_{num}	Numerical viscosity in LES [m^2/s].
ν_t	Turbulent viscosity in LES [m^2/s].
ω	Specific turbulent dissipation [1/s].
ϕ	Flow variable.
ρ	Density [kg/m^3].
σ	Surface tension [kg/m^2].
σ	Viscous stress tensor.
ε	Turbulent dissipation [m^2/s^3].

Latin symbols

$\boldsymbol{n}$	Normal unity vector to the surface [-].
$\dot{M}$	Momentum flux [kgm/s].
$\dot{m}$	Mass flow rate [kg/s].
A	Arrhenius expresion pre-factor [-].
A_0	Geometric area [m^2].
C_p	Specific heat capacity [$m^2\,s^{-2}\,K$].
D_{diff}	Mass Diffusion [m^2/s].
e	Specific internal energy [$m^2\,s^{-2}$].
E_a	Activation energy [J/kmol].
F	Force [N].
G	Filter function [-].
g	Gravitational acceleration [$m^2\,s^{-1}$].
h	Enthalpy heat [m^2/s^2].
K	Conductivity [$W\,m^{-1}\,K^{-1}$].
k	Turbulent kinetic energy [m^2/s^2].
M	Molar weight [mol].
m	Total mass [kg].
P, p	Pressure [Pa].
R, r	Droplet radius [m].
S	Source term .
S_{ij}	Strain rate tensor [1/s].
T	Temperature [K].
t	Time [s].
u	Velocity [$m\,s^{-1}$].

V	Volume [m^3].

Subscripts

a, amb	Ambient.
$crit$	Critical.
ef	Effective.
g	Gas phase.
$ideal$	Ideal.
inj	Injection.
l	Fluid phase.
mod	Modeled.
res	Resolved.
sat	Saturation.
tot	Total.
w	Wall.
x	Coordinate [m].

Chapter 1

Introduction

"Organisms don't think of CO_2 as a poison. Plants and organisms that make shells, coral, think of it as a building block."
—Janine Benyus

1.1 General Context

Internal Combustion Engines (ICE) have seen a continuous increase in demand since their first appearance in 1860 with the Gas Engine from Etienne Lenoir until the last-generation Spark Ignited (SI) and Compression Ignited (CI) combustion philosophies. They serve as the most common powertrain technology for transportation purposes in the maritime and mainland, both for light and heavy-duty applications [1], by transforming chemical energy into mechanical power using liquid fuel combustion. They have allowed excellent mobility of passengers and cargo, becoming one of the main drivers of industrial and economic globalization. Due to that increasing trend, this technology has also increased the awareness of the society on the emission of harmful gases into the atmosphere. EURO norms were created within the European Union to limit such emissions and transition towards cleaner technologies. One of the main objectives of the norm is to reduce CO_2 Greenhouse Gases (GHG) by 2030 by a minimum of 50% compared to 1990 emission levels and make it carbon-neutral according to The European Green Deal project [2]. These limitations have driven the industry and the research community to place great efforts in further developing ICE and auxiliary systems to find

solutions to the broad spectrum of exhaust gases that are generated as a consequence of the combustion process, and increase the performance of it. The latest EURO norms have become restrictive, making it tough to find solutions that meet established limits and resulting necessary to make great efforts to find answers to the emission problem. Not only CO_2 has become the target emission to reduce. Other emission compounds act as indirect GHG, such as Nitrogen Oxides (NO_x), which also directly affect acid rain phenomena, smog, and diseases on human and animal health [3]. These emissions have been severely limited by previous norms (EURO 5 to EURO 6), decreasing the maximum amount of emitted NOx from 180 mg/km down to 80%, and with the introduction of Real Driving Emissions (RDE) tests, on-road mechanisms of dealing with such emissions are needed. EURO 7 will further reduce an additional 35% of the light-duty vehicles' NO_x emissions and 13% from the tailpipe particles [4].

In concordance with the upcoming EURO 7 norm, an ambitious norm to achieve the emission reduction of ICE, the industry is trying to shift towards clean transportation means, such as electric vehicles, or carbon-free ICE fuels. When it comes to electric cars, electricity generation in the European Union is only partially done by renewable energies. Instead, electricity from fossil fuels implied 37% of the power generation in 2021 [5], so GHG and NO_x will be produced when generating electricity for those purposes. In addition to that, the extraction of materials such as lithium, cobalt, graphite, and nickel (needed components for battery manufacturing) also has a specific energy requirement that contributes detrimentally to the idea of *clean* vehicles. It is unlikely that the global transportation industry will start to rely on fully electric vehicles, as although light-duty transportation purposes have already seen a change in their propulsive technologies, heavy-duty applications such as maritime transportation is not to see that change in the immediate future. Moreover, transportation freighters account for a large proportion of CO_2 emissions (over 3% of EU emissions). Regarding innovative combustion engines, alternative fuels such as hydrogen (H_2) or ammonia (NH_3) are the focus of current research due to being carbon-free compounds. Nonetheless, NO_x emissions remain an issue due to high temperatures associated with the combustion process of these alternative fuels [6, 7] and the high availability of nitrogen and oxygen.

To reduce NO_x emissions, various technologies can be employed. In SI engines, a three-way catalyst allows doing so due to having a combustion process in stoichiometric conditions. In CI engines, alternative techniques are used as lean combustion processes take place, and therefore an excess of oxygen is present. NO_x generation can be managed by controlling the amount of air

and fuel in the combustion chamber, but in this way, the engine's performance could be affected. Additionally, in that way, a trade-off between Particulate Matter (PM) and fuel consumption can occur. Selective Catalytic Reduction (SCR) is the most widely used technology for de-NO_x of combustion exhaust gases in CI propulsive systems [8]. It was initially employed on stationary and maritime engines during the 1980 decade by injecting ammonia in the exhaust line. Later on, and with ever more restrictive regulations applied to Europe due to the EURO norms, deNOx systems were mounted in heavy-duty vehicles like lorries, tractors, and buses. Substitutes for ammonia have been analyzed to avoid the toxicological and transportation issues associated with the original fluid, like ammonium formate [9], or methanamide [10]. However, no one has shown the advantages of a Urea-Water Solution (UWS). The injected UWS transforms to NH_3, which is the needed component to reduce the undesired NO_x. It was implemented into light-duty passenger cars to satisfy the EURO VI norm. SCR systems depend strongly on the amount of ammonia present before the catalyst. The urea content of the liquid UWS should evaporate and suffer specific chemical transformations to convert into NH_3 and isocyanic acid (HNCO) through thermolysis and hydrolysis reactions. Therefore, the evaporation process remains critical for SCR performance. On light-duty vehicles, the low available space and time for the UWS to transform into NH_3 leads to liquid impingement with mixing devices, tailpipe, and catalyst, which results in the formation of unwanted deposits of by-products of HNCO (such as biuret, or triuret) on the exhaust line, affecting the expected performance of the engine (e.g. creating back-pressures) [11]. Moreover, incomplete evaporation implies less NH3 amount available for NO_x reduction and, consequently, the possibility of failing to reduce emission as much as possible.

UWS dosing units should be able to introduce an adequate mixture into the exhaust line, providing a rapid decomposition, a uniform ammonia distribution, and minimizing the wall impingement phenomena. Their commonly associated low injection pressures (3 bar - 10 bar [12]) and subsequent low jet velocities hinder this task due to incomplete atomization and undesired deposit formation. For these reasons, it is mandatory to properly understand the kinematic, breakup, and evaporation dynamics of such sprays. Due to the complex nature of the injection process and the reactions that occur before reaching the catalyst, the different physical processes that take place are generally separated to understand them better individually. It involves both physical phenomena, such as the jet instabilities generation leading to primary and secondary atomization, evaporation of the water content; and chemical phenomena to consider the transformation of urea into ammonia and isocyanic acid through thermolysis, and later decomposition of isocyanic acid into fur-

ther ammonia molecules. As mentioned, spray wall impingement is also an essential process as it will rule the later deposit formation.

To achieve the emissions limit established across the years, several types of SCR architectures have been used for the different applications. For example, initially, light-duty applications comprised a unique under-floor catalyst, which enhances urea decomposition, but it could not achieve NO_x limits at startup due to delayed light-off [13]. After that, alternative configurations include close-coupled SCR, merged with the particulate filter. Being close to the engine exit, benefits from the higher temperatures, with the problem of hindering the atomization and evaporation process of the urea, increasing the deposit risk in the swirler geometry. Heavy-duty vehicles were the first to implement multi-dose and multi-brick SCR configurations, in which both close-coupled and under-floor systems were fitted in the exhaust line. These configurations ensured a proper deNOx behaviour during the whole engine cycle. It has has now become state-of-the-art as well for light-duty vehicles [14]. Another issue associated with SCR systems is the so-called ammonia slip, which happens when excessive ammonia is generated and emitted, which could lead to introducing Clean-Up Catalyst (CUC) to compensate [15].

As observed, the SCR system is a functional but complex system for reducing NO_x emissions. For that reason, the subject has undergone a lot of research effort from the scientific community to solve its different challenges. The injection event of UWS has been split up in the several phenomena that is comprised, as jet breakup, droplet evaporation, and liquid impingement, to understand each one of them in depth to know all the factors that can influence the global performance of the deNOx treatment. When it comes to characterizing the UWS spray, optical techniques are commonly used and applied to quiescent and cross-flow conditions, employing Laser Induced Fluorescence (LIF) [16, 17], Phase Droplet Anemometry (PDA) techniques [18–20] or Diffused Backlight Illumination (DBI) [20, 21]. Patternators are also employed to assess the liquid distribution within a spray under quiescent conditions [22]. Other studies analyze the effect of the injector geometry and working conditions on the spray development [23]. Macroscopic and microscopic characteristics of the spray have also been widely analyzed [24, 25]. Research on the influence of exhaust working conditions on necessary spray mixing characteristics has been carried out by some authors [26, 27]. UWS evaporation has also been deeply analyzed in the literature. Evaporation processes have also been assessed on the typical engine working conditions by Postrioti et al. [28]. That analysis can go from the characterization of the phase change of a single droplet [29] under hot air flow to the effect on the whole spray [30]. The degradation of the urea has been studied to assess the needed temperatures

for obtaining a rapid transformation into ammonia. Different studies [31, 32] reported on the stability of the urea in its different phases.

Computational methods have gone a long way since the formulation of the Navier-Stokes equations by Sir George Stokes in the 19th century. Computational calculations have become incredibly cheaper compared to the first simulations performed [33]. The UWS application has benefited from this fact to push forward the proposed technology. Especially, Discrete Droplet Model (DDM) techniques are commonly employed to assess macroscopic (such as penetration) and microscopic data such as droplet size distributions [34–36] of UWS sprays and validate it with experimental results [37]. The evaporation phenomenon has been the focus of computational work as it results quite complex to predict. Some available models as the Diffusion Limited (DL) or Rapid Mixing (RM) have been assessed for the feasibility of the UWS application [38]. Molten-solid models, on the other hand, assume that the urea degrades immediately to ammonia through activation energy, the droplet temperature, and the droplet radius within an Arrhenius expression [38]. Numerous studies have validated their urea degradation model against Kim et al. [39] data in which the urea conversion efficiency was assessed in different test gas velocities and temperatures. More in detail approaches consider all the intermediate reactions of the urea down to the final chemical products [40].

Although there is a wide variety of available research regarding UWS sprays, there is little information about the atomizing process of low velocity jets. Based on that necessity, this Thesis aims to provide a complete computational analysis of the physical and chemical processes that occur before the deNOx step on low-pressure injection systems and provide helpful information on the breakup mechanisms that drive the jet-to-droplet dynamics. To do so, it will employ several models to characterize each one of the main physical aspects that drive the complete process, always paying attention to the current SCR systems available.

The present investigation was carried out at *Departamento de Máquinas y Motores Térmicos* within the Doctorate Programme on Propulsive Systems for Transport Media of *Universitat Politècnica de València (Spain)*. This institution has dedicated its over 40 years of life to the understanding of the relevant physical processes involved in the ICE field, from the injection processes and combustion of fuels to the air-management and noise control techniques. Both deep scientific knowledge and real-life problems in the automotive and aerospace industry have been the priority. To do so, the institute is equipped with state-of-the-art experimental facilities to analyze the processes of interest and enough computational resources (in-house High Performance Comput-

ing HPC facility) to characterize the phenomena that, through experimental means, are difficult to identify, providing useful know-how and scientific results. Both approaches have complemented each other, resulting in a large amount of scientific articles published in high-impact journals. Additionally, with the uprising of novel technologies, new research lines have appeared dealing with topics such as hydrogen combustion and fuel cells. Concerning the present work, this Thesis is established within the injection systems research group. Several theses have been carried out to characterize diesel sprays experimentally [41–43] and computationally [44, 45], as well as in Gasoline Direct Injection (GDI) [46–48]. With the NOx emission limitations, the institute developed an interest in characterizing Diesel Exhaust Fluid (DEF) sprays, resulting in one initial Thesis with this theme [49]. It provided a first insight into the atomization process and the spray behavior under realistic working conditions employing experimental techniques. It lead to this Thesis, which focused on studying DEF sprays computationally.

1.2 Objectives and Methodology

The purpose of this thesis is to deepen the knowledge on deNOx systems, not only for CI engines, but also for carbon-free-fueled engines (i.e. H_2 fueled) by means of Computational Fluid Dynamics (CFD). Within that frame, this work focuses on the generation of computational models capable of reproducing the main physical and chemical events that drive the transformation of the DEF into the deNOx working agent, that is, from the injection process to the obtention of ammonia and urea by-products. Numerical CFD methods have been historically expensive to recreate certain physical events. However, with the increase in computational power from recent computers, the technological barrier has started to vanish, and these studies are becoming more frequent.

The main objective of the Thesis is to implement a complete numerical toolset capable of reproducing the relevant aspects of the injection events of UWS under realistic working conditions using a commercially available DEF injector employing both Reynolds-Averaged Navier-Stokes (RANS) and Large Eddy Simulation (LES) approaches. Multi-fluid and multiphase techniques will be included as phase change episodes should be expected. The elaborated model will be consistently validated against experimental data on a broad range of working conditions to confirm the predicting capabilities under the expected simulation conditions. Once this has been achieved, CFD results will allow to have an insight on the mechanisms that induce the jet breakup under such low velocities, and the best methods to maximize the evaporation and transformation processes that are vital for the future of SCR systems.

The study will be separated into two main aspects of the UWS injection process. The first one will focus on the near-field dynamics of the spray, including the inner flow dynamics of a UWS injector, characterizing the instabilities that disrupt the initial jet, and obtaining a representative droplet size distribution. Eulerian-Eulerian approach's feasibility is important, as two main techniques are commonly used (Mixture Model or Volume-Of-Fluid). Additionally, a proper meshing procedure needs to be identified, as such methods are associated with refined grids and so with high computational costs. With that, the study aims to hydraulically characterize the performance of the injector. Inner characteristics such as the needle lift are also parameters that cannot be easily obtained by other means. Two different injector geometries with two different working principles (pressure and pressure-swirl) will be analyzed in this way.

On the other hand, far-field dynamics simulation will be directed to represent the water and urea content evaporation for different working conditions. Splitting up the whole process into two separate problems allows to deepen further in each one of them, and separate the different time scales that rule the two regions. In this case, a widely used method named Discrete Droplet Model (DDM) will characterize both phases in an Eulerian-Lagrangian framework. For this, it is important to set the proper initial and boundary conditions of the spray simulation. As commonly used breakup models are not suited for low-velocity applications, initial droplet size distributions are typically used, therefore, finding the proper initial distribution is vital for obtaining accurate results. Not only that, but generating a droplet size Probability Density Function (PDF) initialization tool for DDM models similar to the *Blob* breakup models would reduce the need of a previous characterization of the spray. Maximum Entropy Methods (MEP) have gained popularity in predicting spray-like distribution functions and could work as a new breakup model applied to low-injection pressure sprays. Following the stages that the UWS goes through, the degradation of urea should also be modeled, transforming it into its by-products, highlighting the isocyanic acid and the ammonia, being the latter the responsible for the desired deNOx behavior. For that purpose, the *molten solid* approach will be included.

As the evaporation and degradation of the UWS stand as one challenge this technology is facing due to the limited time and space available, the injection angle variation for speeding up the phase change of UWS can be a driving parameter for that purpose. Analyzing and establishing an optimal injection angle for UWS sprays can be beneficial for future SCR systems, especially for light-duty applications.

Applying the generated computational framework and gained knowledge to a realistic SCR geometry is the final activity. It will provide information about the swirler geometry to maximize the ammonia quantity and an optimal uniformity index.

Computational calculations will be done on the commercial CFD code CONVERGE v3 [50], equipped with advanced meshing techniques such as Adaptive Mesh Refinement (AMR, [51]) to obtain time-feasible simulations. The mentioned CFD code has specific advantages over other packages as it includes the needed framework to fulfill the mentioned objectives. Its high amount of spray, turbulence, and chemical models allows recreating many problems, as well as reducing time-consuming tasks (i.e. meshing), which is automatically created with only a reduced set of input parameters.

1.3 Thesis Outline

The document has been organized into nine different chapters that will attempt to provide an insight into the computational methods that are put into practice for SCR reasons.

Chapter 1 is the present introduction, which includes the main objectives and motivations to carry out the research activity.

Chapter 2 will include an overview of the working principle of UWS injection and SCR systems. Additionally, it will cover the basic aspects of spray injection systems, breakup mechanisms, and droplet characteristics needed to understand the results that will be later presented

Chapter 3 will contain a brief literature review of the experimental and computational studies carried out on UWS systems.

Chapter 4 will go across the main computational methods included for the two main simulation types (far-field and near-field), as well as the setups that have been used for this purpose.

Chapter 5 is associated with the main findings and results that have been obtained computationally on the near-field region, covering the main hydraulic results and jet breakup characteristics.

Chapter 6 will show the results obtained through DDM approach on the far-field region of the spray, together with the presentation of the chemical model employed for characterizing the degradation of urea into ammonia.

Chapter 7 will apply the outcomes and knowledge acquired into a realistic close-coupled SCR geometry to assess the effectiveness of the swirler geometry

and the engine working conditions into the degradation of the urea and its uniformity at the entrance of the SCR catalyst.

Chapter 8 will present the Maximum Entropy Principle method for characterizing UWS sprays as an alternative way of predicting droplet size distributions apart from the common CFD approach, together with a comparison of the obtained results with experimental data.

Chapter 9 will conclude the Thesis document by including the main conclusions obtained, together with possible future work proposals to push forward the SCR technology.

References

[1] Kalghatgi, G. "Is it really the end of internal combustion engines and petroleum in transport?" In: *Applied Energy* 225 (2018), pp. 965–974. DOI: 10.1016/j.apenergy.2018.05.076.

[2] EU Commission. *Tracking EU Citizens' Interest in EC Priorities Using Online Search Data: The European Green Deal*. Publications Office, 2021. DOI: doi/10.2760/18216.

[3] Panigrahi, T. H., Sahoo, S. R., Murmu, G., Maity, D., and Saha, S. "Current challenges and developments of inorganic/organic materials for the abatement of toxic nitrogen oxides (NOx) – A critical review". In: *Progress in Solid State Chemistry* 68 (2022), p. 100380. DOI: 10.1016/j.progsolidstchem.2022.100380.

[4] Commission, E. "Questions and Answers : Commission proposal on the new Euro 7 standards". In: November (2022).

[5] Moore, C., Brown, S., MacDonald, P., Ewen, M., and Broadbent, H. "European Electricity Review 2022". In: *Ember* February (2022), p. 34.

[6] Wu, Y., Mei, J., Cai, T., Wang, W., Zhu, H., Sun, T. L., and Liu, D. "Reducing the NOx emissions during NH3 oxidation with Nickel modified Fe2O3-a promising cost-effective and environmentally friendly catalyst for NH3 combustion". In: *Combustion and Flame* 237 (2022), p. 111845. DOI: 10.1016/j.combustflame.2021.111845.

[7] Dinesh, M. H., Pandey, J. K., and Kumar, G. N. "Study of performance, combustion, and NOx emission behavior of an SI engine fuelled with ammonia/hydrogen blends at various compression ratio". In: *International Journal of Hydrogen Energy* 47.60 (2022), pp. 25391–25403. DOI: 10.1016/j.ijhydene.2022.05.287.

[8] Ai, W., Wang, J., Wen, J., Wang, S., Tan, W., Zhang, Z., Liang, K., Zhang, R., and Li, W. "Research landscape and hotspots of selective catalytic reduction (SCR) for NOx removal: insights from a comprehensive bibliometric analysis". In: *Environmental Science and Pollution Research* 30.24 (2023), pp. 65482–65499. DOI: 10.1007/s11356-023-26993-4.

[9] Solla, A., Westerholm, M., Söderström, C., Tormonen, K., Härmä, T., Nissinen, T., and Kukkonen, J. "Effect of ammonium formate and mixtures of urea and ammonium formate on low temperature activity of SCR systems". In: *SAE Technical Papers* (2005). DOI: 10.4271/2005-01-1856.

[10] Kröcher, O., Elsener, M., and Jacob, E. "New reducing agents for the low-NOx SCR technology". In: *5th International Exhaust Gas and Particulate Emissions Forum*. 2008, pp. 19–20.

[11] Budziankou, U., Quissek, M., and Lauer, T. "A Fast Modeling Approach for the Numerical Prediction of Urea Deposit Formation". In: 2020. DOI: 10.4271/2020-01-0358.

[12] Lauer, T. "Preparation of Ammonia from Liquid AdBlue – Modeling Approaches and Future Challenges". In: *Chemie-Ingenieur-Technik* 90.6 (2018), pp. 783–794. DOI: 10.1002/cite.201700107.

[13] Balland, J., Parmentier, M., and Schmitt, J. "Control of a Combined SCR on Filter and Under-Floor SCR System for Low Emission Passenger Cars". In: *SAE International Journal of Engines* 7.3 (2014), pp. 1252–1261. DOI: 10.4271/2014-01-1522.

[14] Bayer, T., Samuelsen, D., Bareiss, S., and Chaineux, M. "Double injection SCR – Bosch's development for future emission regulations". In: ed. by M. Bargende, H.-C. Reuss, and J. Wiedemann. Wiesbaden: Springer Fachmedien Wiesbaden, 2018, pp. 579–593. DOI: 10.1007/978-3-658-21194-3_45.

[15] Sala, R., Bielaczyc, P., and Brzezanski, M. *Concept of vaporized urea dosing in selective catalytic reduction*. 2017. DOI: 10.3390/catal7100307.

[16] Kapusta, Ł. J. "LIF/Mie Droplet Sizing of Water Sprays from SCR System Injector using Structured Illumination". In: *Proceedings ILASS–Europe 2017. 28th Conference on Liquid Atomization and Spray Systems*. Valencia: Universitat Politècnica València, 2017. DOI: 10.4995/ilass2017.2017.5031.

[17] Schiffmann, P., Lecompte, M., and Laget, O. "Experimental Investigation of Novel Ammonia Mixer Designs for SCR Systems". In: *SAE Technical Papers* 2018-April (2018), pp. 1–13. DOI: 10.4271/2018-01-0343.

[18] Hua, L., Zhao, Y. G., Hu, J., Tao, T., and Shuai, S. J. "Comparison between air-assisted and airless urea spray for diesel SCR System by PDA and CFD". In: *SAE Technical Papers* x (2012). DOI: 10.4271/2012-01-1081.

[19] Khan, D., Bjernemose, J. H., and Lund, I. "Confidence interval analysis of urea water solution spray measurement data from Phase Doppler Anemometry using numerical validations from a commercial CFD code". In: *ILASS-Americas 32nd Annual Conference on Liquid Atomization and Spray Systems,* 2022.

[20] Bracho, G., Postrioti, L., Moreno, A., and Brizi, G. "Experimental study of the droplet characteristics of a SCR injector spray through optical techniques". In: *International Journal of Multiphase Flow* 135 (2021), p. 103531. DOI: 10.1016/j.ijmultiphaseflow.2020.103531.

[21] Payri, R., Bracho, G., Gimeno, J., and Moreno, A. *Spray characterization of the urea-water solution (UWS) injected in a hot air stream analogous to SCR system operating conditions.* 2019. DOI: 10.4271/2019-01-0738.

[22] Nocivelli, L., Montenegro, G., Onorati, A., Curto, F., Dimopoulos Eggenschwiler, P., Liao, Y., and Vogel, A. *Quantitative Analysis of Low Pressure-Driven Spray Mass Distribution and Liquid Entrainment for SCR Application through a Mechanical Patternator.* Tech. rep. March. 2017. DOI: 10.4271/2017-01-0965.

[23] Lee, S. I. and Park, S. Y. "Numerical analysis of internal flow characteristics of urea injectors for SCR dosing system". In: *Fuel* 129 (2014), pp. 54–60. DOI: 10.1016/j.fuel.2014.03.031.

[24] Dörnhöfer, J., Börnhorst, M., Ates, C., Samkhaniani, N., Pfeil, J., Wörner, M., Koch, R., Bauer, H.-J., Deutschmann, O., Frohnapfel, B., and Koch, T. "A Holistic View on Urea Injection for NOx Emission Control: Impingement, Re-atomization, and Deposit Formation". In: *Emission Control Science and Technology* 6.2 (2020), pp. 228–243. DOI: 10.1007/s40825-019-00151-0.

[25] Venkatachalam, P., Sahu, S., and Anupindi, K. "Investigation of cross-stream spray injection and wall impingement in a circular channel for SCR application". In: *Thermal Science and Engineering Progress* 32 (2022), p. 101229. DOI: 10.1016/j.tsep.2022.101229.

[26] Spiteri, A. and Dimopoulos Eggenschwiler, P. "Experimental fluid dynamic investigation of urea-water sprays for diesel selective catalytic reduction-denox applications". In: *Industrial and Engineering Chemistry Research* 53.8 (2014), pp. 3047–3055. DOI: 10.1021/ie404037h.

[27] Kaźmierski, B. and Kapusta, Ł. J. "The importance of individual spray properties in performance improvement of a urea-SCR system employing flash-boiling injection". In: *Applied Energy* 329 (2023), p. 120217. DOI: 10.1016/j.apenergy.2022.120217.

[28] Postrioti, L., Brizi, G., Ungaro, C., Mosser, M., and Bianconi, F. "A methodology to investigate the behaviour of urea-water sprays in high temperature air flow for SCR de-NOx applications". In: *Fuel* 150.x (2015), pp. 548–557. DOI: 10.1016/j.fuel.2015.02.067.

[29] Surendran, M., Anand, T. N., and Bakshi, S. "Experimental investigation of the evaporation behavior of urea-water-solution droplets exposed to a hot air stream". In: *AIChE Journal* 66.2 (2020), e16845. DOI: 10.1002/aic.16845.

[30] Lieber, C., Koch, R., and Bauer, H. J. "Spray evaporation of urea–water solution: Experiments and modelling". In: *Experimental Thermal and Fluid Science* 116.February (2020), p. 110108. DOI: 10.1016/j.expthermflusci.2020.110108.

[31] Abu-Ramadan, E., Saha, K., and Li, X. "Modeling of the injection and decomposition processes of urea-water-solution spray in automotive SCR systems". In: *SAE 2011 World Congress and Exhibition* 2011-01-13.x (2011). DOI: 10.4271/2011-01-1317.

[32] Lundströml, A., Waldheim, B., Ström, H., and Westerberg, B. "Modelling of urea gas phase thermolysis and theoretical details on urea evaporation". In: *Proceedings of the Institution of Mechanical Engineers, Part D: Journal of Automobile Engineering* 225.10 (2011), pp. 1392–1398. DOI: 10.1177/0954407011406048.

[33] Tu, J., Yeoh, G. H., Liu, C., and Tao, Y. *Computational fluid dynamics: a practical approach*. Elsevier, 2023.

[34] Nocivelli, L., Montenegro, G., and Dimopoulos Eggenschwiler, P. "Low pressure-driven injection characterization for SCR applications". In: *SAE Technical Papers* 2019-April.April (2019), pp. 1–12. DOI: 10.4271/2019-01-0994.

[35] Varna, A., Boulouchos, K., Spiteri, A., Dimopoulos Eggenschwiler, P., and Wright, Y. M. "Numerical Modelling and Experimental Characterization of a Pressure-Assisted Multi-Stream Injector for SCR Exhaust Gas After-Treatment". In: *SAE International Journal of Engines* 7.4 (2014), pp. 2012–2021. DOI: 10.4271/2014-01-2822.

[36] Varna, A., Spiteri, A. C., Wright, Y. M., Dimopoulos Eggenschwiler, P., and Boulouchos, K. "Experimental and numerical assessment of impingement and mixing of urea-water sprays for nitric oxide reduction in diesel exhaust". In: *Applied Energy* 157 (2015), pp. 824–837. DOI: 10.1016/j.apenergy.2015.03.015.

[37] GÓRKA, K., KAŹMIERSKI, B., and KAPUSTA, Ł. "Numerical analysis of the flow rig for UWS spray examination in exhaust system-relevant conditions". In: *Combustion Engines* 186.3 (2021), pp. 103–112. DOI: 10.19206/ce-141182.

[38] Birkhold, F. *Selektive katalytische Reduktion von Stickoxiden in Kraftfahrzeugen: Untersuchung der Einspritzung von Harnstoffwasserlösung*. Aachen: Shaker Verlag, 2007.

[39] Kim, J. Y., Ryu, S. H., and Ha, J. S. "Numerical prediction on the characteristics of spray-induced mixing and thermal decomposition of urea solution in SCR system". In: *Proceedings of the 2004 Fall Technical Conference of the ASME Internal Combustion Engine Division*. 2004, pp. 165–170. DOI: 10.1115/icef2004-0889.

[40] Ebrahimian, V., Nicolle, A., and Habchi, C. "Detailed modeling of the evaporation and thermal decomposition of urea-water solution in SCR systems". In: *AIChE Journal* 58.7 (2012), pp. 1998–2009. DOI: 10.1002/aic.12736.

[41] Salvador, F. J. *Influencia de la cavitación sobre el desarrollo del chorro Diesel*. Reverté, 2007.

[42] Gimeno, J. "Desarrollo y aplicacion de la medida del flujo de cantidad de movimiento de un chorro diesel". PhD thesis. 2008.

[43] Garcia, A. "Estudio de los efectos de la Post Inyeccion sobre el Proceso de Combustion y la Formacion de Hollin en Motores Diesel". PhD thesis. Universitat Politecnica de Valencia, 2009, p. 237.

[44] Chavez, M. d. J. "Modelado CFD Euleriano-Lagrangiano del Chorro Diesel y evaluacion de su combinacion con modelos fenomenologicos y unidimensionales." PhD thesis. Valencia (Spain): Universitat Politècnica de València, 2013, p. 203. DOI: 10.4995/Thesis/10251/32954.

[45] Martí Gómez-Aldaraví, P. "Development of a Computational Model for a Simultaneous Simulation of Internal Flow and Spray Break-Up of the Diesel Injection Process". PhD thesis. Valencia (Spain): Universitat Politècnica de València, 2014. DOI: 10.4995/Thesis/10251/43719.

[46] Bautista Rodriguez, A. "Study of the Gasoline direct injection process under novel operating conditions". PhD thesis. Valencia (Spain): Universitat Politècnica de València, 2021. DOI: 10.4995/Thesis/10251/167809.

[47] Martínez García, M. "Computational Study of the Injection Process in Gasoline Direct Injection (GDI) Engines". PhD thesis. Valencia (Spain): Universitat Politècnica de València, 2022. DOI: 10.4995/Thesis/10251/185180.

[48] González Montero, L. A. "Computational and Experimental Study of the Primary Atomisation Process under Different Injection Conditions". PhD thesis. Valencia (Spain): Universitat Politècnica de València, 2022. DOI: 10.4995/Thesis/10251/190635.

[49] Moreno, A. E. "Experimental Study of the Urea-Water Solution Injection Process". PhD thesis. Valencia (Spain): Universitat Politècnica de València, 2022. DOI: 10.4995/Thesis/10251/181637.

[50] Convergent Science, ed. *CONVERGE 3.0 Manual*. Middleton, 2019.

[51] Plewa, T., Linde, T., and Weirs, V. G. "Adaptive mesh refinement-theory and applications". In: (2005).

Chapter 2

Fundamentals of SCR systems and UWS sprays

"The only source of knowledge is experience."
—Albert Einstein

2.1 Introduction

Due to the nature of ICE, combustion processes imply the generation of combustion products, which negatively affect the environment. Awareness of these effects appeared with the first *photochemical smog* events early in the 1950s due to the emission of unburnt hydrocarbon into the atmosphere. With the increase in demand of personal transportation solutions, such events became more common, and the first legislation limiting combustion emissions appeared. Although ICE have become incredibly cleaner and more efficient, emission regulations play an essential role in new ICE designs, as it is becoming increasingly harder to meet the established limits. Especially, CI engines have become the focus of recent emission norms due to generating NO_x. To deal with this issue, several technologies are available. SCR was initially implemented in Japan in the early 1970s on stationary applications of refinery processes [1] and oil and gas plants [2], where ammonia was used as the pollutant reduction agent. SCR systems have undergone a long way until the highly-efficient and non-toxic systems that are used in the present were obtained (Figure 2.1). It is worth mentioning the need to adapt these systems to

mobile applications, which has associated a reduction in their size. That is the result of the conjoined efforts of the scientific community towards a cleaner power generation and mobility solutions for the combustion processes.

In order to go from the initial SCR concept to the state-of-the-art systems embedded in today's light-duty vehicles, it has been vital to have knowledge of the NO_x generation mechanisms, limitations imposed by the emission norms, and spray systems. This chapter aims to provide insight into these topics so the reader can easily follow the concepts introduced in later stages of the thesis.

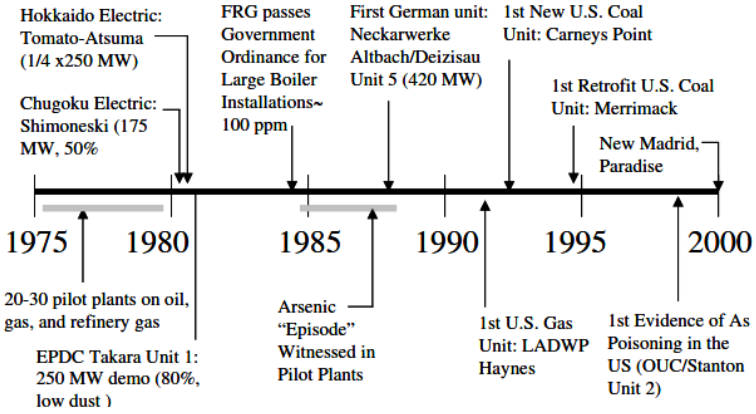

Figure 2.1: Main SCR events during its history [2].

2.2 NO_x formation mechanisms

Nitrogen Oxides, commonly known as NO_x, are mainly the NO_2 and NO compounds formed within combustion processes. NO is usually predominant due to its chemical kinetic dominance against NO_2 [3].

2.2.1 Generation of NO

Three main NO formation mechanisms have been observed as a consequence of combustion processes within ICE:

- Thermal mechanism
- Prompt mechanism
- Intermediate N_2O mechanism

2.2.1.1 Thermal mechanism

The thermal mechanism is achieved at high-temperature conditions (T > 2100 K) and uses the available oxygen on the surrounding air as oxidizer. It does not directly oxidize the diatomic nitrogen due to the high energy it would require to break the N_2 molecule. Instead, a Zeldovich mechanism [4] through a chain reaction is established, which dissociates the diatomic nitrogen into atomic nitrogen, which is reactive (Equation 1, Equation 2). The mono-atomic nitrogen generated, together with the hydroxile OH, form the extended mechanism (Equation 3) [5].

$$N_2 + O \rightleftharpoons NO + N \quad \{1\}$$

$$N + O_2 \rightleftharpoons NO + O \quad \{2\}$$

$$N + OH \rightleftharpoons NO + H \quad \{3\}$$

As observed, the Zeldovich mechanism is initiated through the dissociation of the O_2 molecules at temperatures above 1800 K-2000 K. The rate-limiting step in the NO formation is on the dissociation of the diatomic nitrogen, with an activation energy of 314 kJ mol^{-1}.

2.2.1.2 Prompt mechanism

The prompt mechanism proposed by Fenimore [6] happens in the nearby region of the flame. It is based on the reaction of diatomic nitrogen with partially decomposed hydrocarbons during the early stages of the combustion process to form amines and cyanic components, ending up in forming NO. It has been established that the NO contribution under the prompt mechanism is significant in lean operation and Exhaust Gas Recirculation (EGR) conditions [7], which happens where thermal NO_x lose predominance. This mechanism is not as dependent on the working temperature and has associated short length scales.

2.2.1.3 Fuel mechanism

NO_x can also be formed due to the nitrogen compounds present within the liquid hydrocarbons. The oxidation of that nitrogen leads directly to generating NO_x. The phenomenon is well understood, and it has been established that it is not as temperature-dependent as the thermal NO_x are. Therefore,

reducing the flame front temperature does not significatively helps mitigating them. The contribution of this NO_x source to total NO_x of the system depends on stoichiometry and reaction time of the combustion. For the inherent nature of this mechanism, nitrogen-free fuels such as H_2 cannot generate NO through this pathway.

Figure 2.2 shows the contribution of each one of the NO formation processes to the total NO contribution.

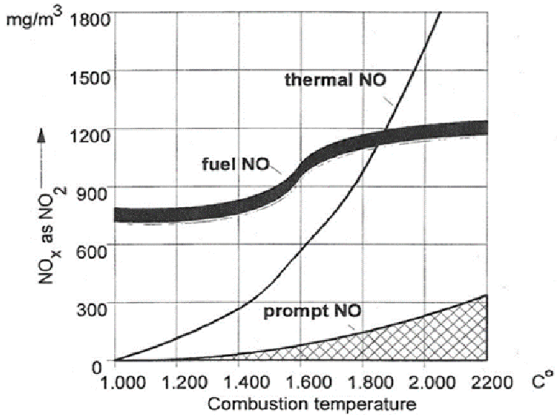

Figure 2.2: Contribution of each one of the formation mechanisms to the total NO_x [8].

A fourth mechanism occurs at low-temperature conditions (T<1500 K), lean and high-pressure conditions, recombining the N_2 and O, where the generation of N_2O dissociates into molecules of NO. The process is driven through Equation 4, Equation 5, Equation 6 according to Turns [9].

$$N_2O + O \rightleftharpoons NO + NO \quad \{4\}$$

$$N_2O + O \rightleftharpoons N_2 + O_2 \quad \{5\}$$

$$N_2O + M \rightleftharpoons N_2 + O + M \quad \{6\}$$

2.2.2 Generation of NO_2

NO_2 generation can not be neglected in combustion processes, as it can account up to the 30% of the total NO_x emissions of an ICE [10]. It occurs

where NO molecules are taken to rich HO_2 regions. It rapidly decomposes into NO molecules at high temperatures, and its importance increases at a low working temperature. NO components can be converted into NO_2. In CI engines, its contribution increases if there is a presence of a Diesel Oxidation Catalyst (DOC), in which in addition to oxidizing unburnt HC and CO, NO is transformed into NO_2. Its formation region is placed where temperature drops are expected, such as in exhaust ducts, chimneys and on free atmosphere conditions [11].

2.3 NO_x limitations, EURO norms

Across the globe, NO_x emissions have been limited thanks to their respective norms. In the United States, the U.S. Environmental Protection Agency (EPA) proposed its limits in 1987, as well as in China, the CH rules were implemented. In the European environment, NO_x emissions have been limited on heavy-duty vehicles since 1988 [12]. From there, more and more restrictive limitations have been imposed not only on heavy-duty but also to light duty applications with the introduction of the EURO norm.

These emission limits are taken depending on the category and purpose of the vehicle [13]. Latin norm numbers (e.g. EURO 6) refer to light-duty vehicles, while roman numbers (e.g. EURO VI) refers to heavy-duty vehicles.

- **M Category**: it corresponds to engine-powered vehicles designed for passenger transportation and their luggage. It is subdivided into several categories depending on the number of seats and the vehicle weight.
  - M1: up to 8 passenger seats
  - M2: more than 8 seats and $W < 5000\,kg$
  - M3: more than 8 seats and $W > 5000\,kg$
- **N Category**: it corresponds to engine-powered vehicles designed for goods transportation. Depending on their weight (W), several subcategories can be found. In this work, only the N1 and N2 limits will be shown.
  - N1 Class I: $W < 1305\,kg$
  - N1 Class II: $1305\,kg < W < 1760\,kg$
  - N1 Class III: $1760\,kg < W < 3500\,kg$
  - N2: $3500\,kg < W < 12\,000\,kg$

Figure 2.3 shows the limits of NO_x emission from past norms (EURO 3 - EURO 6) in addition to the proposed limits of the upcoming EURO 7 [14] legislation.

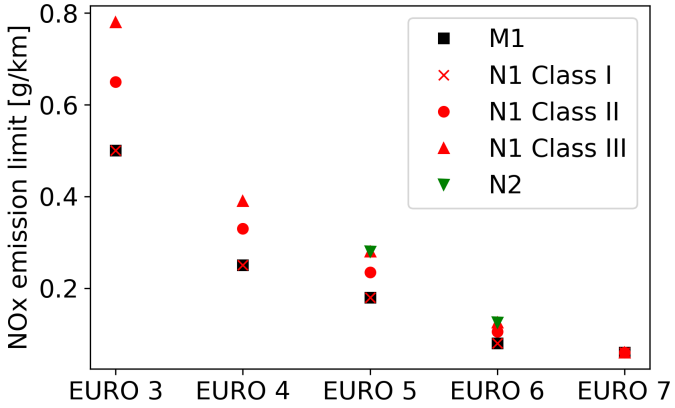

Figure 2.3: NO_x limit evolution of the EURO norms and estimation of the limit of future EURO 7 for light-duty vehicles.

For example, N1 Class III vehicles will have a reduction in NO_x of 92.5% with respect to the limits imposed by EURO 3. Similar reductions have been seen for heavy-duty vehicles. Not only that, but in addition to total mass, PM restricts the size of the particulate that can be emitted within the exhaust gases. NO_x and PM creation are inversely opposed, as NO_x are driven by high-temperature regions, while PM are generated on low-temperature in-cylinder conditions [15]. To prevent the emission of a large amount of PM, it is state-of-the-art introducing a Diesel Particulate Filter (DPF) on the exhaust pipe.

Additionally, Real Driving Emissions (RDE) limitations were introduced for EURO 6 vehicles due to the differences in emissions measured on laboratory or with portable measuring systems (PMS). In that sense, vehicles are also tested on the road with typical weight and driving patterns. Several revisions of the EURO 6 norm have been implemented, reducing the NO_x conformity factors.

All these reductions imply that meeting the limitations is becoming more complicated, and the systems used to mitigate the NO_x and PM need to be increasingly efficient.

2.4 NO_x reduction methods

Regarding the possibilities of reducing NO_x in CI engines, two main approaches can be taken: pre-combustion processes and post-combustion NO_x mitigation.

2.4.1 Pre-combustion methods

Engine parameters such as injection timing, split injection approaches, injection pressure, or using oxygenated fuels can significantly reduce the generated NO_x during the combustion process. For example, advancing the injection timing duration in a pilot-main injection strategy can generate a homogeneous mixture leading to lower combustion temperatures and reducing NO_x emissions. The mentioned oxygenated fuels can also achieve low combustion temperature, as a better homogenization is achieved [16–18]. Other combustion techniques such as Premixed Charge Compression Ignition (PCCI) or water injection processes can also lower the combustion temperature and hence reducing NO_x emissions. Homogeneous Charge Compression Ignition (HCCI) techniques also decrease NO_x production up to a 10% [19] by generating a homogeneous mixture of fuel-air and combusting it by compression.

2.4.2 Post-combustion methods

2.4.2.1 Exhaust Gas Recirculation

Exhaust Gas Recirculation (EGR) is a deNO_x technique in which the combustion gases are redirected into the combustion chamber. The lower air-fuel ratio induces a lower combustion temperature, preventing NO_x formation. On the other hand, a reduction in flame temperature can lead to an increase in PM such as soot. This phenomenon is identified as the NO_x-PM trade-off, in addition to problems related to higher lube degradation and higher engine wear.

2.4.2.2 NO_x Storage Catalyst

A NO_x Storage Catalyst (NSC) is used to capture the emitted gases by using an excess of air. Alkaline metals are used as a capturing material in which NO_2 gets trapped [20]. NO, on the other hand, cannot be stored by this method and therefore needs a previous oxidation reaction. For that purpose, a DOC has to be installed upstream of the NSC to convert NO components into NO_2, and oxidizing CO into CO_2 and HC. The regeneration of NSC is

done by rich operation conditions, in which the stored NO_2 is oxidized thanks to the incoming CO and HC products [21]. Nonetheless, such regeneration can lead to the formation of harmful products such as NH_3 and N_2O.

2.4.2.3 Selective Catalytic Reduction

The most widely deNO_x system used in IC engines is Selective Catalytic Reduction (SCR). SCR employs the transformation of NO_x into non-harmful gases (diatomic nitrogen and water) thanks to the reaction with ammonia (NH_3) inside a catalyst. It exploits the *selective* reactivity of NO_x to react with NH_3 instead of O_2 [22]. Being this technique the main subject of this Thesis, a more in-detail description will be provided in the following section.

2.5 Selective Catalytic Reduction

Several pathways are possible for the NO_x reduction, which depends on the NO_2:NO_x ratio at the system inlet. The called *standard* reaction is depicted by Equations 7 and 8. If there is an equimolar NO:NO_2 ratio, a *fast* reaction occurs (Equation 11) due to its lower activation barrier and higher activation rate at low temperatures [23]. Thus, a DOC is usually fitted upstream of the SCR system to oxidize NO into NO_2 and achieve the *fast* reaction. Nonetheless, this is not perfectly achievable for all the working temperatures of the system, as at low temperatures, the DOC will not be generating sufficient NO_2. The *slow* reaction is given by Equations 9 and 10, and happens where there is a NO:NO_2 ratio greater than unity. This slow reaction can also happen if the fitted DOC produces an excessive amount of NO_2 by oxidation means. These reactions are undesirable as they are considered too slow above 200 °C [24] and can produce unwanted N_2O for intermediate and low temperatures [25], which is considered a potent greenhouse gas and an ozone-depletion substance [26] that perdures for a considerable time [27].

$$6\,NO + 4\,NH_3 \longrightarrow 5\,N_2 + 6\,H_2O \quad \{7\}$$

$$4\,NO + 4\,NH_3 + O_2 \longrightarrow 4\,N_2 + 6\,H_2O \quad \{8\}$$

$$6\,NO_2 + 8\,NH_3 \longrightarrow 7\,N_2 + 12\,H_2O \quad \{9\}$$

$$2\,NO_2 + 2\,NH_3 \longrightarrow N_2 + N_2O + 3\,H_2O \quad \{10\}$$

$$2\,NO + 2\,NO_2 + 4\,NH_3 \longrightarrow 4\,N_2 + 6\,H_2O \quad \{11\}$$

Storage and transportation of NH_3 have associated toxicological issues, and therefore it is not directly injected into the exhaust gases. Instead, a eutectic mixture of innocuous Urea and Water is used, usually called Urea-Water Solution (UWS) or Diesel Exhaust Fluid (DEF), with a proportion of 32.5% wt of urea [28]. The desired ammonia is obtained thanks to the evaporation of water and degradation of urea into ammonia prior to the monolith as it can be seen on Figure 2.4. This ammonia will reduce the NO_x previous to exhausting into the atmosphere. Based on the amount of NO_x observed and the temperature prior to the catalyst entrance, the control unit of the urea dosing module determines the amount of working fluid and its injection pressure to introduce the amount of NH_3 that needs to be generated.

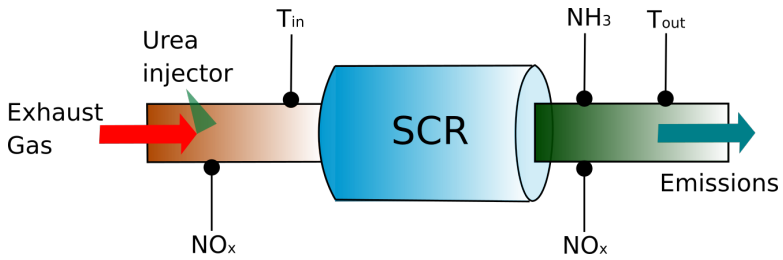

Figure 2.4: Schematic view of the SCR system (based on [29]).

There are two pathways for the transformation of urea into ammonia after the water content has first evaporated and the urea has molten. First, through a thermolysis process, urea is converted into NH_3 and isocyanic acid (HNCO) (Equation 12). From there, the HNCO is hydrolyzed thanks to the evaporated water into a second molecule of NH_3 and CO_2 (Equation 13). The selected proportion of Urea:Water is chosen to minimize the freezing temperature of the mixture. The use of urea has certain drawbacks for its use such as the melting point at $-11\,°C$, which implies the need for de-freezing mechanisms for its use in cold locations, or low NH_3 storage stability as it slowly generates ammonia above $40\,°C$, and the mixture has a low NH_3 capacity ($0.2\,kg\ NH_3/kg$) [30].

Alternative sources of ammonia storage have been sought to achieve transformation at ambient conditions and improve the melting point or increase the ammonia yield. From the possible alternatives, methanamide [30], metal am-

mine chloride salts [31], or ammonium formate [32] are highlighted. Nonetheless, their qualities remain insufficient to substitute commercial UWS.

$$(NH_2)_2CO \longrightarrow HNCO + NH_3 \quad \{12\}$$

$$HNCO + H_2O \longrightarrow NH_3 + CO_2 \quad \{13\}$$

To maximize the performance of the SCR system is vital to achieve enough quantity of NH_3 prior to the catalyst. To do so, appropriate atomization of the UWS and evaporation of the generated droplets are needed. The UWS dosing units employed to do so generally inject at relatively low injection pressures. Additionally, the limited space for the UWS to undergo the relevant physical and chemical processes make it a challenging task. For that reason, a mixer geometry is generally used within the injection point and the monolith entrance. An example of line and swirl-type mixers can be seen in Figure 2.5. The purpose of these elements is to promote the breakup of UWS into smaller droplets and enhance their evaporation. Additionally, it helps achieving flow uniformity at the SCR entrance. Line Mixers help to uniform the flow in the regions near the pipe wall, while Swirl Mixers help to uniform the flow at the pipe center [33]. Introducing this solution to the tight spaces problem inherently induces droplet impingement problems with the exhaust pipe and the mixing geometries.

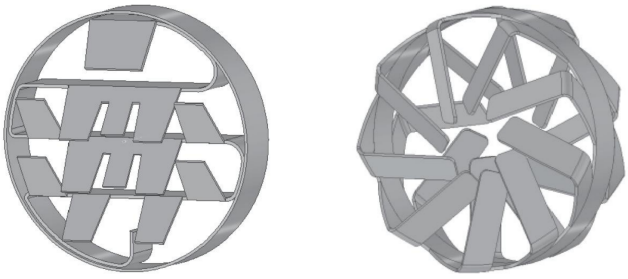

(a) Line Mixer. (b) Swirl Mixer.

Figure 2.5: Mixer typologies (Image extracted from [34]).

The need of implementing a mixer geometry adds an extra level of complexity for SCR systems. Periodic impingement of UWS droplets in this region as well as in the exhaust walls can affect the heat transfer effects and locally decrease the temperature of the surface. Consequently, there is an increase in

risk of film formation and urea precipitation to produce unwanted deposits. Crystallized urea deposits can also degrade into unwanted by-products, such as biuret, triuret, ammeline, melamine or ammelide [35]. Those products are highly dependent on the tailpipe temperature, and their decomposition might need considerably high temperatures to take place (ammeline decomposes at 973 K [35]).

As it can be seen, SCR presents a challenging methodology for $deNO_x$ purposes that involves several physical and chemical processes. To provide an efficient SCR system, each one of the problems (injection, atomization, evaporation, droplet impingement, and urea-to-ammonia transformation) need to be adequately understood.

2.5.1 UWS dosing units

UWS injection systems usually inject at relatively low injection pressures ($\Delta P = 3-10$ bar) to produce a specific droplet size distribution which depends mainly on the application. These low working injection pressures are set to have low-cost low-maintenance systems compared to air-blast atomizers, which need to compress air as well. Additionally, with higher injection velocities the urea might not have time to convert into NH_3 and impinge into the pipe surfaces. The injectors are responsible for delivering the pressurized mixture into the exhaust pipe through the orifices. When the injector is at rest, the spring forces the needle to contact with the needle seat, and the fluid cannot flow through. Once the coil is energized, the needle core moves upwards, freeing the nozzle section and injecting the UWS. At all times, the working fluid is supplied from within the needle thanks to orifices located in it. A schematic and realistic view of such system can be observed in Figure 2.6.

Two main typologies of UWS dosing units can be seen in literature and on commercial systems, depending on the desired spray morphology, which will be seen later in the chapter.

2.5.2 Hydraulic characterization

The inner morphology of the UWS dosing module, together with the shape of the exit orifices heavily influence the formation and characteristics of the consequent UWS spray and, therefore, its later evaporation and urea degradation processes. Usually, the performance of an injector is measured by obtaining non-dimensional parameters at the nozzle exit based on the ratio of actual and theoretical flow variables. Therefore, it depends on the momentum flux mea-

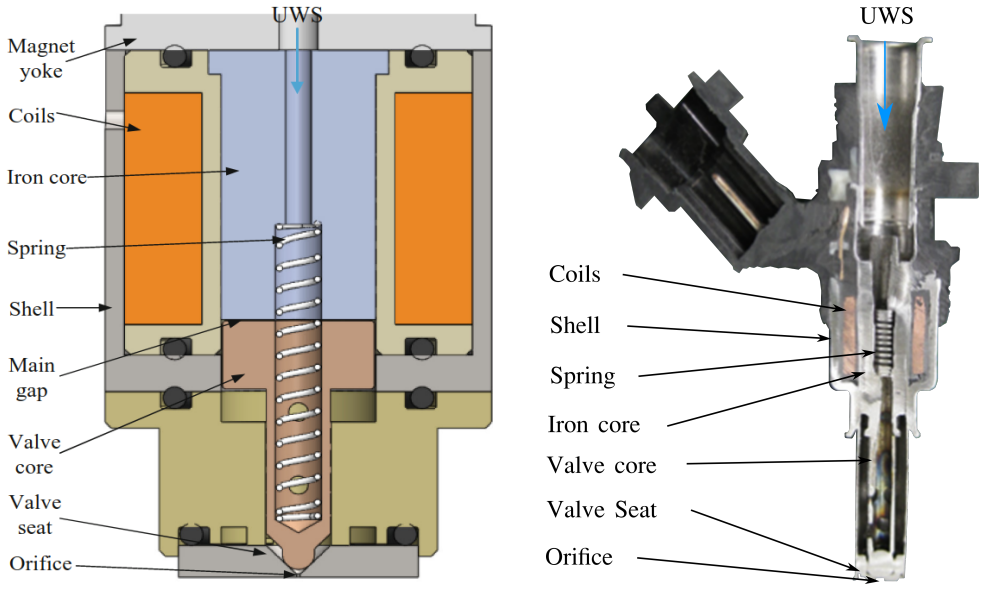

(a) Schematic view [36].

(b) Cross-section view, adapted from [37].

Figure 2.6: Schematic and real representation of the inner mechanism of a UWS dosing unit.

surement in this section (Equation 2.1), and the mass flow rate (Equation 2.2). Note that A_0 is the geometric area of the orifices.

$$\dot{M} = \int_{A_0} \rho_f u^2 dA \tag{2.1}$$

$$\dot{m} = \int_{A_0} \rho_f u dA \tag{2.2}$$

On the one hand, theoretical values of mass flow rate and momentum can be derived from the Bernoulli equation (Equation 2.3), which determines the ideal velocity based on the known pressure difference upstream (p_1) and downstream the orifice section (p_2), taking the shape of Equation 2.4. Based on this velocity, an expression of the ideal mass flow rate can be extracted (Equation 2.5). This expression shows the linear relationship of the mass flow rate with $\sqrt{\Delta p}$.

$$\frac{p_1}{\rho_l} = \frac{p_2}{\rho_l} + \frac{1}{2} u_{ideal}^2 \tag{2.3}$$

$$u_{ideal} = \sqrt{\frac{2\Delta p}{\rho_l}} \tag{2.4}$$

$$\dot{m}_{ideal} = \rho_l u_{ideal} A_0 \tag{2.5}$$

On the other hand, real flux through the orifices will be determined by an effective velocity (u_{ef}) and an effective area (A_{ef}) through which the fluid flows. These can be obtained from the measured momentum and mass flow rate [38]. These variables can simplify the previous equations, rewriting them into the shape of Equation 2.6 and Equation 2.7.

$$\dot{M} = \rho_l u_{ef}^2 A_{ef} \tag{2.6}$$

$$\dot{m} = \rho_l u_{ef} A_{ef} \tag{2.7}$$

Based on these concepts, several flow coefficients can be defined:

Discharge Coefficient (C_d) This coefficient relates the measured mass flow rate to the previously defined theoretical mass flow rate value (Equation 2.8).

$$C_d = \frac{\dot{m}}{\dot{m}_{ideal}} = \frac{\dot{m}}{\rho_l u_{ideal} A_0} \tag{2.8}$$

Velocity Coefficient (C_v) It is the ratio between the effective velocity and the theoretical velocity (Equation 2.9).

$$C_v = \frac{u_{ef}}{u_{ideal}} \tag{2.9}$$

Momentum Coefficient (C_m) In the same way, the momentum coefficient is represented by the ratio between the measured momentum ($\dot{M}$) and the theoretical momentum ($\dot{M}_{ideal}$) (Equation 2.10).

$$C_m = \frac{\dot{M}}{\rho_l u_{ideal}^2 A_0} \tag{2.10}$$

Area Coefficient (C_a) The area coefficient relates the effective area to the geometric area of the discharge orifice (see Equation 2.11).

$$C_a = \frac{A_{ef}}{A_0} \tag{2.11}$$

2.5.3 Spray characterization

The purpose of the UWS injectors is to transform the bulk working fluid into the desired NH_3 component. The kinetic energy of the fluid disintegrates the initial jet and produces a set of tiny droplets and ligaments whose evaporation is enhanced. The breakup is the result of growing instabilities due to the effect of different forces that disintegrate the initial jet into a distribution of droplet sizes resulting from its chaotic nature. The instabilities are a consequence of the disruptive and cohesive forces that act on the liquid jet. The disruptive forces are composed of the turbulent fluctuations of the jet, the aerodynamic interaction with the surrounding gases, and the transition from inner flow to free jet, which can cause instabilities on the liquid surface. On the other hand, cohesive forces are mainly composed of surface tension, which opposes the disruptive forces and tries to restore the initial shape of the jet.

There are two main typologies of UWS sprays for commercial applications:

Solid cone This type of sprays are formed by plain orifices on a pressure injector, forming an even spray over a circular area. They generally show narrow spray cone angles, and droplet coalescence is a critical phenomenon to consider. It has a relatively low performance on atomizing the liquid jet, as larger droplets can be found in the core, and smaller particles are to be found in the outskirts. A representation can be seen in Figure 2.7a.

Hollow cone This other typology is formed by pressure-swirl atomizers, where a swirling motion is transferred to the working fluid using a swirling chamber within the device. The fluid, once injected, converts its swirling momentum into tangential momentum, creating a hollow-cone shape. Due to the tangential nature of the injected spray, the angle of these sprays is considerably larger, reducing the problem of coalescence, and reducing the size of the resulting droplets, in addition to providing a more uniform set of drop sizes. An example is shown in Figure 2.7b.

2.5.3.1 Primary Atomization

Primary atomization is the disintegration of a liquid jet due to the growth of instabilities up to a critical oscillation that causes total disruption forming a

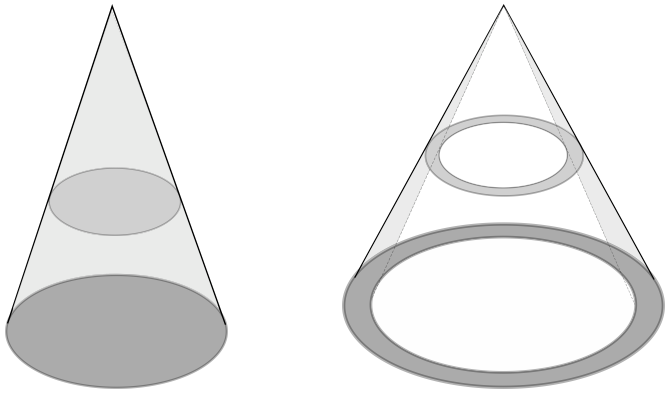

(a) Solid cone spray. (b) Hollow cone spray.

Figure 2.7: Graphical representation of the two main spray typologies employed for UWS applications.

set of subsequent droplets. The initially injected jet, due to the aerodynamic interaction, forms droplets to which it progressively transfers its mass and momentum until it disappears (see Figure 2.8). Several breakup regimes have been identified, and through a Ohnesorge number (Equation 2.12) - Reynolds number (Equation 2.13) chart proposed by Ohnesorge [39], such disruptive mechanism can be depicted.

$$Oh = \frac{\mu_l}{(\rho_l \gamma d_0)^{0.5}} \tag{2.12}$$

$$Re = \frac{\rho_l u_l d_0}{\mu_l} \tag{2.13}$$

Based on the Oh-Re chart, Reitz [42] identified four breakup regimes depending on the injection velocity by analyzing the data obtained on diesel sprays.

- **Rayleigh breakup.** This regime is caused by the growth of axisymmetric oscillations on the jet, mainly caused by the surface tension forces. The size of the droplets is greater than the orifice diameter.
- **First wind induced.** With increasing injection velocities, the relative motion between the liquid and the gas phase produces a static pressure distribution that opposes the surface tension forces, producing a set of droplets of a similar diameter to the orifice size.

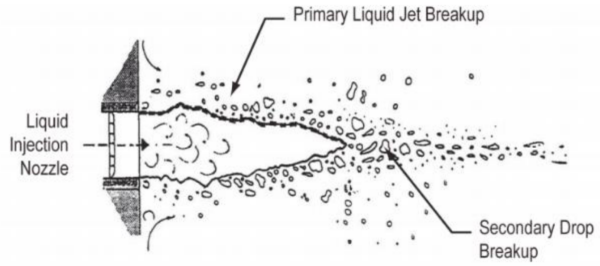

(a) Schematic view of jet breakup (Image adopted from [40]).

(b) UWS breakup (adapted from [41]).

Figure 2.8: Representation of the primary and secondary breakup mechanism.

- **Second wind induced.** Short wavelength waves grow due to the increasing relative motion of the jet and the surroundings, again opposed by the surface tension forces. Generated droplets are now considerably smaller than the initial jet diameter.
- **Atomization.** The jet instabilities grow considerably faster and closer to the orifice exit due to the exacerbated effect of the aerodynamic forces.

A graphic depiction of the different breakup regimes based on the Re and Oh is shown in Figure 2.9. Several expressions have been obtained through numerous studies to determine in which conditions the transition happens [43–45]. Although the figure shows clear differentiation between the regimes, the transition between one regime and the other is not abrupt. It needs to be highlighted that these obtained regimes were obtained for a plain-orifice nozzle with an aspect ratio of 1:10, hence these breakup regimes could move for different nozzle geometries and applications. With a fixed stability number, increasing the jet velocity transitions the breakup typology from lower to upper regimes. On the other hand, for an established Reynolds number, if

the surface tension is decreased, the stability number increases, and higher breakup regimes are achieved.

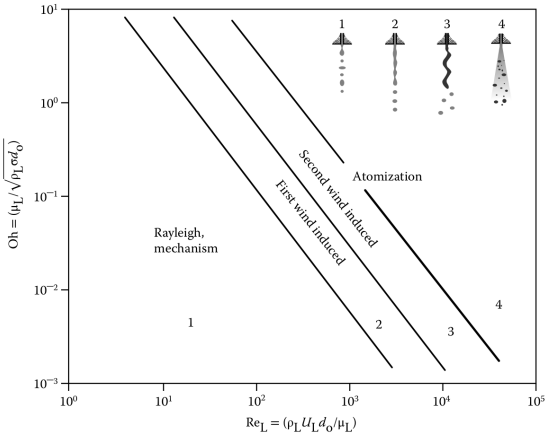

Figure 2.9: Ohnesorge-Reynolds chart (extracted from [46]). Numbers indicating the breakup regime.

The point where the initial liquid jet has wholly disintegrated into ligaments and droplets is commonly known as intact core length, which directly relates with the atomization regime the jet is subjected to.

2.5.3.2 Secondary Atomization

Once the initial liquid jet has broken up into a set of ligaments and droplets, the aerodynamic forces acting on this initial droplet outcome may again overcome their cohesive forces, breaking up once again into another set of droplets with smaller characteristic diameters. This phenomenon is called secondary atomization. As mentioned, aerodynamic forces compete against surface tension forces to determine if a droplet will break again or not. For that purpose, the Weber number based on the droplet radius r (Equation 2.14) provides a reasonable approach in determining the droplet outcomes. Different breakup regimes have been observed based on the critical We number according to wide research previously done on the subject. Five main regimes were observed, and critical We numbers according to [47], have been included in Table 2.1.

$$We = \frac{\rho_a u_r^2 D}{\gamma} \tag{2.14}$$

Breakup Regime	Critical We number
Vibrational breakup	We <= 12
Bag break	12 < We <= 50
Bag and stamen breakup	50 < We <= 100
Sheet stripping	100 < We <= 350
Catastrophic breakup	We > 350

Table 2.1: Critical Weber for different droplet breakup regimes [47].

The previous transitional We values are obtained for a specific Ohnesorge number. Hence, this non-dimensional number also can modify the mode, as detailed in the work by [48], and depicted in Figure 2.10.

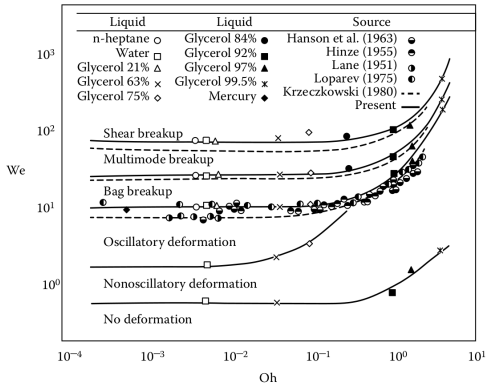

Figure 2.10: Droplet breakup modes based on the Weber and Ohnesorge number (Image adapted from [48]).

Due to the low injection pressures used in UWS applications, the primary breakup of the liquid jet results in low We droplets, and therefore vibrational deformation should happen. In this regime, unequal pressure distribution due to aerodynamic effects deform the droplet. At very low We numbers, surface tension forces can restore the droplets' initial shape, but droplet breakup can be induced with higher energy oscillations. This first breakup regime does not always occur [47], and therefore there is little information about it. The corresponding Oh of UWS sprays under the conditions used in this Thesis are very similar to each other (comparable to Oh values from [41]), hence the dependency on Oh will not be considered for the following study.

2.5.3.3 Microscopic spray characteristics

The microscopic aspect of the characterization of a spray focuses on describing the dynamics undergone by the droplets generated through the liquid vein breakup. These dynamics will be of great importance for proper mixing with the surrounding air and enhancing the evaporation rate. Once the primary and secondary breakup have happened, the number of droplets formed can show a wide range of characteristics. Each one of these droplets depicts different size, shape and velocity characteristics. These characteristics are additionally variable in time due to the physical processes that they undergo (e.g. drag, coalescence, evaporation).

Droplet size characterization As mentioned, the breakup process does not generate a specific droplet size but provides a broad spectrum of droplet size possibilities. When it specifically comes to UWS sprays, it can be stated that generated sprays can have droplets ranging from 10 µm-160 µm [49]. Based on that, the spray can be characterized by two means, either a representative droplet size, or a Probability Distribution Function (PDF).

Droplet size PDFs are obtained from histogram distributions of the droplet diameters found within a spray. In a histogram, each one of the droplets is assigned to a bin with specific size width. If the size of the bins of the histogram is progressively reduced to an infinitesimal width, it no longer represents the number of droplets that fall within each bin, but it represents the frequency of each one of the droplet sizes. This transition can be observed in Figure 2.11. Additionally, droplet size can also be represented using Cumulative Distribution Functions (CDF). CDFs represent the percentage of the total amount of droplets (in number-based distributions) that fall below each one of the droplet sizes. This procedure is usually taken as well to represent the velocity of the droplets on the spray. Mathematical functions are commonly used to approach experimentally-obtained droplet size distributions, and are helpful in representing sprays. From the different statistical distributions known, Rosin-Rammler mathematical function [50] is the most widely used representation of droplet size distributions. In its mathematical expression given by Equation 2.15, two constants, q and X, define the shape of the distribution. At the same time, Q represents the fraction of total volume contained in drops whose diameter is smaller than D. q in the other hand, represents the spread of the droplet size distribution. X represents the diameter such that 63.5% of the liquid volume is in smaller droplets.

$$1 - Q = \exp\left(-\left(D/X\right)^{q}\right) \tag{2.15}$$

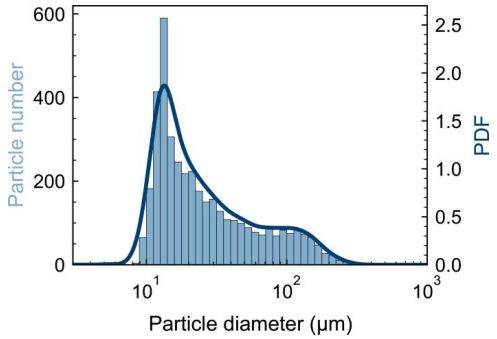

Figure 2.11: Number-based histogram and PDF (in μm^{-1}) of a spray data set (Image extracted from [51]).

Out of this distribution, some characteristic diameters can be extracted that help to understand the droplet size distribution further. These diameters are included in Table 2.2. Additionally, Figure 2.12 shows the location of the introduced diameters into a PDF plot.

Name	Symbol	Q value
Peak diameter	D_{peak}	Peak value
Mass median diameter	$D_{0.5}$	Q = 50%
Characteristic diameter	$D_{0.632}$	Q = 63.2%
Maximum diameter	$D_{0.999}$	Q = 99.9%

Table 2.2: Representative diameters from a droplet size distribution.

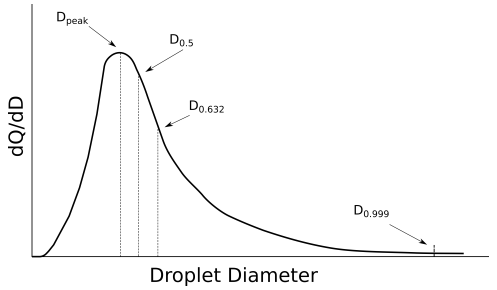

Figure 2.12: Location of the representative diameters in a PDF (based on [52]).

Another way of representing the droplet sizes of a spray is through droplet mean diameters. In this way, the complete set of droplets conforming a spray

is reduced to a single value. Several definitions are available, and they are shown in Table 2.3.

Mean Name	Symbol	Meaning	Expression
Length	D_{10}	Mean Geometrical Diam.	$\frac{\sum N_i D_i}{\sum N_i}$
Surface Area	D_{20}	Mean surface area	$\left(\frac{\sum N_i D_i^2}{\sum N_i}\right)^{0.5}$
Volume	D_{30}	Mean volume/mass	$\left(\frac{\sum N_i D_i^3}{\sum N_i}\right)^{0.5}$
Volume-length	D_{31}	Mean volume/length	$\left(\frac{\sum N_i D_i^3}{\sum N_i D_i}\right)^{0.5}$
Sauter Mean Diam.	D_{32}	Mean vol/surface	$\frac{\sum N_i D_i^3}{\sum N_i D_i^2}$

Table 2.3: Characteristic droplet mean diameters [53].

Droplet-droplet collision Sprays can generally be divided into three distinct regions. The first one is where the aerodynamic effects breakup the liquid vein into a set of droplets. The second one takes place immediately after the jet has broken up, and there is a high amount of droplets located in a close region. This zone is commonly known as the dense region, and there are strong interactions between the droplets. As the spray cone widens, the separation between the droplets increases, and the influence between them decreases. Within the dense region, it is very likely that collision between two droplets take place. This collision can affect the spray characteristics and modify the evaporation dynamics. Different outcomes can be obtained depending on the trajectories of two-colliding droplets, their relative velocities, and their size ratio. Several studies have focused on the possible outcomes of these interactions. Based on the work of Ashgriz and Givi [54], the outcomes of a water droplet-droplet collision can be summarized in *Bouncing*, *Grazing*, *Coalescence*, *Temporary Coalescence*, and *Shattering*. The *bouncing* phenomenon occurs when the two droplets do not physically collide to the formation of a gas film between them, causing them to bounce off. *Grazing* refers to the situation where the two droplets touch slightly. On the other hand, *coalescence* means that the two droplets collide, forming a new droplet. *Temporal coalescence* happens where the coalescence effect is not permanent, causing the joined droplet to separate again into two individual drops. Finally, *shattering* occurs on high energy impacts, where a set of smaller droplets is generated due to the collision.

On the other hand, other studies came up with five different regimes, depending on the Weber number of the droplet, and a non-dimensional impact factor B (see Equation 2.16), which takes into account their diameter (d_1 and d_2) and the alignment of the two colliding droplets (b). It results in the collision map [55] shown in Figure 2.13. At low Weber numbers, there is a slow coalescence effect after minor deformation. Another coalescence region is found at a relatively higher We. These two regimes would fit within the *coalescence* regime found by Ashgriz and Givi. A bouncing regime is also detected at a higher We than the first coalescence regime, and two types of *temporary coalescence* are found. At low impact factor values (almost head-on collision) and high We, droplets initially merge, and the surface tension forces, together with the internal flow formed caused the merged droplet to elongate and separate. At higher impact factors (higher droplet-to-droplet offset) the momentum of the non-impacted region of the droplets causes to produce satellite droplets.

$$B = \frac{2b}{d_1 + d_2} \tag{2.16}$$

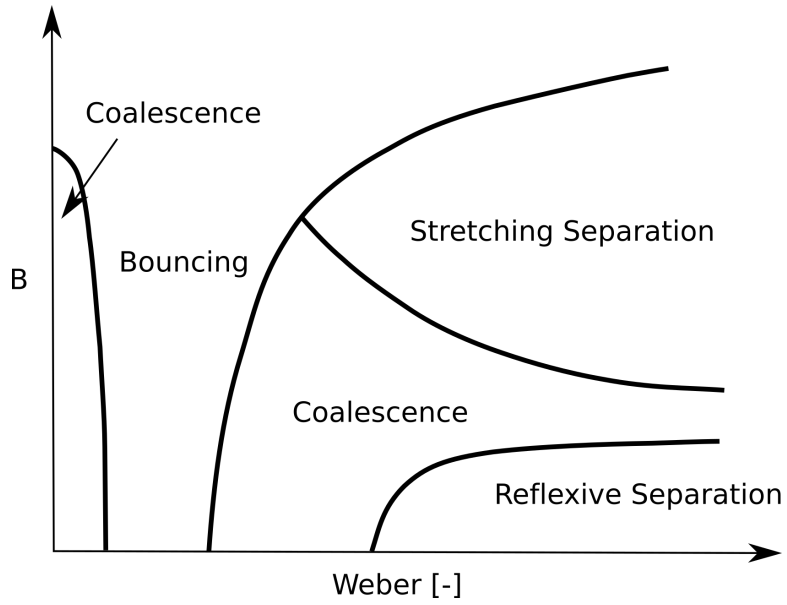

Figure 2.13: Droplet collision regimes depending on the Weber number and impact parameter (from [56]).

Droplet drag The generated droplets due to spray breakup acquire their momentum from the initial liquid vein. Nonetheless, due to aerodynamic effects, they exchange their momentum with the surrounding. Drag effects need to be considered to predict the trajectories of these droplets. Drag is mainly taken into account through the droplet drag coefficient. Several correlations to calculate the force undergone by a droplet in a viscous fluid have been carried out. Stokes, for example, came up with Equation 2.17, and non-dimensional value (Equation 2.18) which applies to low Reynolds numbers, where viscous forces dominate.

$$F = 3\pi D \mu_L U_R \tag{2.17}$$

$$C_D = \frac{24}{Re} \tag{2.18}$$

Empirical correlations are commonly used to characterize the droplet drag for the different regimes it may encounter. For example, Putnam [57] introduced Equation 2.19 for $\mathrm{Re} < 1000$, while for higher values, the drag coefficient converges to a fixed value (Equation 2.20, [58]).

$$C_D = \frac{24}{Re}\left(1 + \frac{1}{6}Re^{2/3}\right) \tag{2.19}$$

$$C_D = 0.44 \tag{2.20}$$

Nonetheless, these equations may change depending on the experimental correlation performed by the different studies available, the typologies of the sprays (thin sprays such as in UWS or dense sprays), and the conditions of the surrounding gas. Generically, it is assumed that the droplets would have a spherical shape, but different shapes might be found due to distortion and instabilities that might be present on the droplet surface. These non-spherical droplets need to be taken into account as the drag coefficient for highly distorted droplets (disk-shaped) is considerably higher than that of perfect spherical drops. In such a situation, Equation 2.21 is a possible approximation of a drag coefficient for a distorted droplet, where y stands for the droplet distortion (ranging from 0 to 1)[59].

$$C_D = C_{D_{sphere}}(1 + 2.632y) \tag{2.21}$$

This dynamic droplet drag approach will be used during the simulations performed for the development of this Thesis.

2.5.3.4 Macroscopic spray characteristics

As previously described, liquid atomizers intend not only to breakup the initial liquid jet into smaller droplets, but also to mix these newly formed droplets with the surrounding gaseous phase. For that purpose, several spray macroscopic parameters describe the global behavior of the formed spray and play a role in characterizing it.

Penetration The spray penetration (S) is usually defined as the distance of the tip of the spray to the injector outlet when injected into stagnant or cross-flow conditions. By assessing its evolution over time, the effect of the surrounding gas on the spray velocity can be observed, as the aerodynamic resistance of the gas will try to counteract the initial spray momentum at the orifice outlet. Depending on stagnant or cross-flow conditions, gravitational effects or momentum transfer to the cross-flow direction will gain importance once the initial kinetic energy of the spray diminishes. The spray penetration will also be influenced by the opening of the spray, as the wider the spray opening, the lower penetration will be. Its importance is also related to the possible droplet-wall impingement. If the penetration value observed exceeds the available space, the spray will not have properly evaporated, and a spray/wall collision will take place. In UWS applications, wall impingement of urea droplets can cause deposit formation on the engine's tail pipe, leading to ICE back-pressures creation [60], which acts detrimentally to the engine performance, and ends up in blockage [61]. A visual representation is given by Figure 2.14. UWS sprays depict a linear trend in its penetration values [28, 62], showing little deceleration due to aerodynamic effects. Therefore, the temporal evolution of the penetration (the velocity of the tip) can be related to the Bernoulli equation (Equation 2.3) in the shape of Equation 2.22.

$$\frac{\partial S}{\partial t} \propto \sqrt{\Delta P} \tag{2.22}$$

Cone Angle The cone angle of the spray (θ) is given by opening of the boundary of the sprays. Its value comes from the angle between two lines that represent the spray contours at some distance from the injector orifice, which indicates the steady part of the spray. The definition of this angle is controversial, as several authors define their own criteria to obtain it. Sometimes it is determined based on the spray area calculation [63]. It represents the opening of the spray after being introduced into the discharge volume. A higher cone angle generally means a spray with a high dispersion and low

penetration values. It is mainly driven by the injector dimensions as the orifice diameter, and the injection conditions. When it comes to pressure-swirl orifices, it gains more importance. The orifice length or the swirl chamber dimension can cause slight changes in the produced cone angle. The orifice diameter (d_0) causes a direct effect on the cone angle [64]. Injection pressure also affects the cone angle, increasing it with greater differences, but there is no precise quantification of this phenomenon. Liquid properties can also cause variations in the resulting angle. For example, increasing the liquid density of the spray also increases the measured angle. Viscosity, on the other hand, shows the opposite effect due to the variation in the friction force caused by the velocity gradient. Figure 2.14 also shows the schematic definition of the spray angle.

Dispersion The dispersion of the spray is the ratio between the occupied volume compared to the volume of liquid within the spray [46]. A highly dispersed spray has inherent mixing benefits, as the liquid can easily mix with the surrounding gas. Generally, sprays that depict a high penetration show less dispersion than those with smaller tip penetration values. As it can be expected, cone angle of the spray can also influence its dispersion.

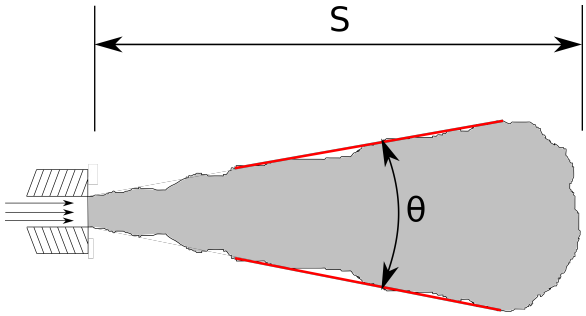

Figure 2.14: Definition of spray penetration (S) and spray angle (θ).

Breakup Length The breakup length (BL) is the length of the continuous portion of the jet measured from the orifice exit to where its breakup occurs, or the length in which the liquid vein is completely broken up. This parameter depends among other parameters on the breakup regime and therefore on the injection velocity the liquid is subjected to (see Figure 2.15). On the laminar region, the breakup occurs due to the growth of axisymmetric disturbances until its characteristic size is the one of the liquid jet radii. In it, with increasing jet velocity, the breakup length also increases with a varicose

breakup manner. On the inflection point (point B in Figure 2.15), the varicose breakup shifts toward sinuous wave growth. The growth rate of the instabilities is increased due to those aerodynamics effects, leading to a decrease of the breakup length with increasing Reynolds number. According to Grant and Middleman [65], this peak is achieved at a critical Re number represented by Equation 2.23. Once the flow is fully turbulent, the BL again increases with higher velocities, the perturbations are no more axisymmetric, and the aerodynamic instabilities drive the breakup process. From point D onward, there is no clear information about the evolution of the BL.

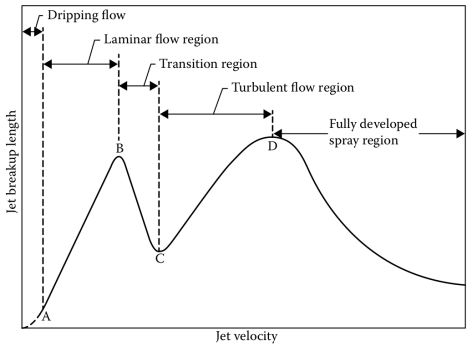

Figure 2.15: Evolution of the breakup length with the injection velocity (Extracted from [46]).

$$Re_{crit} = 3.25Oh^{-0.28} \tag{2.23}$$

Other working parameters can also affect this value. UWS, as mentioned, is generally injected into the exhaust pipe of CI ICE. Under these conditions, the higher the momentum of the cross-flow air, the greater the aerodynamic instabilities on the jet surface. The jet is initially bent by the incoming cross-flow conditions, and induces three-dimensional instabilities (in the tangential and jet centerline direction). Additionally, the ratio between the jet momentum and the incoming air momentum (Equation 2.24) significantly affects not only the breakup length, but also will the breakup regime map [66]. With a low q value, the spray will behave similarly to stagnant conditions, with the previously described breakup dynamics. With high q values, the breakup of the liquid column becomes similar to the aerodynamic instabilities of a spherical particle, through an initial deformation and a subsequent flattening and

disintegration driven by the aerodynamic forces. Surface breakup can also take place if the momentum ratio is high enough.

$$q = \frac{\rho_a u_a^2}{\rho_l u_l^2} \tag{2.24}$$

2.5.3.5 Droplet evaporation

In deNOx applications, an appropriate evaporation of the UWS droplets into gas phase is essential, so that an adequate amount of is generated to later reduce the NO_x molecules. The evaporation of liquid droplets implies heat and diffusive mass transfer processes from the surroundings to the liquid phase and vice versa. By producing a droplet distribution using an atomizer, an increase in the surface area-to-volume ratio is achieved. Increasing the exposed area, heat transfer dynamics are enhanced, and so the evaporation rate. Additionally, this process is not instantaneous, and it needs that the surrounding gas contains sufficient thermal energy, and that the residence time of the droplets is enough to perform the phase change.

When it comes to evaporating UWS droplets, four different stages can be defined according to Wei et al. [67]. In the first step, the UWS droplet absorbs thermal energy from the surroundings, increasing its temperature up to the boiling temperature of the water content of the droplet. During this phase, the size of the droplet remains invariant, or suffers a slight inflation. During the second step, the water content of the droplet starts to evaporate. Liquid urea still does not change its phase. Hence the change in droplet size depends only on the transformation of water. The absorbed heat is employed to evaporate the water, and the shift in droplet diameter follows the D^2 law [68] (see Figure 2.16). After the entire water content has disappeared from the droplet, the evaporation rate significantly decreases due to the higher energy needed for the urea phase change. The heat starts to be absorbed by the urea until it reaches its boiling temperature and starts to decompose. Once at the boiling point, the temperature remains constant, and the heat absorption is used to evaporate the urea. At this point, bubble formation appears and microexplosions can be detected due to the increase in pressure within the droplet, implying a non-uniform evolution of the droplet diameter. Additionally, crystallization of the urea can also be observed. The last step corresponds to the crystallization of the urea, which leads to solidification.

Nonetheless, the separation between the four phases is not strict as they can blend into each other. For example, urea evaporation can start prior to the complete phase change of the water content. As the diffusion velocity of

the water is limited, the evaporation of water content in the droplet core is slower than at the droplet surface. With increasing mass fraction of urea, the vapor pressure decreases, leading to droplet to further temperature increase, which implies a higher urea evaporation rate.

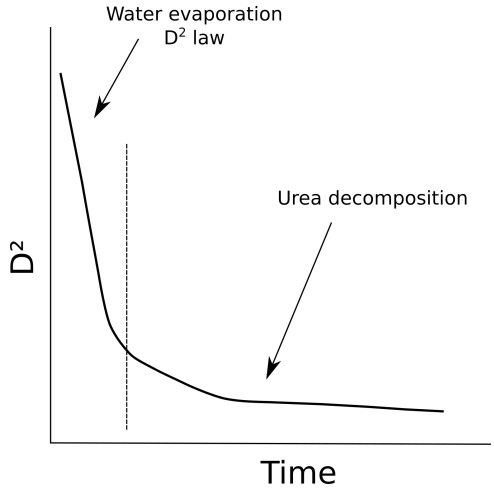

Figure 2.16: UWS droplet evaporation curve.

Several computational models are available to represent the evaporation of liquid droplets that range from simple (e.g. constant and uniform droplet temperature) to highly complex models (e.g. evaporation process coupled with Navier-Stokes equations). This increase in complexity can also increase the accuracy of the phase-change representation, but also imply an increase in computational cost. If a whole spray is to be represented, high-fidelity models may become unfeasible. For that purpose, simplifications are common when representing UWS evaporation. Diffusion controlled model [69], for example, assumes no internal droplet convection, considering only diffusive species and energy transport, which leads to radial concentration and temperature gradients. Another employed model is the called Rapid mixing [70]. In it, droplet properties (concentration and temperature) change with time, but within the droplet remain uniform as infinite transport coefficients are assumed. Other models assume the thermolysis process to be a vaporization process, or employ Arrhenius formulations to depict the thermolysis.

In addition to the normal phase-change process, a phenomenon called *flash-boiling* accelerates the evaporation process. *Flash-boiling* events occur when a liquid is injected into a surrounding gas whose ambient pressure is lower than the saturation vapor pressure of the liquid. The liquid, once in-

jected, lowers its pressure below the saturation point, generating vapor phase, which after exiting the injector orifice expands, shattering the liquid [71]. This phenomenon improves the atomization process of the spray, generating considerably lower droplet diameters. For UWS applications, it has been considered to be beneficial as it reduces the wall film formation in SCR walls, together with improving the uniformity of the NH_3 at the inlet of the catalyst [72].

2.5.3.6 Droplet impingement

Spray-wall interaction is one of the main challenges spray systems have to deal with, not only for UWS applications but also in other applications such as fuel sprays. In after-treatment systems, mixing elements are commonly introduced to enhance further atomization of the injected spray (Figure 2.5). This is translated into impingement of liquid droplets with these elements.

Initial analysis of droplet impingement has been performed on individual droplets impacting solid surfaces. The impingement's possible outcomes depend on the droplet's hydrodynamics characteristics and the surface's heating, in addition to its characteristics. In typical engine applications, impact walls are commonly heated targets; therefore, those outcomes should be expected. According to the study from Kuhnke [73], four different impingement situations can be found: *deposition*, *splash*, *rebound*, and *thermal breakup*. Deposition can be described as the complete adhesion of the impinging droplet into the wall. Splashing, on the other hand, represents the droplet's breakup into smaller particles, while part of it attaches to the wall forming a liquid film. Rebounding represents the reflection of the droplet once contacting the wall due to the Leidenfrost effect [74]. This phenomenon is caused by the creation of a vapor layer separating the droplet from the wall, reducing the heat transfer toward the surface and preventing contact between the two bodies. Although not considered by the Kuhnke regime map, rebounding can also take place due to fluid-mechanic dynamics in which a droplet at cold impingement conditions might initially spread over the wall, and recoil afterward, separating from the surface [75]. Finally, the thermal breakup indicates the atomization of the droplet due to thermal mechanisms. These regimes are identified based on the droplet's kinetic energy, represented by the non-dimensional parameter K (function of the droplet We and Re); and the non-dimensional temperature T^* (defined in Equation 2.25). The dependency on those parameters can be observed in Figure 2.17. These regimes differ depending on the properties of the impinging droplet, the incoming angle and the characteristics of the wall surface. Transition regimes can also be detected, as non-strict values differentiate the different regimes. For example, the Leidenfrost temperature

can determine additional impingement regimes, as for example rebound with breakup can be observed at droplet temperatures above boiling and below the Leidenfrost value. Most UWS models rely on the Kuhnke approach. Still, some others have also employed the Bai-Gosman model [76], in which a more detailed regime classification is provided, additionally to giving possible outcomes depending of working with a dry or a wet wall.

$$T^* = \frac{T_w}{T_{sat}} \tag{2.25}$$

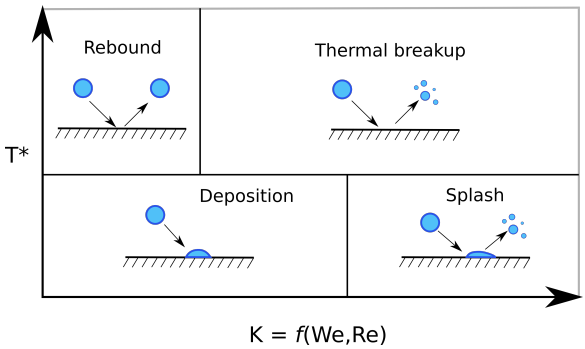

Figure 2.17: Spray/Wall interaction regime map according to Kuhnke [73].

References

[1] Cobb, D., Glatch, L., Ruud, J., and Snyder, S. "Application of selective catalytic reduction (SCR) technology for NOx reduction from refinery combustion sources". In: *Environmental Progress* 10.1 (1991), pp. 49–59. DOI: 10.1002/ep.670100116.

[2] Cichanowicz, J. E. and Muzio, L. J. "Twenty-Five Years of SCR Evolution: Implications For US Application And Operation". In: 2006.

[3] Pisupadti, S. V. "Fuel Chemistry". In: *Encyclopedia of Physical Science and Technology*. Elsevier, 2003, pp. 253–274. DOI: 10.1016/B0-12-227410-5/00933-9.

[4] Zel'dovich, Y., Sadonikov, P., and Frank-Kamenetskii, D. A. *Oxidation of Nitrogen in Combustion (Okislenie azota pri gorenii)*. Publishing House of the Acad of Sciences of USSR, 1947.

[5] Lavole, G. A., Heywood, J. B., and Keck, J. C. "Experimental and theoretical study of nitric oxide formation in internal combustion engines". In: *Combustion Science and Technology* 1.4 (1970), pp. 313–326. DOI: 10.1080/00102206908952211.

[6] Fenimore, C. P. "Formation of nitric oxide in premixed hydrocarbon flames". In: *Symposium (International) on Combustion* 13.1 (1971), pp. 373–380. DOI: 10.1016/S0082-0784(71)80040-1.

[7] Lavoie, G. A. and Blumberg, P. N. "A Fundamental Model for Predicting Fuel Consumption, NOx and HC Emissions of the Conventional Spark-Ignited Engine". In: *Combustion Science and Technology* 21.5-6 (1980), pp. 225–258. DOI: 10.1080/00102208008946939.

[8] Semakula, M. and Inambao, P. F. "The Formation, Effects and Control of Oxides of Nitrogen in Diesel Engines". In: *International Journal of Applied Engineering Research* 13.6 (2018), pp. 3200–3209.

[9] Turns, S. R. "An introduction to combustion: concepts and applications". In: *System* 499 (2000), p. 411. DOI: 10.1016/j.ijhydene.2008.07.121.

[10] Carslaw, D. C. and Rhys-Tyler, G. "New insights from comprehensive on-road measurements of NOx, NO2 and NH3 from vehicle emission remote sensing in London, UK". In: *Atmospheric Environment* 81 (2013), pp. 339–347. DOI: 10.1016/j.atmosenv.2013.09.026.

[11] Alagumalai, A., Jodat, A., Mahian, O., and Ashok, B. "NOx formation chemical kinetics in IC engines". In: *NOx Emission Control Technologies in Stationary and Automotive Internal Combustion Engines: Approaches Toward NOx Free Automobiles* (2021), pp. 39–68. DOI: 10.1016/B978-0-12-823955-1.00002-4.

[12] European Council. *Directive 88/77/EEC on the approximation of the laws of the Mermber States relating to the measures to be taken against the emission of gaseous pollutants from diesel engines for use in vehicles*. 1987.

[13] EEA Relevance. *REGULATION (EU) No 167/2013 OF THE EUROPEAN PARLIAMENT AND OF THE COUNCIL of 5 February 2013 on The Approval and Market Surveillance of Agricultural and Forestry Vehicles*. 2013.

[14] N/N. *Proposal for Regulation of the European Parliament and of the Council on Type-Approval of Motor Vehicles and Engine of such Systems, Components and Separate Technical Units Intended for Such Vehicles, with Respect to thir Emissione and Battery Durability*. 2022.

[15] Jacob, A., Ashok, B., Vignesh, R., Balusamy, S., and Alagumalai, A. "NOx and PM trade-off in IC engines". In: *NOx Emission Control Technologies in Stationary and Automotive Internal Combustion Engines: Approaches Toward NOx Free Automobiles*. Ed. by B. B. T. N. E. C. T. i. S. Ashok and A. I. C. Engines. Elsevier, 2021, pp. 69–93. DOI: 10.1016/B978-0-12-823955-1.00003-6.

[16] MohamedMusthafa, M., Sivapirakasam, S. P., and Udayakumar, M. "Comparative studies on fly ash coated low heat rejection diesel engine on performance and emission characteristics fueled by rice bran and pongamia methyl ester and their blend with diesel". In: *Energy* 36.5 (2011), pp. 2343–2351. DOI: 10.1016/j.energy.2010.12.047.

[17] Uludamar, E. "Effect of hydroxy and hydrogen gas addition on diesel engine fuelled with microalgae biodiesel". In: *International Journal of Hydrogen Energy* 43.38 (2018), pp. 18028–18036. DOI: 10.1016/j.ijhydene.2018.01.075.

[18] Aldhaidhawi, M., Chiriac, R., Bădescu, V., Descombes, G., and Podevin, P. "Investigation on the mixture formation, combustion characteristics and performance of a Diesel engine fueled with Diesel, Biodiesel B20 and hydrogen addition". In: *International Journal of Hydrogen Energy* 42.26 (2017), pp. 16793–16807. DOI: 10.1016/j.ijhydene.2017.01.222.

[19] Saiteja, P., Ashok, B., Saiteja, P., and Vignesh, R. "NOX reduction through various low temperature combustion technologies". In: *NOx Emission Control Technologies in Stationary and Automotive Internal Combustion Engines: Approaches Toward NOx Free Automobiles* (2021), pp. 423–459. DOI: 10.1016/B978-0-12-823955-1.00014-0.

[20] Börnhorst, M. and Deutschmann, O. "Advances and challenges of ammonia delivery by urea-water sprays in SCR systems". In: *Progress in Energy and Combustion Science* 87 (2021), p. 100949. DOI: 10.1016/j.pecs.2021.100949.

[21] Liu, G. and Gao, P. X. "A review of NOx storage/reduction catalysts: Mechanism, materials and degradation studies". In: *Catalysis Science and Technology* 1.4 (2011), pp. 552–568. DOI: 10.1039/c1cy00007a.

[22] Forzatti, P. "Present status and perspectives in de-NOx SCR catalysis". In: *Applied Catalysis A: General* 222.1-2 (2001), pp. 221–236. DOI: 10.1016/S0926-860X(01)00832-8.

[23] Bröer, S. and Hammer, T. "Selective catalytic reduction of nitrogen oxides by combining a non-thermal plasma and a V2O5-WO3/TiO2 catalyst". In: *Applied Catalysis B: Environmental* 28.2 (2000), pp. 101–111. DOI: 10.1016/S0926-3373(00)00166-1.

[24] Koebel, M., Madia, G., and Elsener, M. "Selective catalytic reduction of NO and NO2 at low temperatures". In: *Catalysis Today* 73.3-4 (2002), pp. 239–247. DOI: 10.1016/S0920-5861(02)00006-8.

[25] Devadas, M., Kröcher, O., Elsener, M., Wokaun, A., Söger, N., Pfeifer, M., Demel, Y., and Mussmann, L. "Influence of NO2 on the selective catalytic reduction of NO with ammonia over Fe-ZSM5". In: *Applied Catalysis B: Environmental* 67.3-4 (2006), pp. 187–196. DOI: 10.1016/j.apcatb.2006.04.015.

[26] Tian, H., Xu, R., Canadell, J. G., Thompson, R. L., Winiwarter, W., Suntharalingam, P., Davidson, E. A., Ciais, P., Jackson, R. B., Janssens-Maenhout, G., Prather, M. J., Regnier, P., Pan, N., Pan, S., Peters, G. P., Shi, H., Tubiello, F. N., Zaehle, S., Zhou, F., Arneth, A., Battaglia, G., Berthet, S., Bopp, L., Bouwman, A. F., Buitenhuis, E. T., Chang, J., Chipperfield, M. P., Dangal, S. R., Dlugokencky, E., Elkins, J. W., Eyre, B. D., Fu, B., Hall, B., Ito, A., Joos, F., Krummel, P. B., Landolfi, A., Laruelle, G. G., Lauerwald, R., Li, W., Lienert, S., Maavara, T., MacLeod, M., Millet, D. B., Olin, S., Patra, P. K., Prinn, R. G., Raymond, P. A., Ruiz, D. J., Werf, G. R. van der, Vuichard, N., Wang, J., Weiss, R. F., Wells, K. C., Wilson, C., Yang, J., and Yao, Y. "A comprehensive quantification of global nitrous oxide sources and sinks". In: *Nature* 586.7828 (2020), pp. 248–256. DOI: 10.1038/s41586-020-2780-0.

[27] Prather, M. J., Hsu, J., DeLuca, N. M., Jackman, C. H., Oman, L. D., Douglass, A. R., Fleming, E. L., Strahan, S. E., Steenrod, S. D., Søvde, O. A., Isaksen, I. S., Froidevaux, L., and Funke, B. "Measuring and modeling the lifetime of nitrous oxide including its variability". In: *Journal of Geophysical Research* 120.11 (2015), pp. 5693–5705. DOI: 10.1002/2015JD023267.

[28] Kapusta, Ł. J., Sutkowski, M., Rogóż, R., Zommara, M., and Teodorczyk, A. "Characteristics of water and urea-water solution sprays". In: *Catalysts* 9.9 (2019). DOI: 10.3390/catal9090750.

[29] Wang, Y. Y., Zhang, H., and Wang, J. "NOx Sensor Reading Correction in Diesel Engine Selective Catalytic Reduction System Applications". In: *IEEE/ASME Transactions on Mechatronics* 21.1 (2016), pp. 460–471. DOI: 10.1109/TMECH.2015.2434846.

[30] Kröcher, O., Elsener, M., and Jacob, E. "New reducing agents for the low-NOx SCR technology". In: *5th International Exhaust Gas and Particulate Emissions Forum*. 2008, pp. 19–20.

[31] Elmøe, T. D., Sørensen, R. Z., Quaade, U., Christensen, C. H., Nørskov, J. K., and Johannessen, T. "A high-density ammonia storage/delivery system based on Mg(NH 3)6Cl2 for SCR-DeNOx in vehicles". In: *Chemical Engineering Science* 61.8 (2006), pp. 2618–2625. DOI: 10.1016/j.ces.2005.11.038.

[32] Solla, A., Westerholm, M., Söderström, C., Tormonen, K., Härmä, T., Nissinen, T., and Kukkonen, J. "Effect of ammonium formate and mixtures of urea and ammonium formate on low temperature activity of SCR systems". In: *SAE Technical Papers* (2005). DOI: 10.4271/2005-01-1856.

[33] Park, T., Sung, Y., Kim, T., Lee, I., Choi, G., and Kim, D. "Effect of static mixer geometry on flow mixing and pressure drop in marine SCR applications". In: *International Journal of Naval Architecture and Ocean Engineering* 6.1 (2014), pp. 27–38. DOI: 10.2478/IJNAOE-2013-0161.

[34] Zhang, C., Sun, C., Wu, M., and Lu, K. "Optimisation design of SCR mixer for improving deposit performance at low temperatures". In: *Fuel* 237 (2019), pp. 465–474. DOI: 10.1016/j.fuel.2018.10.025.

[35] Schaber, P. M., Colson, J., Higgins, S., Thielen, D., Anspach, B., and Brauer, J. "Thermal decomposition (pyrolysis) of urea in an open reaction vessel". In: *Thermochimica Acta* 424.1-2 (2004), pp. 131–142. DOI: 10.1016/j.tca.2004.05.018.

[36] Shi, Y., Li, Z., Cao, W., and Dong, Q. "Investigation on Internal Flow Characteristics of a Pressure-Driven Swirling Injector for Urea-SCR System BT - Proceedings of the International Conference of Fluid Power and Mechatronic Control Engineering (ICFPMCE 2022)". In: Atlantis Press, 2022, pp. 376–392. DOI: https://doi.org/10.2991/978-94-6463-022-0_32.

[37] Lee, S. I. and Park, S. Y. "Numerical analysis of internal flow characteristics of urea injectors for SCR dosing system". In: *Fuel* 129 (2014), pp. 54–60. DOI: 10.1016/j.fuel.2014.03.031.

[38] Gimeno, J. "Desarrollo y aplicacion de la medida del flujo de cantidad de movimiento de un chorro diesel". PhD thesis. Valencia (Spain): Universitat Politècnica de València, 2008. DOI: 10.4995/Thesis/10251/8306.

[39] Ohnesorge, W. "Formation of Drops by nozzles and the breakup of liquid jets". In: *Z. Angew. Math. Mech.* 16 (1936), pp. 355–358.

[40] Trinh, H. P. and Chen, C. P. "Modeling of turbulence effects on liquid jet atomization and breakup". In: *43rd AIAA Aerospace Sciences Meeting and Exhibit - Meeting Papers*. Aerospace Sciences Meetings. American Institute of Aeronautics and Astronautics, 2005, pp. 5781–5801. DOI: 10.2514/6.2005-154.

[41] Kapusta, Ł. J., Sutkowski, M., Rogóż, R., Zommara, M., and Teodorczyk, A. *Characteristics of water and urea-water solution sprays*. 2019. DOI: 10.3390/catal9090750.

[42] Reitz, R. D. "Atomization and other breakup regimes of a liquid jet". PhD thesis. AA(Princeton University, New Jersey), 1978.

[43] Sterling, A. M. and Sleicher, C. A. "The instability of capillary jets". In: *Journal of Fluid Mechanics* 68.3 (1975), pp. 477–495. DOI: 10.1017/S0022112075001772.

[44] Miesse, C. C. "Correlation of Experimental Data on the Disintegration of Liquid Jets". In: *Industrial & Engineering Chemistry* 47.9 (1955), pp. 1690–1701. DOI: 10.1021/ie50549a013.

[45] Ranz, W. E. "Some experiments on orifice sprays". In: *The Canadian Journal of Chemical Engineering* 36.4 (1958), pp. 175–181. DOI: 10.1002/cjce.5450360405.

[46] Lefebvre, A. H. and McDonell, V. G. *Atomization and sprays*. Second. Boca Raton, FL: Press, CRC, 2017, pp. 1–284. DOI: 10.1201/9781315120911.

[47] Pilch, M. and Erdman, C. A. "Use of breakup time data and velocity history data to predict the maximum size of stable fragments for acceleration-induced breakup of a liquid drop". In: *International Journal of Multiphase Flow* 13.6 (1987), pp. 741–757. DOI: 10.1016/0301-9322(87)90063-2.

[48] Hsiang, L.-P. and Faeth, G. "Drop deformation and breakup due to shock wave and steady disturbances". In: *International Journal of Multiphase Flow* 21.4 (1995), pp. 545–560. DOI: 10.1016/0301-9322(94)00095-2.

[49] Lauer, T. "Preparation of Ammonia from Liquid AdBlue – Modeling Approaches and Future Challenges". In: *Chemie-Ingenieur-Technik* 90.6 (2018), pp. 783–794. DOI: 10.1002/cite.201700107.

[50] Rosin, P. and Rammler, E. "The laws governing the fineness of powdered coal". In: *Journal of the Institute of Fuel*. Vol. 7. 1933, pp. 29–36.

[51] Fritzsche, L., Schwarze, R., Junghans, F., and Bauer, K. "Toward unraveling the mechanisms of aerosol generation during phonation". In: *Physics of Fluids* 34.12 (2022), p. 121904. DOI: 10.1063/5.0124944.

[52] Chin, J. S. and Lefebvre, A. H. "Some comments on the characterization of drop-size distribution in sprays". In: *IN: ICLASS-85; Proceedings of the Third International Conference on Liquid Atomisation and Spray Systems*. Vol. 2. 1986.

[53] Mugele, R. A. and Evans, H. D. "Droplet Size Distribution in Sprays". In: *Industrial & Engineering Chemistry* 43.6 (1951), pp. 1317–1324. DOI: 10.1021/ie50498a023.

[54] Ashgriz, N. and Givi, P. "Binary collision dynamics of fuel droplets". In: *International Journal of Heat and Fluid Flow* 8.3 (1987), pp. 205–210. DOI: 10.1016/0142-727X(87)90029-4.

[55] Qian, J. and Law, C. K. "Regimes of coalescence and separation in droplet collision". In: *Journal of Fluid Mechanics* 331 (1997), pp. 59–80. DOI: 10.1017/S0022112096003722.

[56] Kropotova, S. and Strizhak, P. "Collisions of Liquid Droplets in a Gaseous Medium under Conditions of Intense Phase Transformations: Review". In: *Energies* 14.19 (2021), p. 6150. DOI: 10.3390/en14196150.

[57] Putnam, A. *Integratable form of droplet drag coefficient*. 1961.

[58] Clift, R., Grace, J. R., and Weber, M. E. "Bubbles, drops, and particles". In: (2005).

[59] Liu, A. B., Mather, D., and Reitz, R. D. "Modeling the effects of drop drag and breakup on fuel sprays". In: *SAE Technical Papers*. Vol. 298. 1993, pp. 1–6. DOI: 10.4271/930072.

[60] Qian, F., Lü, L., and Yang, D. "Simulation of Deposit Formation Inside the Exhaust Pipe on a Diesel Engine with SCR". In: *Neiranji Xuebao/Transactions of CSICE (Chinese Society for Internal Combustion Engines)* 36.2 (2018), pp. 144–152. DOI: 10.16236/j.cnki.nrjxb.201802019.

[61] Su, C. "Commercial Vehicle Post-processing system of Urea Crystallization Problem Research". In: *Automob. Appl. Technol* (2016), pp. 10–223.

[62] Sapio, F., Millo, F., Fino, D., Monteverde, A., Sartoretti, E., Bianco, A., Postrioti, L., Tarabocchia, A., Buitoni, G., and Brizi, G. "Experimental and Numerical Analysis of Latest Generation Diesel Aftertreatment Systems". In: *SAE Technical Papers*. Vol. 2019-Septe. September. SAE International, 2019. DOI: 10.4271/2019-24-0142.

[63] Naber, J. D. and Siebers, D. L. *Effects of gas density and vaporization on penetration and dispersion of diesel sprays*. 1996. DOI: 10.4271/960034.

[64] Rizk N.K. and Lefebvre A.H. "Prediction of Velocity Coefficient and Spray Cone Angle for Simplex Swirl Atomizers". In: International Journal of Turbo and Jet Engines 4.1-2 (1987), pp. 65–74. DOI: 10.1515/TJJ.1987.4.1-2.65.

[65] Grant, R. P. and Middleman, S. "Newtonian jet stability". In: *AIChE Journal* 12.4 (1966), pp. 669–678. DOI: 10.1002/aic.690120411.

[66] Wu, P. K., Kirkendall, K. A., Fulle, R. P., and Nejad, A. S. "Breakup processes of liquid jets in subsonic crossflows". In: *Journal of Propulsion and Power* 13.1 (1997), pp. 64–73. DOI: 10.2514/2.5151.

[67] Wei, L., Youtong, Z., and Asif, M. "Investigation on UWS evaporation for vehicle SCR applications". In: *AIChE Journal* 62.3 (2016), pp. 880–890. DOI: 10.1002/aic.15078.

[68] Stein, M., Bykov, V., Bertótiné Abai, A., Janzer, C., Maas, U., Deutschmann, O., and Olzmann, M. "A reduced model for the evaporation and decomposition of urea–water solution droplets". In: *International Journal of Heat and Fluid Flow* 70 (2018), pp. 216–225. DOI: 10.1016/j.ijheatfluidflow.2018.02.005.

[69] Kneer, R., Schneider, M., Noll, B., and Wittig, S. "Diffusion controlled evaporation of a multicomponent droplet: theoretical studies on the importance of variable liquid properties". In: *International Journal of Heat and Mass Transfer* 36.9 (1993), pp. 2403–2415. DOI: 10.1016/S0017-9310(05)80124-3.

[70] Sirignano, W. A. "Fuel droplet vaporization and spray combustion theory". In: *Progress in Energy and Combustion Science* 9.4 (1983), pp. 291–322. DOI: 10.1016/0360-1285(83)90011-4.

[71] Mojtabi, M., Chadwick, N., Wigley, G., and Helie, J. "The effect of flash boiling on break up and atomization in GDI sprays". In: *22nd European Conference on Liquid Atomization and Spray Systems*. 2008, pp. 8–10.

[72] Kaźmierski, B. and Kapusta, Ł. J. "The importance of individual spray properties in performance improvement of a urea-SCR system employing flash-boiling injection". In: *Applied Energy* 329 (2023), p. 120217. DOI: 10.1016/j.apenergy.2022.120217.

[73] Kuhnke, D. *Spray/Wall-Interaction Modelling by Dimensionless Data Analysis*. Berichte aus der Strömungstechnik. Shaker, 2004.

[74] Gottfried, B. S., Lee, C. J., and Bell, K. J. "The leidenfrost phenomenon: film boiling of liquid droplets on a flat plate". In: *International Journal of Heat and Mass Transfer* 9.11 (1966), pp. 1167–1188. DOI: 10.1016/0017-9310(66)90112-8.

[75] Mao, T., Kuhn, D. C. S., and Tran, H. "Spread and rebound of liquid droplets upon impact on flat surfaces". In: *AIChE Journal* 43.9 (1997), pp. 2169–2179. DOI: 10.1002/aic.690430903.

[76] Bai, C. and Gosman, A. D. "Development of methodology for spray impingement simulation". In: *SAE Technical Papers* 412 (1995). DOI: 10.4271/950283.

Chapter 3

Literature review

"I have always considered that the substitution of the internal combustion engine for the horse marked a very gloomy milestone in the progress of mankind."
—Winston Churchill

3.1 Introduction

As explained in Section 2.5, Selective Catalytic Reduction (SCR) has become a mandatory after-treatment system for heavy and light-duty applications if NO_x emission limitations are to be met. For that reason, significant effort has been placed during the last decades to understand further the spray injection and evaporation dynamics of Urea Water Solution (UWS) sprays. This increase of interest resulted in a high volume of scientific documents describing the main areas of interest. The SCR after-treatment's main challenges are the low-injection velocities that lead to relatively coarse droplets, which subsequently implies incomplete evaporation. Mixer geometries are therefore necessary to enhance secondary atomization, which improves the evaporation rate but introduces a droplet impingement issue that can derive in deposit formation and engine malfunctioning.

As Chapter 1 introduced, this thesis aims to provide a complete computational framework that covers the main dynamics of interest that allows further understanding of the main driving mechanisms of the injection of UWS jets without the need to employ experimental approaches. In order to achieve

that objective, a deep review of the state-of-the-art is essential to acknowledge the main findings and limitations discovered by previous authors and push forward the knowledge regarding after-treatment systems. This Chapter aims to present a current state-of-the-art regarding UWS SCR systems and provide the main tools that are employed in the scientific community to analyze them. Specifically, it will be divided into two main sections. The first one will cover experimentally-driven studies regarding the characteristics and injection events of UWS, in addition to the evaporation phenomena. UWS impingement will also be covered. Afterward, a similar review will be carried out regarding the studies done using computational methodologies.

3.2 Experimental studies

This section will focus on the most significant experimental studies that have been carried out on NO_x after-treatment systems.

The first researches applied on diesel engines after-treatment were focused on general aspects of the SCR system. Held et al. [1] did perform an initial comparative analysis of the deNO_x properties using either urea or ammonia in an exhaust gas stream, obtaining higher NO_x reduction by injecting urea instead of ammonia in a specific temperature range and a specific catalyst material. From there, the urea injection substituted ammonia for mobile applications, and interest in UWS sprays raised.

The development of the spray characteristics has been widely studied. When it comes to spray penetration, it is not only affected by the inner geometry of the atomizer but also depends on the working conditions. This analysis has been performed on typical diesel sprays, such as the work of Araneo et al. [2], where the density ratio plays an important role in affecting the penetration depth of the spray. One of the defining parameters of the penetration of the droplets is the injection pressure, as seen in the work carried out by Payri et al. [3]. As described in Chapter 2, the spray tip velocity sees a deceleration due to the surrounding gas density, which forces the spray to exchange its momentum with the environment. Nonetheless, UWS sprays generally show a linear penetration profile [4]. Due to the low density of the air and the relatively large droplets formed, the aerodynamic forces generated are not able to slow down the jet. Similar behavior is observed on other studies [5–7].

This spray penetration is dependent on the initial jet velocity. In automotive applications, typical injection pressures have associated typical velocities within the range of 5-25 m/s [8]. Nonetheless, newer systems can afford injecting at higher injection pressures (13 bar [9]), which effectively increases the

jet velocity according to the analysis performed by Spiteri et al. [7]. These authors detected that the gas flow rate (100 kg/h -400 kg/h) did not affect the spray tip penetration or its angle. Additionally, a dense droplet region was found on the spray core, while the outskirts of it represented a more diluted zone. This depiction helps to represent which regions of the spray are more prone to impact the exhaust line walls. When it comes to microscopic characterization, the velocity of the droplets was found to converge toward the corresponding gas flow velocity at large penetration values. Increasing the mass flow rate of the gas did show an increase of air entrainment within the dense region of the spray. In contrast, at low gas flow velocities, a characteristic vortex was found downstream of the spray core, which moved closer to the nozzle region as the velocity of the gas kept decreasing. The impinging of the droplets was also found to be similar between the tested gas mass flow rates.

When analyzing the angle of UWS jets, Payri et al. [3] observed the influence of the injection pressure. It caused a slight increment (from 16° to 19°). Later studies performed on the same injector [10] returned that no clear trend on the angle was found by increasing the injection pressure. On the other hand, the gas temperature negatively affected the spray angle at low injection pressures (4 bar), while this effect was dampened at high injection pressures (9 bar). Lower injection angles (< 10 °) were obtained for a 6-hole UWS injector by Canyurt et al. [11]. This mentioned study focused on characterizing the deposit formation of urea by-products through experimental means, and correlating it with the temperature of the impinging wall, indicating that the regions suffering the largest temperature drop corresponded to where urea deposits appeared.

Van Vuuren has contributed significantly to the characterization of UWS sprays as well. In his work, he started using high-speed video measurements to understand the behavior of actively heated injectors (e.g. increasing the temperature of the liquid phase) [12]. A qualitative analysis was done, observing differences in the spray shape for the different temperatures. A higher vapor fraction was observed with increasing fluid temperature, a widening of the cone angle, and the appearance of a liquid film formation in the orifices, which had the potential to convert into solid deposit formation. The deposit formation phenomenon in the orifice region, shown in Figure 3.1, was briefly described in other works [10]. In follow-up studies, Van Vuuren et al. [13], as already presented studies, modified the chamber gas temperature in addition to varying the liquid temperature. In *non-flash-boiling* conditions, the gas temperature slightly affected the spray characteristics, in concordance with

previous studies. Flash-boiling conditions were achieved at high gas temperature (490 °C) and high liquid temperature (130 °C). Under these conditions the spray angle was expanded, with an improvement of the spray atomization and an increased vapor fraction. These conclusions were reaffirmed in a later study done by the same authors [14].

Figure 3.1: Urea deposits formed at the orifices of a UWS dosing module [10].

Some available studies have focused on characterizing the size and velocity of droplets generated from the injection of UWS. Most of them try to recreate the working conditions of an engine exhaust within a test rig with optical accesses. Several optical techniques can be employed to obtain the main spray characteristics. In 2015, Postrioti et al. [15] applied Phase-Doppler Anemometry (PDA) and Back-light imaging on a UWS spray under cross-flow conditions. From the analysis, the strong influence of the cross-flow conditions on the global behavior of the jet could be extracted. It was found that an increase in the cross-flow gas temperature implies a higher jet velocity due to the decrease in air density. On the other hand, the Sauter Mean Diameter (SMD) is reduced with higher air thermal energy due to the enhanced evaporation rates. A similar analysis was performed by Liao et al. [16], where several injector typologies were tested, and the spray characteristics were obtained. PDA techniques were also used for this work on an optically accessible flow channel. Three different UWS injectors were employed, differing in the amount of delivering orifices (3 or 6 orifices) and the working mechanism (pressure-driven or air-assisted-driven). From that, it could be highlighted how the 3-hole pressure-driven injector provided larger characteristic droplet

sizes than the 6-hole pressure-driven unit. On the other hand, the air-assisted dosing unit showed the smallest droplet due to the enhancement of jet instabilities thanks to the surrounding air. The smaller characteristic drop sizes of the air-assisted unit allowed the spray to bend completely in the direction of the incoming cross-flow, significantly decreasing the impingement of the droplets in the opposite wall, as shown on Figure 3.2.

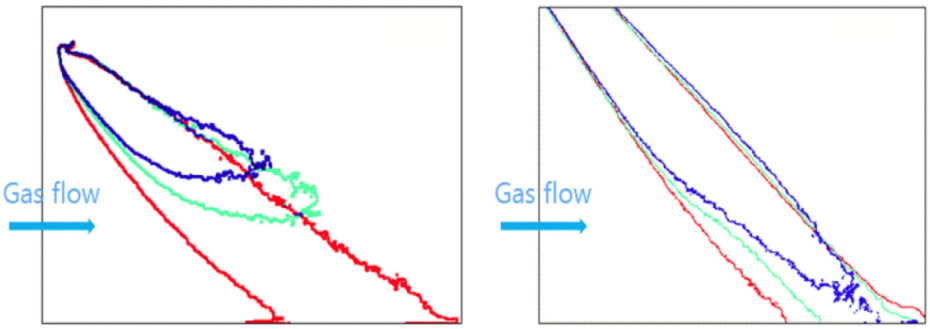

Figure 3.2: Spray contours for the Air-Assisted injector (left) and pressure-driven (right) for different gas flow velocities [16].

In experimental studies regarding injection of after-treatment fluid, it is common to see that UWS injection is not used but pure water, as UWS has a large proportion of water (67.5% wt.). This substitution is done to avoid the deposit formation problems that UWS implies. Using water instead of UWS is, in theory, appropriate due to their similarities in their physical properties, specifically regarding their surface tension and viscosity values. In 2013, a first comparison between the two fluids was carried out [17], and they concluded that similar spray characteristics were found for both sprays on the near-field region, while some trajectory deviations were found further down the spray. From there, several studies followed up using solely water. For example, Kapusta and Teodorczyk [18, 19] performed a comparison between the Laser Induced Fluorescence (LIF)/Mie method and the Structured Laser Illumination Planar Imaging (SLIPI) in a water spray in a recreation of an after-treatment system. Additionally, the shadowgraphy method was applied to the near-nozzle region. After their first study using water, Spiteri et al. [7] kept using water for their follow-up analysis. Nonetheless, more recent studies have again focused on comparing the two fluids of interest and assessing their similarities and differences again. Payri et al. [20] have characterized the injection rate of a commercial UWS dosing unit using water and UWS. To do so, a methodology to obtain the mass flow rate from the spray momentum

was applied. They concluded that water showed a higher mass flow rate for the same working conditions due to the lower density and increased velocity at the nozzle exit. On the other hand, Kapusta et al. [6] compared spray characteristics like spray tip penetration, spray angle, droplet characteristics, and unbroken liquid length to provide a detailed comparison between UWS and water. In the end, they showed that the liquid substitution altered almost all the study parameters. Higher momentum of the water spray was obtained (as in [20]), but higher initial jet velocity (and therefore spray tip penetration) was found for the UWS spray. This effect was attributed to the higher density of the UWS, which increased the inertia of the jet. The spray angle was also affected, with higher values for the UWS spray for all the injection pressures tested. Concerning the spray breakup, the unbroken liquid length of the water cases was observed to increase with the injection pressure, while for the UWS spray, the opposite behavior was found. This trend indicated that substituting the UWS by water changed the breakup phenomena from the first-wind to the second-wind-induced regime for the conditions tested. Not only that, but droplet size diameters changed while maintaining similar SMD. With this information, it remains clear that although both fluids have similar physical properties, the spray development can change considerably, which needs to be considered if a liquid substitution is to be made for experimental and computational purposes.

In addition to characterizing the UWS sprays, several works have focused on the evaporation of UWS droplets. The authors that obtained the evaporation dynamics described in Chapter 2 were Musa et al. [21], by suspending UWS droplets at the end of a quartz fiber. The evaporation behavior was captured through a video camera, detecting three regimes: the so-called D^2 *law*, the bubble formation, and the crystallization stage. Three years later, Wang et al. [22] performed a similar study covering the temperature range of the ambient gas temperature of a diesel engine exhaust. They observed that at high temperatures, after the linear region, the expected bubble formation, distortion and microexplosions happened. This stage takes place due to the formation of polymerization products on the droplet surface, forming an external crust. Further vaporization of water within the droplet increases the internal pressure until a quick distortion occurs. This phenomenon was previously reported by [21]. If increasingly high gas temperatures were set, the diameter decrease rate of the second region (after most of the water has evaporated) exceeded the rate of the D^2 *law* due to the presence of microexplosions, as indicated in Subsection 2.5.3.5, which reduced the droplet sizes. On the other hand, at lower temperatures (between 373 K and 423 K), no differentiation between the water rates and urea evaporation rates was found, due to

the moderation of the microexplosion events. From the original three droplet evaporation regimes, Wei et al. [23] understood that the first one could be subdivided into two, considering the temperature rise of the UWS droplet until the water boiling point as one, followed by the D^2 regime.

With respect to transforming the urea to ammonia through thermolysis and hydrolysis reactions, some research has been done for later applying the knowledge acquired to computational models. Fourier Transform Infra-Red (FTIR) resulted useful for quantifying the thermolysis reaction of injected urea [24]. Fang et al. [25] analyzed the urea degradation process using Thermal Gravimetric Analysis (TGA) and Infra-Red (IR) spectroscopy to detect the urea by-products formation. Two urea thermolysis stages were observed, where the first involved generation of ammonia content, and the second involved ammonia consumption. The second stage is highly undesirable as it reduces the available ammonia for NO_x reduction and promotes deposit formation. The speed of thermolysis depends on the gas temperature [26], which has been also reported to be incomplete under temperatures of 623 K for residence times above 0.1 s, while at temperatures above 673 K the needed time to complete is reduced. Isocyanic acid produced during thermolysis has been reported to have high stability in the gas phase [27] and imply a risk in space-limited systems. Certain catalysts have been reported to accelerate the hydrolysis reaction [28].

Due to the time and space limitation for the UWS to undergo phase change, spray impingement is a common phenomenon in SCR systems. The studies focusing in this topic range from the impingement of single droplets [29, 30] or of full UWS sprays [31]. They consider the impingement of the liquid droplets into a wall that is located opposite to the injector location, and from there, they try to assess the impingement process, film formation and deposit formation as shown in Figure 3.3. Single droplet studies focus on classifying the impingement regimes depending on the droplet We and the target wall temperature (Figure 2.17). Through shadowgraphy, some studies have focused on studying the effect of impingement of UWS droplets in porous walls [32], indicating that the porosity lowers the critical We to transition to splash regimes, in addition to lowering the T^* value to move from deposition/splash to rebound/breakup. The study found that high wall temperatures and porous walls enhanced the *rebound with breakup* regimes, reducing the evaporation time. This is not the only work focused on analyzing the modification of impingement regimes of UWS droplets [33]. As described in the previous chapter, film formation is dependent on the wall temperature and the presence or not of liquid on the surface. The main objectives of the research done on spray impingement events are to assess the deposition risk of urea deposits

and analyze the heat exchange between the walls and the impacting droplets. The work from Shahariar et al. [31] has this goal. The wetting effect is increased at low wall temperatures, making it more prone to film formation. On the other hand, at high temperatures, thermal breakup and bouncing are observed, decreasing this effect. The heat transfer between the walls and the droplets is also increased, helping the evaporation and degradation of the impinging droplets, and reducing the chances of film formation. One of the main findings is the dependency of the deposit composition with the temperature, such as biuret, cyanuric acid, ammeline, and melamine. When it comes to characterizing full sprays, PDA techniques are very useful to determine which droplets are impinging in the exhaust walls and which ones are entrained by the cross-flow gas, and therefore evaporate before impacting the boundaries of the system. Liao et al. [34] focused on this topic, showing that the droplets with a diameter below 20 µm evaporate before reaching the opposite wall. For larger droplets, the impingement rate increases until the value of 90 µm, from where almost all droplets impact the surface. Using high-speed imaging, they were able to identify all the processes prior to deposit creation. It was also found that the regions where high liquid film deposition was formed matched the regions that afterward created the most deposits.

Some additional work was carried out by Scheweigert et al. [35], who identified by Infra-Red Thermography (IRT) and high-speed imaging the evaporated mass fraction of the formed liquid films at the different initial wall temperatures. A maximum of urea evaporation was obtained at convective and nucleate boiling, while at higher temperatures, Leidenfrost effect started to appear, insulating the liquid film from the wall surface, and significantly reducing the heat transfer towards the wall and the evaporation rate of the urea.

Apart from characterizing the wall impingement, several parameters could help preventing the formation of liquid films on the exhaust lines. According to the study of Shi et al. [36], reducing the injection pressure of the atomizer improved the mixing distance of the spray. In that way, a completely developed spray was obtained at a closer distance to the injector orifice at a low injection pressure. The angle of the atomizer with respect to the cross-flow gas can also affect the development of the spray, showing a shorter mixing distance if injecting in a perpendicular direction with respect to the gas flow direction. Nonetheless, the larger wall-normal velocity component of the droplets implied a greater amount of impinging droplets compared to injecting in a more coaxial direction.

3.3 Computational studies

As this review has shown, a large research community has allowed a general understanding of each of the different physics taking place in UWS systems to reduce the NO_x emissions employing experimental methods. Nonetheless, these methods implicitly have several limitations that prevent having an in-detail description of UWS sprays. Several unknowns remain that need to be further addressed. Experimental methods are limited in the information obtained, whether they are intrusive or non-intrusive approaches. The complexity of the physics, in addition to the different lengths and time scales that take place within the problem, can imply introducing expensive experimental campaigns, in addition to the time consumption for preparing the setup, performing the experiment, and processing the data obtained. Computational Fluid Dynamics (CFD) allows to have an in-detail view of the physical and chemical processes undergone by the urea from its injection until its transformation into NH_3 through the discretization of the domain into discrete volumes. This section summarize the main studies focused on UWS sprays, and the main findings obtained are included. Ström et al. [37] assessed the fidelity of Eulerian-Lagrangian methods to represent UWS sprays. They indicated that the droplet motion was mainly described by buoyancy and drag forces, although the droplet distortion could affect the drag coefficient and modify the associated forces. Therefore, such distortion should be adequately modeled, especially on large droplets where more distortion effects will occur. Moreover, turbulent effects are high enough to be considered in CFD simulations. The injection of UWS sprays involves a lot of different phenomena that play an essential role for $deNO_x$ purposes. A visual representation of these physics is shown in Figure 3.3.

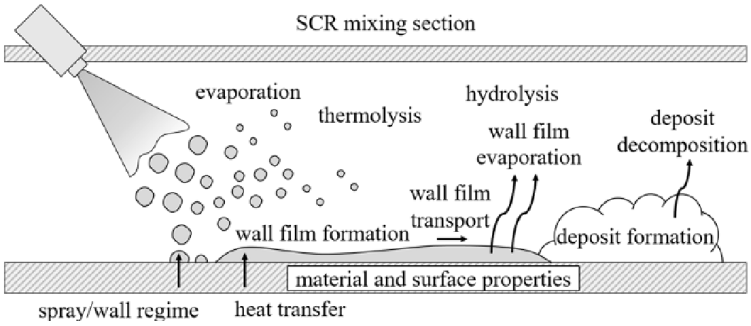

Figure 3.3: Main processes undergone by UWS sprays, including the wall impingement and deposit formation (from [38]).

3.3.1 UWS evaporation

In a multi-component mixture, differences in evaporation behavior are expected. The vapor pressure of pure water is higher than for urea, and the evaporation rate is also higher. For that reason, as the urea concentration increases due to water depletion, gradients of temperature and species appear within the liquid phase. Urea concentrates at the droplet surface, decreasing the vapor pressure of the mixture, and diminishing its evaporation rate. Initial computational studies focused on characterizing the phase change of UWS droplets. Two computational models used to capture this effect were compared by Birkhold et al. [38]. The Diffusion Limit (DL) model assumes that diffusion phenomena drive the species and energy transport. This assumption allowed capturing the greater urea concentration on the surface, trapping the remaining water on the inside. On the other hand, Rapid Mixing (RM) approach assumes infinitely high transport coefficients, showing a uniform distribution of the mixture on the droplet. Then, the evaporation rate is calculated according to the gradient in the concentration across the interface. The evolution of the droplet evaporation for the two models is shown in Figure 3.4 in which the evolution with time of a droplet mass is analysed for the DL and RM models. The two models have little effect on the evaporation of the water content while RM is more computationally efficient, suggesting its use for later applications. Abu-Ramadan et al. [39] performed a similar approach, comparing DL and RM models. The same conclusion was obtained, as RM underpredicted the evaporation rate by less than 10%, while having a more feasible approach. Nonetheless, the DL helps to explain some phenomenon of the UWS evaporation curve, such as the microexplosion and droplet size fluctuation in the second phase of UWS droplet evaporation (Figure 2.16), caused by the formation of a solid crust in the gas-liquid interface. The vaporization of the inner urea content of the droplet increases internal pressure until an explosion occurs. The DL model shows that the ideal conditions for this by-product formation at the surface take place. Nonetheless, as Fischer states [40], the droplets used in experiments performed by these authors are considerably larger than the droplet sizes of industrial applications, resulting in being unlikely to observe the creation of crust in the droplets for real applications.

When assessing the phase change of the urea content, Birkhold et al. [8] included in the RM model the capability of thermally decomposing it. Two possibilities arised to tackle thermolysis. The first one evaporates the molten urea into a gaseous state through a sublimation phenomenon, and then the gaseous urea reacts to give a molecule of NH_3 and HNCO. The second ap-

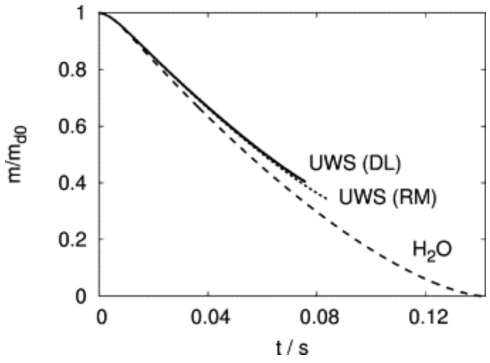

Figure 3.4: Evolution of the mass of a droplet of UWS with time, according to two evaporation models [8].

proach exploits the instability of gaseous urea, directly transitioning from molten urea to the thermolysis products. Therefore, the melting, evaporation, and thermolysis enthalpies are included in an Arrhenius expression. It needs to be highlighted that in this approach, urea vaporization takes place after no liquid water is present in the droplet. Nonetheless, it is stated that the saturation pressure considered in this work is overestimated in compared with experimental data [41]. Also, the authors highlight the possible uncertainties that can arise when determining the Arrhenius expression parameters. The approach of Abu-Ramadan et al. [39], on the other hand, allows vaporization of urea before the complete phase change of water content through a multi-component vaporization model. In that study the Arrhenius-type decomposition and the urea vaporization model were compared, concluding that the vaporization model works better in a single droplet study.

These introduced models, as described, do not consider undesired products produced through the polymerization of the urea (biuret, triuret, etc). A semi-detailed model proposed by Ebrahimian et al. [42] considers their formation. These reactions were obtained from the findings of several studies and the associated activation energies [25, 43–45], and proposed a 12-step kinetic scheme that covered 9 reactions for dry conditions (water completely evaporated) and 3 for aqueous urea conditions. The vapor pressure of the UWS is obtained assuming that it changes with the increase in urea concentration within the droplet. The non-ideality of the mixture is considered with the non-random two-liquid (NRTL) activity model. This model provided a suitable methodology for capturing the urea decomposition dynamics, and explained to the formation mechanism of unwanted products. Nonetheless, this approach is computationally more expensive than Arrhenius-type expres-

sions, which could not handle unwanted products. Brack et al. [46] proposed a 15-reaction kinetic scheme for the thermal decomposition of urea based on the results obtained by TGA and an FTIR, in which several heating rates were tested in the model.

3.3.2 Spray/wall interaction models

Another topic of great interest in UWS systems is the impinging of these sprays into the exhaust and mixer walls. As mentioned, it is widespread in NO_x aftertreatment systems that the spray collides with the solid surfaces, leading to the possibility of deposit formation. That is why so many studies have focused on developing proper predictive models for this interaction. Most of them try to validate the obtained results with the outcomes from experimental studies explained in the previous section (Section 3.2). For example, Shahariar et al. [31, 47] applied the Kuhnke and Bai-Gosman methods and compared the results with experiments performed on quiescent conditions. Additionally, information on wall cooling is also needed to predict the regions with a high deposition risk. Those studies assessed the effects of the interaction in the spray droplets. Wall temperature was revealed to have a high impact on the spray development. Increasing the wall temperature increased the heat transfer towards the droplets, implying more considerable front projection lengths, smaller droplet sizes, and a faster phase change of the droplets. Apart from impinging the exhaust walls, UWS sprays also impact on the mixer geometries used to improve the flow uniformity and trigger secondary atomization. It also is of a precursor of liquid impingement and deposit formation. Smith et al. [48] developed a cross-flow facility in which a mixing element is introduced, and a computational model was included for the deposit prediction through an adapted multi-regime Bai-Gosman approach from [40]. It was observed that the primary wall impingement zones implied continuous dilution and high film dynamics, which prevented the solid nuclei from growing in there. It was on the regions where no continuous spray impinging took place where the solid deposits appeared. The regions where urea locally solidified were enhancers of further deposit formation. Although through experimental means, it took 4 h to conclude on the regions where deposits were created, on computational means, only 20 s were captured to make the simulations feasible, and from the collected information, predictions were made. The deposition risk is assessed through a Wall Film Dynamics (WFD) coefficient which introduced the maximum and minimum accumulated film mass over a period of time. In that sense, high WFD implies low deposition risk, and vice-versa. For the mixer of study, it could be detected that even though the rear side of the mixer

geometry was not exposed to the initial footprint, it was still wet, and due to its low WFD, it was a precursor of deposit formation. Börnhorst et al. [49] implemented the urea kinetic model that Brack et al. [46] proposed into a CFD code. Wall-impingement was also considered, together with wall-cooling and evaporative cooling. To consider the different time-scales of the different phenomena taking place, a single injection event was simulated, from which source terms for the conservation equations were calculated and introduced into a subsequent simulation with larger time step values. The comparison between experimental and computational film results showed relatively good agreement in projected film area and wall temperature variation due to spray cooling.

3.3.3 Treatment of the spray

Lagrangian approaches are generally employed to characterize the UWS spray by computational means. The droplet spray size and velocity distributions for typical injection applications are obtained thanks to breakup models. These models recreate when a droplet of determined size and velocity should break into smaller droplets or not. Generally, a droplet with the diameter of the orifice is injected, and the model starts working. For UWS, it has been severely reported that due to the low injection velocities the droplet We number is below the breakup threshold [7, 50, 51]. Therefore, breakup is not expected, making it useless to employ well-established breakup algorithms. Hence, computational UWS studies use experimentally-defined droplet size distributions. Over those distributions, a Rosin-Rammler fitting is done (e.g. Nocivelli et al. [52]), and the distribution is introduced into the model. Secondary breakup models can be used [51], such as the KH-RT, but those are not expected to trigger breakup. Nonetheless, Khan et al. [53] indicated that there are no guidelines on obtaining the Rosin-Rammler parameters to represent the spray properly, and little work has been done on the velocity distributions. The work indicates a set of steps to obtain the optimum parameters. Other studies [54] have tried to improve the representation of the dispersed phase by introducing two Rosin-Rammler distributions to represent the differences in diameter between the spray core and its outskirts. The inner cone represented the dense region of the spray, with a higher characteristic diameter than the representation of the dilute region. This approach also helped in representing the spray impingement process, as an underprediction of the wall film deposition was found on standard Lagrangian approaches.

As indicated by Ström et al. [37], turbulent effects affect the spray development of UWS jets. The associated computational studies generally

use Reynolds-Averaged Navier-Stokes (RANS) approaches, assuming isotropic turbulence, in which k-ϵ model is used [38, 55–57]. In their work, Fischer et al. [58] performed a study on the influence of turbulence modeling on SCR systems. Two k-ϵ models were assessed (*RNG* and *high Re*) against a Reynolds Stress Model (RSM). The turbulent kinetic energy (TKE) and the dissipation after the swirl were adequately captured by the RSM model, improving the ammonia uniformity underestimation suffered from k-ϵ models. They also reported high numerical diffusion on first-order spatial discretization schemes using state-of-the-art mesh element sizes. The computational effort of RSM models resulted in 20% more expensive than standard k-ϵ modeling. Large Eddy Simulation (LES) are more demanding in computational resources but provide a more realistic representation of the unsteady flow in after-treatment applications. Hence, not many studies can be found in the literature that use the LES approach. However some works suggest that they would be helpful to properly know the working behavior of mixer geometries [59]. One of them is the study performed by Nishad et al. [60], where the spray dynamics under cross-flow conditions were captured. The Wall-Adapting Local Eddy-Viscosity (WALE) subgrid model was used as most of the turbulence was assumed to be wall-bounded. As in presented experimental studies, water-spray characteristics were compared to the dynamics of the UWS, both showing a similar trend, reaching the same outcomes that were given by experimental means [34]. Hybrid RANS-LES have also been used for high-pressure SCR sprays [61], where the near-wall regions model all the turbulent scales (RANS), while the LES equations are used for the regions away. This study performed a preliminary validation analysis on the turbulent boundary layer on the exhaust wall. The better representation of the spray due to the hybrid approach allowed assessing the largest UWS droplet diameter that could completely evaporate for the tested pipe. Additionally, it was found that the characteristic size of the spray did not significantly affect the uniformity of the vapor phase.

As mentioned, Lagrangian-Eulerian methods are an efficient technique to recreate the disperse phase of the spray. Trying to recreate both the gas and liquid phase in an Eulerian way would result in significantly more computationally expensive model. However, this approach allows characterizing the near-field spray dynamics, such as the primary and secondary breakup of liquid sprays, and avoid the need to calibrate breakup models. Additionally, the time scales of the near-field dynamics are smaller than the ones of the macroscopic spray development, as seen in Figure 3.5.

For that reason, Eulerian-Eulerian models are only used to characterize near-field dynamics, predict the breakup outcomes, and use this data to initialize Lagrangian-Eulerian models. The amount of research done using this

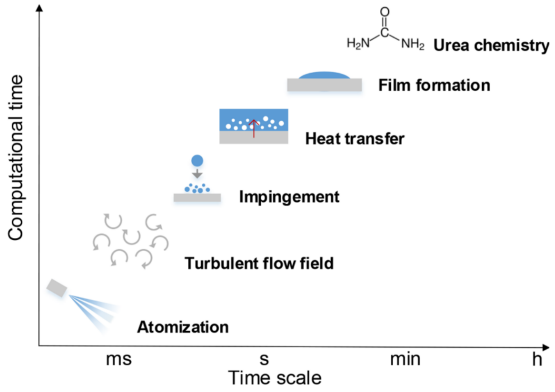

Figure 3.5: Different time scales associated with the different phenomena that take place in UWS applications (from [62]).

technique is therefore limited. On low-injection pressure sprays, Ishimoto et al. [63] recreated the orifices of a gasoline injector and simulated the breakup of the spray in the first millimeters. They could assess the intact core length for the velocity studied and the droplet size distribution functions. Macroscopic data such as the initial spray angle matched data experimentally obtained. It was in 2017, when the first Eulerian-Eulerian simulation was carried out on UWS sprays. Edelbauer et al. [64] characterized the primary breakup of a UWS injector through a LES simulation of one of the three orifices that with a 10 mm long domain was attached to the orifice exit, and the domain was discretized by a static mesh. In it, the minimum element size was 8 µm, which determined the minimum droplet size that could be detected. Establishing that minimum element size resulted in a mesh of 173.66 million elements, which gives an insight into the computational cost of performing Eulerian-Eulerian simulations. The interface reconstruction algorithm used was the Compressive Interface Capturing Scheme for Arbitrary Meshes (CICSAM) approach, based on the work from Hirt and Nichols [65]. This approach showed good agreement between the droplet size distributions and the characteristic diameters generated at the primary breakup phenomena. At the last 3 mm, a droplet evaluation algorithm was introduced, which allowed coupling the results obtained with an Eulerian-Lagrangian simulation, so that cheaper simulations could be initialized without the need for previously known droplet size distributions. Edelbauer et al. [66] also applied the same methodology to the injector of the study of Ishimoto et al. [63], but with a finer mesh and five times the original number of cells. It was highlighted the need of LES equations to characterize the highly transient flow that contributes to the liquid

jet primary breakup. Additionally, the droplets were further characterized by identifying the non-spherical droplets and detecting their different ligament topologies.

References

[1] Held, W., König, A., Richter, T., and Puppe, L. "Catalytic NOx Reduction in Net Oxidizing Exhaust Gas". In: *SAE Technical Papers*. SAE International, 1990. DOI: 10.4271/900496.

[2] Araneo, L., Coghe, A., Brunello, G., and Cossali, G. E. "Experimental investigation of gas density effects on diesel spray penetration and entrainment". In: *SAE Technical Papers* (1999), pp. 679–693. DOI: 10.4271/1999-01-0525.

[3] Payri, R., Bracho, G., Gimeno, J., and Moreno, A. *Spray characterization of the urea-water solution (UWS) injected in a hot air stream analogous to SCR system operating conditions*. 2019. DOI: 10.4271/2019-01-0738.

[4] Baleta, J., Vujanović, M., Pachler, K., and Duić, N. "Numerical modeling of urea water based selective catalytic reduction for mitigation of NOx from transport sector". In: *Journal of Cleaner Production* 88 (2015), pp. 280–288. DOI: 10.1016/j.jclepro.2014.06.042.

[5] Sapio, F., Millo, F., Fino, D., Monteverde, A., Sartoretti, E., Bianco, A., Postrioti, L., Tarabocchia, A., Buitoni, G., and Brizi, G. "Experimental and Numerical Analysis of Latest Generation Diesel Aftertreatment Systems". In: *SAE Technical Papers*. Vol. 2019-Septe. September. SAE International, 2019. DOI: 10.4271/2019-24-0142.

[6] Kapusta, Ł. J., Sutkowski, M., Rogóż, R., Zommara, M., and Teodorczyk, A. "Characteristics of water and urea-water solution sprays". In: *Catalysts* 9.9 (2019). DOI: 10.3390/catal9090750.

[7] Spiteri, A. and Dimopoulos Eggenschwiler, P. "Experimental fluid dynamic investigation of urea-water sprays for diesel selective catalytic reduction-denox applications". In: *Industrial and Engineering Chemistry Research* 53.8 (2014), pp. 3047–3055. DOI: 10.1021/ie404037h.

[8] Birkhold, F., Meingast, U., Wassermann, P., and Deutschmann, O. "Modeling and simulation of the injection of urea-water-solution for automotive SCR DeNOx-systems". In: *Applied Catalysis B: Environmental* 70.1-4 (2007), pp. 119–127. DOI: 10.1016/j.apcatb.2005.12.035.

[9] Wang, M., Liu, X., Bao, J., Li, Z., and Hu, J. "Simulation Study on Prediction of Urea Crystallization of a Diesel Engine Integrated after-Treatment Device". In: *ACS Omega* 6.10 (2021), pp. 6747–6756. DOI: 10.1021/acsomega.0c05785.

[10] Moreno, A. E. "Experimental Study of the Urea-Water Solution Injection Process". PhD thesis. Valencia (Spain): Universitat Politècnica de València, 2022. DOI: 10.4995/Thesis/10251/181637.

[11] Canyurt, T. G., Ergin, S., Zeren, H. B., and Savcı, İ. H. "Experimental and numerical investigation on the urea-deposit formation at different severities in selective catalytic reduction systems". In: *Applied Thermal Engineering* 214 (2022), p. 118884. DOI: 10.1016/j.applthermaleng.2022.118884.

[12] Van Vuuren, N. and Sayar, H. "High speed video measurements of a heated tip urea injector spray". In: *SAE Technical Papers* 9 (2012). DOI: 10.4271/2012-01-1747.

[13] Van Vuuren, N., Brizi, G., Buitoni, G., Postrioti, L., and Ungaro, C. "AUS-32 Injector Spray Imaging on Hot Air Flow Bench". In: *SAE Technical Papers* 2015-April.April (2015). DOI: 10.4271/2015-01-1031.

[14] Van Vuuren, N., Brizi, G., Buitoni, G., Postrioti, L., and Ungaro, C. "Experimental analysis of the urea-water solution temperature effect on the spray characteristics in SCR systems". In: *SAE Technical Papers* 24.2500 (2015). DOI: 10.4271/2015-24-2500.

[15] Postrioti, L., Brizi, G., Ungaro, C., Mosser, M., and Bianconi, F. "A methodology to investigate the behaviour of urea-water sprays in high temperature air flow for SCR de-NOx applications". In: *Fuel* 150.x (2015), pp. 548–557. DOI: 10.1016/j.fuel.2015.02.067.

[16] Liao, Y., Dimopoulos Eggenschwiler, P., Spiteri, A., Nocivelli, L., Montenegro, G., and Boulouchos, K. "Fluid Dynamic Comparison of AdBlue Injectors for SCR Applications". In: *SAE International Journal of Engines* 8.5 (2015), pp. 2303–2311. DOI: 10.4271/2015-24-2502.

[17] Spiteri, A. C., Srna, A., and Dimopoulos Eggenschwiler, P. "Characterization of Sprays of Water and Urea-Water Solution from a Commercial Injector for SCR DeNOx Applications". In: *Proceedings 13. Internationales Stuttgarter Symposium* (2013), pp. 193–201.

[18] Kapusta, Ł. J. "LIF/Mie Droplet Sizing of Water Sprays from SCR System Injector using Structured Illumination". In: *Proceedings ILASS–Europe 2017. 28th Conference on Liquid Atomization and Spray Systems*. Valencia: Universitat Politècnica València, 2017. DOI: 10.4995/ilass2017.2017.5031.

[19] Kapusta, L. J. and Teodorczyk, A. "Laser diagnostics for urea-water solution spray characterization". In: *MATEC Web of Conferences* 118 (2017), p. 00029. DOI: 10.1051/matecconf/201711800029.

[20] Payri, R., Bracho, G., Martí-Aldaraví, P., and Moreno, A. "Using momentum flux measurements to determine the injection rate of a commercial Urea Water Solution injector". In: *Flow Measurement and Instrumentation* 80 (2021). DOI: 10.1016/j.flowmeasinst.2021.101999.

[21] Musa, S. N. A., Saito, M., Furuhata, T., and Arai, M. "Evaporation characteristics of a single aqueous urea solution droplet". In: *10th International Conference on Liquid Atomization and Spray Systems, ICLASS 2006*. 2006.

[22] Wang, T. J., Baek, S. W., Lee, S. Y., Kang, D. H., and Yeo, G. K. "Experimental investigation on evaporation of urea-water-solution droplet for SCR applications". In: *AIChE Journal* 55.12 (2009), pp. 3267–3276. DOI: 10.1002/aic.11939.

[23] Wei, L., Youtong, Z., and Asif, M. "Investigation on UWS evaporation for vehicle SCR applications". In: *AIChE Journal* 62.3 (2016), pp. 880–890. DOI: 10.1002/aic.15078.

[24] Bernhard, A. M., Peitz, D., Elsener, M., and Kröcher, O. "Quantification of gaseous urea by FT-IR spectroscopy and its application in catalytic urea thermolysis". In: *Topics in Catalysis* 56.1-8 (2013), pp. 130–133. DOI: 10.1007/s11244-013-9941-4.

[25] Fang, H. L. and DaCosta, H. F. "Urea thermolysis and NOx reduction with and without SCR catalysts". In: *Applied Catalysis B: Environmental* 46.1 (2003), pp. 17–34. DOI: 10.1016/S0926-3373(03)00177-2.

[26] Yim, S. D., Kim, S. J., Baik, J. H., Nam, I. S., Mok, Y. S., Lee, J. H., Cho, B. K., and Oh, S. H. "Decomposition of urea into NH3 for the SCR process". In: *Industrial and Engineering Chemistry Research* 43.16 (2004), pp. 4856–4863. DOI: 10.1021/ie034052j.

[27] Koebel, M., Elsener, M., and Kleemann, M. "Urea-SCR: a promising technique to reduce NOx emissions from automotive diesel engines". In: *Catalysis Today* 59.3 (2000), pp. 335–345. DOI: 10.1016/S0920-5861(00)00299-6.

[28] Koebel, M. and Strutz, E. O. "Thermal and hydrolytic decomposition of urea for automotive selective catalytic reduction systems: Thermochemical and practical aspects". In: *Industrial and Engineering Chemistry Research* 42.10 (2003), pp. 2093–2100. DOI: 10.1021/ie020950o.

[29] Börnhorst, M. and Deutschmann, O. "Single droplet impingement of urea water solution on a heated substrate". In: *International Journal of Heat and Fluid Flow* 69 (2018), pp. 55–61. DOI: 10.1016/j.ijheatfluidflow.2017.10.007.

[30] Börnhorst, M., Langheck, S., Weickenmeier, H., Dem, C., Suntz, R., and Deutschmann, O. "Characterization of solid deposits from urea water solution injected into a hot gas test rig". In: *Chemical Engineering Journal* 377 (2019), p. 119855. DOI: 10.1016/j.cej.2018.09.016.

[31] Hasan Shahariar, G. M., Jo, H., and Lim, O. "Analysis of the spray wall impingement of urea-water solution for automotive SCR De-NOx systems". In: *Energy Procedia* 158 (2019), pp. 1936–1941. DOI: 10.1016/j.egypro.2019.01.448.

[32] Kuhn, C., Schweigert, D., Kuntz, C., and Börnhorst, M. "Single droplet impingement of urea water solution on heated porous surfaces". In: *International Journal of Heat and Mass Transfer* 181 (2021), p. 121836. DOI: 10.1016/j.ijheatmasstransfer.2021.121836.

[33] Kumar, A., Muddapur, A., and Sahu, S. "Experimental investigation of Urea-water solution (UWS) spray impingement on a heated flat surface". In: *Proceeding of Proceedings of the 26thNational and 4th International ISHMT-ASTFE Heat and Mass Transfer Conference December 17-20, 2021, IIT Madras, Chennai-600036, Tamil Nadu, India*. Connecticut: Begellhouse, 2022, pp. 609–615. DOI: 10.1615/IHMTC-2021.910.

[34] Liao, Y., Dimopoulos Eggenschwiler, P., Rentsch, D., Curto, F., and Boulouchos, K. "Characterization of the urea-water spray impingement in diesel selective catalytic reduction systems". In: *Applied Energy* 205 (2017), pp. 964–975. DOI: 10.1016/J.APENERGY.2017.08.088.

[35] Schweigert, D., Damson, B., Lüders, H., Becker, C., and Deutschmann, O. "New experimental insights in AdBlue-spray/wall interaction and its impacts on EGT system design BT - 19. Internationales Stuttgarter Symposium". In: ed. by M. Bargende, H.-C. Reuss, A. Wagner, and J. Wiedemann. Wiesbaden: Springer Fachmedien Wiesbaden, 2019, pp. 142–154.

[36] Shi, X., Deng, J., Wu, Z., and Li, L. "Effect of injection parameters on spray characteristics of urea-SCR system". In: *SAE International Journal of Engines* 6.2 (2013), pp. 873–881. DOI: 10.4271/2013-01-1067.

[37] Ström, H., Lundström, A., and Andersson, B. "Choice of urea-spray models in CFD simulations of urea-SCR systems". In: *Chemical Engineering Journal* 150.1 (2009), pp. 69–82. DOI: https://doi.org/10.1016/j.cej.2008.12.003.

[38] Birkhold, F. *Selektive katalytische Reduktion von Stickoxiden in Kraftfahrzeugen: Untersuchung der Einspritzung von Harnstoffwasserlösung.* Aachen: Shaker Verlag, 2007.

[39] Abu-Ramadan, E., Saha, K., and Li, X. "Modeling of the injection and decomposition processes of urea-water-solution spray in automotive SCR systems". In: *SAE 2011 World Congress and Exhibition* 2011-01-13.x (2011). DOI: 10.4271/2011-01-1317.

[40] Fischer, S. "Simulation of the Urea-water-solution Preparation and Ammonia-homogenization with a Validated CFD-model for the Optimization of Automotive SCR-systems". PhD thesis. Technische Universität Wien, 2012.

[41] Emelyanenko, V. N., Kabo, G. J., and Verevkin, S. P. "Measurement and Prediction of Thermochemical Properties: Improved Increments for the Estimation of Enthalpies of Sublimation and Standard Enthalpies of Formation of Alkyl Derivatives of Urea". In: *Journal of Chemical & Engineering Data* 51.1 (2006), pp. 79–87. DOI: 10.1021/je050230z.

[42] Ebrahimian, V., Nicolle, A., and Habchi, C. "Detailed modeling of the evaporation and thermal decomposition of urea-water solution in SCR systems". In: *AIChE Journal* 58.7 (2012), pp. 1998–2009. DOI: 10.1002/aic.12736.

[43] Schaber, P. M., Colson, J., Higgins, S., Thielen, D., Anspach, B., and Brauer, J. "Thermal decomposition (pyrolysis) of urea in an open reaction vessel". In: *Thermochimica Acta* 424.1-2 (2004), pp. 131–142. DOI: 10.1016/j.tca.2004.05.018.

[44] Lundströml, A., Waldheim, B., Ström, H., and Westerberg, B. "Modelling of urea gas phase thermolysis and theoretical details on urea evaporation". In: *Proceedings of the Institution of Mechanical Engineers, Part D: Journal of Automobile Engineering* 225.10 (2011), pp. 1392–1398. DOI: 10.1177/0954407011406048.

[45] Kieke, M. L., Schoppelrei, J. W., and Brill, T. B. "Spectroscopy of hydrothermal reactions. 1. The CO2-H2O system and kinetics of urea decomposition in an FTIR spectroscopy flow reactor cell operable to 725 K and 335 bar". In: *Journal of Physical Chemistry* 100.18 (1996), pp. 7455–7462. DOI: 10.1021/JP950964Q/ASSET/IMAGES/LARGE/JP950964QF00010.JPEG.

[46] Brack, W., Heine, B., Birkhold, F., Kruse, M., Schoch, G., Tischer, S., and Deutschmann, O. "Kinetic modeling of urea decomposition based on systematic thermogravimetric analyses of urea and its most important by-products". In: *Chemical Engineering Science* 106 (2014), pp. 1–8. DOI: 10.1016/j.ces.2013.11.013.

[47] Shahariar, G. M. H., Wardana, M. K. A., and Lim, O. T. "A study on post impingement effects of urea-water solution spray on the heated wall of automotive SCR systems". In: *IOP Conference Series: Earth and Environmental Science* 133 (2018), p. 012025. DOI: 10.1088/1755-1315/133/1/012025.

[48] Smith, H., Lauer, T., Mayer, M., and Pierson, S. "Optical and Numerical Investigations on the Mechanisms of Deposit Formation in SCR Systems". In: *SAE International Journal of Fuels and Lubricants* 7.2 (2014), pp. 525–542. DOI: https://doi.org/10.4271/2014-01-1563UI-2014-01-1563.

[49] Börnhorst, M., Kuntz, C., Tischer, S., and Deutschmann, O. "Urea derived deposits in diesel exhaust gas after-treatment: Integration of urea decomposition kinetics into a CFD simulation". In: *Chemical Engineering Science* 211 (2020), p. 115319. DOI: https://doi.org/10.1016/j.ces.2019.115319.

[50] Spiteri, A., Dimopoulos Eggenschwiler, P., Varna, A., Boulouchos, K., and Wright, Y. M. "Numerical Modelling and Experimental Characterization of a Pressure-Assisted Multi-Stream Injector for SCR Exhaust Gas After-Treatment". In: *SAE International Journal of Engines* 7.4 (2014), pp. 2012–2021. DOI: https://doi.org/10.4271/2014-01-2822UI-2014-01-2822.

[51] Varna, A., Spiteri, A. C., Wright, Y. M., Dimopoulos Eggenschwiler, P., and Boulouchos, K. "Experimental and numerical assessment of impingement and mixing of urea–water sprays for nitric oxide reduction in diesel exhaust". In: *Applied Energy* 157 (2015), pp. 824–837. DOI: https://doi.org/10.1016/j.apenergy.2015.03.015.

[52] Nocivelli, L., Montenegro, G., Onorati, A., Curto, F., Dimopoulos Eggenschwiler, P., Liao, Y., and Vogel, A. *Quantitative Analysis of Low Pressure-Driven Spray Mass Distribution and Liquid Entrainment for SCR Application through a Mechanical Patternator*. Tech. rep. March. 2017. DOI: 10.4271/2017-01-0965.

[53] Khan, D., Bjernemose, J. H., and Lund, I. "Experimental Characterization and Numerical Modelling of Urea Water Solution Spray in High-Temperature Crossflow for Selective Catalytic Reduction Applications". In: *SAE International Journal of Sustainable Transportation, Energy, Environment, & Policy* 3.2 (2022), pp. 139–153. DOI: https://doi.org/10.4271/13-03-02-0012UI-13-03-02-0012.

[54] Rogóż, R., Kapusta, Ł. J., Bachanek, J., Vankan, J., and Teodorczyk, A. "Improved urea-water solution spray model for simulations of selective catalytic reduction systems". In: *Renewable and Sustainable Energy Reviews* 120 (2020), p. 109616. DOI: 10.1016/j.rser.2019.109616.

[55] Habchi, C., Nicolle, A., and Gillet, N. "Numerical study of deposits formation in SCR systems using urea-water solution injection". In: *J Mater Sci Nanotechnol* 6.2 (2018), p. 201.

[56] Wardana, M. K. and Lim, O. *Investigation of Solid Deposit Inside L-Type Urea Injector and NOx Conversion in a Heavy-Duty Diesel Engine*. 2021. DOI: 10.3390/catal11050595.

[57] Khristamto Aditya Wardana, M. and Lim, O. "Investigation of ammonia homogenization and NOx reduction quantity by remodeling urea injector shapes in heavy-duty diesel engines". In: *Applied Energy* 323 (2022), p. 119586. DOI: https://doi.org/10.1016/j.apenergy.2022.119586.

[58] Fischer, S., Bitto, R., Lauer, T., Krenn, C., Tauer, J., and Pessl, G. "Impact of the Turbulence Model and Numerical Approach on the Prediction of the Ammonia Homogenization in an Automotive SCR System". In: *SAE International Journal of Engines* 5.3 (2012), pp. 1443–1458. DOI: https://doi.org/10.4271/2012-01-1291UI-2012-01-1291.

[59] Kaźmierski, B., Górka, K., and Kapusta, Ł. "A conceptual design and numerical analysis of the mixerless urea-SCR system". In: *Combustion Engines* 60.4 (2021). DOI: 10.19206/CE-140539.

[60] Nishad, K., Ries, F., Janicka, J., and Sadiki, A. "Analysis of spray dynamics of urea–water-solution jets in a SCR-DeNOx system: An LES based study". In: *International Journal of Heat and Fluid Flow* 70 (2018), pp. 247–258. DOI: 10.1016/j.ijheatfluidflow.2018.02.017.

[61] Kaario, O. T., Vuorinen, V., Zhu, L., Larmi, M., and Liu, R. "Mixing and evaporation analysis of a high-pressure SCR system using a hybrid LES-RANS approach". In: *Energy* 120 (2017), pp. 827–841. DOI: 10.1016/j.energy.2016.11.138.

[62] Börnhorst, M. and Deutschmann, O. "Advances and challenges of ammonia delivery by urea-water sprays in SCR systems". In: *Progress in Energy and Combustion Science* 87 (2021), p. 100949. DOI: 10.1016/j.pecs.2021.100949.

[63] Ishimoto, J., Sato, F., and Sato, G. "Computational prediction of the effect of microcavitation on an atomization mechanism in a gasoline injector nozzle". In: *Journal of Engineering for Gas Turbines and Power* 132.8 (2010). DOI: 10.1115/1.4000264.

[64] Edelbauer, W., Birkhold, F., Rankel, T., Pavlović, Z., and Kolar, P. "Simulation of the liquid break-up at an AdBlue injector with the volume-of-fluid method followed by off-line coupled Lagrangian particle tracking". In: *Computers and Fluids* 157 (2017), pp. 294–311. DOI: 10.1016/j.compfluid.2017.09.003.

[65] Hirt, C. W. and Nichols, B. D. "Volume of fluid (VOF) method for the dynamics of free boundaries". In: *Journal of Computational Physics* 39.1 (1981), pp. 201–225. DOI: 10.1016/0021-9991(81)90145-5.

[66] Edelbauer, W., Kolar, P., Schellander, D., Pavlovic, Z., and Almbauer, R. "Numerical simulation of spray break-up from cavitating nozzle flow by combined Eulerian–Eulerian and volume-of-fluid methods". In: *International Journal of Computational Methods and Experimental Measurements* 6.2 (2017), pp. 314–325. DOI: 10.2495/CMEM-V6-N2-314-325.

Chapter 4

Computational Methodology

"Remember that all models are wrong; the practical question is how wrong do they have to be to not be useful."
—George P.E. Box

4.1 Introduction

As mentioned in Chapter 1, the primary purpose of the doctoral Thesis is to develop a computational framework capable of describing the relevant processes associated with the injection of Urea Water Solution (UWS) jets for after-treatment applications. To address this objective, the near and far-field flow of a UWS injector will be characterized using a commercial Computational Fluid Dynamics (CFD) package, specifically the CONVERGE software. Regarding the near-field characterization, two computational approaches will be carried out. One injection chamber will be recreated reproducing the far field region, although several approaches will be shown. In both of them and to reduce the computational cost of these simulations, an automated meshing approach has been used with a dynamic mesh generation named Adaptive Mesh Refinement (AMR) to refine the mesh only where it is needed. Either Volume-Of-Fluid (VOF), Mixture Model (MM) or Discrete Droplet Modeling (DDM) models will be chosen to represent the liquid phase.

The relevant processes of the UWS are different both in time and space scales. Although the different processes undergone by the UWS jet are dependent on each other, recreating its injection under a single simulation would

result in a highly expensive approach. For that reason, it is common in spray-related research to separate the near-field and the far-field dynamics into different simulations whose results are coupled off-line.

The near-field simulations will focus on characterizing the hydraulic behavior of the injectors of interest, in addition to representing the primary breakup phenomena at the typical after-treatment working conditions. The time scales and the mesh resolution are critical to properly capture all the droplets generated from the atomization process. The far-field characterization has larger time and space scales, and therefore the mesh resolution will not need to be as high as in the near-field. In this region, the most relevant characteristics to be assessed will be the macroscopic depiction of the spray, the droplet evaporation, the urea content degradation, and the spray/wall impingement with the nearby surfaces. This characterization will be performed on a three-hole UWS injector.

When needed, the outcomes from experimental studies will be used to validate and calibrate the models used and check the sanity of the obtained results. These models will be in charge of representing the effect of the turbulence upon the development of the liquid phase, the primary breakup, and the phase change reactions. The selection of these models will be done in the stage of pre-processing, and they will be selected based on their applicability to the specific problem of interest. The description of the computational methods used in addition to the representation of the physical devices used will be included in the following sections. The simulations will be based on the numerical discretization of the Navier-Stokes equations, which are responsible for representing the flow-field and will be presented in Section 4.2. As mentioned, turbulence effects have to be considered, depending on the relevant scales of the problem, LES or RANS approaches will be used, which will be shown on Section 4.2 as well.

4.2 Computational Fluid Dynamics Modeling

The CFD method is a part of the fluid dynamics field, which tries to study the governing laws of the fluids under different conditions by using numerical methods. The theoretical equations obtained through research to depict the behavior of the flow field are usually not feasible to be solved analytically. Numerical discretization is then applied to those equations by dividing the geometry of interest into a set of small volumes. This technique is commonly known as Finite Volume Method (FVM). In each of these volumes, the conservation of the variables of interest is always satisfied. The advantage of this

method is that it allows reaching where experimental methods are not able to, with a high level of detail. Additionally, with properly made CFD modeling, the costs associated with building and preparing an experimental campaign are avoided.

With respect to the characterization of after-treatment sprays, CFD approaches are challenging to apply as several physical events take place in short amounts of time. Additionally, these systems can have high Reynolds numbers within the injector due to accelerations, and low velocities once the fluid has been injected. Flow turbulence needs to be addressed to capture the effect of the surrounding gas on the injected fluid. Additionally, the generated droplets have sizes smaller than the Kolmogorov scale [1], while the integral scale can be considerably higher. This implies that not all turbulent scales can be solved simultaneously without compromising the computational cost of the simulation. This section will aim to provide an insight into the equations used to perform the numerical calculations, and show how the difficulties associated with the problem of interest have been dealt with, in addition to the sub-models used to represent the spray droplets and their phase change.

4.2.1 Navier-Stokes equations

The dynamics of the gas and liquid flow during the injection process are governed by the Navier-Stokes equations, which represent the momentum, mass, and energy conservation equations [2, 3]. The representation of the continuity, momentum, and internal energy for compressible fluids is given by Equations 4.1, 4.2, and Equation 4.3 respectively.

$$\frac{\partial \rho}{\partial t} + \frac{\partial \left(\rho u_i\right)}{\partial x_i} = S_{mass} \tag{4.1}$$

$$\frac{\partial \left(\rho u_i\right)}{\partial t} + \frac{\partial \left(\rho u_i u_j\right)}{\partial x_j} = -\frac{\partial P}{\partial x_i} + \\ + \frac{\partial}{\partial x_j}\left[\mu\left(\frac{\partial u_i}{\partial x_j} + \frac{\partial u_j}{\partial x_i}\right) - \frac{2}{3}\mu\frac{\partial u_k}{\partial x_k}\delta_{ij}\right] + \frac{\partial \tau_{ij}}{\partial x_i} + S_{mom} \tag{4.2}$$

$$\frac{\partial \rho e}{\partial t} + \frac{\partial \left(\rho u_j e\right)}{\partial x_j} = -P\frac{\partial \left(u_j\right)}{\partial x_j} + \\ + \sigma_{ij}\frac{\partial \left(\rho u_i\right)}{\partial x_j} + \frac{\partial}{\partial x_j}\left(K\frac{\partial T}{\partial x_j}\right) + \frac{\partial}{\partial x_j}\left(\rho D_{\text{diff}}\sum_m h_m\frac{\partial Y_m}{\partial x_j}\right) + S_e \tag{4.3}$$

For multi-component problems, the species transport equation (Equation 4.4) is also considered. In that expression $\rho_m = Y_m \rho$, being the density of each one of the fluids within the domain, and Y_m represents the mass fraction of each species, while n is the total amount of species considered.

$$\frac{\partial \rho_m}{\partial t} + \frac{\partial \left(\rho_m u_j\right)}{\partial x_j} = \frac{\partial}{\partial x_j}\left(\rho D \frac{\partial Y_m}{\partial x_j}\right) + S_{mass}, \quad m = 1, ..., n \tag{4.4}$$

In these transport equations, the source terms are indicated by S_x, representing for example the evaporation or condensation on the continuity equation, the body forces in the momentum equation or the condensation latent heat on the energy expression. Additionally, ρ, μ and e stand for the density, viscosity and specific internal energy. δ_{ij} is the Kronecker delta, τ_{ij} is the Reynolds stress, and σ_{ij} is the stress tensor. Lastly, D_{diff}, h_m and Y_m show the mass diffusion, the enthalpy heat and the species mass fraction.

4.2.2 Turbulence modeling

The turbulence is the chaotic three-dimensional structures that are formed on a high Reynolds fluid flow. Its presence implies a higher energy dissipation, mixing, drag, and heat transfer [4]. Representing the wide range of spatial and temporal scales is a challenge that computational methods have to deal with. Solving all these scales directly would result in excessively computationally expensive simulations. Therefore several modeling techniques are usually employed, which can be narrowed down into three main approaches: Reynolds-Averaged Navier-Stokes (RANS), Large Eddy Simulation (LES), and Direct Numerical Simulation (DNS).

- **RANS** approach does not solve the fluctuating flow variables, but considers the mean flow characteristics by averaging them. To do so, the instantaneous flow variables are decomposed into mean and fluctuating components. This decomposition (usually referred to Reynolds decompositions) is applied to the Navier-Stokes equations previously introduced. By doing so, additional terms appear on the mean equations which account for the interaction between turbulent structures. To model these new terms, additional equations are included in RANS methods. Additionally, the unsteady behavior on mean flow properties can be captured by Unsteady RANS (URANS) methods. This is achieved by using averaging periods considerably smaller than the time scale of the unsteady mean flow, but still larger than the time scale of

the turbulence fluctuations [5]. Modeling all the turbulent scales reduces the computational cost, and therefore most of the industrial studies are done with this approach.

- **LES** aims to solve the largest generated eddies (integral scales and inertial range scales), while the smallest turbulent scales (dissipative) scales are modeled. This differentiating is done using a space filtering of the Navier-Stokes equations (which is usually done thanks to the grid size), solving only the largest structures. The effects of the smallest turbulent structures are taken into account using sub-grid scale (SGS) models, helping the smallest resolved structures to dissipate. A sufficient amount of energy needs to be solved in this approach, implying sufficiently small mesh elements are required. This leads to an increase in computational power, being unfeasible for complex geometries.
- **DNS** does not model any of the turbulent scales but solves the mean and fluctuating flow variables for all the fluctuating scales present. Therefore, a substantial amount of small-enough mesh elements are needed in order to capture the integral scales as well as the Kolmogorov scales. Additionally, capturing the fastest flow fluctuations implies solving the Navier-Stokes equations at a sufficiently small time step. The cost for DNS is therefore higher than for LES approach. For that reason, and being unnecessary to have such a high level of detail, industrial applications do not employ this technique, and it is generally used for scientific purposes to further understand turbulence.

A visual comparison of the behavior of the three described turbulence approaches has been included in Figure 4.1. In it, a temporal evolution of a flow variable ϕ in a specific point in space is included. DNS approach shows a highly unsteady variable fluctuation due to the contribution of the large and small scales. On the opposite side, URANS modeling does not show any fluctuation contribution from the turbulent scales, while obtaining the variable mean characteristics. Between the both of them, LES filters the smallest fluctuations, while captures the largest structures.

As the cost of performing DNS would be excessive for the purposes of this thesis, only RANS and LES approaches will be used. For that reason, these will be further described in the following pages.

4.2.2.1 Reynolds-Averaged Navier-Stokes

Applying the Reynolds decomposition to the Navier-Stokes equations and retaining the mean contribution of the flow introduces additional terms known

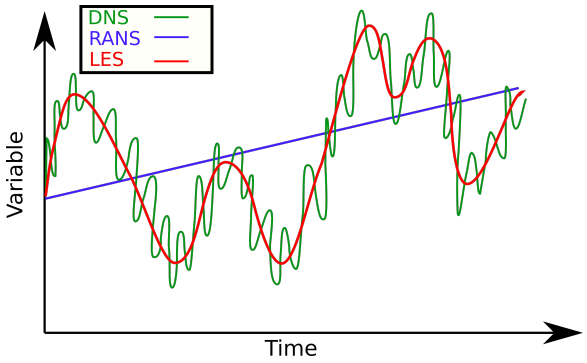

Figure 4.1: Temporal evolution of a flow variable represented by RANS, LES and DNS approaches.

as the Reynolds stress tensor, which represent the effect of flow turbulence. In order to solve the full set of variables, additional equations are needed to close the problem. Several linear eddy viscosity models are available for this purpose that can be classified depending on the number of additional transport equations introduced. For example, algebraic (*zero-equation*) models can directly model the turbulence from the flow variables, but cannot obtain the convection and diffusion of the turbulent energy. An example of this approach is the Baldwin and Lomax model [6] or the Cecebi-Smith approach [7]. *One-equation* models introduce an additional transport equation to solve a turbulent property, such as the kinematic turbulent viscosity. An example of these are the Prandtl model [8] or the Spallart-Allmaras approach [9]. *Two-equation models* allow accounting for the convection and diffusion effects of turbulence. This approach is the most commonly used for RANS applications, and among them the most employed are the $k-\epsilon$ [10] or the $k-\omega$ [11] models. In these, in addition to including an equation for the turbulent kinetic energy (k), include a second equation for the turbulent dissipation rate ϵ and the specific dissipation ω respectively. Lastly, Reynolds Stress Model (RSM) is a higher fidelity turbulence model that attempts to directly compute the Reynolds stress tensor.

The $k-\epsilon$ *RNG* model has been traditionally used for spray-like applications [12–16] which gave reasonable results, more specifically on low-velocity sprays [17, 18] as in UWS applications. For that reason, this model will be used when RANS simulations have been needed, hence a deeper explanation is included.

$\mathbf{k-\epsilon}$ RNG

The $k-\epsilon$ *RNG* model aims to determine the Reynolds stress tensor, which takes the shape of Equation 4.5. In it, the stresses are proportional to the mean rates of deformation according to the Boussinesq assumption [19]. In it, the turbulent viscosity term appears (μ_t), the strain rate (S_{ij}) and the turbulent kinetic energy (k) need to be addressed. The turbulent viscosity depends additionally on k and ϵ via Equation 4.6, where C_μ is a constant.

$$\tau_{ij} = 2\mu_t S_{ij} - \frac{2}{3}\delta_{ij}\left(\rho k + \mu_t \frac{\rho \tilde{u}_i}{\partial x_i}\right) \tag{4.5}$$

$$\mu_t = \rho C_\mu \frac{k^2}{\epsilon} \tag{4.6}$$

The Re-Normalisation Group (RNG) method [20] allows the Navier-Stokes equation to include the effects of the turbulence smaller scales by a random function application, as on the original $k-\epsilon$, the eddy viscosity was obtained from a specific length scale, hence only depicting the contribution of a speficied length scale. The ϵ equation is modified for that purpose, taking the shape of Equation 4.7, in which is similar to the standard $k-\epsilon$ except for the C_2^* term.

$$\frac{\partial(\rho\epsilon)}{\partial t} + \frac{\partial(\rho\epsilon u_i)}{\partial x_i} = \frac{\partial}{\partial x_j}\left[\left(\mu + \frac{\mu_t}{\sigma_\epsilon}\right)\frac{\partial \epsilon}{\partial x_j}\right] + C_{1\epsilon}\frac{\epsilon}{k}P_k - C_{2\epsilon}^*\rho\frac{\epsilon^2}{k} \tag{4.7}$$

Where $C_{2\epsilon}^*$ term is given by Equation 4.8 and η by Equation 4.9.

$$C_{2\epsilon}^* = C_{2\epsilon} + \frac{C_\mu \eta^3 (1-\eta/\eta_0)}{1+\beta\eta^3} \tag{4.8}$$

$$\eta = \frac{\sqrt{2S_{ij}S_{ij}}k}{\epsilon} \tag{4.9}$$

On the other hand, the transport equation for the turbulent kinetic energy is given by Equation 4.10.

$$\frac{\partial(\rho k)}{\partial t} + \frac{\partial(\rho k u_i)}{\partial x_i} = \frac{\partial}{\partial x_j}\left[\left(\mu + \frac{\mu_t}{\sigma_k}\right)\frac{\partial k}{\partial x_j}\right] + P_k - \rho\epsilon \tag{4.10}$$

The coefficients C_ϵ take into account expansion and compression effects. In the RNG approach, the constant values are explicitly obtained, while the β constant is obtained experimentally. The values obtained by Yakhot et al. are given by Table 4.1.

Model constant	Value
C_μ	0.0845
$C_{\epsilon 1}$	1.42
$C_{\epsilon 2}$	1.68
σ_ϵ	0.7194
σ_k	0.7194
η	4.38
β	0.012

Table 4.1: RANS $k-\epsilon$ RNG constant values.

4.2.2.2 Large Eddy Simulation

Although RANS models have been suitable for a large amount of turbulence problems, they account for the contribution of all large and small scales through one turbulence model, while their behavior is different. Large eddies are more anisotropic, driven by the domain geometry, while the smaller scales are almost isotropic [3]. Alternative turbulence models try to separate the scales and characterize the behavior of the larger scales through an unsteady simulation, while accounting for the small fluctuations through models thanks to their isotropic characteristics. That is the case with Large Eddy Simulation (LES).

The mathematical separation of the scales is done by a filtering function ($G\left(x, x', \Delta\right)$) whose defining parameter is the cutoff width Δ, and the filtered variable $\bar{\phi}\left(x, t\right)$ takes the shape of Equation 4.11.

$$\bar{u}\left(x, t\right) \equiv \int_{-\infty}^{\infty}\int_{-\infty}^{\infty}\int_{-\infty}^{\infty} G\left(x, x', \Delta\right) u\left(x', t\right) dx'_1 dx'_2 dx'_3 \tag{4.11}$$

In LES formulation the overbar symbol implies the filtered variable. In CFD, the cutoff width Δ is determined by the size of the grid elements (Equation 4.12).

$$\Delta = \sqrt[3]{\Delta x \Delta y \Delta z} \tag{4.12}$$

By applying the filtering operation, the flow variables are decomposed into a resolved part ($\bar{\phi_i}$) and a modeled part (ϕ'_i) as shown in Equation 4.13.

$$u_i = \bar{u_i} + u'_i \tag{4.13}$$

By applying this decomposition to the Navier-Stokes equations of the velocity field (Equation 4.2) the filtered Navier-Stokes equations are obtained (Equation 4.14).

$$\frac{\partial\left(\bar{\rho}\tilde{u}_i\right)}{\partial t}+\frac{\partial\left(\bar{\rho}\tilde{u}_i\tilde{u}_j\right)}{\partial x_j}=-\frac{\partial\bar{P}}{\partial x_i}+\frac{\partial\bar{\sigma}_{ij}}{\partial x_j}-\frac{\partial\tau_{ij}}{\partial x_j} \tag{4.14}$$

In the previous equation, the contribution of the sub-grid turbulence effects is included in the τ_{ij} term, defined as the sub-grid stress tensor, whose development is shown in Equation 4.15. This term is the focus of the numerous sub-grid models that are commonly used for LES applications.

$$\tau_{ij}=\bar{\rho}\left(\tilde{u_i u_j}-\tilde{u_i}\tilde{u_j}\right) \tag{4.15}$$

By expanding the SGS stresses, three different terms are observed. One of them is due only to the resolved fluctuations, a second one happens due to the interaction between the resolved scale and the SGS effects. It is the third term that represents the Reynolds stresses which is solely affected by the SGS structures.

For the LES simulations carried out in this work, *zero-equation* models have been used to model the SGS term. From them, the Dynamic Smagorinsky approach has been employed due to its advantages in modeling the turbulent viscosity term for a wide range of problems, compared to the traditional Smagorinsky SGS model. Therefore, it will be briefly described here.

Dynamic Smagorinsky SGS model

The Dynamic Smagorinsky approach is based on the original Smagorinsky model [21]. In it, the turbulent viscosity was related to the magnitude of the strain rate tensor and the cell size. Therefore, the SGS stresses are developed as in Equation 4.16.

$$\tau_{ij}=-2\bar{S}_{ij}\nu_t=-2\bar{S}_{ij}C_{SGS}^2\Delta^2\sqrt{S_{ij}S_{ij}} \tag{4.16}$$

The value of the model constant C_{SGS} was initially approximated by Lilly [22] by analyzing the decay rates of turbulent eddies in the inertial range. Nonetheless, other authors suggested other constant values for turbulent channel flow cases. These differences in the constant value are due to the effect of the mean flow shear, indicating that the small scale fluctuations do not behave equally for all the cases, so an adjustment of the C_{SGS} might be needed. The

Dynamic Smagorinsky model tries to overcome this problem by determining its local value for a broad range of flow situations.

In it, a second filtering operation with a second filter width is applied. The contribution of the resolved scales on the stress term (Leonard term, L_{ij}) is obtained by the difference between the stress tensor of the original and the second filtering operation (referred to as Germano identity [23]). From it, an expression to designate the value of C_{SGS} is given by Equation 4.17, which is the result of a least-squares approach to evaluate the values of the constant [24]. In this expression, M_{ij} depends on the strain tensor and the filter width of the second filtering operation $\hat{}$.

$$C_{SGS} = \frac{M_{ij}L_{ij}}{M_{kl}M_{kl}} \tag{4.17}$$

4.2.3 Liquid phase representation

UWS applications imply multi-phase, multi-component flows that interact with each other. Specifically, the liquid phase suffers a large amount of events that contribute towards the main goal of deNOx after-treatment systems, which is showing a proper flow disruption, leading to a primary breakup event that tries to minimize the size of the generated UWS droplets. Historically, there are two differentiated ways of representing the liquid phase in computational fluid dynamics. Each one of them has distinct philosophies and certain advantages and disadvantages that result in different applicability for spray injection systems. The two typologies are known as *Eulerian-Eulerian* or *Eulerian-Lagrangian*, and both of them are used within this work.

4.2.3.1 Eulerian-Eulerian treatment

The Eulerian-Eulerian approach to represent the liquid phase makes use of the very same domain discretization as the gas phase, therefore having a continuous transport field. What is characteristic of this method is the tracking of the liquid-gas interface by the computation of the void fraction (α) in each one of the volumes the domain has been discretized in. The void fraction represents the ratio of gas volume respect to the cell total volume (Equation 4.18).

$$\alpha = \frac{V_{gas}}{V_{cell}} \tag{4.18}$$

This method is capable of dealing both with compressible and incompressible fluids. However, for the low-pressure applications, as it is the case

for UWS applications, it can be assumed that the liquid is incompressible, while the gas components are compressible. During this work, two different Eulerian-Eulerian approaches have been taken to track the behavior of the UWS mixture with the surrounding air.

Mixture Model

The Mixture Model tracks the presence of the liquid phase by solving the species transport equation (Equation 4.4). Then, the void fraction is built from the species mass fraction within each cell. The sum of the mass of gas species is computed, and the remaining mass is understood as the liquid mass, as it is shown in Equations 4.19 and 4.20. In them, n_g is the total amount of gas species, m_g is the corresponding‘ total mass fraction, and m_l is the total liquid mass fraction.

$$m_g = \sum_{m=1}^{n_g} Y_m \qquad (4.19) \qquad\qquad m_l = 1 - m_g \qquad (4.20)$$

From there, the void fraction can be computed according to Equation 4.21.

$$\alpha = \frac{m_g}{\rho_g} \left(\frac{m_g}{\rho_g} + \frac{m_l}{\rho_l} \right)^{-1} \qquad (4.21)$$

The advantage of the Mixture Model approach is that it allows multi-component-made liquid phases, as it is the case for the UWS (a urea-water mixture). The main drawback is that without the use of interface reconstruction schemes, the liquid-gas interface remains diffusive, and therefore the shape of such interface remains unknown. This approach is capable to characterize compressible or incompressible liquids, although as mentioned, for its application to UWS injection systems, the liquid phase can be treated as incompressible due to its low-pressure conditions.

Volume-Of-Fluid

The Volume-Of-Fluid (VOF) approach is based on the marker-and-cell method [25]. This approach does not make use of the species transport equation but includes an additional transport equation for the volumetric void fraction α along with the rest of the Navier-Stokes equations. It takes the

shape of Equation 4.22, and therefore tracks the evolution of the void fraction field along the domain.

$$\frac{\partial \alpha}{\partial t} + u \cdot \nabla \alpha = 0 \tag{4.22}$$

Based on the resolution of the α field, it can be obtained whether a cell is filled with gas or liquid. Additionally, the cell density (Equation 4.23) and viscosity (Equation 4.24) can be extracted based on the void fraction value through linear relationships.

$$\rho = \rho_g \alpha + \rho_l (1 - \alpha) \tag{4.23}$$

$$\mu = \mu_g \alpha + \mu_l (1 - \alpha) \tag{4.24}$$

As the void fraction is tracked along the domain, and not the individual species that the liquid phase is composed of, the VOF approach does not allow the inclusion of multi-component liquid phases, but can only model single-component fluids. In the simulations carried out for this Thesis, the similarities shown by the studies shown in Chapter 3 between UWS and pure water have been accepted. Then, water has been used as surrogate liquid in these simulations.

Reconstruction of the liquid interface

The resolution of the convective terms in the Navier-Stokes equations for VOF approaches (including transport of α) generally introduces numerical diffusion effects due to the use of an Upwind Differential Scheme (UDS) or dispersion of the solution when using Central Differential Schemes (CDS) [26]. Therefore, the interface between both phases is not accurately captured and additional interface reconstruction schemes are needed. Two types of interface reconstruction are shown in Figure 4.2.

In this work, a donor-acceptor interface reconstruction scheme proposed by Waclawczyk and Koronowicz [28] is employed, named High Resolution Interface Capturing (HRIC). The HRIC scheme is based on a blending function that transitionally smooths upwind and downwind differencing schemes to satisfy the Convective Boundedness Criterion (CBC). The dynamic blending between differencing schemes allows capturing the local distribution of the void fraction.

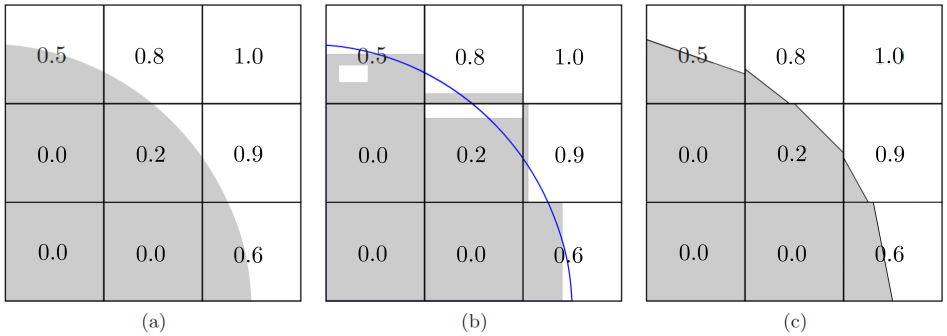

Figure 4.2: VOF reconstruction of the interface. (a) Real interface position (b) Donor-Acceptor reconstruction scheme (c) Piece-wise linear reconstruction (from [27]).

Surface tension modeling

For low-velocity atomizing applications, as it is on UWS applications, the importance of the surface tension forces increases as the inertial forces lose significance. The effect of the surface tension is also included in the VOF model through the inclusion of a source term in the momentum transport equation (Equation 4.2). This force only acts on the liquid surface, and helps to maintain equilibrium between the inward inter-molecular attractive forces and the outward pressure gradient force between the liquid and gas. As the interface between both phases is not tracked explicitly, but the void fraction is a continuum field, a Continuum Surface Force (CSF) model is used [29]. In it, as it happens for the void fraction field, the surface tension is also modeled as a continuous field.

4.2.3.2 Eulerian-Lagrangian treatment

The second possibility of representing the liquid phase from sprays is the called Eulerian-Lagrangian approach, or Droplet Discrete Model (DDM). In it, the Eulerian description of the gas flow is coupled with a Lagrangian method of tracking the liquid droplets. These droplets are introduced into the computational domain using parcels, which are groups of drops that share the same characteristics (size, temperature, and velocity) that statistically represent the spray. As they are treated in a Lagrangian way, the reference frame of the liquid phase moves with the position of the particles. In each iteration, the parcels and the discretized volumes interact with each other, exchanging

mass, momentum and energy. Numerically, the motion of the parcels can be determined by solving ordinary differential equations, while the coupling with the Eulerian frame is done by treating the parcels as source terms, suitable for the partial differential Navier-Stokes equations. In this way, the representation of the liquid phase is significantly cheaper. The equation that rules the motion of each one of the parcels is given by Equation 4.25.

$$\rho_l V_d \frac{du_i}{dt} = F_{d,i} \tag{4.25}$$

In it, ρ_l represents the liquid density, V_d is the droplet volume, and $F_{d,i}$ is the sum of drag forces and gravitational forces (Equation 4.26).

$$F_{d,i} = F_{drag,i} + F_{g,i} = C_D A_f \frac{\rho_g |U_i|}{2} U_i + \rho_l V_d g_i \tag{4.26}$$

Nonetheless, the interaction between the discrete parcels and the Eulerian frame needs some consideration. As shown by the previous equation, the exchange between phases is done in two ways, from the droplet to the gas, and from the gas to the liquid. The force exerted on a liquid particle is generally applied to the centroid of the droplet. It needs to be calculated based on the undisturbed gas velocity where the droplet center is located. The undisturbed velocity is represented by the gas velocity without the effect of the presence of the droplet. For small-enough droplet sizes, the perturbation exerted on the flow by the particle is negligible. In those cases, the fluid velocity of the cell would equal the fluid velocity on the undisturbed situation, and therefore the force calculation can be done without problems. In the case of greater-than-cell particle sizes, this is not applicable, as the disturbance of the droplet on the flow is significant, and the fluid velocity of the cell does not equal the undisturbed case. Therefore, for Eulerian-Lagrangian frameworks, it is important to have significantly large cell-to-droplet diameter ratios. If not, an incorrect calculation of the disturbed gas velocity would imply a error in the droplet force, and an unrealistic effect of the droplet presence on the fluid velocity [30, 31]. Additionally, with larger than cell droplets, the simulations would be more similar to an Eulerian-Eulerian approach, as shown in Figure 4.3.

Drop drag

As it has been already mentioned, obtaining the drag force exerted by the gas phase into the parcel is a critical step. During this work, the Taylor

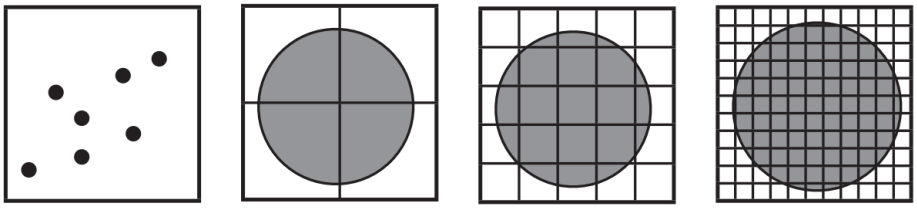

(a) $d_p \approx \Delta x/10$ (b) $d_p \approx \Delta x$ (c) $d_p \approx 4\Delta x$ (d) $d_p \approx 10\Delta x$

Figure 4.3: Droplet representation at different grid resolutions (From [32]).

Analogy Breakup (TAB) developed by O'Rourke and Amsden [33], was implemented. In it, the deformation of a droplet is characterized by assuming the droplet as a damped forced oscillator (Equation 4.27), where x represents the displacement of the drop from its spherical shape.

$$F - kx - d\dot{x} = m\ddot{x} \tag{4.27}$$

Based on that, and by specifying certain model constants (C_k, C_F, C_b), the model accounts for that drop distortion by linearly modifying the drag from a perfectly spherical to a disk-shaped droplet [34] (Equation 4.28).

$$C_D = C_{D,sphere}\,(1 + 2.632x) \tag{4.28}$$

When it comes to computing the effect of the momentum exchange from the Lagrangian particle to the Eulerian mesh, a nearest-node approach is followed, using a Taylor series expansion to calculate the Eulerian field velocity where the particle is located.

Coalescence model

In order to represent droplet collision effects depicted in Subsubsection 2.5.3.3, the No Time Counter (NTC) method has been employed. It is based on the techniques used in gas dynamics for Monte Carlo calculations, and it is faster and more accurate than the traditional O'Rourke model [35]. It is derived from the probability model for stochastic collision. It sorts the parcels into groups residing in a determined cell, and picks an stochastic subsample of the possible collision pairs. Further information about this method can be found in the work of Schmidt and Rutland [36].

Primary and secondary breakup

To take into account the primary and secondary breakup of the injected spray using the DDM technique, several models are available in the literature. The jet instabilities need to be accounted for to predict the consequent droplet size distribution from that primary breakup event. Nonetheless, in this study the input of the DDM model is already the outcomes of such primary breakup. The Kevin-Helmholtz (KH) has been selected to model the primary breakup. It is based on the liquid jet stability analysis. In that analysis, a viscous, liquid and cylindrical jet is assessed. An axissymetric surface infinitesimal displacement is considered, and the most unstable wave generated is considered (obtaining maximum growth rate Ω and wavelength Λ). This specific wave propagation is the one considered to disrupt the initial jet. The breakup of the parcel and the subsequent drops in secondary atomization conditions is calculated assuming that the breakup drop radius is proportional to the obtained wavelength (Equation 4.29), and the breakup time follows Equation 4.30. The model needs from specific constants (e.g. B_0 and B_1) that need to be tuned for each particular case. A more in-depth explanation can be located on the original work [37].

$$r_c = B_0 \Lambda_{KH} \qquad (4.29) \qquad\qquad \tau_{KH} = \frac{3.726 B_1 r_p}{\Lambda_{KH} \Omega_{KH}} \qquad (4.30)$$

In addition to the KH breakup model, the Rayleigh-Taylor (RT) instabilities have been assessed. These instabilities appear due to the deceleration of the drops due to the drag force acting on them. From that analysis, also the fastest growing wavelength in addition to the associated growth rate are extracted. When sufficient time has passed ($\tau_{RT} = f\left(\Omega_{RT}^{-1}\right)$), breakup takes place. In this model, additional constants need to be adjusted.

On the implemented breakup models during the UWS simulations, both previous methods (KH and RT) have been combined into one. In it, both models compete between each other to see which instability is responsible for the secondary breakup as the parcels are introduced into the domain [38]. The one that shows a shorter breakup time is responsible for carrying out the droplet division.

Water evaporation modeling

In addition to the breakup models previously described, the computational solution should take into account the transformation of the water and urea content of the droplets into a gaseous state.

The water evaporation rate is given by Equation 4.31 [39].

In it, α_{spray} is a model scaling factor for the mass transfer coefficient and D is the mass diffusivity. r_0 is the droplet size, while B_d is a the Spalding number, depending on the vapor liquid mass fraction Y_1^* on the surface of the drop and the vapor mass fraction Y_1 (Equation 4.32). The Sherwood number represents the ratio between mass transfer by convection with respect to diffusion. Through the Frossling correlation [40], the Sherwood number is related to the Reynolds and Schmidt numbers using Equation 4.33. The value of the constant K is assumed to have the proposed value from Ranz and Marshall work [41], $K = 0.6$, used to relate their data of mass and heat transfer.

$$\frac{dr_0}{dt} = -\frac{\alpha_{spray}\rho_g D}{2\rho_l r_0} B_d Sh_d \tag{4.31}$$

$$B_d = \frac{Y_1^* - Y_1}{1 - Y_1^*} \tag{4.32}$$

$$Sh_d = \left(2.0 + K\ Re_d^{1/2} Sc^{1/3}\right) \frac{ln(1 + B_d)}{B_d} \tag{4.33}$$

Y_1^* can be obtained from Equation 4.34 through the molar weights if it is assumed that the partial pressure of the vapor is equal to the equilibrium vapor pressure.

$$Y_1^* = \frac{MW_{liquid}}{MW_{liquid} + MW_{mix}\left(\frac{p_g}{p_v} - 1\right)} \tag{4.34}$$

In the previous equation, the $\mathrm{MW_{mix}}$ refers to the molecular weight of the mix without including the vapor from the liquid species, whie p_g refers to the gas pressure and p_v refers to the vapor pressure at the current droplet temperature.

Modeling of the thermolysis reaction

The transformation from liquid urea to gaseous ammonia (thermolysis), as indicated in the literature, can be done by means of a kinetic model that represents the intermediate reactions, or a direct step called *molten solid*. The *molten solid* approach has been adopted in this work as the stability of the gaseous urea has been observed to be low (Section 3.3) and the usage of a detailed kinetic model would result in more computationally expensive simulations.

This direct transition can be tackled in two ways: by evaporating the molten urea into a gaseous state through a sublimation process, and afterward a reaction to give a molecule of NH_3 and HNCO. As gaseous urea is understood to be highly unstable, so this approach merges the two transformation enthalpies (evaporation and reaction) into one single step, transitioning from molten urea to NH_3 and HNCO. This transition is done using an Arrhenius correlation in which the rate of change of the droplet radius is computed (Equation 4.35).

$$\frac{dm_d}{dt} = 2\pi R_d A \exp\left(\frac{-E_a}{RT_d}\right) \tag{4.35}$$

In this expression, m_d is the droplet mass, R_d is the droplet radius, A is a prefactor, T_d is the droplet temperature, and the activation energy is represented by E_a. For large droplets (more than hundred micrometers), the temperature change of the liquid phase is done using a spherically symmetric heat equation (Equation 4.36).

$$k_d \frac{\partial T}{\partial r}\bigg|_{r=R_d} = h\left[T_g - T\left(r_0, t\right)\right] + \rho_d H_{vap} \frac{dR_d}{dt}\bigg|_{vap} + \rho_d H_{dcmp} \frac{dR_d}{dt}\bigg|_{dcmp} \tag{4.36}$$

Where k_d is the thermal conductivity of the droplet, r_0 is the distance from the droplet center, h is the convection coefficient between the droplet and the gas, T_g is the gas temperature, $T\left(R_d, t\right)$ is the temperature at the droplet surface, ρ_d is the droplet density, H_{vap} is the latent heat of vaporization at the drop temperature, while H_{dcmp} is the latent heat of decomposition of the urea.

For small-enough droplets, the model considered assumes that the temperature is uniform across the droplet volume, being the changes in temperature instantaneous for the whole droplet. The equation representing this model is shown on Equation 4.37. In it, C_{p_d} is the specific heat capacity of the droplet, while k_g is the thermal conductivity of the surrounding gas and Nu_d is the Nusselt number of the droplets.

$$C_d m_d \frac{dT_d}{dt} = 2\pi R_d k_g N u_d \left(T_g - T_d\right) + \frac{dm_d}{dt}\bigg|_{vap} H_{vap} + \frac{dm_d}{dt}\bigg|_{dcmp} H_{dcmp} \tag{4.37}$$

The thresholding diameter that differentiates which model deals with the temperature evolution is a user-given input which should be set to a value

that best matches the problem of interest. The mass change of the droplet due to urea degradation or water vaporization is used to calculate the heat loss from the thermal decomposition and water evaporation respectively.

Based on the previous equations, the generation of the thermolysis products are obtained from the degradation rate of the urea content $\dot{m}_{deg-urea}$. Generation of NH_3 is given by Equation 4.38, while HNCO is given by Equation 4.39.

$$\dot{m}_{NH_3} = -\frac{M_{NH_3}}{M_{urea}}\dot{m}_{deg-urea} \tag{4.38}$$

$$\dot{m}_{HNCO} = -\frac{M_{HNCO}}{M_{urea}}\dot{m}_{deg-urea} \tag{4.39}$$

In these equations, $\dot{m}_x$ represents the mass generation/depletion rate of each one of the species, while M_x is the molar fraction of the species that play a role in the degradation process.

Modeling of the hydrolysis reaction

As specified in Chapter 2, during the thermolysis process, from a molecule of urea, a molecule of NH_3 and HNCO are obtained. HNCO is considered an intermediate product that can further react together with the evaporated water to form an additional molecule of NH_3 and CO_2. To do so, the SAGE kinetic solver [42] is used. The ordinary differential equations present in the model are solved using the CVODE solver of the SUNDIALS package [43]. The SAGE solver calculates the reaction rates of the introduced reaction mechanism, and defines the rate of ammonia generation through Equation 4.40. This NH_3 generation ($\dot{\omega}_{NH_3}$) depends on the reaction rate (q), and the stoichiometric coefficient (v) of the reactants (HNCO and H_2O).

$$\dot{\omega}_{NH_3} = \left(v''_{m,r} - v'_{m,r}\right) q_r \tag{4.40}$$

Droplet/Wall impingement and film formation

The interaction between the liquid phase and the boundary walls of the simulations has been considered using the previously described Kuhnke regime map [44] in subsubsection 2.5.3.6. The possible outcomes depended completely of the characteristic temperature (T^*) and the K number. This characteristic

temperature is a non-dimensional value which relates the wall temperature to the saturation temperature (Equation 2.25), and the K number is a function of the Weber and Laplace number.

$$K = \frac{(\rho d)^{\frac{3}{4}} U^{\frac{5}{4}}}{\sigma^{\frac{1}{2}} \mu^{\frac{1}{4}}} = We^{\frac{5}{8}} La^{1/8} \tag{4.41}$$

The Laplace number is given by Equation 4.42.

$$La = \frac{\sigma \rho 2 r_0}{\mu^2} \tag{4.42}$$

In the previous equations, σ is the surface tension, ρ is the density, μ is the viscosity of the droplet, while r_0 represents the radius of the impinging droplet. In that sense, the K number is a representation of the size and kinematics of the droplet. The critical K number that separates deposition from splash criteria is obtained based on the surface roughness and wall temperature for dry wall conditions, while for wet surfaces, it is dependent on the Laplace number.

In *splash* conditions, where a set of secondary droplets are generated after an initial droplet has impinged. The properties of this newly formed droplets are based on the following equations. The mass fraction of the secondary droplets is given by Equation 4.43, where m_{wf} is the film mass, and p is a random number that goes from 0 to 1.

$$v_m = \left\{ \begin{array}{ll} \min\left\{1, \frac{T^*-0.8}{T^*_{crit}}(1-B)+B\right\}, B = 0.2+0.6p & \text{Dry cond.} \\ \min\left\{1+\frac{m_{wf}}{m_d}, \frac{T^*-0.8}{T^*_{crit}}(1-B)+B\right\}, B = 0.2+0.9p & \text{Wet cond.} \end{array} \right\} \tag{4.43}$$

The diameters are obtained according to Equation 4.44, based on the wall normal droplet Weber number and the impinging angle α. From there, the amount of generated droplets is established so to satisfy the mass conservation.

$$\gamma_{10} = \frac{D_{10}}{D_0} = \left\{ \begin{array}{ll} 3.3 \exp^{3.6\left(\frac{\alpha}{\pi}\right)^2} We^{-0.65} & \text{Dry cond.} \\ 2.2 \exp^{3.6\left(\frac{\alpha}{\pi}\right)^2} We^{-0.36} & \text{Wet cond.} \end{array} \right\} \tag{4.44}$$

The velocity of these droplets is based on an approximation of the droplet We, which is given in Equation 4.45. In it, We_{a0} represents the incoming

droplets We, and v_{32} has an associated value of 2. The velocity computed from the resulting We is given by Equation 4.46.

$$We_{a1} = \left\{ \begin{array}{ll} \gamma_{10}\left[We_{a0}\left(1-0.85\sin^2\alpha\right)\right] - \frac{12}{v_{32}} & \text{Dry} \\ \max\left\{51-7.1e^{3.4\frac{\alpha}{\pi}}, We_{a0}\left[-0.378\left(\frac{\alpha}{\pi}\right)^2 - \frac{1}{8}\left(\frac{\alpha}{\pi}\right)+0.156\right]\right\} & \text{Wet} \end{array} \right\} \tag{4.45}$$

$$U_{a1} = \sqrt{\frac{\sigma We_{a1}}{\rho D_{10}}} \tag{4.46}$$

Lastly, the ejection angle of the droplets is given by β, whose definition is located in Equation 4.47.

$$\beta = \log\frac{p}{1-p} + \bar{\beta} \tag{4.47}$$

Where the value of $\bar{\beta}$ depends on the wall roughness and the wall working conditions (Equation 4.48).

$$\bar{\beta} = \left\{ \begin{array}{ll} 9.3 + \ln\left(\varepsilon_a\right)\left(2.7-0.003\alpha\right) + 0.22\alpha & \text{Cold, Dry} \\ 0.225\alpha e^{(0.017\alpha-0.937)^2} & \text{Cold, Wet} \\ \alpha 0.96 e^{-0.0045We} & \text{Hot} \end{array} \right\} \tag{4.48}$$

4.2.4 Numerical methods

The conservation laws are applied to control volumes within the domain in the FVM. For that, the differential equations (Eq. 4.49) are converted to integral form (Eq. 4.50) using the Green-Gauss theorem. In it, V is the volume, S is the surface area and n is the normal vector to the surface.

$$\frac{\partial\phi}{\partial t} + \frac{\partial u\phi}{\partial x} = 0 \tag{4.49}$$

$$\frac{\partial\phi}{\partial t} + \frac{1}{V}\int_S u\cdot n\phi dS = 0 \tag{4.50}$$

From the integral form, the discrete form (Eq. 4.51) can be obtained.

$$\frac{\partial\phi}{\partial t} + \frac{1}{V}\sum_i u_{f,i}\phi_{f,i}S_i \tag{4.51}$$

The values are stored at the cell center, but to solve the integral form of the differential equations, the velocity and the variable ϕ need to be computed

at the cell surface. First-order interpolation methods result from upwinding the surface value from the cell center, which results on a first-order scheme.

$$\phi_{i+1/2} = \phi_i \tag{4.52}$$

A second-order scheme can be obtained by averaging the value on the center of the adjacent cells (Equation 4.53).

$$\phi_{i+1/2} = \frac{1}{2}\phi_i + \frac{1}{2}\phi_{i+1} \tag{4.53}$$

Depending on the flow variable solved, and the typology of the simulation performed, a specific scheme has been chosen (see Table 4.2). The selection of the discretization schemes has been done based on maximizing the accuracy of the results while ensuring stability of the simulations. For that reason, VOF simulations include first order schemes to ensure stability which could not be achieved using second order schemes. The instabilities found in regions near the injector walls where artifacts from the micro-CT scan were present. In the remaining simulations, generally a second order scheme was stable and therefore provided more accurate results.

Simulation	Equation	Discretization Scheme
Volume-Of-Fluid	Momentum	1st-Order Upwind
	Density	1st-Order Upwind
	Energy	1st-Order Upwind
	Passives	1st-Order Upwind
	Turbulence	1st-Order Upwind
Mixture Model	Momentum	2nd-Order Central
	Density	2nd-Order Central
	Energy	2nd-Order Central
	Passives	2nd-Order Central
	Turbulence	1st-Order Upwind
Discrete Droplet Model	Momentum	2nd-Order Central
	Density	2nd-Order Central
	Energy	2nd-Order Central
	Passives	2nd-Order Central
	Turbulence	1st-Order Upwind

Table 4.2: Spatial discretization schemes used for the different simulations performed.

After spatial discretization of the conservation equations, a term remains in differential form in Equation 4.51, which represents the temporal evolution of the variables. That discretization, as for the spatial discretization can have several discretization orders (1st order, Equation 4.54 and 2nd order, Equation 4.55). In them, the superindexes *n*, *n-1*, and *n+1* represent the current, previous and next time steps, correspondingly.

$$\frac{\partial \phi}{\partial t} = \frac{\phi^{n+1} - \phi^{n}}{\Delta t} \quad (4.54) \qquad \frac{\partial \phi}{\partial t} = \frac{3\phi^{n+1} - 4\phi^{n} + \phi^{n-1}}{2\Delta t} \quad (4.55)$$

The PISO algorithm

In order to solve the discretized equations, an iterative algorithm is needed, which in this case has been the Pressure Implicit with Splitting of Operators (PISO)[45]. This algorithm allows coupling the pressure and velocity fields. It initially solves the momentum equation through a predictor step. From that momentum solution, the pressure field is solved, which is input again to correct the predicted momentum equation. This iterative process is repeated to achieve the desired accuracy. After the first predictor and corrector step has been completed, the remaining transport equations are then solved (density, species, energy). The pressure field is then corrected, in addition to the velocity field, which are input again in order to correct the remaining variables. This iterative process can be repeated as many times to achieve a proper convergence of the fields. The loop is considered converged if the density correction error is lower than an established value in compressible cases, while for the incompressible cases, the error considered is of the pressure field.

Once the loop has been considered converged, a Jacobi iteration is applied to ensure that the conservation of the variables is achieved (energy, density, species and scalar transport equations). The turbulence equations are solved in the last step in the PISO algorithm for a specific time step, as observed in Figure 4.4.

The checkerboard effect

In numerical approaches that approach the conservation equations by solving the flow variables in the cell center, a decoupling of the pressure and velocity fields can occur. The pressure value on the center of a cell does not depend on the pressure of the neighbor cells but on the cells adjacent to the neighbors. According to Figure 4.5, the pressure at cell p depends on the

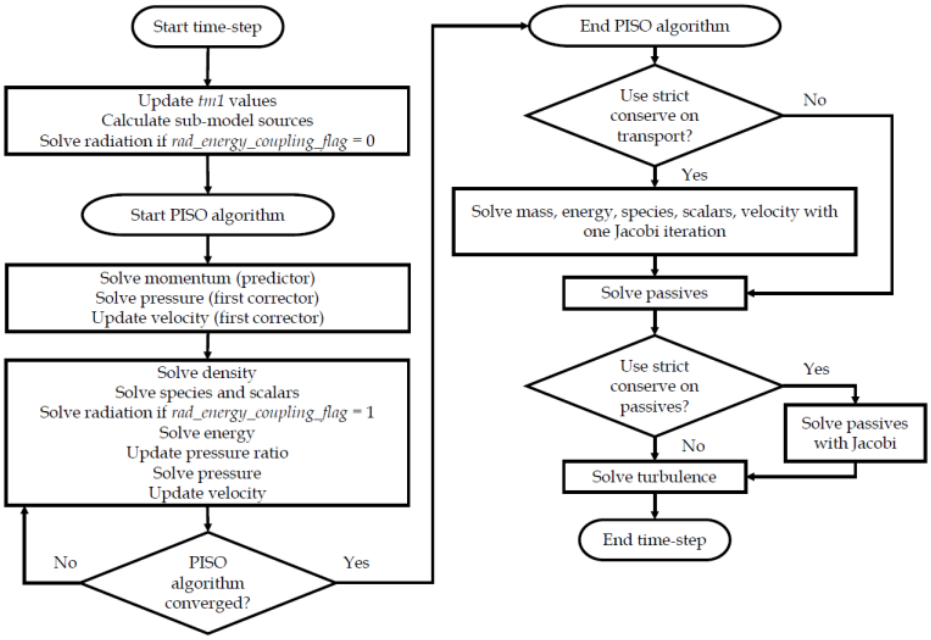

Figure 4.4: Solution order of the transport equations in the PISO algorithm.

pressure-value at cell WW and EE. In that way, two independent solutions appear in the same mesh, looking like a checkerboard. To deal with this, the Rie-Chow algorithm [46] has been used to deal with this effect

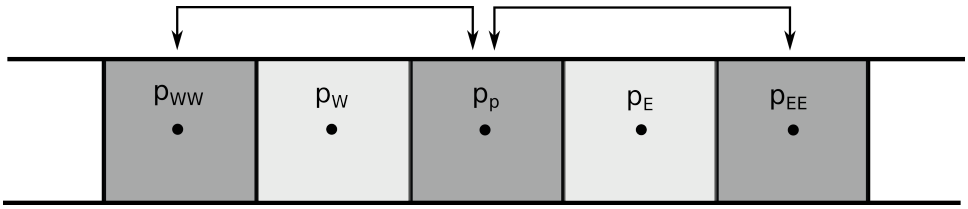

Figure 4.5: Representation of the checkerboard effect.

4.3 Pre-processing

To perform the several simulations planned to characterize the UWS sprays, several geometries are introduced in the computational framework. These represent the real geometries in which the experimental campaigns have been carried out.

4.3.1 Internal flow campaign

It is mandatory to recreate the inner geometry of the UWS dosing unit of interest to perform the characterization of the internal flow and the near-field spray. The injector of interest consists of a UWS commercial dosing unit having three co-axial holes. It has a solenoid actuator and allows injection pressures from 3 to 9 bar (absolute). It is shown in Figure 4.6. It is liquid-cooled through two water ports.

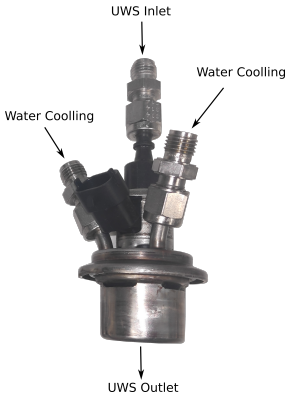

Figure 4.6: UWS dosing unit.

Figure 4.7a, on the other side, shows the disposition of the injector holes, separated 120° each, from which the orifice external characteristics have been extracted using optical microscopy techniques (Figure 4.7b). The main characteristics of the injector of interest have been summarized in Table 4.3.

Parameter	**Value**	**Units**
Nº Holes	3	-
Outlet diameter	135	µm
Injection Pressure (abs)	3-9	bar
Max. Fluid Temperature	120	°C
Emission Target	Euro 6	-

Table 4.3: Main UWS injector characteristics.

The internal characteristics of these orifices remain unknown using optical microscopy, and more advanced techniques are needed to assess them. X-Ray tomography [47] is capable of penetrating the metal sheets and providing

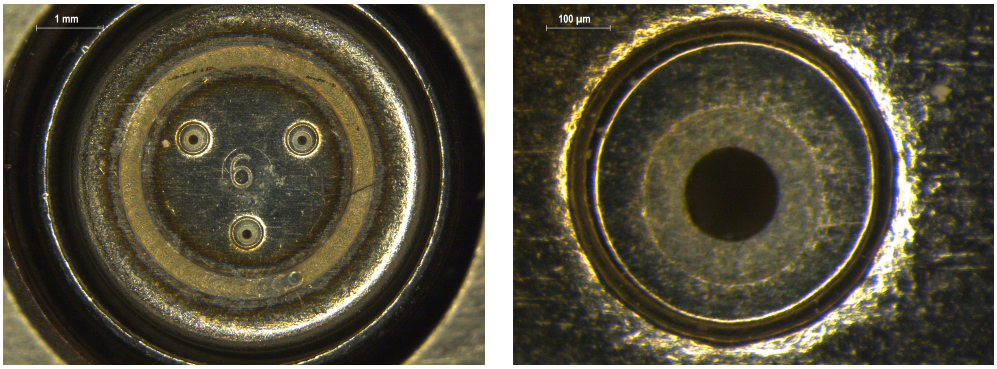

(a) Three holes. (b) One hole zoom.

Figure 4.7: Orifices of the UWS injector.

insight into the inner cavities of the dosing module without the need of disassembling the unit. Two different X-Ray facilities have been employed for it, and the results of such reconstructions will be introduced.

4.3.1.1 *Generation 1*

The first X-Ray tomography was carried out at "Museo Nacional de Ciencias Naturales" (MNCN-CSIC). During the process, several 2-Dimensional slices were obtained in the three spatial directions. The spatial resolution of Computerized Tomography (CT) is a compromise between penetration power and resolution. In this case, the tolerance associated was 20 µm. From these CT slices, a geometry model was obtained through a Computer-Aided Design (CAD) software. The reconstruction showed a pentagonal-shaped needle body, which blends into a semi-sphere at the tip of its length. The sac volume is considered to be significantly larger than typical gasoline and diesel applications. The measured orifice diameters from the CT approach resulted in values close to 150 µm which contrasts with the measured values of the optical microscopy imaging. Nonetheless, the spatial discretization as indicated was considered quite coarse, and the tolerance fits within the different measured outlet orifices. Figure 4.8 shows two views of the CT scan applied. It is visible that for Figure 4.8b, the resolution obtained is not sufficient to have an accurate representation of the critical regions of the injector, which is the sac and orifices.

Needle lift dynamics were not measured during the CT scan. Therefore a preliminary study was done to observe the needle lift at which the area between the needle and its seat became a flow limiter (Figure 4.9). Then, the lift

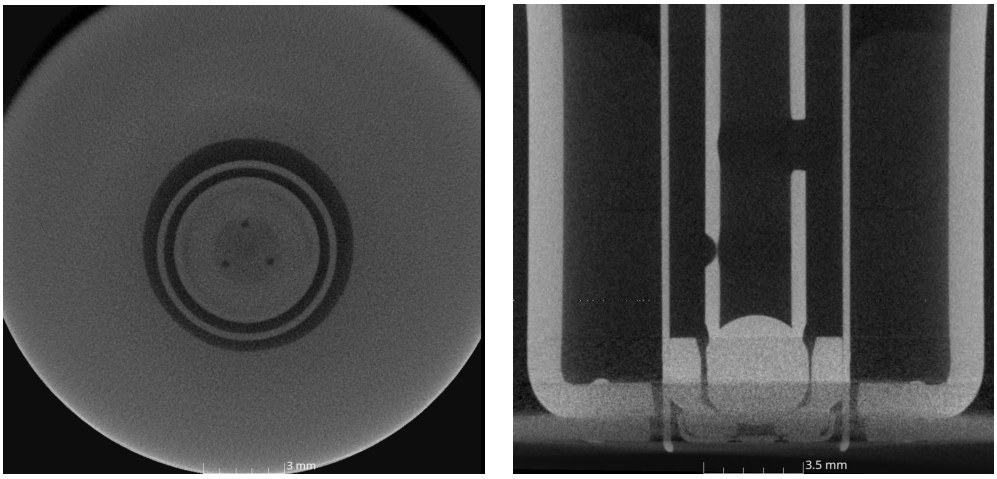

(a) Top view. (b) Lateral view.

Figure 4.8: CT images of *Generation 1* geometry.

was fixed in a value sufficiently high not to become a flow restrictor (550 µm). Due to insufficient spatial accuracy on the regions near the orifices, individual images were analyzed to estimate the near-orifice regions. A schematic representation of the reconstructed geometry is included in Figure 4.10.

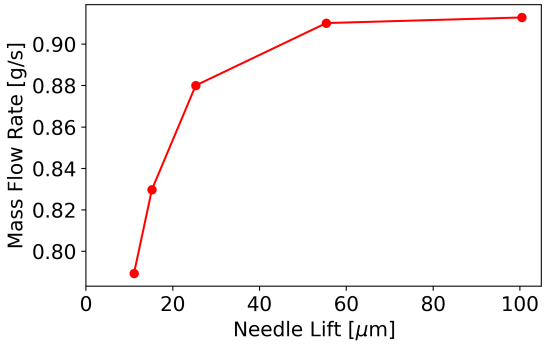

Figure 4.9: Evolution of the mass flow rate within the injector for several needle lift values for a simulation performed at 6 barG.

In it, the established needle lift can be visualized, and the large volume of the sac is present. On the zoom-in view (Figure 4.10b), the uncertain region that could not be accurately measured is visualized upstream of section D5. In addition, it will act as a flow restrictor for the UWS flow as it is the tighter

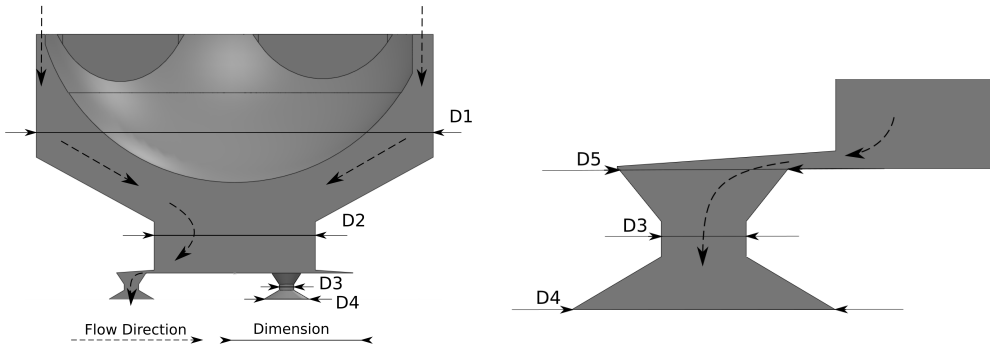

(a) Top view. (b) Lateral view.

Figure 4.10: Reconstruction of the *Generation 1* geometry through CT scan.

region on the injector geometry. In order to quantify the dimension of that gap, a specific study has been performed in which several distances have been simulated to see which one of them, within the spatial uncertainty of the CT scan shows the best agreement with experimental data. This dimension, along with the remaining geometrical dimensions of the rest of the model have been included in Table 4.4.

Dimension	**Value**
D1	3.94 mm
D2	1.60 mm
D3	0.15 mm
D4	0.29 mm
D5	0.45 mm

Table 4.4: Main UWS *Generation 1* injector dimensions.

A discharge volume has been attached to the injector that represents the region where the UWS is injected. The diameter of the truncated cone attached to the injector is large enough (2.7 mm) not to affect the solution of the simulations, and its length varies depending on the simulation typology performed on it (Mixture-Model or Volume-Of-Fluid). For the Mixture-Model simulation, the discharge volume has a length of 5 mm, while for VOF approaches, in order to detect the primary breakup droplets, a length of 10 mm has been set.

4.3.1.2 *Generation 2*

The second reconstruction of the injector of interest has been done through a high-resolution X-Ray micro-CT scan performed at the Advance Photon Source (APS) of Argonne National Laboratory. This facility allows reproducing the manufacturing imperfections that could play a role in the liquid injection and atomization [48]. The spatial precision of this method can detect characteristics of the scale of µm. Figure 4.11 shows two slices of the micro-CT scan, in which it can be appreciated the considerably higher spatial resolution than of the initial CT scan applied. Thanks to it, some differences can be detected related to the approximated geometry shown in Figure 4.10.

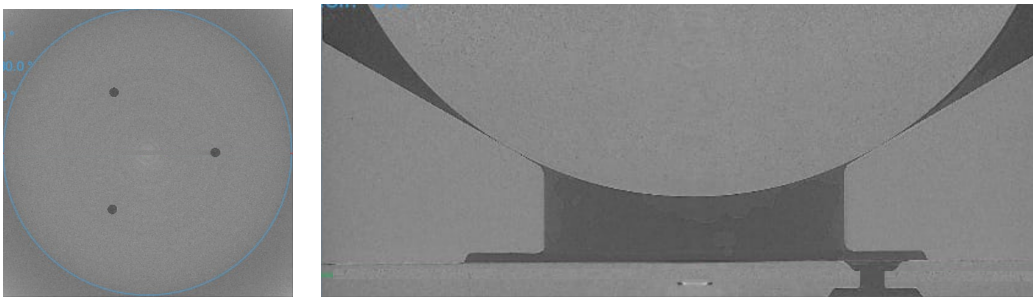

(a) Top view. (b) Lateral view.

Figure 4.11: Micro-CT images of *Generation 2* geometry.

From the applied methodology, the geometry can be extracted, and a smoothing is applied to remove the voxel geometries that arise from the spatial discretization of the technique. An average value of 136 µm has been obtained for the diameter of the injector holes, which matched the microscopy imaging values. This geometry will be used to perform the Volume-Of-Fluid simulations during this work.

When it comes to the needle lift value, it has been set so that the momentum and mass flow rate values match with the experimental results.

4.3.1.3 Boundary conditions

It is necessary to define the boundary conditions of the simulation to be able to solve the conservation equations. These represent in the most faithful way the injector working conditions. In the case of study, the fluid is injected into quiescent conditions, driven by a single inlet and outlet surfaces. The location of these boundaries is shown in Figure 4.12.

Although the assignation of the boundary surfaces is the same one applied in the *Generation 1* and *Generation 2* geometries, the values of the boundary conditions do change depending on if a Mixture-Model or a Volume-Of-Fluid simulation is carried out. A summary of the boundary condition values is included in Table 4.5 and Table 4.6 for Mixture-Model or VOF respectively. No cross-flow conditions have been considered due to the significant increase in the domain size needed to develop appropriately the boundary layer of the incoming gas. Then, the needed mesh refinement to take into account such boundary layer effects would result in highly expensive simulation, as in quiescent conditions, the cell count reached a value of 40 million (Table 4.10).

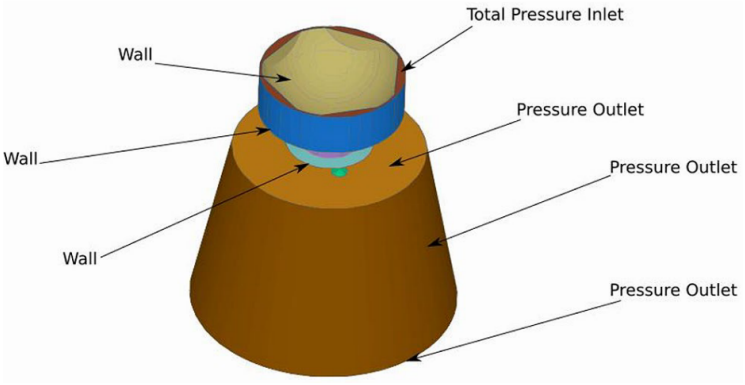

Figure 4.12: Main boundary conditions of the *Generation 1* geometry.

Boundary	**Flow Variable**	**Value**
Inlet	Total Pressure	4,6,8 barG
	Temperature	298 K
	Species	32.5 % Urea - 67.5 % Water
Outlet	Pressure	1 bar
	Backflow Temperature	298 K
	Backflow Species	Air
Wall	Velocity	Law-Of-Wall
	Temperature	298 K

Table 4.5: Boundary conditions for the Mixture Model simulations carried out.

Boundary	Flow Variable	Value
Inlet	Total Pressure	4,6,8 barG
	Temperature	393 K
	Species	100% Water
Outlet	Pressure	1 bar
	Backflow Temperature	373 K
	Backflow Species	Air
Wall	Velocity	Law-Of-Wall
	Temperature	393 K

Table 4.6: Boundary conditions for the Volume-Of-Fluid simulations carried out.

4.3.1.4 Initial conditions

In order to start solving the transport equations and characterize the spray behavior, it is necessary to generate an initial solution in the fluid domain. The injector body and the injector holes have been filled with liquid (either UWS or H_2O depending on the simulation) with the corresponding liquid temperature of the inlet boundary condition. The pressure field inside the injector has also been set to the operating injection pressure of the liquid phase. The discharge volume on the other hand has been initialized with the conditions of the surrounding air, with its associated temperature and pressure. Therefore, at the orifice section, there is a discrete pressure gradient, although due to the low-injection pressures of the injector the pressure field is rapidly smoothed on the first iterations. Regarding to the turbulence field, being the Mixture-Model and VOF simulations zero-equation LES approaches, no initialization is required.

4.3.2 External flow campaign

For the external spray characterizations, the geometry of the injector is not of importance, but the initial spray characteristics and the geometry in which that spray is injected. Previous experimental work was carried out using a high-flow high-temperature installation capable of recreating the injection conditions under which the UWS is subjected [49, 50]. Therefore, an approximations of that geometry has been done to introduce it into the computational framework.

4.3.2.1 Reproduction of the experimental test rig

The incoming flow is not a representation of the real combustion exhaust gas composition, but can adapt the air mass flow rate and its associated temperature through a blower and an electrical heater respectively. Figure 4.13 shows a comparison between the injection chamber used for the experimental campaign from previous work [51], and the geometry used for the computational simulations. As seen, it consists of a parallelogram injection chamber to which a cylindrical inlet and outlet ducts are attached. These ducts have been considered in order to take into account the possible effects of gas velocity profiles. The incoming air flows into the injection chamber from the ∅92 mm duct and leaves it through the ∅50 mm duct.

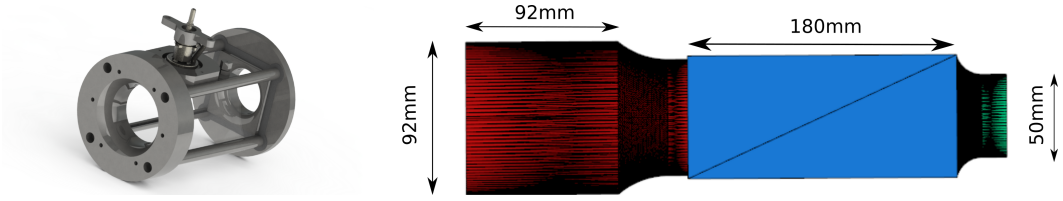

(a) Experimental injection chamber. (b) Computational geometry.

Figure 4.13: Experimental and computational geometry of the high-flow and high-temperature injection chamber.

A simplified geometry is also considered for DDM simulations, in which neither of the inlet and outlet ducts are present, and only the injection chamber box is represented (Figure 4.14a), which keeps the original chamber dimensions of 70 mm × 70 mm × 180 mm. A preliminary study in the experimental conditions showed no differences if the geometry suffered a further simplification, considering only a box of 70 mm × 70 mm × 70 mm as shown in Figure 4.14b. The simplified version of the injection chamber has been used to characterize the spray characteristics and the UWS degradation, while the full in-detail geometry will be used to characterize the effects of varying the injection angle on the generation of NH_3.

4.3.2.2 Boundary conditions

All external flow simulations share the same boundary conditions, consisting of a mass flow inlet for the gas phase, a liquid injection, a pressure outlet, and a wall in-between. The configuration of the location of the specified boundaries is shown in Figure 4.14c. The details of the boundary conditions are located in Table 4.7.

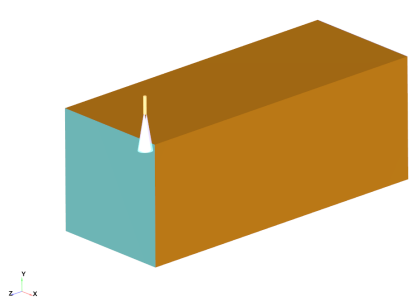

(a) Injection chamber.

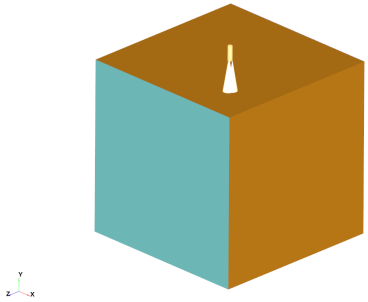

(b) Simplified injection chamber.

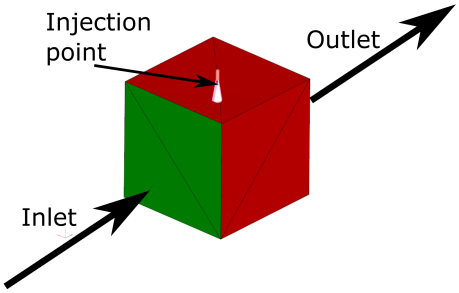

(c) Boundary conditions.

Figure 4.14: Computational models used for the reproduction of the experimental injection chamber.

As indicated on Table 4.7, the profile of the spray injection is determined from experimental means obtained is being recreated. The shape of the rate of injection values shown in Figure 4.15 has been extracted and imposed into the computational model.

4.3.2.3 Initial conditions

In these simulations where cross-flow air is present, the boundary layer of the incoming air needs to be initialized on the injection chamber walls. To do so, a prior simulation where no UWS was present was needed. In it, the mass flow rate specified on Table 4.7 was imposed together with its corresponding temperature and pressure, and it was run until steady-state conditions were achieved. The solution of that initial simulation was used to initialize the fluid field in the simulations where the UWS injection was present.

Boundary	Flow Variable	Value
Inlet	Mass Flow	$40\,\mathrm{kg\,h^{-1}}$
	Temperature	473 K-673 K
	Species	Air
	Turbulent Intensity	$1\mathrm{m}^2/\mathrm{s}^2$
	Turbulent Dissipation	0.018 m
Outlet	Pressure	1 bar
	Backflow Temperature	373 K
	Backflow Species	Air
	Backflow Turb. Intensity	$1\mathrm{m}^2/\mathrm{s}^2$
	Backflow Dissipation	0.018 m
Spray Injection	Injection Pressure	4, 6, 8 barG
	Injected Mass	3.90, 4.80, 5.40 mg
	Temperature	300 K
	Injection Time	5 ms
	Injection Angle	90,80,70,60,50,40,30°
	Profile	Experimental [-]
Wall	Velocity	Law-Of-Wall
	Temperature	473 K-673 K

Table 4.7: Boundary conditions for the DDM simulations carried out.

4.3.3 Reproduction of a close-coupled SCR system

Although the previous test rig allowed characterizing the spray on realistic engine conditions, as specified in Chapter 2, most of the NO_x after-treatment systems need a swirler to further atomize the injected droplets and therefore evaporation. During this work, the opportunity of disassembling a close-coupled SCR system arose. The inner flow geometry dimensions could be extracted and introduced into a computational model. Figure 4.16 shows the inner shape of the system, in which the location of the DOC, the injector seating and the catalyst entrance are highlighted.

Regarding the swirler (Figure 4.17a), it consists of a 7-blade helix geometry with a characteristic thickness of 3 mm located downstream of the injection point and prior to the catalyst entrance. The catalyst, as seen in Figure 4.17b, is not included in the model as assessing the deNOx performance is not an objective of the study. As deposit formation was not the focus of this work, the thickness of the swirler was not considered as solid phase to prevent heat

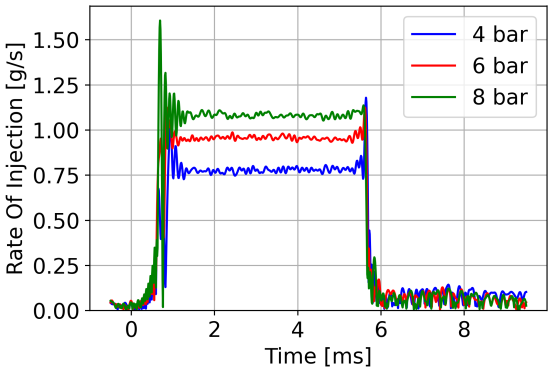

Figure 4.15: Experimental Rate of Injection profiles [51].

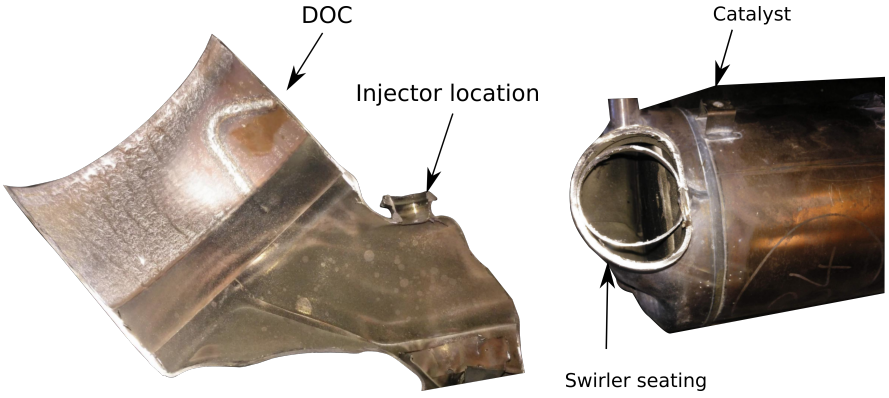

(a) DOC and Injection region. (b) Swirler seat and Catalyst.

Figure 4.16: Disassembled CC-SCR system.

transfer gradients across it, and was treated as a isotherm wall boundary condition.

4.3.3.1 Boundary conditions

The boundary conditions have been configured as follows. The inlet surface has been set at the entrance to the DOC region as a mass flow inlet, while the entrance to the catalyst has been considered as the pressure outlet condition of the simulation. The injection of the spray has been located in its corresponding position, prior to the swirler and after the DOC (Figure 4.17b). The air mass flow rate is considerably higher than for the cases recreating the test-rig conditions (Table 4.7), and has been extracted from the work of Rogóz et al.

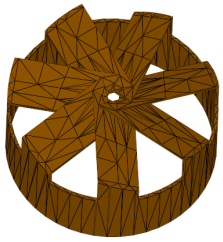

(a) Swirler reproduction.

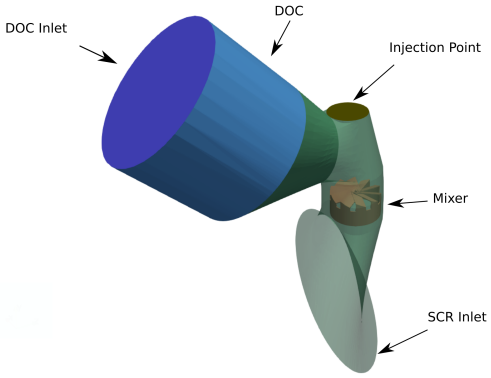

(b) Computational model of the SCR.

Figure 4.17: Swirler and bounday condition characteristics for the CC-SCR simulations.

OP3 [52] for close-coupled applications. The incoming air conditions, as well as the spray characteristics, have been taken from the test-rig conditions, as observed in Table 4.8.

4.3.3.2 Initial conditions

As it happened to the spray characterization simulations, the incoming flow was first initialized using a simulation where no injection was present, and the flow field variables of velocity, temperature and pressure were obtained. That simulation was also initialized with the corresponding values of the boundary conditions and a zero-velocity field. Once steady conditions were achieved, the solution was introduced as an initial solution. Then the spray at the different conditions shown in Table 4.8 was introduced.

4.3.4 Meshing

The meshing strategy for the simulations carried out during this Thesis needs to take into account the necessity of dealing with larger scales of the spray, together with being capable of resolving the tightest regions within the injector itself. For that reason, the cartesian mesh that uses CONVERGE^{TM} needs to be refined accordingly through an octree division applied to the original cell size, represented in Equation 4.56. The p variable in that equation determines

Boundary	Flow Variable	Value
Inlet	Mass Flow	$300\,\mathrm{kg\,h^{-1}}$
	Temperature	573 K, 623 K
	Species	Air
Outlet	Pressure	1 bar
	Backflow Temperature	573 K
	Backflow Species	Air
Spray Injection	Injection Pressure	4, 6, 8 barG
	Injected Mass	3.90, 4.80, 5.40 mg
	Temperature	300 K
	Injection Time	5 ms
	Injection Angle	90°
	Profile	Experimental [-]
Wall	Velocity	Law-Of-Wall
	Temperature	573 K, 623 K

Table 4.8: Boundary conditions for the DDM simulations carried out on the SCR geometry.

the number of divisions to be applied on the original cell size L_{base}, resulting in a refined cell of size L.

$$L = \frac{L_{base}}{2^p} \tag{4.56}$$

The two refinement techniques have been applied available on the software are the following ones:

- **Fixed Embedding** This technique refines the grid defined by the specified base size, based on user-input parameters that determine the time, location, and shape of the refined region in order to properly solve the field in the critical regions (i.e. the flow through the tightest regions of the inner injector geometry), and leaving the rest of the domain with its original cell size, allowing to minimize the number of needed cells.
- **Adaptive Mesh Refinement (AMR)** It allows to dynamically refine the mesh in the regions where it is locally and temporally needed. AMR refines the mesh in the regions where it is needed without needing to keep the refinement for the whole duration of the simulation. The magnitude of the sub-grid field is estimated at run-time to determine where further

refinement is needed, or based on specified values. For it, the sub-grid field of a variable (ϕ') is estimated as the difference between the actual field (ϕ) and the resolved part ($\bar{\phi}$). The magnitude of the sub-grid field is approximated through a series expansion [53] in which the first term is retained (Eq. 4.57). If that value is above the threshold value (user-defined), a cell embedding is introduced in that region. If the sub-grid value is below 1/5 of the threshold specified value, then the embedding is released, restoring the original cell size.

$$\phi' = -\frac{dx_k^2}{24}\frac{\partial^2\bar{\phi}}{\partial x_k \partial x_k} \tag{4.57}$$

4.3.4.1 Internal flow simulations

The meshing strategy varies depending if a Mixture Model is going to be applied, or if it is a VOF simulation. Regarding the Mixture-Model simulations applied to *Generation 1*, only Fixed Embedding (FE) techniques were applied. As Figure 4.18 shows, the base size is present in the discharge volume, while FE is applied mainly inside the injector, with the smallest cell size applied in the region upstream of the nozzle, in the uncertain gap mentioned on the description of the *Generation 1* geometry. Additionally, refinement cones are placed within the discharge volume where the spray is expected. The main parameters driving the mesh for the MM simulations are included in Table 4.9.

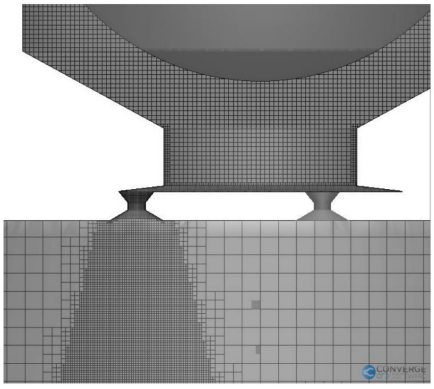

Figure 4.18: Computational mesh generated for the Mixture-Model simulations applied to *Generation 1*.

For the VOF simulations (applied to *Generation 1* and *Generation 2*), two approaches were followed in order to determine the optimum configuration for

Variable	Value
Base size	150 µm
Minimum cell size	5 µm
Number of elements	7.5 Million

Table 4.9: Mesh parameters used for the MM simulations.

a simulation where the discharge volume length changes significantly (from 5 mm to 10 mm). Including a conical fixed embedding would result in an excessively large amount of cells that would result in an unfeasible simulation for the largest domain. FE was introduced only inside of the injector geometry, while AMR was activated to embed the cells in the discharge volume region. Figure 4.19 shows how the meshing is applied through this dynamic mesh mechanism, and Table 4.10 shows the mesh parameters set for both approaches. The only FE approach has an overall smaller amount of cells on the simulation, but is not capable of maintaining the same level of refinement for the whole discharge volume length. AMR approach on the other hand, once stabilized, shows around 50 million cells, but is capable of maintaining the same embedding level on the whole domain. The regions close to the injector walls have been refined in order to capture the possible flow gradients that may take place, with a cell size of 8 µm at the throat locations that cause the greatest pressure drop on the solution. AMR was set to trigger in the locations where sub-grid values of the velocity (0.5 m/s) and the α (0.0005) field were found.

Variable	Fixed Embedding	AMR
Base size	260 µm	260 µm
Minimum cell size	4 µm	4 µm
Peak number of elements	24 Million	40 Million

Table 4.10: Mesh parameters used for the VOF simulations.

4.3.4.2 External flow simulations

On the simulations in which the test-rig is represented, a common meshing approach has been followed. In them, the mesh consisted in hexahedral cells of 1.5 mm of size, as it is the common approach for low-injection-pressure

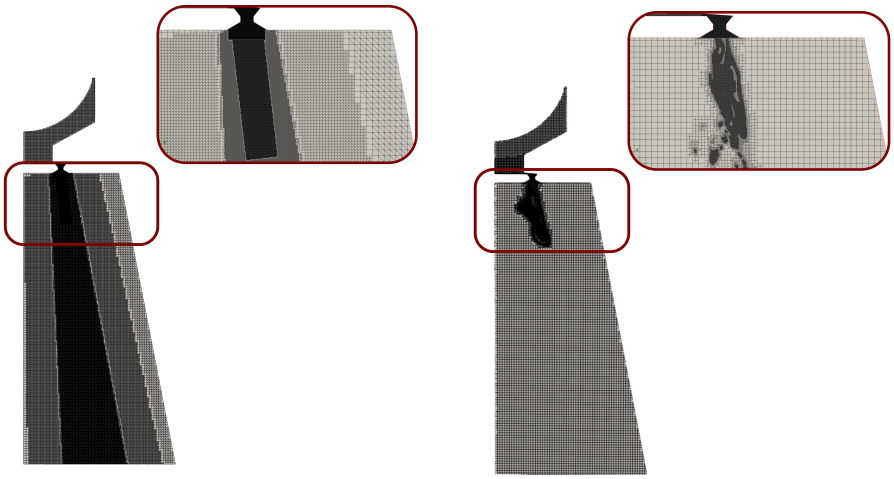

(a) FE approach. (b) AMR approach (start of injection).

Figure 4.19: Meshing strategies for the VOF simulations.

sprays [54], although it is the result of a mesh independence study. FE was placed on all the wall boundary conditions to properly capture the effects of the boundary layer development, and AMR was placed in order to refine the mesh where a significant amount of *parcels* were detected and on regions where a sub-grid value for the evaporated water and ammonia (1e-7) where present, as well with the velocity ($0.5\,\mathrm{m\,s^{-1}}$). The parameters set on the mesh are included in Table 4.11.

Variable	**Test Rig**	**Simplification**
Base size	1.5 mm	1.5 mm
Minimum cell size	0.375 mm	0.375 mm
Number of elements	0.8 Million	0.5 Million

Table 4.11: Mesh parameters used for the test rig DDM simulations.

With respect to the meshing of the realistic CC-SCR geometry, a similar approach has been followed. In this case, the presence of the swirler, together with the considerably larger air mass-flow rates imply that turbulent structures gain importance. Hence, a LES approach is more suitable for this application. Therefore, the base size is lower than for the previous cases. The summary of the mesh characteristics is shown in Table 4.12. In Figure 4.21

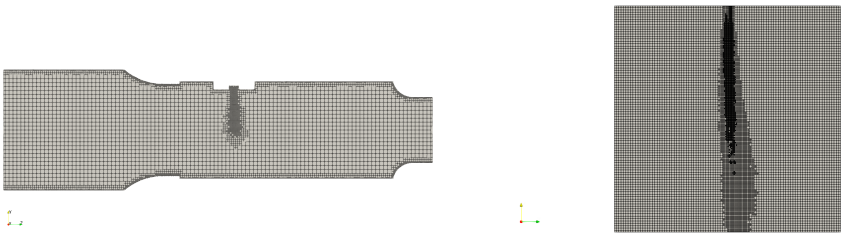

(a) Test Rig. (b) Simplification.

Figure 4.20: Meshing of real and simplification of the test rig for the DDM simulations.

it is seen how the AMR triggers in the section reaching the injection point, and the swirler generates sufficient velocity gradients to refine significantly the SCR inlet section.

Variable	**CC-SCR**
Base size	0.4 mm
Minimum cell size	0.05 mm
Peak number of elements	2.5 Million

Table 4.12: Mesh parameters used for the CC-SCR DDM simulations.

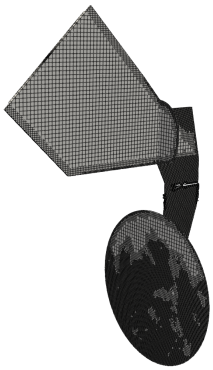

Figure 4.21: Isometric view of the meshing of the CC-SCR.

4.4 Solver

This section will focus on presenting in a brief way the numeric schemes used to characterize the UWS sprays in the different applied methodologies (MM, VOF and DDM). Additionally, it will sum up the models used for each one of the simulations performed for further clarification. For in-detail explanation, the reader is referred to Saad's work [55].

4.4.1 Mixture Model simulations

As mentioned in Section 4.2, the CONVERGE package uses the FVM to discretize the fluid volume and solves the pressure-velocity coupling through the PISO algorithm. The Rie-Chow algorithm has been employed to avoid the checkerboard effect that was previously described. The discretization schemes used were already defined in Table 4.2, in which the space was discretized using second-order schemes except for the turbulence equation. With respect to the iterative linear solver needed for solving each governing equation, the pointwise Successive Over-Relaxation (SOR) solver has been selected for the momentum, density, energy and species equations with a convergence tolerance of 10^{-5} and a maximum of 50 iterations, while the BiConjugate Gradient STABilized (BiCGSTAB) method has been used for the pressure equation with a tolerance of 10^{-6} and a maximum of 500 iterations. The time step set during the calculation is varied dynamically in order to satisfy a maximum value of the convective Courant-Friedrichs-Lewy (CFL) number set at 0.8. The PISO algorithm tolerance has been set to a value of 10^{-3}, with a minimum amount of 2 iterations, and a maximum of 50. The simulations were initially run until the spray had fully stabilized (i.e. when velocity profiles stopped varying and the momentum and rate of injection stabilized), and the simulation was run for an additional millisecond to achieve statistically representative results.

4.4.2 Volume-Of-Fluid simulations

In these cases, the same PISO algorithm was used, but due to the convergence problems derived of this approach, the maximum number of iterations was rose to 100 iterations. The spatial discretization was done using first order schemes to ensure stability (Table 4.2), together with the Rie-Chow algorithm as it happened with the MM simulations. Also, the momentum equation was resolved through the BiCGSTAB solver, with a tolerance of 10^{-6}, as it happened to the pressure equation. The HRIC reconstruction algorithm has been used in order to mantain a sharp interface between the liquid and gas. As for this approach only LES simulations were carried out, the Werner and Wengle

model was used once again. The same maximum CFL numbers as on the MM were selected, which limited the maximum permitted time-step. Macroscopic and microscopic characteristics were obtained to assess the stabilization of the injected sprays, and the simulations were run for an additional 1.2 ms in order to achieve statistically representative results (Section 5.3.4). This statistical convergence was assessed through the characterization of the generated droplet distribution.

4.4.3 DDM approach of the test rig

The DDM simulations performed on this study share the same PISO numerical setup as of the Eulerian-Eulerian simulations previously described. The spatial discretization applied is of second order for most of the conservation equations except for the turbulence equation. In these cases, the SOR solver has been used for all the conservation equations with convergence tolerance of 10^{-5} for all the equations except for the pressure equation, with a value of 10^{-8}. Either RANS k-ϵ RNG or LES simulation have been applied, and either standard wall model or Werner and Wengle model has been applied accordingly. These simulations, once initialized with steady state solutions, were run during one injection event (5 ms), and let it run for additional 15 ms so that the urea decomposition after the injection could take place.

A depiction of the Navier-Stokes solver algorithm has been included in Table 4.13 for all the types of simulations performed, while the description of the linear solvers for the transport equations is located in Table 4.14.

Simulation	**N-S Scheme**	**Parameter**	**Value**
Mixture Model	PISO	Min. Iteration	2
		Max. Iteration	30
		Tolerance	1e-3
Volume-Of-Fluid	PISO	Min. Iteration	2
		Max. Iteration	100
		Tolerance	1e-3
DDM	PISO	Min. Iteration	2
		Max. Iteration	20
		Tolerance	1e-3

Table 4.13: Navier-Stokes solver configuration for the three typologies of simulations performed

A summary of the solvers used for each of the simulations performed is located in Table 4.14.

Simulation	Equation	Linear Solver	Parameter	Value
Mixture Model	Momentum	SOR	Tolerance	1e-5
			Min It.	0
			Max It.	100
	Pressure	BiCGSTAB	Tolerance	1e-6
			Min It.	2
			Max It.	500
	Density	SOR	Tolerance	1e-5
			Min It.	0
			Max It.	50
	Energy	SOR	Tolerance	1e-5
			Min It.	0
			Max It.	50
	Species	SOR	Tolerance	1e-5
			Min It	0
			Max It.	50
Volume-Of-Fluid	Momentum	BiCGSTAB	Tolerance	1e-6
			Min It.	0
			Max It.	1000
	Pressure	BiCGSTAB	Tolerance	1e-6
			Min It.	2
			Max It.	5000
	Density	SOR	Tolerance	1e-5
			Min It.	0
			Max It.	50
	Energy	SOR	Tolerance	1e-5
			Min It.	0
			Max It.	50
	Void Fraction	SOR	Tolerance	1e-5
			Min It	0
			Max It.	500
DDM	Momentum	SOR	Tolerance	1e-5
			Min It.	0
			Max It.	100
	Pressure	SOR	Tolerance	1e-8
			Min It.	2
			Max It.	500
	Density	SOR	Tolerance	1e-5
			Min It.	0
			Max It.	50
	Energy	SOR	Tolerance	1e-5
			Min It.	0
			Max It.	50
	Species	SOR	Tolerance	1e-5
			Min It	0
			Max It.	50

Table 4.14: Linear solvers for the transport equations in each of the simulation of interest.

4.5 Post-processing

After the simulations have been run, the results of interest need to be extracted. For that purpose, several post-processing routines have been generated to obtain penetration, spray angle, LES quality index, among others.

4.5.1 Internal Flow characterization

In RANS applications, the accuracy of a simulation is partially assessed through a mesh independence study, in which the convergence of the solution is achieved at a specific grid refinement. This approach is not applicable to LES, as with increasing refinement, the solution solves more turbulent energy content, tending to a solution of a DNS. Therefore, a criteria needs to be introduced to check whether the LES solution solves enough turbulent energy. In the literature, two indexes have been proposed and will later be applied to the corresponding LES performed.

4.5.1.1 Index based on viscosity

This quality index (IQ_ν) proposed by Celik et al. [56] evaluates the contribution of numerical (ν_{num}), sub-grid (ν_{SGS}) and laminar viscosity (ν) through Equation 4.58.

$$IQ_\nu = \frac{1}{1 + \alpha_\nu \left(\frac{\nu_{SGS}+\nu+\nu_{num}}{\nu}\right)^n} \tag{4.58}$$

In it, the n and α_ν are coefficients obtained through DNS results [57] taking values of 0.05 and 0.53 respectively. The authors recommend values for IQ_ν from 0.75 to 0.85 for LES applications.

4.5.1.2 Index based on TKE

The second index of quality, proposed by Pope [58], is widely accepted for LES applications and relates the contribution of the resolved part of the turbulent kinetic energy to the total turbulent kinetic energy (resolved and sub-grid). The resolved part is obtained from the filtered fluctuations through Equation 4.59.

$$k_{res} = \frac{1}{2}\left(\bar{u}^2_{x,RMS} + \bar{u}^2_{y,RMS} + \bar{u}^2_{z,RMS}\right) \tag{4.59}$$

The modeled part, which is considered through the sub-grid model, can be approximated through Equation 4.60.

$$k_{mod} = \frac{\nu_{SGS}^2}{(C_m \Delta_e)^2} \tag{4.60}$$

In these equations, Δ_e represents the filter width (which is the characteristic cell length, $\sqrt[3]{\Delta_x \Delta_y \Delta_z}$), and C_m on the other hand is a constant with a value of 0.091 [59]. Based on these TKE contributions, the index of quality can be calculated according to Equation 4.61. A good index of quality is then achieved when at least the 80% of the turbulent energy is solved, that is $IQ_k > 0.8$.

$$IQ_k = \frac{k_{res}}{k_{res} + k_{mod}} \tag{4.61}$$

4.5.1.3 Index of quality for droplet characterization

In VOF simulations, it is important to be able to properly capture the shape and size of the droplets generated from the primary breakup phenomenon. A droplet that is defined by a single cell will have its shape misrepresented and the physics associated (drag, evaporation, coalescence) will be calculated with considerable errors. In this thesis, an index of quality has been proposed in order to determine if the detected droplets in a VOF simulation are either properly resolved (i.e. their shape is properly represented) or under-solved. A resolved droplet is identified as a particle that has an equivalent diameter of 6 grid cells [60]. Then, an index of quality is created through the ratio of solved droplet mass to total droplet mass (Equation 4.62).

$$IQ_{VOF} = 1 - \frac{m_{undersolved}}{m_{droplets}} \tag{4.62}$$

4.5.1.4 Hydraulic characteristics

The hydraulic characterization of the UWS is done by calculating the Rate Of Injection (ROI) and Rate Of Momentum (ROM) of the injected spray. This is done by using Equations 2.2, and 2.1. The integrals have been approached numerically thanks to the sum of the mass flow rates and momentum of each one of the cells. Although experimentally these variables have been calculated on a plane at a certain distance of the injector orifices [61], computationally, these values have been obtained at the orifice section. These values have

been used to obtain the hydraulic coefficients of area (C_a), velocity (C_v) and discharge (C_d), whose definition has been given in Chapter 2.

4.5.2 Droplet detection and characterization

The purpose of LES VOF calculations is to predict the distribution of droplets generated during the primary breakup process. Characterization of these droplets is done through a droplet/ligament size evaluation algorithm generated specifically for this work.

This process consists on the following steps:

1. First, the liquid phase is separated from the gas phase through the transported α variable. A user-defined threshold (α_{liq}) value of 0.5 has been chosen, although this value should not be critical due to the compression of the phase interface implemented (HRIC). A cell-long array is initialize with values of -1. This array will later indicate to which droplet each cell belongs to.

2. The amount of total droplets is obtained by assessing how many cells do not share an immediate neighbor. Cells within the same droplet share their boundaries with each other, while cells of different droplets show a gap between them of at least one cell distance. A droplet array is created and initialized, with an individual value assigned to each one of them.

3. The cell index array is filled with the droplet index each cell belongs to, which ranges from 1 to the total number of detected droplets n_{drop}.

4. The droplet characteristics are obtained, including the droplet mass, volume, equivalent diameter, velocity and centroid location.

5. The last step of the algorithm removes from the domain the droplet which has associated the largest volume, which represents the intact core region. Additionally, all the droplets that are touching a boundary of the domain are not considered for the spray characterization.

   The droplet characteristics are determined from the following equations. The volume and mass are calculated according to Equations 4.63 and 4.64.

$$V_{drop} = \sum_{i=1}^{n_{drop}} \alpha_{cell} V_{cell} \tag{4.63}$$

$$m_{drop} = \sum_{i=1}^{n_{drop}} \rho_{cell} \alpha_{cell} V_{cell} \tag{4.64}$$

A equivalent droplet diameter is approximated through the droplet volume obtained (Equation 4.65).

$$D_{drop} = \left(\frac{6}{\pi} V_{drop} \right)^{\frac{1}{3}} \tag{4.65}$$

Droplet velocity can also be characterized (Equation 4.66), together with the calculation of the centroid of the droplet (Equation 4.67).

$$U_{drop} = \frac{1}{m_{drop}} \sum_{i=1}^{n_{drop}} \alpha_{cell} \rho_{cell} V_{cell} U_{cell} \tag{4.66}$$

$$x_{drop} = \frac{1}{m_{lig}} \sum_{i=1}^{n_{drop}} \alpha_{cell} \rho_{cell} V_{cell} x_{cell} \tag{4.67}$$

The shape of the droplets is also assessed through a sphericity factor. It relates the maximum distance of the droplet surface to the calculated centroid, and compares it to the equivalent diameter obtained through Equation 4.68. Then, a sphericity Sp of 1 represents a spherical diameter, while greater values show elongated ligaments.

$$Sp = \frac{r_{max}}{r_{drop}} \tag{4.68}$$

4.5.3 Spray tip penetration and spray angle

The spray tip penetration is an important parameter that needs to be characterized in many spray applications [62, 63]. Its importance resides in analyzing the mixing of the fluid with the surrounding gas and specifically in characterizing the risk of deposit formation in the exhaust pipe region. To calculate the spray tip penetration, the density projection is first calculated through a parallel plane to the injection direction. To do so, the solution has been first interpolated into a uniform grid whose characteristic cell size is known in order to avoid the variability of cell sizes caused by the AMR presence. Then, the liquid mass has been projected into one of the axes direction, which has been later transformed into *density* through the characteristic interpolation

grid size. From there, and through a threshold value, the largest liquid distance from that region to the orifice is considered to be the tip distance, as represented in Figure 4.22a. On the other hand, the spray angle calculation followed the criteria described in Chapter 2. As observed in Figure 4.22b, at specific distances of the spray (based on the spray tip penetration S) two lines are fitted in the boundaries of the spray (represented by the green lines) which between them define the angle of interest.

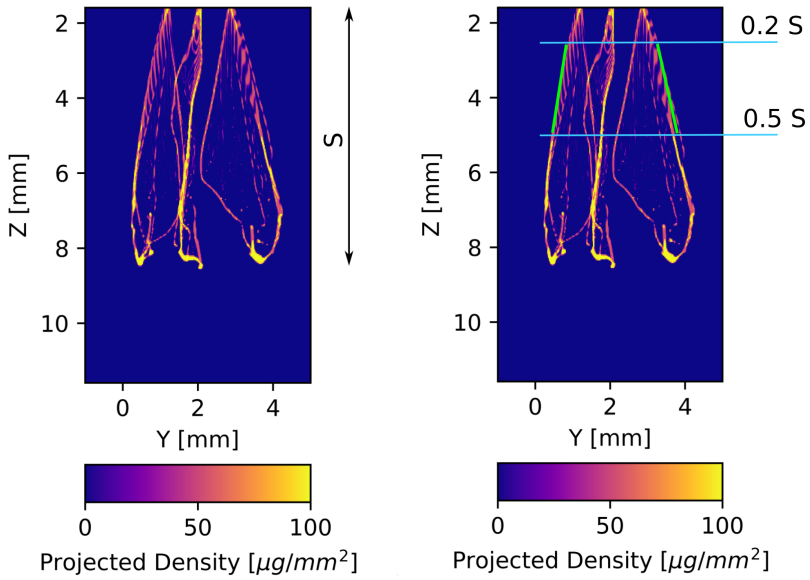

(a) Spray tip penetration. (b) Spray angle.

Figure 4.22: Calculation of the macroscopic characteristics through the density projection procedure.

4.5.4 Breakup Length

The jet breakup length during the Eulerian-Eulerian simulations has been calculated based on the location where a 99.9% of the mass fraction is found. The distance defined by that point and the injection point gives the desired breakup length.

4.5.5 Chemistry

4.5.5.1 Uniformity Index

The Uniformity Index (UI) characterizes how homogenized a flow variable is on a specific geometry section. In UWS applications, it is a useful way to assess how distributed the NH_3 content is at the entrance of the catalyst monolith. It is calculated according to Equation 4.69 [64]. In it, ϕ is the the flow variable of interest, $\bar{\phi}$ is the average value of the field function, while A_f represents the surface area of the ϕ_f measurement.

$$UI = 1 - \frac{\sum |\phi_f - \bar{\phi}| A_f}{2|\bar{\phi}| \sum A_f} \tag{4.69}$$

4.5.5.2 Conversion Efficiency

The ammonia conversion efficiency is a measure of how much of the injected UWS has fully transformed into NH_3 (including thermolysis and hydrolysis reactions). This is done by calculating the maximum amount of NH_3 would be present if all the UWS had undergone transformation, through the molar masses of each chemical reaction. Then, the NH_3 mass obtained during the simulations has been compared against that theoretical value, defining an efficiency of the generated NH_3.

References

[1] Khan, D., Bjernemose, J. H., and Lund, I. "Experimental Characterization and Numerical Modelling of Urea Water Solution Spray in High-Temperature Crossflow for Selective Catalytic Reduction Applications". In: *SAE International Journal of Sustainable Transportation, Energy, Environment, & Policy* 3.2 (2022), pp. 139–153. DOI: https://doi.org/10.4271/13-03-02-0012UI-13-03-02-0012.

[2] Versteeg, H. K. (K. *An introduction to computational fluid dynamics : the finite volume method*. Harlow, Essex, England ; Longman Scientific Technical : New York : Wiley, 1995., 1995.

[3] Versteeg, H. K. and Malalasekera, W. *An introduction to computational fluid dynamics: the finite volume method*. Pearson education, 2007.

[4] Monin, A. S. "On the nature of turbulence". In: *Soviet Physics Uspekhi* 21.5 (1978), p. 429.

[5] Wegner, B., Maltsev, A., Schneider, C., Sadiki, A., Dreizler, A., and Janicka, J. "Assessment of unsteady RANS in predicting swirl flow instability based on LES and experiments". In: *International Journal of Heat and Fluid Flow* 25.3 (2004), pp. 528–536. DOI: https://doi.org/10.1016/j.ijheatfluidflow.2004.02.019.

[6] Baldwin, B. and Lomax, H. "Thin-layer approximation and algebraic model for separated turbulentflows". In: *16th aerospace sciences meeting*. 1978, p. 257. DOI: https://doi.org/10.2514/6.1978-257.

[7] Smith, A. M. and Cebeci, T. *Numerical solution of the turbulent-boundary-layer equations*. Tech. rep. 1967.

[8] Wilcox, D. C. *Turbulence modeling for CFD*. Vol. 2. DCW industries La Canada, CA, 1998.

[9] P., S. and Allmaras, S. "A one-equation turbulence model for aerodynamic flows". In: *30th Aerospace Sciences Meeting and Exhibit*. Reston, Virigina: American Institute of Aeronautics and Astronautics, 1992. DOI: 10.2514/6.1992-439.

[10] Launder, B. E. and Spalding, D. B. "The numerical computation of turbulent flows". In: *Computer Methods in Applied Mechanics and Engineering* 3.2 (1974), pp. 269–289. DOI: https://doi.org/10.1016/0045-7825(74)90029-2.

[11] Wilcox, D. C. "Reassessment of the scale-determining equation for advanced turbulence models". In: *AIAA Journal* 26.11 (1988), pp. 1299–1310. DOI: 10.2514/3.10041.

[12] Han, Z. and Reitz, R. D. "Turbulence Modeling of Internal Combustion Engines Using RNG κ-ϵ Models". In: *Combustion Science and Technology* 106.4-6 (1995), pp. 267–295. DOI: 10.1080/00102209508907782.

[13] Yang, H. C., Ryou, H. S., Hong, K. B., Kim, H. S., and Park, S. K. "Application of the RNG k-ϵ Model to the Analysis of Flows and Spray Characteristics". In: *Atomization and Sprays* 7.6 (1997), pp. 581–601. DOI: 10.1615/AtomizSpr.v7.i6.20.

[14] Kaario, O., Larmi, M., and Tanner, F. "Relating integral length scale to turbulent time scale and comparing k-ϵ and RNG k-ϵ turbulence models in diesel combustion simulation". In: *SAE Transactions* (2002), pp. 1886–1900.

[15] Taskinen, P. "Modeling of spray turbulence with the modified rng k-epsilon model". In: *Energy and Process Engineering, Tampere University of Tehnology* (2004).

[16] Desantes, J. M., Garcia-Oliver, J. M., Pastor, J. M., and Pandal, A. "A Comparison of Diesel Sprays CFD Modeling Approaches: DDM Versus E-Y Eulerian Atomization Model". In: *Atomization and Sprays* 26.7 (2016), pp. 713–737. DOI: 10.1615/AtomizSpr.2015013285.

[17] Varna, A., Boulouchos, K., Spiteri, A., Dimopoulos Eggenschwiler, P., and Wright, Y. M. "Numerical Modelling and Experimental Characterization of a Pressure-Assisted Multi-Stream Injector for SCR Exhaust Gas After-Treatment". In: *SAE International Journal of Engines* 7.4 (2014), pp. 2012–2021. DOI: 10.4271/2014-01-2822.

[18] Varna, A., Spiteri, A. C., Wright, Y. M., Dimopoulos Eggenschwiler, P., and Boulouchos, K. "Experimental and numerical assessment of impingement and mixing of urea-water sprays for nitric oxide reduction in diesel exhaust". In: *Applied Energy* 157 (2015), pp. 824–837. DOI: 10.1016/j.apenergy.2015.03.015.

[19] Boussinesq, J. *Essai sur la théorie des eaux courantes*. Impr. nationale, 1877.

[20] Yakhot, V., Orszag, S. A., Thangam, S., Gatski, T. B., and Speziale, C. G. "Development of turbulence models for shear flows by a double expansion technique". In: *Physics of Fluids A* 4.7 (1992), pp. 1510–1520. DOI: 10.1063/1.858424.

[21] Smagorinsky, J. "General Circulation Experiments With the Primitive Equations". English. In: *Monthly Weather Review* 91.3 (1963), pp. 99–164. DOI: 10.1175/1520-0493(1963)091<0099:gcewtp>2.3.co;2.

[22] Lilly, D. K. "The representation of small-scale turbulence in numerical simulation experiments". In: *IBM Form* (1967), pp. 195–210.

[23] Germano, M., Piomelli, U., Moin, P., and Cabot, W. H. "A dynamic subgrid-scale eddy viscosity model". In: *Physics of Fluids A* 3.7 (1991), pp. 1760–1765. DOI: 10.1063/1.857955.

[24] Lilly, D. K. "A proposed modification of the Germano subgrid-scale closure method". In: *Physics of Fluids A: Fluid Dynamics* 4.3 (1992), pp. 633–635. DOI: 10.1063/1.858280.

[25] Harlow, F. H. and Welch, J. E. "Numerical calculation of time-dependent viscous incompressible flow of fluid with free surface". In: *Physics of Fluids* 8.12 (1965), pp. 2182–2189. DOI: 10.1063/1.1761178.

[26] Wacławczyk, T. and Koronowicz, T. "Modeling of the flow in systems of immiscible fluids using volume of fluid method with cicsam scheme". In: *Modelling of Multiphase Flows in Thermo-Chemical Systems Advanced Measurement Techniques* 8 (2005), pp. 267–276.

[27] Zuzio, D. "Direct numerical simulation of two phase flows with adaptive mesh refinement". PhD thesis. ONERA - The French Aerospace Lab, 2010.

[28] Waclawczyk, T. and Koronowicz, T. "Modeling of the wave breaking with CICSAM and HRIC high resolution schemes". In: *European Conference on Computational Fluid Dynamics*. 2006, pp. 1–19.

[29] Brackbill, J. U., Kothe, D. B., and Zemach, C. "A continuum method for modeling surface tension". In: *Journal of Computational Physics* 100.2 (1992), pp. 335–354. DOI: 10.1016/0021-9991(92)90240-Y.

[30] Balachandar, S. "A scaling analysis for point–particle approaches to turbulent multiphase flows". In: *International Journal of Multiphase Flow* 35.9 (2009), pp. 801–810. DOI: https://doi.org/10.1016/j.ijmultiphaseflow.2009.02.013.

[31] Eaton, J. K. "Two-way coupled turbulence simulations of gas-particle flows using point-particle tracking". In: *International Journal of Multiphase Flow* 35.9 (2009), pp. 792–800. DOI: https://doi.org/10.1016/j.ijmultiphaseflow.2009.02.009.

[32] Ling, Y., Zaleski, S., and Scardovelli, R. "Multiscale simulation of atomization with small droplets represented by a Lagrangian point-particle model". In: *International Journal of Multiphase Flow* 76 (2015), pp. 122–143. DOI: 10.1016/j.ijmultiphaseflow.2015.07.002.

[33] O'Rourke, P. J. and Amsden, A. A. "The tab method for numerical calculation of spray droplet breakup". In: *SAE Technical Papers*. 1987. DOI: 10.4271/872089.

[34] Liu, A. B., Mather, D., and Reitz, R. D. "Modeling the effects of drop drag and breakup on fuel sprays". In: *SAE Technical Papers*. Vol. 298. 1993, pp. 1–6. DOI: 10.4271/930072.

[35] O'Rourke, P. J. "Collective Drop Effects on Vaporizing Liquid Sprays". PhD thesis. Princeton University, 1981.

[36] Schmidt, D. P. and Rutland, C. J. "A New Droplet Collision Algorithm". In: *Journal of Computational Physics* 164.1 (2000), pp. 62–80. DOI: 10.1006/jcph.2000.6568.

[37] Reitz, R. D. and Bracco, F. V. "Mechanism of atomization of a liquid jet". In: *Physics of Fluids* 25.10 (1982), pp. 1730–1742. DOI: 10.1063/1.863650.

[38] Patterson, M. A. *Modeling the effects of fuel injection characteristics on diesel combustion and emissions*. The University of Wisconsin-Madison, 1997.

[39] Amsden, A. A., O'Rourke, P. J., and Butler, T. D. *KIVA-II: A computer program for chemically reactive flows with sprays*. Tech. rep. Los Alamos, NM (United States): Los Alamos National Laboratory (LANL), 1989. DOI: 10.2172/6228444.

[40] Frössling, N. "Über die verdunstung fallender tropfen". In: *Gerlands Beiträge zur Geophysik* 52.1 (1938), pp. 170–216.

[41] Ranz, W. E. and Marshall, W. R. "Evaporation from drops: Part II". In: *Chemical Engineering Progress* 48 (1952), pp. 141–146.

[42] Senecal, P. K., Pomraning, E., Richards, K. J., Briggs, T. E., Choi, C. Y., McDavid, R. M., and Patterson, M. A. "Multi-dimensional modeling of direct-injection diesel spray liquid length and flame lift-off length using cfd and parallel detailed chemistry". In: *SAE Technical Papers*. 2003, p. 23. DOI: 10.4271/2003-01-1043.

[43] *Suite of Nonlinear and Differential Algebraic equation Solvers*. 2008. DOI: 10.1002/0471686786.ebd0076.

[44] Kuhnke, D. *Spray/Wall-Interaction Modelling by Dimensionless Data Analysis*. Berichte aus der Strömungstechnik. Shaker, 2004.

[45] Issa, R. I. "Solution of the implicitly discretised fluid flow equations by operator-splitting". In: *Journal of Computational Physics* 62.1 (1986), pp. 40–65. DOI: 10.1016/0021-9991(86)90099-9.

[46] Rhie, C. M. and Chow, W. L. "Numerical study of the turbulent flow past an airfoil with trailing edge separation". In: *AIAA Journal* 21.11 (1983), pp. 1525–1532. DOI: 10.2514/3.8284.

[47] Matusik, K. E., Duke, D. J., Kastengren, A. L., Sovis, N., Swantek, A. B., and Powell, C. F. "High-resolution X-ray tomography of Engine Combustion Network diesel injectors". In: *International Journal of Engine Research* 19.9 (2018), pp. 963–976. DOI: 10.1177/1468087417736985.

[48] Yue, Z., Battistoni, M., and Som, S. "Spray characterization for engine combustion network Spray G injector using high-fidelity simulation with detailed injector geometry". In: *International Journal of Engine Research* 21.1 (2020), pp. 226–238. DOI: 10.1177/1468087419872398.

[49] Payri, R., Bracho, G., Gimeno, J., and Moreno, A. "Spray Characterization of the Urea-Water Solution (UWS) Injected in a Hot Air Stream Analogous to SCR System Operating Conditions". In: *SAE Technical Papers*. Vol. 2019-April. April. 2019. DOI: 10.4271/2019-01-0738.

[50] Payri, R., Bracho, G., Gimeno, J., and Moreno, A. *Spray characterization of the urea-water solution (UWS) injected in a hot air stream analogous to SCR system operating conditions*. 2019. DOI: 10.4271/2019-01-0738.

[51] Moreno, A. E. "Experimental Study of the Urea-Water Solution Injection Process". PhD thesis. Valencia (Spain): Universitat Politècnica de València, 2022. DOI: 10.4995/Thesis/10251/181637.

[52] Rogóż, R., Kapusta, Ł. J., Bachanek, J., Vankan, J., and Teodorczyk, A. "Improved urea-water solution spray model for simulations of selective catalytic reduction systems". In: *Renewable and Sustainable Energy Reviews* 120 (2020), p. 109616. DOI: 10.1016/j.rser.2019.109616.

[53] Pomraning, E. "Development of Large Eddy Simulation Turbulence Models Development of Large Eddy Simulation Turbulence Models By the requirements for the degree of Doctor of Philosophy (Mechanical Engineering) At the University of Wisconsin–Madison". PhD thesis. University of Wisconsin, 2000.

[54] Varna, A., Spiteri, A. C., Wright, Y. M., Dimopoulos Eggenschwiler, P., and Boulouchos, K. "Experimental and numerical assessment of impingement and mixing of urea–water sprays for nitric oxide reduction in diesel exhaust". In: *Applied Energy* 157 (2015), pp. 824–837. DOI: https://doi.org/10.1016/j.apenergy.2015.03.015.

[55] Saad, Y. *Iterative Methods for Sparse Linear Systems*. Second. Society for Industrial and Applied Mathematics, 2003. DOI: 10.1137/1.9780898718003.

[56] Celik, I. B., Cehreli, Z. N., and Yavuz, I. "Index of resolution quality for large eddy simulations". In: *Journal of Fluids Engineering, Transactions of the ASME* 127.5 (2005), pp. 949–958. DOI: 10.1115/1.1990201.

[57] Celik, I., Klein, M., and Janicka, J. "Assessment measures for engineering LES applications". In: *Journal of fluids engineering* 131.3 (2009).

[58] Pope, S. B. "Ten questions concerning the large-eddy simulation of turbulent flows". In: *New Journal of Physics* 6 (2004), p. 35. DOI: 10.1088/1367-2630/6/1/035.

[59] Sagaut, P. *Large eddy simulation for incompressible flows: an introduction*. Springer Science & Business Media, 2006.

[60] Sun, X., Yan, H., and Chen, F. "Numerical investigation of atomization of swirling liquid sheets using transforming algorithm". In: *International Journal of Multiphase Flow* 152 (2022), p. 104084. DOI: 10.1016/j.ijmultiphaseflow.2022.104084.

[61] Payri, R., Bracho, G., Martí-Aldaraví, P., and Moreno, A. "Using momentum flux measurements to determine the injection rate of a commercial Urea Water Solution injector". In: *Flow Measurement and Instrumentation* 80 (2021). DOI: 10.1016/j.flowmeasinst.2021.101999.

[62] Payri, R., Salvador, F. J., Martí-Aldaraví, P., and Vaquerizo, D. "ECN Spray G external spray visualization and spray collapse description through penetration and morphology analysis". In: *Applied Thermal Engineering* 112 (2017), pp. 304–316. DOI: https://doi.org/10.1016/j.applthermaleng.2016.10.023.

[63] Bardi, M., Payri, R., Malbec, L. M., Bruneaux, G., Pickett, L. M., Manin, J., Bazyn, T., and Genzale, C. "Engine Combustion Network: Comparison Of Spray Development, Vaporization, and Combustion in Different Combustion Vessels". In: *Atomization and Sprays* 22.10 (2012), pp. 807–842. DOI: 10.1615/AtomizSpr.2013005837.

[64] Halonen, S., Pitkäaho, S., Pääkkönen, T. M., Väisänen, E., and Haataja, M. "A novel method for automated SCR catalyst uniformity measurement". In: *Chemical Engineering Journal* 425 (2021), p. 130257. DOI: https://doi.org/10.1016/j.cej.2021.130257.

Chapter 5

Analysis of the UWS near-field spray

"The world's an exciting place when you know CFD."
—John Shadid

5.1 Introduction

This chapter will focus on the characterization of the inner flow of the introduced pressure-driven injector (Chapter 4) through the Mixture-Model (MM) and Volume-Of-Fluid (VOF) methods applied to *Generation 1* and *Generation 2* geometries. A hydraulic characterization will be performed on the Mixture-Model study by first validating against experimental data [1], and will assess the similarity between the three orifices of the injector through RANS and LES turbulence framework. Breakup length will be assessed, and it will be related to velocity fluctuations. The VOF approach will show the same characterization as the MM simulations but will push forward the analysis by obtaining droplet distributions which will be compared to experimental results [2].

5.2 Mixture Model simulations

This section will focus on the main results of the Mixture Model simulations. As stated, RANS and LES procedures were followed and therefore different

meshes were assessed to see which configuration best fitted each simulation typology.

5.2.1 RANS mesh sensitivity study

The mesh sensitivity analysis for the RANS $k - \epsilon$ *RNG* simulations were done using four different mesh refinements. Between them, the base sizes were modified into finer and coarser cell lengths while maintaining the levels of cell embedding across the domain. The variables considered to determine the optimum cell size have been the hydraulic characteristics of the injector, that is, ROI and ROM for a specific injection pressure of 6 barG. The information regarding the ROI and ROM results have been included in Table 5.1, together with the variation between these values with respect to the immediately coarser mesh.

Element size	**ROI**	**ROM**	**ROI Diff.**	**ROM Diff.**
350 µm	1.271 g/s	0.0347 gm/s	-	-
300 µm	1.249 g/s	0.0335 gm/s	1.75 %	3.45 %
150 µm	1.246 g/s	0.0333 gm/s	0.24 %	0.29 %
75 µm	1.246 g/s	0.0333 gm/s	0 %	0 %

Table 5.1: ROI and ROM results for the RANS mesh sensitivity study of the *Generation 1* geometry at a working injection pressure of 6 bar (gauge).

In addition to the grid convergence analysis performed on the ROI and ROM parameters, the Breakup length values have also been extracted for the same RANS meshes. An alternative injection pressure condition has been used in this case, and the results have been presented in Table 5.2.

According to these results, the mesh with a base size of 300 µm and containing 0.8 million elements represents the minimum element number mesh capable of minimizing the numerical deviations associated to the solution.

5.2.2 LES quality study

In order to be sure that enough turbulent scales are adequately resolved during the LES studies, the introduced Indexes of quality in Chapter 4 have been calculated. Achieving an IQ greater than 0.8 (80% of the turbulent kinetic energy resolved) leads to an acceptable simulation, according to Pope [3]. The quality based on the viscosity proposed by Celik [4] has also been obtained, and both are presented in Figure 5.1. The index based on the TKE shows overall

Element size	Breakup Length	Breakup Length Diff.
350	1.805 mm	-
300	1.885 mm	4.43 %
150	1.895 mm	0.53 %
75	1.895 mm	0 %

Table 5.2: Breakup length results for the RANS mesh sensitivity study of the *Generation 1* geometry at a working injection pressure of 4 bar (gauge).

good values throughout all the discharge volume region except for locations where no spray is present, as it will be later seen. Within the injector geometry, there is also a low-quality zone. It corresponds to a region where almost null velocity is present, and therefore the LES meshing remains optimum for these simulations. Regarding the index based on the viscosity, all the domain has values between 0.8 and 0.9, which according to Celik's criteria, shows sufficient mesh refinement for this application. This quality index remains almost equal for the three injection pressures (4, 6, 8 barG) tested.

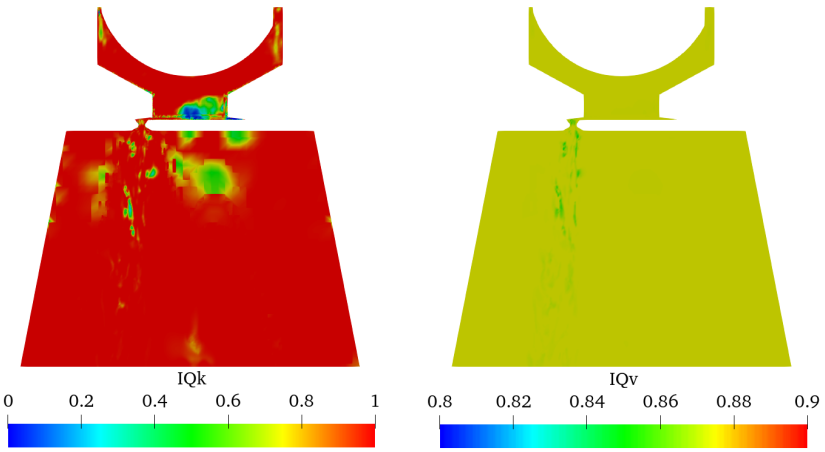

(a) Index based on TKE. (b) Index based on viscosity.

Figure 5.1: Index of Quality applied to the MM simulations.

To achieve these quality index contours, a mesh with a characteristic size of 150 µm is generated together with an embedding strategy that leads to a time average of approximately 8 million elements at the three injection pressures.

5.2.3 Hydraulic characterization

The accuracy of the performed simulations has been considered prior to performing a further analysis of the behavior under typical working conditions. ROI and ROM are of high importance as they show the amount of working fluid they can introduce and the momentum associated with each injection. The values of ROI and ROM have been extracted for a specific amount of time once their curves have stabilized (Figure 5.2). These results have been compared with the same data obtained through experimental means [1]. Experimentally, both values were obtained through momentum flux measurements and the total injected mass value. This process is described in detail in the work of Payri et al. [5]. The results for each one of the injection pressures are shown in Table 5.3.

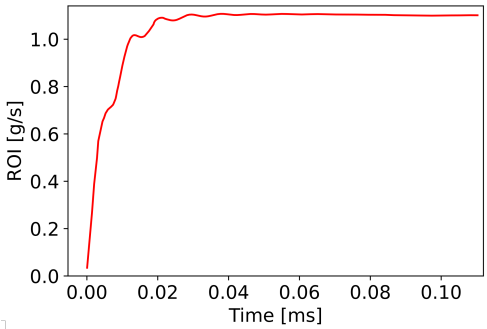

Figure 5.2: ROI temporal evolution for the MM simulation performed at a $P_{inj} = 8$ barG.

From these results, a good agreement of the mass flow rate in each injection pressure condition is obtained for both RANS and LES approaches. LES results diminish the deviations from experimental results for all three working conditions if compared to RANS simulations, with a minimum ROI error of less than 1% for the 8 barG conditions. Momentum results, on the other hand, show significant deviations from experimental data. It is generally underestimated for all the conditions, with slightly higher deviation values for the LES cases. Mohapatra et al. [6] have also shown these deviations, where the ROM deviations reached values as high as 10%. These discrepancies could be associated with the lack of needle lift dynamics in the simulations performed, as a constant value was set for this purpose. The reason for the difference in accuracy between ROI and ROM values can be assessed by obtaining the flow coefficients. These coefficients have been obtained according to the equations

P_{inj}	Data Source	ROI	ROM	ROI Error	ROM Error
4 barG	Experimental	0.778 g/s	0.0172 N	-	-
	RANS	0.725 g/s	0.0112 N	6.81%	34.85 %
	LES	0.748 g/s	0.0111 N	3.85 %	35.45 %
6 barG	Experimental	0.949 g/s	0.0260 N	-	-
	RANS	0.985 g/s	0.0184 N	3.65 %	30.00 %
	LES	0.919 g/s	0.0166 N	3.16 %	36.15 %
8 barG	Experimental	1.102 g/s	0.0349 N	-	-
	RANS	1.085 g/s	0.0256 N	1.54 %	27.90 %
	LES	1.110 g/s	0.0241 N	0.72 %	30.94 %

Table 5.3: ROI and ROM results for the experiment [1] and the RANS and LES approaches applied to *Generation 1* geometry and the error with respect to the experiment.

shown in Chapter 2, and have been included in Table 5.4. In them, it is observed how, as expected, the discharge coefficients are accurate, as the same ROI values were previously obtained. Nonetheless, for the three injection pressures, the velocity coefficient starts to show deviations, being the coefficient significantly lower, while the area coefficients are on the other hand, higher than experimental values. This shows that *Geometry 1* has a lower effective velocity, and a higher effective area than for experimental results. Therefore, the lower effective velocity and the higher effective area compensate for achieving the appropriate ROI values, but once the momentum is obtained, the lower velocity weighs more, leading to lower ROM values. These differences are associated to the approximation of the *Generation 1* geometry due to the insufficient CT spatial resolution, as explained in Section 4.3.

5.2.4 Flow morphology

A compelling characteristic of the injector flow on the proposed geometry (*Geometry 1*) is the different flow between the different orifices it is composed of when considering the LES simulations. First, differences between the orifices are observed in the volumetric void fraction for a injection pressure of 6 barG (Figure 5.3). In Orifice 1, there is a slower liquid volume fraction decay in the direction of injection compared to the results in Orifices 2 and 3, which look similar. In Orifice 1, at 2 mm from the injection point, the value at the spray core is above $\alpha = 0.3$, while for the remaining two orifices, this happens at around 1 mm.

P_{inj}	Data source	C_d	C_v	C_a	C_m
4 barG	Experimental	0.62	0.81	0.76	0.50
	RANS	0.57	0.56	0.85	0.32
	LES	0.59	0.55	0.88	0.32
6 barG	Experimental	0.61	0.82	0.75	0.50
	RANS	0.63	0.53	0.85	0.35
	LES	0.59	0.54	0.88	0.32
8 barG	Experimental	0.61	0.82	0.75	0.50
	RANS	0.60	0.61	0.83	0.36
	LES	0.62	0.56	0.89	0.34

Table 5.4: Flow coefficients for the experiment and the RANS and LES approaches applied to *Generation 1* geometry.

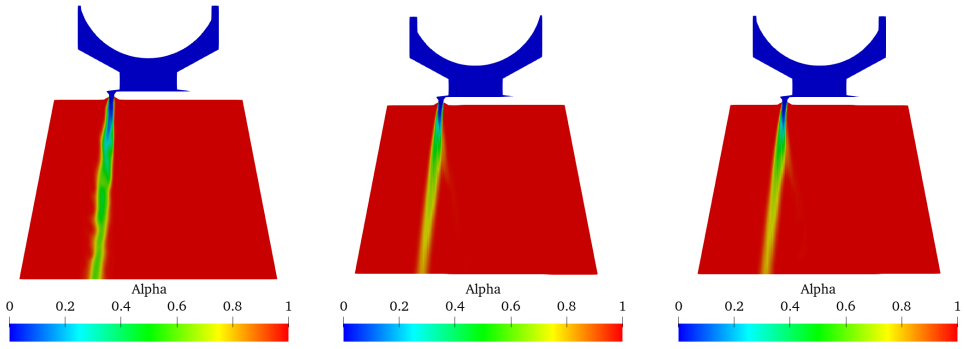

(a) Orifice 1. (b) Orifice 2. (c) Orifice 3.

Figure 5.3: Volumetric Void Fraction contours for an injection pressure of 6 barG obtained through LES.

Nonetheless, these differences are better visualized with the liquid mass fraction (Figure 5.4). It can be seen how the mass contribution of the injected fluid expands right after the injection point. For Orifices 2 and 3, there is mass diffusion towards the center of the domain, with an oscillatory behavior. Orifice 1, on the other hand, depicts a utterly different mass void fraction distribution with a continuous expanding jet. These differences could be caused by the introduction of numerical viscosity into the nozzles, due to the misalignment of the flow with respect to the cell faces [7].

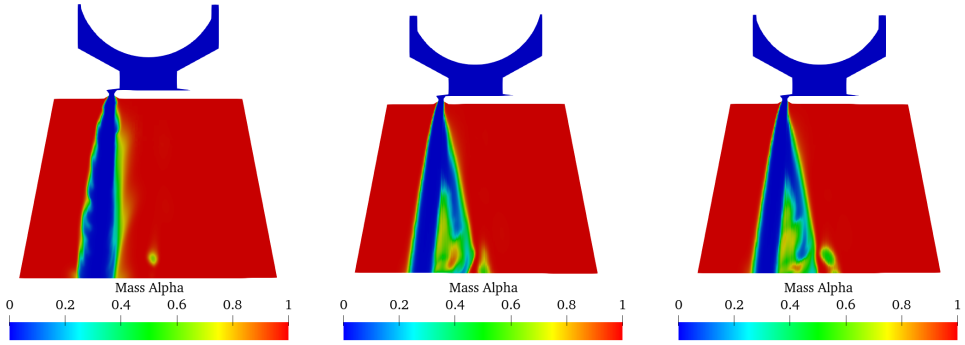

(a) Orifice 1. (b) Orifice 2. (c) Orifice 3.

Figure 5.4: Mass Fraction contours for an injection pressure of 6 barG obtained through LES.

RANS simulation (Figure 5.5), on the other hand, does not show those differences between the three Orifices . The solution given for the mass void fraction under RANS method is more similar to the solution shown by Orifices 2 and 3 (Figures 5.4b and 5.4c) obtained by a LES approach. In this case, the numerical viscosity due to the grid alignment effect is more pronounced in the unsteady behavior captured during the LES approach.

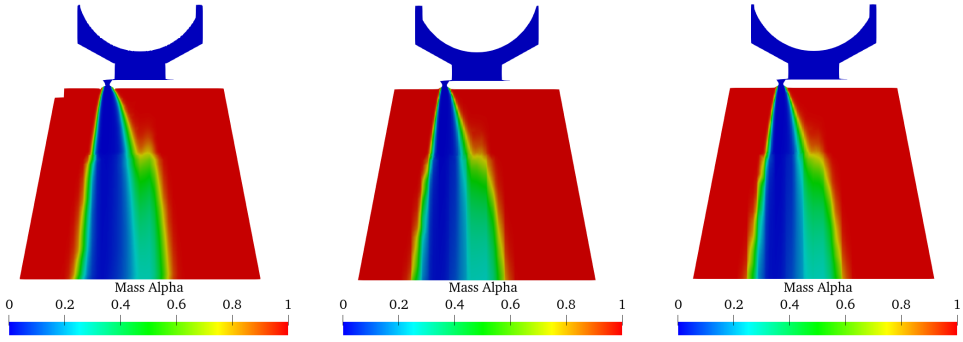

(a) Orifice 1. (b) Orifice 2. (c) Orifice 3.

Figure 5.5: Mass Fraction contours for an injection pressure of 6 barG through RANS $k - \epsilon$.

Figure 5.6 and Figure 5.7 show the contribution in ROI and ROM of the three orifices for the tested injection pressures, as the differences in morphol-

ogy could indicate changes in the hydraulic performance. When it comes to ROI, although the differences between them are not significant, it can be appreciated a slight deviation in the values between Orifice 1, and the other two, both for RANS and LES approaches, which is more noticeable at higher injection pressures (8 barG). The same phenomenon happens in the momentum results, where at the 8 barG condition Orifice 1 has lower momentum values also for the RANS simulation.

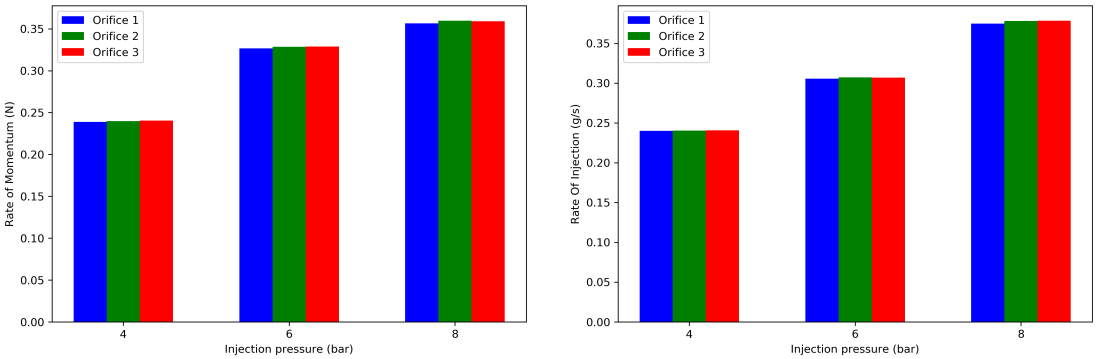

(a) RANS. (b) LES.

Figure 5.6: ROI results for the three orifices and the three injection pressures for the RANS and LES approaches.

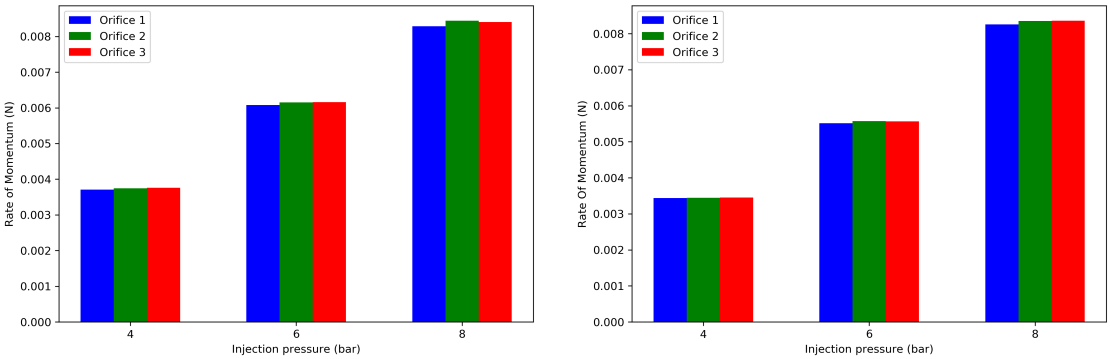

(a) RANS. (b) LES.

Figure 5.7: ROM results for the three orifices and the three injection pressures for the RANS and LES approaches.

To detect at which section those differences arise, plots of the velocity components at the orifices exit plane have been extracted. The cartesian

velocity components have been converted into cylindrical coordinates, allowing a better understanding of the differences in magnitude and topology. The axial component of the velocity shown in Figure 5.8 (which accounts for most of the momentum contribution) does show similar velocity distributions between the three orifices, rotated each one 120° due to their respective location within the injector circumference. A higher velocity is located closer to the orifice walls (close to $30\,\mathrm{m\,s^{-1}}$), while on the orifice center, an average of $25\,\mathrm{m\,s^{-1}}$ is found.

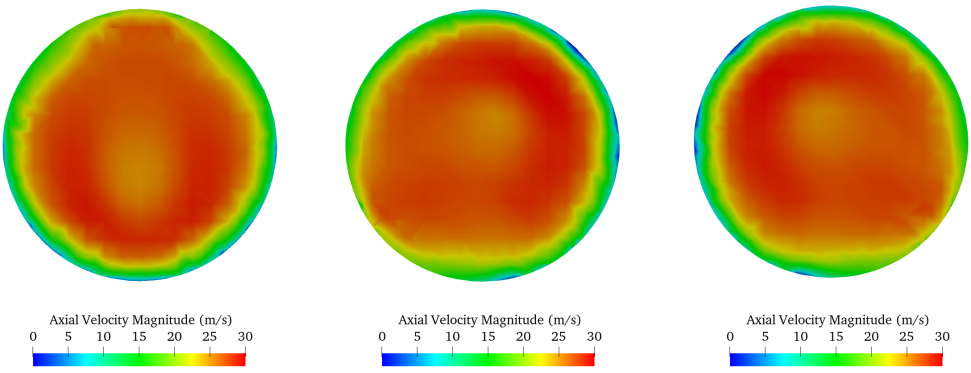

(a) Orifice 1. (b) Orifice 2. (c) Orifice 3.

Figure 5.8: Axial average velocity magnitude contours at the orifice section for the LES approach.

The swirling component of the velocity is represented in Figure 5.9. Greater differences are found in the intensity and location of the swirling motion. Orifice 1 shows a symmetric swirl distribution, in which two high-velocity regions are located, directing the flow towards the orifice walls. On Orifices 2 and 3, an asymmetric behavior is observed. The two high-velocity regions still exist, but one gains strength compared to the other, which will later lead to the previously observed differences in void fraction and mass void fraction.

The RANS results, as expected from Figure 5.5, show the same swirling behavior for the three orifices; therefore, they have not been included. Nonetheless, RANS simulations were run for hydraulic validation purposes and had a coarser resolution at the orifice section, with a possible misrepresentation of the flow-swirling motion.

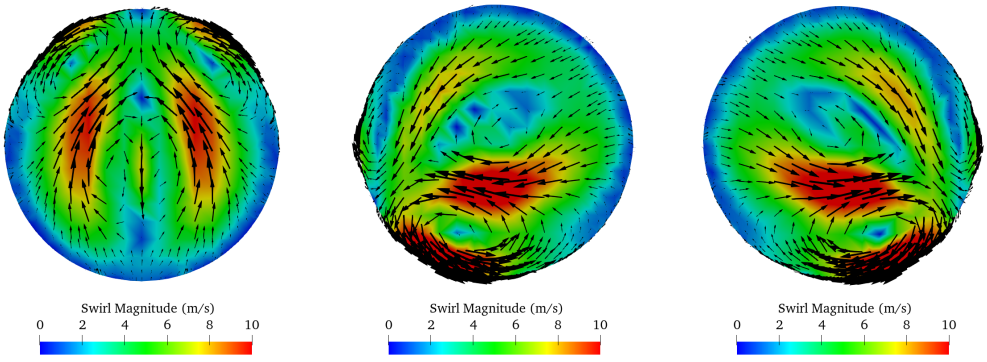

(a) Orifice 1. (b) Orifice 2. (c) Orifice 3.

Figure 5.9: Swirl average magnitude contours, and the in-plane vector field at the orifice section for the LES approach.

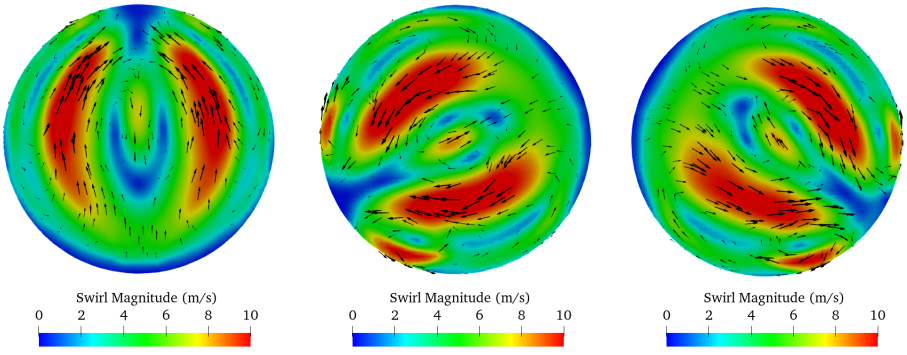

(a) Orifice 1. (b) Orifice 2. (c) Orifice 3.

Figure 5.10: Swirl average magnitude contours, and the in-plane vector field at the orifice section for the RANS approach.

5.2.5 Breakup length

Due to the differences observed in the behavior of the three orifices, the jet breakup length has been calculated for each of them for the RANS and LES approaches. The criterion followed has been the 99.9% of the mass fraction. The solution of the UWS flow has been thresholded at that value, and the length has been measured from the orifice outlet section up to the point that satisfies the 99.9% criterion. The results have been collected and presented in Figure 5.11. The slight differences in the ROI and ROM results magnify when

representing the breakup length. Orifice 1 generally has a greater breakup length value than the other two orifices, independently of the working injection pressure and the turbulence treatment applied to the simulations. Differences in the trend are obtained for LES and RANS approaches. On RANS, there is a slight increase in the breakup length values of the orifices, while Orifice 1 does show a diminishing trend. LES results show a decreasing length for the three orifices with increasing injection pressure. This trend in breakup length values is consistent with unbroken liquid length values reported by experimental results from Kapusta et al. [8]. Nonetheless, the lack of interface capturing schemes, together with the numerical diffusion importance of the presented results, makes these results not fully reliable. Furthermore, they are sensitive to the breakup length criterion value. On the other hand, the trends found for the breakup length provides an insight of which breakup regime the injector is working at with the chosen injection pressures.

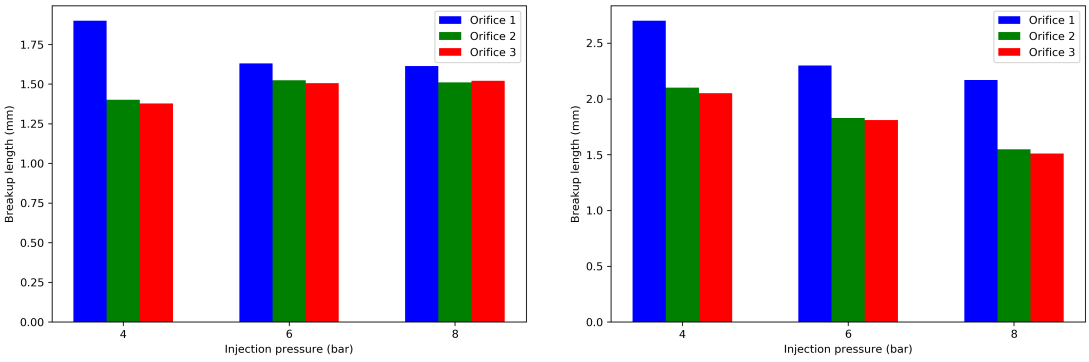

(a) RANS. (b) LES.

Figure 5.11: Breakup length results for the three orifices and the three injection pressures for the RANS and LES approaches.

The breakup regime can be obtained by calculating the Reynolds and Ohnesorge number at the orifices exit section (Figure 5.12). In it, the breakup regimes obtained for a plain-orifice and a ratio of 1:10 is included. According to these non-dimensional parameters, the calculated points fall in the transition region between the 1st wind-induced and the 2nd wind-induced regimes. These result helps validate the breakup length trend with the increasing injection pressure. According to Lin and Reitz [9], at the 1st wind-induced regime, the breakup length should decrease with increasing injection velocity. Knowing that the boundaries depicted between breakup regimes are not strict limits

[10], it can be safely stated that the main breakup phenomenon is due to the 1st wind-induced regime, close to the 2nd wind-induced regime.

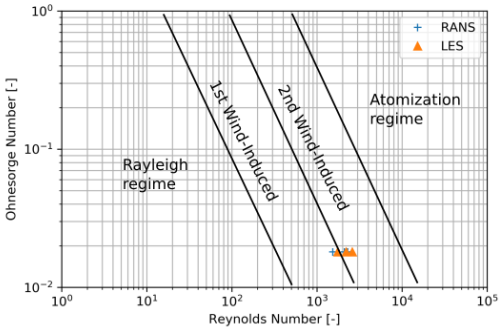

Figure 5.12: Ohnesorge-Reynolds chart of the RANS and LES performed using the MM approach.

Performing an LES MM approach on UWS sprays can also be helpful for detecting the region where the liquid jet starts to break up. A qualitative correlation between the breakup length and the RMS of the velocity shown in Figure 5.13 can be stated for all three orifices, as a peak of RMS velocity in addition to an enlargement of the velocity fluctuation region is observed where breakup should occur. Once the jet instabilities grow in frequency and size, the RMS values also observe a rise due to the presence of velocity fluctuations in the three directions. These instabilities are also the driving mechanism for jet breakup and droplet generation.

5.2.6 Effect on the rotation of the geometry on the LES results

After performing the MM study, and to confirm that the numerical viscosity is introduced by the misalignment of the flow direction with the cell's normal direction, an additional simulation was carried out by rotating the injector along its axis. In this case, the injector has been rotated an angle of 22.5° so none of the three orifices gets aligned with any of the cell's normal directions, as shown in Figure 5.14.

The effect of the numerical viscosity is seen by plotting the mass fraction in Figure 5.15. Orifice 1, which initially was differentiated from the other two, now has seen an expansion in the mass fraction contour. The other two orifices see a decrease in the width of their mass distribution, especially when it comes to Orifice 3, which sees a significant contraction, looking similar to the shape of Orifice 1 in its original disposition (Figure 5.4a). This effect is in

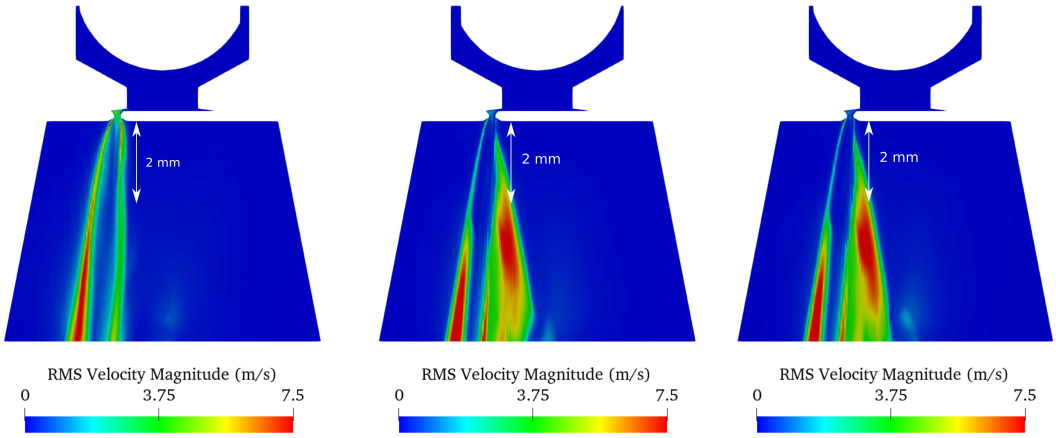

(a) Orifice 1. (b) Orifice 2. (c) Orifice 3.

Figure 5.13: RMS velocity contours of the three orifices for an injection pressure of 6 barG.

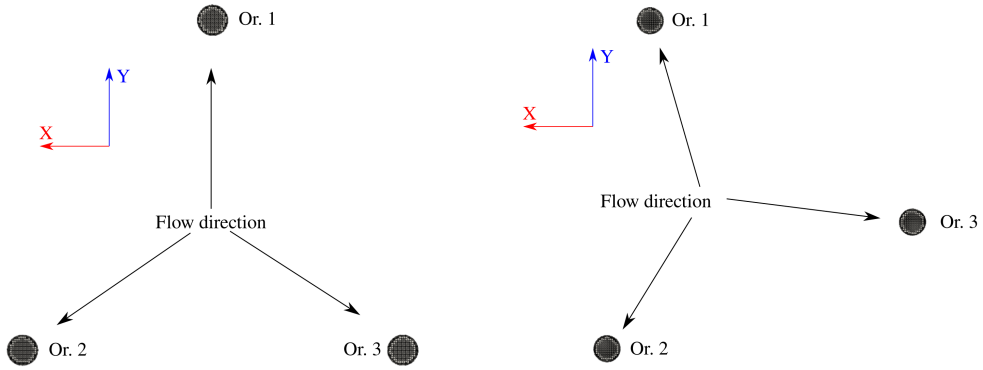

(a) Original distribution. (b) Rotated distribution.

Figure 5.14: Disposition of the orifices of the UWS injector before the geometry rotation and after the geometry rotation.

concordance with the location of this orifice after the rotation, which is now closer to being aligned with one of the cartesian axis (X-Axis).

The velocity distribution drives that change in mass fraction distribution at the nozzle exit plane. By representing the flow field in that section (Figure 5.16), it is observed how all three orifices depict a non-symmetric behavior, more similar to each other, and allows to check the effect of numerical viscosity

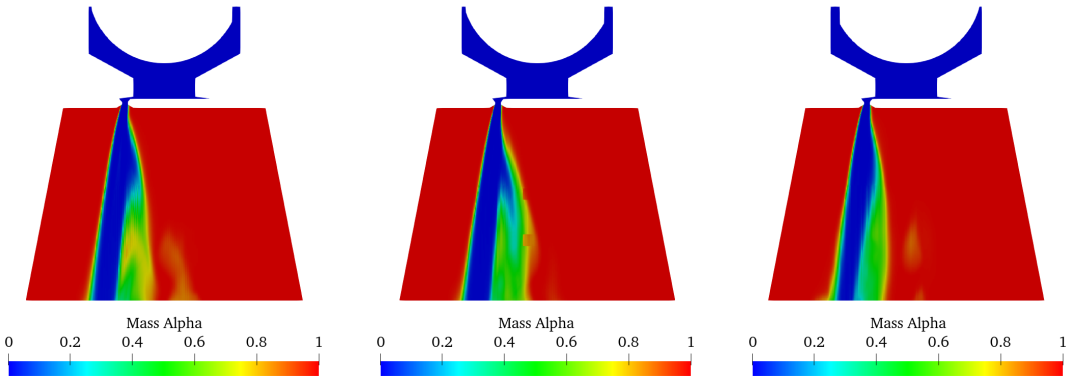

(a) Orifice 1. (b) Orifice 2. (c) Orifice 3.

Figure 5.15: Mass fraction contours of the three orifices for an injection pressure of 6 barG on the rotated geometry.

and the need for further refinement in these regions to mitigate the detected issue. Nonetheless, the solely usage of FE refinement limits the amount of cells that can be introduced. For that reason, subsequent studies will employ FE together with AMR.

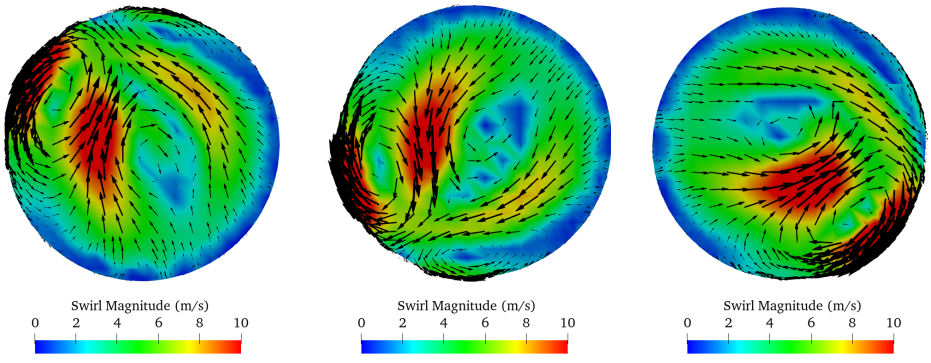

(a) Orifice 1. (b) Orifice 2. (c) Orifice 3.

Figure 5.16: Swirl magnitude contours, and the in-plane vector field at the orifice section for the LES approach for the rotated geometry.

In the same way, the breakup length values can also be extracted for the simulation carried out with the rotated geometry. The results are shown in Table 5.5. It can be observed how the differences between the three orifices

are mitigated in certain way. Again, Orifice 3 as become the most aligned with the cartesian mesh has shown a larger value.

	Orifice 1	**Orifice 2**	**Orifice 3**
Breakup Length	2.32 mm	2.15 mm	2.38 mm

Table 5.5: Breakup length values obtained for an injection pressure of 6 barG in the rotated geometry.

5.3 Volume-Of-Fluid simulations

The Mixture Model approach allowed the prediction of the hydraulic performance of the injector and provided an approximation of the breakup length and their trend with the increasing injection pressure. However, it could not show the outcomes of the primary breakup events and the instabilities that appear on the initial jet due to the high diffusivity of that technique. Therefore, it cannot characterize the distribution of droplets generated on the proposed UWS injector. As described in Chapter 4, the Volume-Of-Fluid (VOF) approach does transport the void fraction instead of the species. An interface capturing scheme can improve the representation of jet breakup dynamics at the expense of additional computational cost. It is important to remind that for the VOF cases, no UWS was used as the working fluid, but pure H_2O due to limitations of the VOF of dealing with multi-component liquids.

5.3.1 Introduction of the AMR technique

The meshing approach used on the MM simulations was the Fixed Embedding (FE). As the MM approach could not detect droplet detachment, the discharge volume length was short (5 mm), and a really fine mesh was not needed, which ended in a feasible amount of elements in the mesh. If the objective is to capture the breakup phenomenon, the discharge length needs to be increased to a value of 10 mm to give enough space for the breakup event to occur. Additionally, the element size on the discharge volume will be critical to predict the droplet characteristics correctly. The minimum cell size will determine the minimum droplet diameter detected. The droplets below that size will not appear on the solution. Additionally, to preserve the generated droplets and adequately predict the forces exerted on them, a minimum amount of elements should form each droplet, not a single cell.

The two meshing approaches (FE and AMR) have been compared in *Generation 1* to check if the AMR technique can be applied to this methodology. The two meshes used are the ones presented in Figure 4.19a and Figure 4.19b for the FE and AMR meshes, respectively. The combination of AMR and LES techniques generates theoretical errors related to the commutativity property of the differencing and filtering operations on the Navier-Stokes equations. Commutativity is only achieved when the filtering operations to remove the smallest turbulent scales consider a constant filter size. Hence the LES-filtered equations would have the same shape as the unfiltered N-S equations [11]. To assess the possible errors introduced, Pope [3] LES criteria has been adopted, and both simulations have been considered to fulfill the proposed guideline, as observed in Figure 5.17. Only low-quality regions are observed where no AMR is triggered, hence indicating that no liquid phase is present, being the mesh resolution not critical.

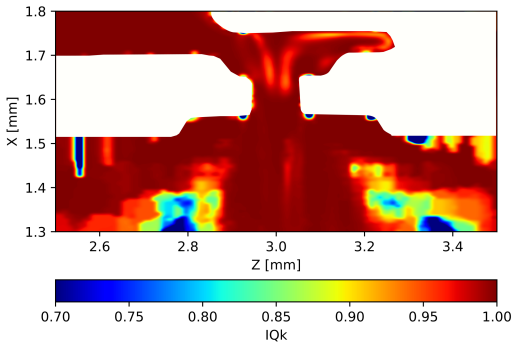

Figure 5.17: Representation of the LES Index of Quality according to Pope criteria [3].

5.3.1.1 Hydraulic validation

As happened during the MM approach, similar results are obtained through both meshing methods using VOF. The ROI value stays close to the experimental values, with differences with the experimental results lower than 1%, with slightly better results of the AMR meshing. The ROM values again have high deviations, as in the previous analysis. This issue will later be addressed using the *Generation 2* geometry.

Data Source	ROI	ROM	ROI Error	ROM Error
Experimental	1.102g/s	0.0349 N	-	
Fixed Refinement	1.092 g/s	0.0243 N	0.92 %	30.37%
AMR Refinement	1.106 g/s	0.0244 N	0.42 %	30.08%

Table 5.6: ROI and ROM results for the LES-VOF simulation for 8 barG of injection pressure, and the error of each mesh used, compared to experimental data [1].

5.3.1.2 Flow morphology

The influence of the mesh has also been assessed qualitatively by representing the liquid phase on a temporal snapshot (1 ms After Start Of Injection (ASOI)) on both simulations. Significant differences in the spray morphology have been detected. In Figure 5.18, FE mesh shows a uniform breakup along the discharge volume with a distinct droplet formation, while the AMR mesh looks more chaotic. The velocities of the jet and droplets are also affected. As for the FE case, a rapid slowdown to $15\,\mathrm{m\,s^{-1}}$ is observed, and the detached droplets' velocities show a greater slowing down to velocities of $7\,\mathrm{m\,s^{-1}}$. The AMR solution shows a larger amount of droplets and ligaments and a wider range of diameters. The slowdown effect is not as significant, with droplet velocities greater than $10\,\mathrm{m\,s^{-1}}$, while the initial jet and ligaments show velocities closer to $30\,\mathrm{m\,s^{-1}}$.

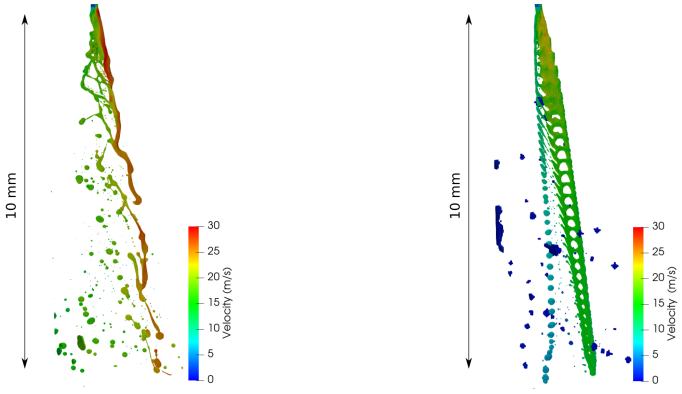

(a) Adaptive Mesh Refinement. (b) Fixed Refinement.

Figure 5.18: Temporal snapshot of the liquid phase for the two mesh refinement approaches.

5.3.1.3 VOF Index of quality

So far, morphological differences have been detected, but it is important to know which meshing approach results are more appropriate for the present application. The VOF quality index proposed in Chapter 4 has been applied to both simulations. According to the literature, a resolved droplet has been defined as a liquid particle whose equivalent diameter is made of 6 minimum-sized grid cells [12]. Applying that criterion, Figure 5.19 results. In it, few spray droplets have been represented colored depending whether they are resolved or not. It can be observed how the unresolved droplets are the ones that are composed of very few cells, misrepresenting their shape (*box-shaped*), which will probably lead to significant errors when calculating the aerodynamic forces. Resolved droplets depict smooth interfaces, with a better approximation of the shape of each droplet.

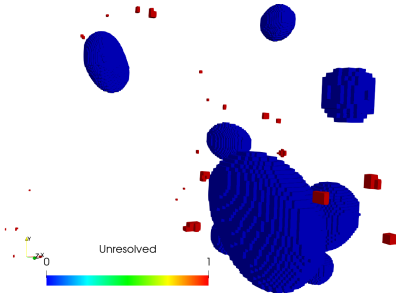

Figure 5.19: Representation of unresolved and resolved droplets within a VOF simulation.

Table 5.7 shows the results of the VOF IQ calculated for both simulations. The FE simulation shows a 20% lower IQ with more elements in its mesh than the one with AMR. FE approach is incapable of maintaining the same level of refinement in the regions away from the injector orifice, resulting in a larger amount of unresolved mass. On the other hand, AMR can refine locally in the zones where needed, maintaining the same droplet resolution throughout the domain without needing a constantly large amount of elements.

Due to this better resolution, together with the ability to use only the amount of elements needed for each time instant, the AMR approach has been applied for the subsequent VOF simulations that have been carried out.

5.3.2 Performance of *Generation 2* geometry

When performing the micro-CT scan technique on the UWS injector, the high-fidelity geometry (*Generation 2*) was obtained. Knowing the hydraulic

Simulation	VOF IQ
FE	0.798
AMR	0.989

Table 5.7: Index of Quality proposed for VOF results applied to the two types of meshing strategies for a specific time-snapshot.

limitations of the *Generation 1*, the main purpose of simulating the new UWS geometry was to assess whether it solved the previous hydraulic deviations, and have a more realistic representation of the injector of interest. In this case, higher liquid temperature was tested, according to Table 4.6. Additionally, as VOF simulations use H_2O as the working liquid, experimental data obtained by injecting water at the corresponding conditions have been used.

Hydraulic characterization

The ROI and ROM results have been extracted, and their evolution with the injection pressure has been analyzed. In this geometry, the correlation between the experimental and computational data has significantly improved concerning the results obtained for the original geometry. The trend is well captured, and if the deviations are again represented (Table 5.8), the improvement in accuracy is confirmed. ROI deviations have increased for the 8 barG case, but the ROM deviations are below 8% for all the cases, with a minimum error of 6% for the highest injection pressure.

Inj.Pressure	Data	ROI	ROM	ROI Error	ROM Error
8 barG	Exp.	1.154 g/s	0.034 N	-	-
	LES	1.124 g/s	0.036 N	2.59 %	7.14 %
6 barG	Exp.	0.995 g/s	0.025 N	-	-
	LES	0.976 g/s	0.027 N	1.91 %	8 %
4 barG	Exp.	0.854 g/s	0.017 N	-	-
	LES	0.793 g/s	0.018 N	7.05 %	5.88 %

Table 5.8: ROI and ROM results for the experiment [1] and the LES approach applied to *Generation 2* geometry for the different injection pressures.

This improvement in the overall performance of the injector shows the importance of the accuracy of the geometry in the nozzle section [13]. The

approximated features on *Generation 1* might have generated a too-narrow passage to the orifices, generating a pressure drop within the injector, satisfying the mass flow rate of the experimental results, but leading to considerably lower momentum. This pressure drop effect can be observed in Figure 5.20, where the pressure in the region previous to the orifice is lower than the one observed in the *Generation 2* geometry.

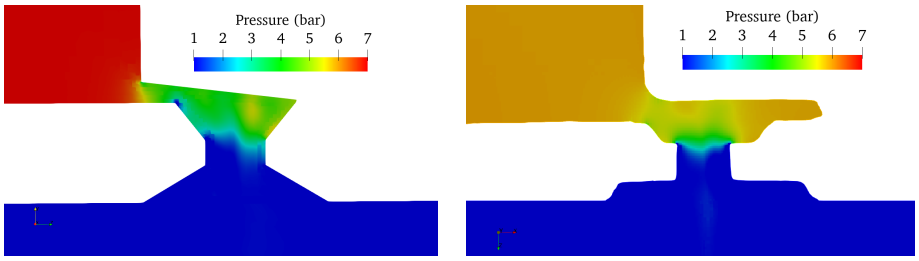

(a) Generation 1. (b) Generation 2.

Figure 5.20: Pressure contours obtained at a specific time instant for the two geometries employed.

These ROI and ROM values are transmitted into the characteristic hydraulic coefficients, which depict the orifice behavior with respect to the theoretical mass flow rate (C_d), effective velocity (u_{ef}), geometric area (A_0), and momentum (C_M). Table 5.9 indicates the corresponding flow coefficients for the different conditions tested. The expected agreement between C_d and C_M is observed based on the ROI and ROM data. The computational approach generally shows an effective velocity closer to the theoretical value than the experimental results while employing a lower percentage of the geometric area of the injector orifices. The discharge coefficient does show a similar behavior between CFD and experimental approaches due to the compensation between the higher velocity and the lower area of the CFD results. The working fluid is not occupying the totality of the orifice. Gas coming from the discharge volume is set at the orifice section, reducing the available area and consequently reducing the mass flow rate that the injector can introduce into the chamber.

Based on these results and the better overall agreement of the hydraulic parameters, the subsequent VOF analysis has been performed solely on this higher-resolution CT scan geometry.

Inj.Pressure	Data	Cd	Cv	Ca	Cm
8 barG	Exp.	0.63	0.73	0.86	0.46
	LES	0.59	0.83	0.71	0.49
6 barG	Exp.	0.60	0.75	0.80	0.45
	LES	0.59	0.83	0.71	0.49
4 barG	Exp.	0.60	0.77	0.78	0.46
	LES	0.59	0.83	0.71	0.49

Table 5.9: Flow coefficients results for the experiment and the LES approach applied to *Generation 2* geometry for the different injection pressures.

5.3.3 Macroscopic characteristics

5.3.3.1 Near-field spray morphology

Firstly, a qualitative assessment of the evolution of the spray within the discharge volume has been done on the three injection pressures to depict the spray morphology, its breakup mechanism, and the development of all three sprays that the UWS injector is composed of. Figures 5.21, 5.22, and 5.23 show the evolution of the liquid phase for simulation times of 0.06 ms, 0.026 ms, and 0.046 ms ASOI, respectively. The first differences arise concerning the injection pressure differences. Higher pressures imply a deeper penetration length for the same time ASOI, and therefore the liquid reaches earlier the outlet boundary condition, as for the last time representation the low injection pressure condition is still developing, while the other two injection pressures do not show the spray tip. At time in-between 0.06 ms and 0.26 ms, the liquid jet expands radially (inwards and outwards) with respect to the injector axis. It generates within that expanded region a set of initial droplets and ligaments. At further ASOI times, the spray further develops, and the initial generated droplets and ligaments leave the domain. The total disruption of the initial jet is not observed for any of the injection conditions at any of the times represented. Between the different injection pressures, the spray morphology shown is similar, in addition to the location in which the droplets and ligaments are first created.

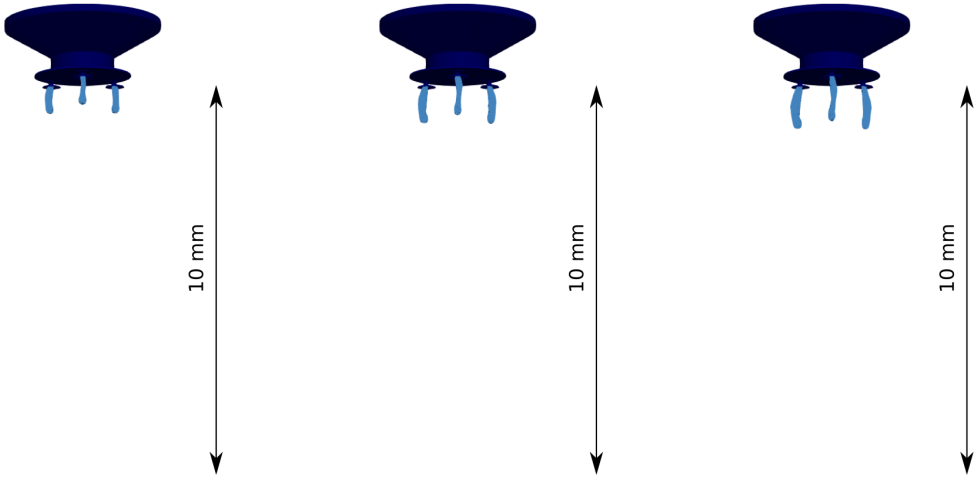

(a) $P_{inj} = 4$ barG. (b) $P_{inj} = 6$ barG. (c) $P_{inj} = 8$ barG.

Figure 5.21: Near-field view of the liquid phase ($\alpha < 0.5$) at a time of 0.06 ms ASOI.

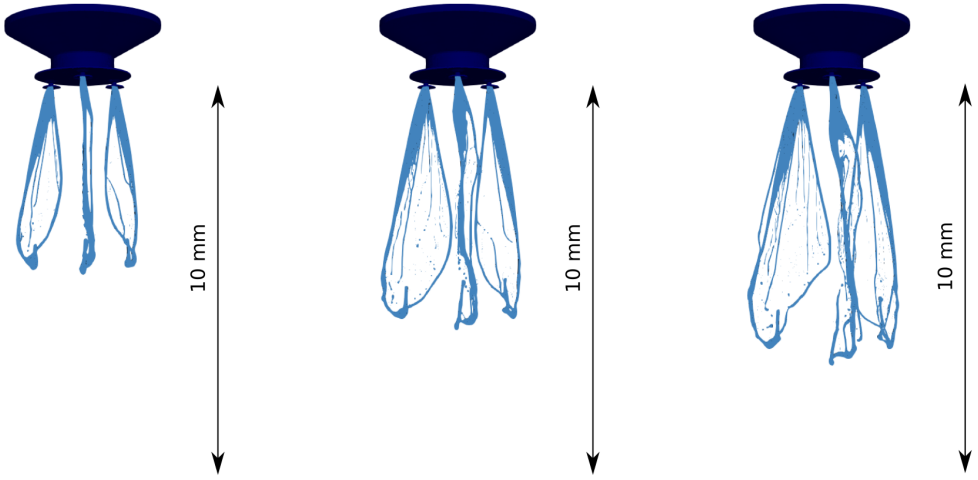

(a) $P_{inj} = 4$ barG. (b) $P_{inj} = 6$ barG. (c) $P_{inj} = 8$ barG.

Figure 5.22: Near-field view of the liquid phase ($\alpha < 0.5$) at a time of 0.26 ms ASOI.

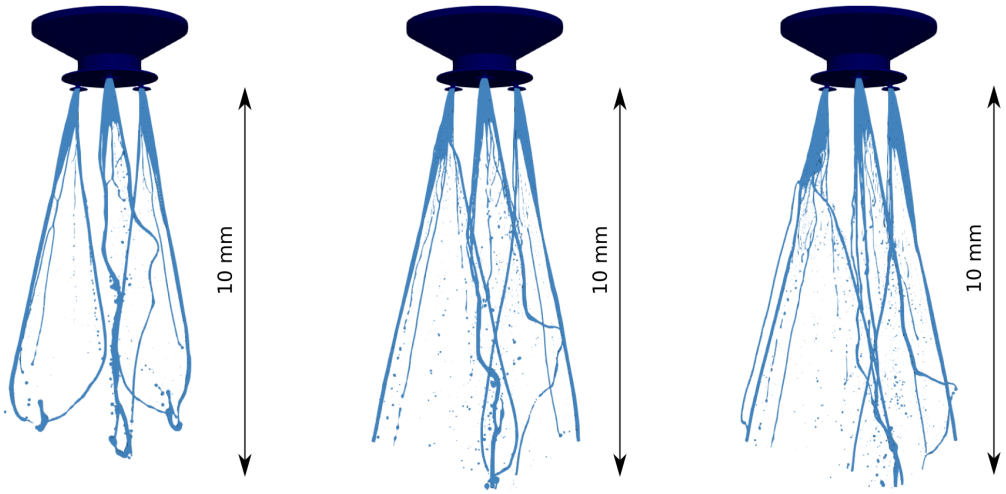

(a) P_{inj} = 4 barG. (b) P_{inj} = 6 barG. (c) P_{inj} = 8 barG.

Figure 5.23: Near-field view of the liquid phase ($\alpha < 0.5$) at a time of 0.46 ms ASOI.

Several characteristic parameters can be obtained, such as the tip penetration length, the spray angle, the intact core length, the mass transfer between structures, and the characterization of the distribution of droplets generated during the breakup process.

5.3.3.2 Spray penetration

The penetration values were calculated according to the density projection procedure described in Section 4.5, and have been compared against experimental data obtained at the same conditions as the simulations. Figure 5.24 shows this comparison. The represented experimental curve corresponds to the main spray body and not the spray burst depicted in [1]. A general agreement in the evolution of the spray tip penetration is achieved for the three injection pressures tested. The conditions in Figure 5.24b depict the most significant deviation of all injection pressures, with a higher experimental penetration slope. Although not included, the penetration curves applied to the *Generation 1* geometry strongly differed with respect to the experimental data set with lower spray tip velocities. This deviation, together with the disagreements observed for the momentum values, reinforces the idea of a pressure drop prior to the orifices caused by the CT spatial resolution.

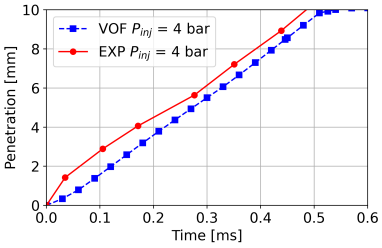

(a) P_{inj} = 4 barG.

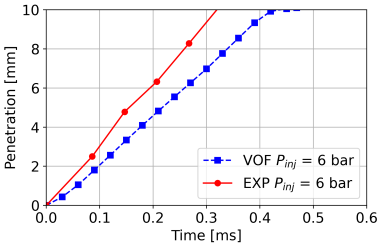

(b) P_{inj} = 6 barG.

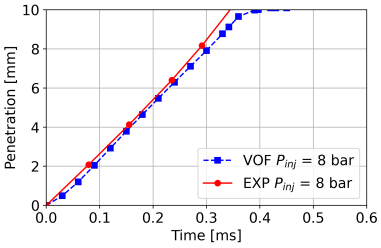

(c) P_{inj} = 8 barG.

Figure 5.24: Spray tip penetration evolution for the three injection pressures simulated, in addition to the corresponding experimental [1] results.

5.3.3.3 Spray angle

The spray angle values have been obtained through the procedure described in Chapter 4.5, and match the procedure used to extract the experimental data. Although the methodology is the same, the domain size during the experiments is significantly different from the one used in CFD. As indicated during the penetration comparison study, experiments discharge into a chamber with a characteristic size of 75 mm. The measuring distances on the spray angle determination have been 0.06 S, and 0.12 S, representing a distance of 4.5 mm and 9 mm from the orifice location when the spray reaches the outlet of the domain. The reader is informed that the experimental data that is going to be presented is not included for validation purposes, as CFD calculations have been performed on quiescent conditions, while experimental angles were obtained under cross-flow conditions. Table 5.10 depicts these results for the three injection pressure conditions. All the obtained angles are located around a value of 15°, while no clear trend as injection pressure changes is observed neither for the CFD approach, nor experimental values. This lack of trend was also observed within the complete angle values previously obtained for several

injection temperatures, ambient temperatures, and cross-flow rates [1]. This may be an effect of other factors with higher importance, such as enhanced evaporation from finer atomization, the interaction between the gas and the droplets, or the turbulence taking place at the orifice region. From the MM study, it could be assessed that the operating range for the specified injection pressures locates the breakup regime in the transition region between the first and second wind-induced regimes.

$\mathbf{P_{inj}}$	**Data Source**	**Spray Angle**
4 barG	Exp.	14.37°
	CFD	15.13°
6 barG	Exp.	15.64°
	CFD	14.43°
8 barG	Exp.	15.48°
	CFD	16.58°

Table 5.10: Spray angle results for the computational and experimental [1] approaches.

5.3.3.4 Plume interaction

The proposed injector comprises three orifices that inject into the same discharge volume. From experimentally-obtained images, these three jet plumes merge at a certain distance into a single spray in which the coalescence phenomenon becomes important, and the three jets interact. Therefore, a time average of the velocity field has been obtained in a perpendicular plane to the spray plumes at two distances to the orifices, 3 mm and 8 mm. The results are shown in Figure 5.25. At a distance of 3 mm, the three jets are separated, and no interaction is visible between them. At a larger distance from the orifices (8 mm), the expansion previously detected in Figure 5.22 is confirmed, and the velocity field of a spray breaking up is observed. Although the three sprays have also expanded toward the injector axis, they have not mixed with each other. From the velocity plot, the three different sprays can still be easily differentiated. Therefore, it can be stated that within the domain considered for the VOF application, there is no strong interaction between the three UWS plumes.

From the interaction outcomes previously observed, the three orifices act as almost independent sprays. Therefore, to reduce the number of cells in the

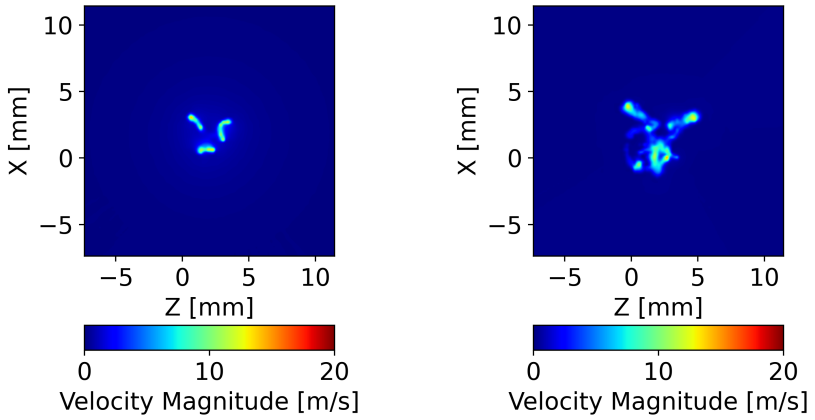

(a) Z = 3 mm. (b) Z = 8 mm.

Figure 5.25: Average velocity contours at two distances from the orifice section for the VOF simulation with an injection pressure of 8 barG.

domain needed for these simulations, only one of the three holes will be further considered. In these simulations, two out of three orifices will be considered *dummy* orifices, which will not introduce liquid into the discharge volume. In that way, the AMR embedding triggered would only affect one orifice, reducing the computational cost of the calculations and speeding them up.

5.3.4 Microscopic characteristics

5.3.4.1 Determination of the steady-state behavior

The main interest of this study resides in determining the droplet characteristics generated during the steady-state phase of the injection process. Additionally, the simulations performed do not consider the movement of the needle; therefore, the transient effects would not be realistic. In order to determine at which time this transitory period ends and the injector behaves in steady-state conditions, the steady-state behavior has been assessed by comparing a macroscopic characteristic of the spray angle (Figure 5.26a) and a microscopic characteristic such as the intact length, Figure 5.26b). The spray angle shows fluctuations throughout the whole simulation time, although, from 0.75 ms, the angle values oscillate around the average angle given by the three-hole case (Table 5.10). Additionally, the intact length also shows variations in its magnitude, although it seems to vary around an average value.

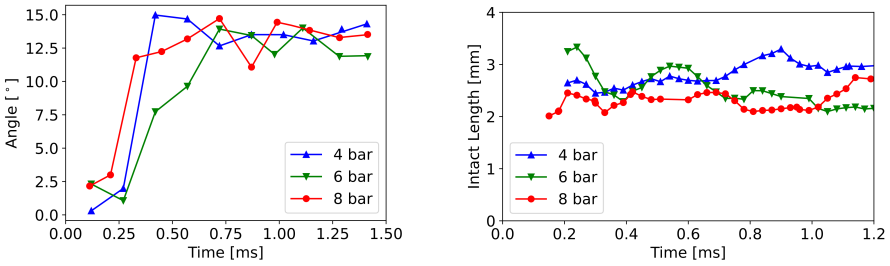

(a) Spray Angle. (b) Jet intact length.

Figure 5.26: Temporal analysis of the spray angle and the intact length for the one-hole injector.

Figure 5.27 also shows the temporal evolution of the hydraulic characteristics of the injector. These variables stabilize to constant values quicker than the macroscopic and microscopic spray characteristics. Additionally, it is highlighted how both ROI and ROM values do not show the unsteadiness present on the spray angle and the intact length, but rise to a constant value. Some unsteadiness is expected at the orifice section thanks to the LES approach, but the employed mesh might filter out the scale of these fluctuations.

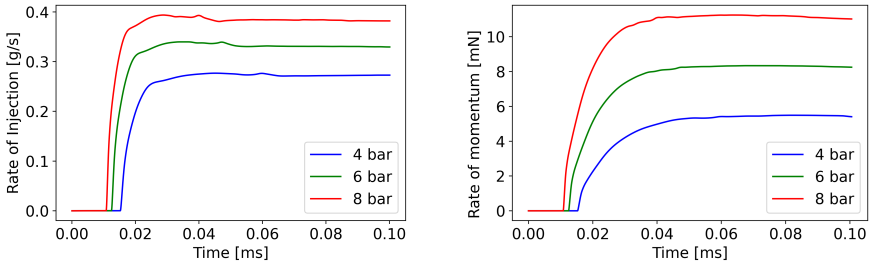

(a) ROI. (b) ROM.

Figure 5.27: Temporal analysis of the evolution of the ROI and ROM obtained for one of the three holes.

From the specified time (0.75 ms) the results have been averaged for enough time to have statistically representative results. In order to check the minimum amount of time needed to achieve this statistical independence, two sets of parameters have been considered. The first one is the Total Integrated Mass (TIM), which consists of integrating the projected mass in two perpendicular

directions to the spray, giving a value of TIM for several distances from the nozzle. Time steps have been progressively added into the time-averaged data until the TIM deviations have reduced to an acceptable value (<1%). The second set of parameters used are the Rosin-Rammler distribution's defining constants (Subsubsection 2.5.3.3). The PDF distribution of the generated droplets is extracted for each time value, and a least-square fitting is applied using the Weibull distribution function. From the fitted curve, the defining parameters of the Rosin-Rammler are extracted. A similar approach to the averaged TIM is performed. Progressively the Rosin-Rammler parameters are added into the time-averaging, and the deviations with respect to the time-averaged without the present time data is obtained. This processing is shown for the specific injection pressure of 6 barG in Figure 5.28. From this Figure, it can be quickly concluded that by averaging a total of 1.2 ms (the maximum amount of data available from the simulations), the data becomes representative of the performance of the injector at steady-state conditions.

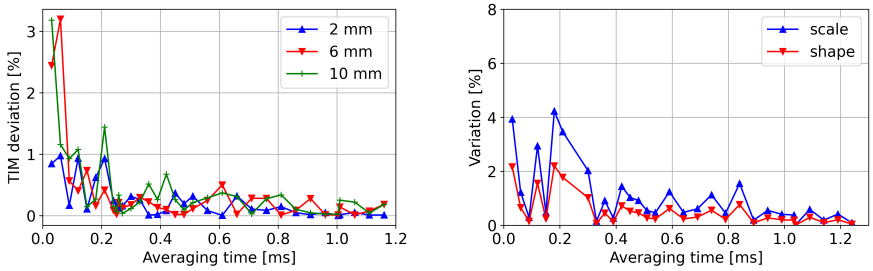

(a) ROI. (b) ROM.

Figure 5.28: Statistical significance of the TIM and fitted RR parameters with time.

5.3.4.2 Droplet characterization

In order to perform the microscopic characterization of the after-treatment sprays, the droplet size and droplet velocity PDF have been extracted. First, the distribution of droplets will be validated against experimental data captured using High-Resolution Laser Backlight Imaging (HRLBI). A complete description of the technique can be found in [14]. The location of the experimental measuring is at a distance of 30 mm from the injection point, which is considerably larger than the maximum distance modeled through computational methods 10 mm. Nonetheless, secondary breakup is not expected to occur due to the low velocities and the low We numbers. However, at the

CFD distances modeled, the three jets have not yet merged into a single one, and therefore coalescence phenomena might occur in between the measuring locations. Evaporation can also start to gain importance in distances out of the computational domain, closer to the experimental measuring section.

To obtain the droplet size and droplet velocity PDF, only the droplets located at the last 2 mm of the domain in the axial direction (Z-axis) have been considered. The droplets located in the volume of interest have been identified and their data extracted. These characteristics have been time-averaged for the available simulated time indicated in Subsubsection 5.3.4.1. In order to avoid over-representation of the slow droplets and their double detection in two consecutive time-steps, each detected droplet has its velocity vector calculated and based on its direction and magnitude it is assessed whether it was present in the domain of interest previously or not.

A comparison has been made on the diameter distribution function of both methods. Figure 5.29 compares the number-based PDF and the Cumulative Volume Fraction (CVF) of the corresponding distribution. The characteristic numbers *Dv10*, *Dv50*, *Dv90*, and the Sauter Mean Diameter (SMD) have also been compared. The comparison depicts an over-prediction of the number of droplets of small diameter at all the conditions included. Additionally, the spread of the PDF is more skewed towards the small diameters (<20 µm), as the number of drops with a diameter greater than 50 µm rapidly decays. With increasing the injection pressure, the probability peak of the experimental distribution shifts toward smaller diameters, raising the probability peak and showing closer diameter distributions with the CFD results. On the other side, the CVF introduces which percentage of the total volume of the spray is located under a specified droplet diameter. Due to the simulations having smaller droplets than in the experiments, the computational CVF curve is shifted towards the left. In the case of $P_{inj} = 4$ *barG*, the computational curve has most of the volume in smaller diameters. From a diameter of 150 µm, the curves cross each other, indicating that the CFD results have more large droplets. This behavior indicates that these large droplets/ligaments, although uncommon, have more associated volume in the computational result than in the experiment. This situation does not happen at the other injection pressure conditions. Additionally, in the $P_{inj} = 4$ *barG* and $P_{inj} = 8$ *barG* conditions, the maximum diameter detected from the CVF curves is the same for both methodologies (≈300 µm), while for the middle case, the computational approach has a maximum diameter of 200 µm.

The characteristic diameters differ due to the shifting in the CVF curves, with deviations as low as 10 µm for the lowest injection pressure case and as

high as 30 µm for the $Dv90$ characterization in the highest injection pressure case. The SMD value has generally lower values for the CFD case than those obtained through HRLBI. Remind that the computational domain was short enough to give little time to characterize evaporation dynamics which would eliminate the smallest diameters and reduce the diameter of the largest ones. Additionally, the three spray plumes did not merge into a single spray at these distances. Therefore there are no coalescence events taking place which could shift the PDF curves to larger values, becoming more similar to the experimental results.

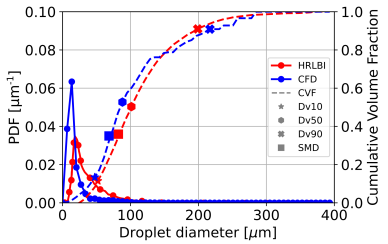

(a) P_{inj} = 4 barG.

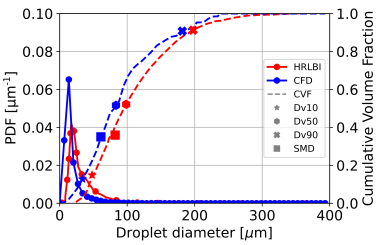

(b) P_{inj} = 6 barG.

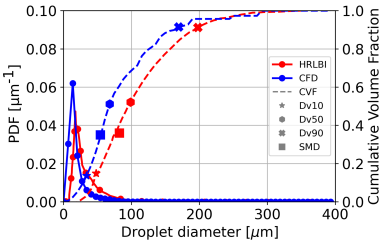

(c) P_{inj} = 8 barG.

Figure 5.29: Number-weighted PDF distribution and CVF comparison between experimental [1] and computational methods.

The volume-weighted PDF gives another way of depicting the distribution of droplets. In it, the distribution is not weighted by the number of droplets of each characteristic diameter but by the volume of the spray associated with each diameter. In situations where evaporation and mass transfer is most important, it is useful to characterize the probability of finding a determined working fluid volume in each diameter. Figure 5.30 represents this distribution. In all three injection pressures, the computational results show a *noisy* distribution at relatively large droplet diameters due to the low amount of

droplets of these sizes. In contrast, a smoother distribution is observed for small diameters (<50 µm), where a larger amount of droplets are detected. Regarding the comparison with experimental data, good agreement is achieved for all the injection pressure conditions. Figure 5.30a does underpredict the volume contained in the diameters below 75 µm, while for larger diameters, a better agreement is achieved. On the $P_{inj} = 6\ barG$ case, all the volume in the diameters is properly predicted, while for the largest injection pressure case, the prediction of large diameters is slightly underpredicted. This agreement indicates that the computational procedure properly captures the large mass and momentum-carrying droplets.

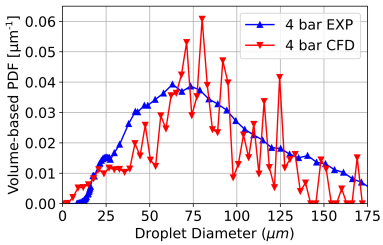

(a) P_{inj} = 4 barG.

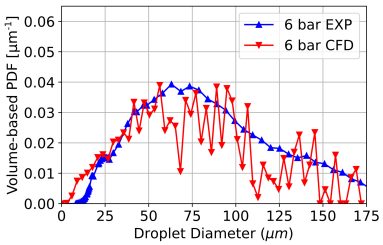

(b) P_{inj} = 6 barG.

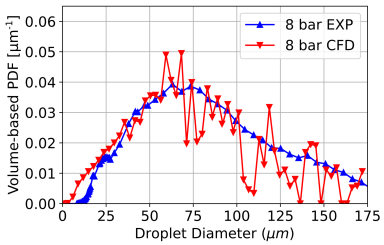

(c) P_{inj} = 8 barG.

Figure 5.30: Volume-weighted PDF distribution comparison between experimental [1] and computational methods.

Considering the relative good matching between the experimental and computational results, the effect of the injection pressure on the droplet distribution has been studied. Figure 5.31 includes the number-based PDF and with the CVF curves at the three injection pressures. Almost no differences are detected in the PDF distribution, as the three curves show the exact same peak diameter and almost identical maximum probability value. On the other hand, less amount of large droplets are observed with increasing injection

pressure. The highest injection pressure shows a higher probability of finding droplets between 25 µm-125 µm. This is also seen in the evolution of the CVF curves, where there is a higher volume located below droplets of 125 µm. On the other hand, the lowest injection pressure shows the largest droplets. The characteristic diameters are affected accordingly. The SMD also sees a decrease in its value with increasing jet velocity.

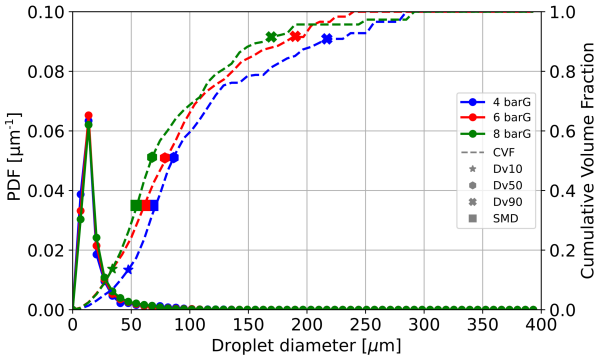

Figure 5.31: PDF and CVF comparison between the three injection pressure conditions simulated.

Further analysis has been carried out regarding the primary breakup phenomena of the spray. It has already been seen that the completeness of the initial jet has not undergone full atomization in the first 10 mm as the breakup length (total disruption of the liquid jet) does not fall within the considered domain. Nonetheless, a partial breakup is observed. In order to understand the evolution of the droplet generation process, the distribution of droplets has been obtained at two regions of the computational domain, from 2 to 6 mm and from 6 to 10 mm, generating two new volumes of interest, and the results have been included in Figure 5.32. The same evolution for the different injection pressures is obtained. Regarding the number-based PDF, there is a slight increase in the probability of the most common droplet. This indicates that the predominant droplet size is generated mainly in the region nearby the orifices. On the other hand, the CVF curves are displaced toward larger sizes, increasing the maximum diameter detected in each injection pressure. Based on that evidence, large droplets/ligaments are being detached from the main liquid core on further distances from the injector. A reason for that could be that initial jet instabilities are only capable of separating small amounts of droplets from the liquid/gas interface, but their wavelength is still lower than of the jet diameter. It is not until largest distances from the orifices that the wavelength grows enough to generate a largest jet disruption.

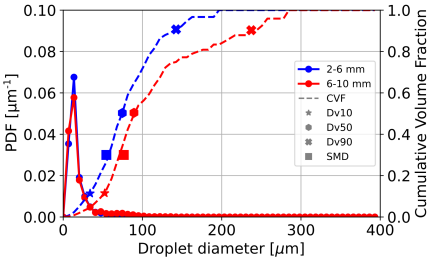

(a) P_{inj} = 4 barG.

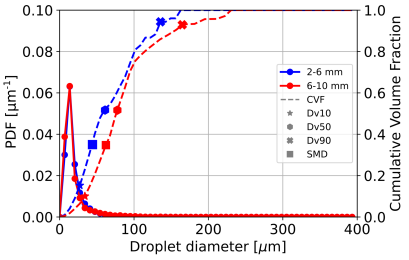

(b) P_{inj} = 6 barG.

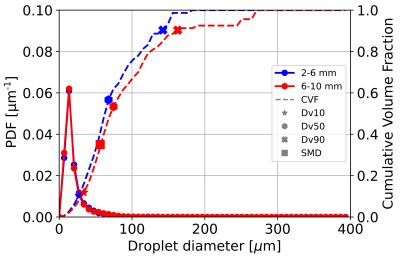

(c) P_{inj} = 8 barG.

Figure 5.32: PDF and CVF curves for two regions within the discharge volume.

The velocity of the droplets has also been represented through PDF plots to detect the effects of the different injection pressures. Figure 5.33 depicts this characterization for two velocity components, the Z-velocity, which is aligned with the axis of the orifices, and the Y-velocity, in a perpendicular direction to the spray. Due to the absence of any cross-flow, the choosing of the secondary velocity axis (X or Y) was not relevant. Same results are expected when increasing the injection pressure, a clear trend is observed when representing the Z-velocity distribution (Figure 5.33a). At higher injection pressures, the characteristic velocity of the spray increases, moving from a peak of 20 $\mathrm{m\,s^{-1}}$ at the 4 barG condition to 25 $\mathrm{m\,s^{-1}}$ and 30 $\mathrm{m\,s^{-1}}$ at the 8 barG condition. Additionally, increasing the range of possible velocities for the droplets diminishes the probability of the most common droplet. Regarding the Y-velocity distribution, all three distributions remain centered around the null y-velocity value, with its probability peak at that position. The increase in velocity magnitude caused by the increase in the injection pressure does not only rise the velocity in the injector axis, but due to its spread angle, the velocity in the perpendicular direction increases accordingly. Hence, the spread of possible velocities increases with higher injection pressure, decreasing the probability peak of the most common Y-velocity. A slight shifting

toward negative velocities is detected for the 6 and 8 barG cases, which could be caused by fluctuations in the velocity field due to the breakup phenomena or the increase in the asymmetric velocity distribution observed in the orifices (Figure 5.16).

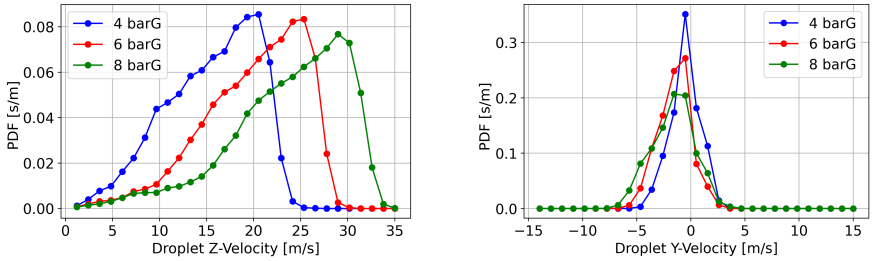

(a) Z-Velocity. (b) Y-Velocity.

Figure 5.33: Two velocity-component PDF obtained at the three injection pressure simulated.

The relationship between the diameter of the captured droplets and their associated axial (Z-direction) and transverse (Y-direction) axes has been obtained. Figure 5.34 represents the mean droplet velocity together with the standard deviation of the measure. With respect to the axial velocity, the effect of the injection pressure is also seen, and it can be observed how the small droplets show the smallest of the velocities with a considerable dispersion of the measurements, while the largest droplets/ligaments, which are the most inertia carrying particles show larger velocities and less deviation around their mean value. This is expected as the small droplets are more easily slowed down once injected. The increase in velocity associated with larger droplets is not much significant in droplets bigger than 40 µm. With respect to the results obtained for the transverse velocity (Y-direction), there is a general shifting of the droplets velocities toward negative values, as seen on the PDF. The differences observed due to the injection pressure are only seen for droplets up to 50 µm, in which the higher the injection pressure, the more negative the Y-velocity would be. Largest droplets are not affected by this parameter.

An additional analysis of the droplets morphology has been performed through the sphericity parameter (defined in Equation 4.68). The reader is reminded that the mentioned parameter acquires the value of the unity when the corresponding droplet represents a perfect sphere shape. Higher values, on the other hand represent elongated droplets or ligaments. To describe the morphology of the spray droplets, a Kernel Density Estimation (KDE)(a

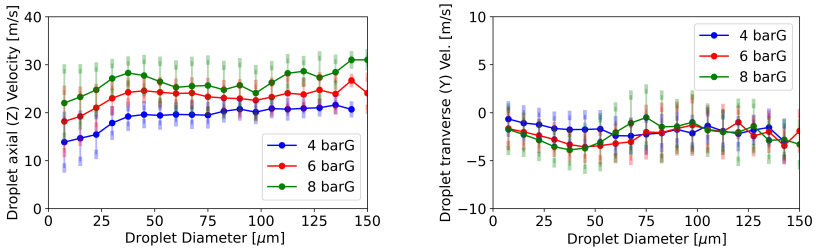

(a) Z-Velocity.

(b) Y-Velocity.

Figure 5.34: Evolution of the mean and standard deviation (error bars) of the velocity of the droplets with their associated diameter.

method of estimating probability density [15]) has been applied to the set of captured droplets, and they have been represented in Figure 5.35. At the 4 barG condition, most detected droplets are located at diameters smaller than 25 µm, as observed during the PDF representations. The most common diameter (≈8 µm) is not represented solely by spherical droplets but ranges up to sphericity values of $Sp = 5$. In that working condition, there is a higher probability of finding spherical droplets up to a droplet equivalent diameter of 75 µm. However there is a high spread of non-spherical droplets as well. Additionally, there is an increase of sphericity with increasing equivalent diameter from the 100 µm mark onward, where no more spherical particles are detected. This trend progressively changes when increasing the injection pressure, as the amount of non-spherical droplets decreases, obtaining the largest spherical droplet at a diameter of 125 µm for the 8 barG case. Increasing the injection pressure reduces the amount of ligament-shaped particles, increasing the sphericity of the droplet distribution. For that reason, also at the 8 barG case, the most probable diameters are located at a more spherical region of the map than compared with the low injection pressures.

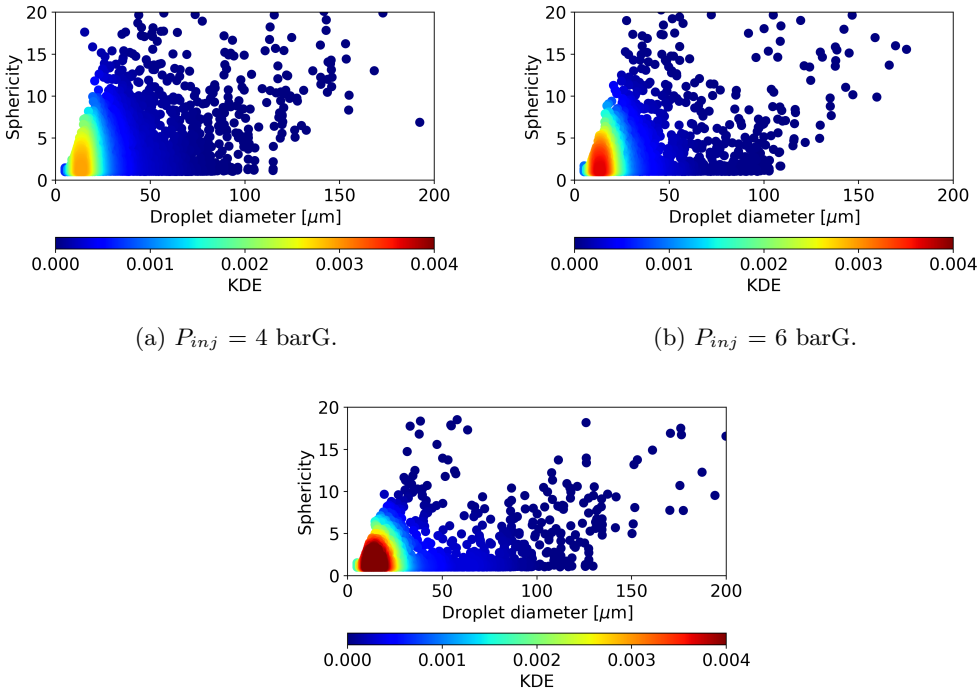

(a) $P_{inj} = 4$ barG.

(b) $P_{inj} = 6$ barG.

(c) $P_{inj} = 8$ barG.

Figure 5.35: Sphericity plots obtained at the three injection pressure conditions simulated.

Finally, the non-dimensional numbers of the generated droplets have been obtained to observe whether they will undergo secondary breakup. The We and Re numbers have been considered appropriate for this purpose, and the results have been included in Figure 5.36. As expected, with increasing injection pressure, the maximum value of both the Re and We increases due to the rise in characteristic velocity. The interesting parameter to be assessed is the We, indicating whether further breakup will occur. The maximum We value observed for the complete data set is close to 1, significantly lower than the threshold value of 12 needed to reach secondary breakup [10].

5.3.5 Coupling with DDM simulations

Other of the purposes of performing VOF simulations resides in not depending on previously obtained experimental data for its initialization either with prescribed droplet distributions or with experimental curves. The VOF approach

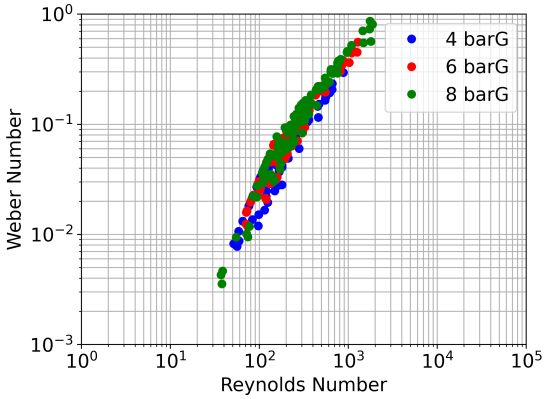

Figure 5.36: Non-dimensional numbers of the droplets obtained during the simulations.

can provide these initialization parameters within a computational framework based on a realistic representation of the injector body and its orifices. As the intention of the present thesis is to characterize the behavior of the SCR system as a whole, the studies included in the following chapters will be done on the far-field region of the injector, the droplet size distributions obtained in this chapter will be input into a DDM model. In this preliminary study, an initial DDM simulation will be performed to compare the droplet characteristics with the experimental data obtained through HRLBI at a distance of 30 mm, as the previous VOF simulations were only capable of capturing the dynamics up to 10 mm. In these DDM simulations, no cross-flow was considered but the gas temperature conditions set corresponded to the experimental ones. The computational model used will be the simplification of the injection test chamber used during the experiments (Figure 4.14b). Figure 5.37 compares the PDF and CVF curves for both methods. As expected, the coalescence and evaporation effects allow the diameter distributions to be more similar between both methods. Although the most probable diameter remains almost unaffected, the probability peak is significantly closer to the experimental value. The characteristic diameters up to *Dv50* are smaller in a magnitude around 10 µm respect to the experiments, although the 6 barG case deviates more at higher diameter values.

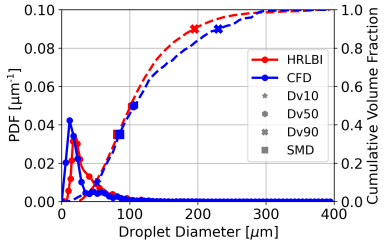

(a) P_{inj} = 4 barG.

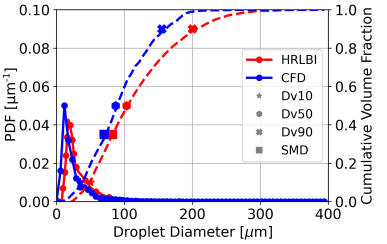

(b) P_{inj} = 6 barG.

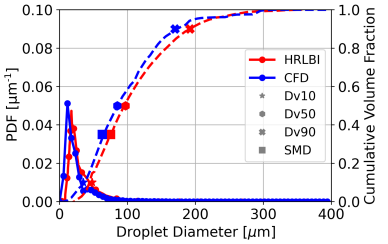

(c) P_{inj} = 8 barG.

Figure 5.37: Number-weighted PDF distribution and CVF comparison between experimental [2] and DDM approach captured at a distance of 30 mm of the injector position.

5.4 Conclusions

This section will summarize the main findings obtained during the studies done using the MM and VOF approaches. These will be grouped according to the methodology employed and the version of the geometry used.

5.4.1 Mixture Model approach

The simulations performed using the MM approach, applied to the *Generation 1* geometry, had as their main purpose to hydraulically characterize the injector of interest. Three different injection pressures were simulated to match the conditions at which these characteristics were obtained through experimental means. Two turbulence frameworks were used (RANS $k-\epsilon$ and LES), and their results were compared. A mesh of 0.8 million elements was enough to achieve a mesh independence, while a mesh of 8 million elements showed good quality indexes for the LES technique. The ROI values were accurately captured at all the injection pressure conditions for RANS and LES, but high

deviations were observed for the ROM results. The flow coefficients have also been obtained to assess the performance of the orifices and detect where the high deviation in ROM comes from. The computational results showed lower effective velocities on the nozzle, and higher effective area than in experiments, leading to a proper prediction of the ROI. However, on ROM, where velocity-dependence is larger, the obtained accuracy is lower. The breakup length was also obtained on the three orifices. A decreasing trend with higher injection pressures was captured, concluding that the injector was working within the first wind-induced regime, close to the second wind-induced regime. A qualitative relation was presented between the velocity RMS values and the breakup length. Differences in the spray morphology between the three orifices were detected, which were caused by the influence of the mesh orientation and the introduction of numerical viscosity within the solution. Additionally, the importance of performing a CT scan with enough spatial resolution was highlighted, as the zone prior to the orifices was approximated due to the lack of information in that region.

5.4.2 Volume-Of-Fluid approach

The VOF simulations performed aimed toward a further characterization of the injected spray. Pure H_2O was used instead of UWS due to the limitations of this technique. The experimental conditions were imposed into the simulations. Additionally, a high-fidelity geometry obtained through micro-CT means substituted the original geometry. The hydraulic characterization applied to this geometry returned good ROI results, and considerably better ROM values with reduced deviations. The spray morphology has been described, and the spray tip penetration has been compared against experimental results. The overall tip velocity was well-captured for the three injection pressures tested. No clear trend could be detected regarding the spray angle. An average angle of $\approx 15°$ in all conditions is obtained. Further analysis was done simulating solely one out of three orifices as no strong interaction between the spray plumes was observed at the furthest discharge volume distance. Droplet size and kinematics were extracted. The number-based PDF and CVF curves were compared to the droplet characterization obtained through HRLBI. VOF simulations returned a droplet distribution skewed toward a smaller diameter, with a most probable droplet of 8 µm, and a higher probability peak than experimental results. Additionally, the CVF curves showed a distribution representing smaller diameters for all cases. Hence, the characteristic diameters such as *Dv50*, *SMD*, and *Dv90* were smaller than the experimental ones. Volume-weighted PDF of the droplet diameter was also obtained, and good

agreement was found, indicating that the large mass and momentum-carrying droplets were properly characterized, considering the computational model validated.

The PDF and CVF curves of the three injection pressures were compared. The PDF curves showed little deviation, but greater differences were observed in the CVF. Increasing the injection pressure enhanced atomization as the characteristic diameters progressively decreased. The most common droplet was generated in the region closer to the orifices (2-6 µm). On the other hand, the largest droplets/ligaments appeared in the simulation at larger distances from the orifices. The PDF of two velocity components was obtained, showing the effect of increasing the injection pressure. A wide spectrum was observed for the droplets' velocity in the axial direction, while for the radial velocity, the values were centered around the null value. The sphericity of the droplets was also analyzed. Increasing the injection pressure enhanced the formation of spherical droplets, increasing the chance of finding low-diameter high-spherical particles. On lower injection pressures, the highest probability was located on low-diameter particles and sphericities ranging from the unit to a value of 5. The chance of secondary droplet breakup was analysed, but the low We number of the droplets was significantly lower than the threshold value for that phenomenon. To conclude the analysis, the droplet characteristics were introduced into a DDM model to compare again with experimental results. Coalescence and evaporation were observed to be of importance once the VOF droplets left the domain, as the PDF and CVF curves resulted more similar to experimental distributions at a distance of 30 mm to the orifices.

References

[1] Moreno, A. E. "Experimental Study of the Urea-Water Solution Injection Process". PhD thesis. Valencia (Spain): Universitat Politècnica de València, 2022. DOI: 10.4995/Thesis/10251/181637.

[2] Bracho, G., Postrioti, L., Moreno, A., and Brizi, G. "Experimental study of the droplet characteristics of a SCR injector spray through optical techniques". In: *International Journal of Multiphase Flow* 135 (2021), p. 103531. DOI: 10.1016/j.ijmultiphaseflow.2020.103531.

[3] Pope, S. B. "Ten questions concerning the large-eddy simulation of turbulent flows". In: *New Journal of Physics* 6 (2004), p. 35. DOI: 10.1088/1367-2630/6/1/035.

[4] Celik, I., Klein, M., and Janicka, J. "Assessment measures for engineering LES applications". In: *Journal of fluids engineering* 131.3 (2009).

[5] Payri, R., Bracho, G., Martí-Aldaraví, P., and Moreno, A. "Using momentum flux measurements to determine the injection rate of a commercial Urea Water Solution injector". In: *Flow Measurement and Instrumentation* 80 (2021). DOI: 10.1016/j.flowmeasinst.2021.101999.

[6] Mohapatra, C. K., Schmidt, D. P., Sforozo, B. A., Matusik, K. E., Yue, Z., Powell, C. F., Som, S., Mohan, B., Im, H. G., Badra, J., Bode, M., Pitsch, H., Papoulias, D., Neroorkar, K., Muzaferija, S., Martí-Aldaraví, P., and Martínez, M. "Collaborative investigation of the internal flow and near-nozzle flow of an eight-hole gasoline injector (Engine Combustion Network Spray G)". In: *International Journal of Engine Research* (2020), p. 1468087420918449. DOI: 10.1177/1468087420918449.

[7] Bender, E. "Numerical heat transfer and fluid flow. VonS. V. Patankar. Hemisphere Publishing Corporation, Washington - New York - London. McGraw Hill Book Company, New York 1980. 1. Aufl., 197 S., 76 Abb., geb., DM 71,90". In: *Chemie Ingenieur Technik* 53.3 (1981), pp. 225–225. DOI: 10.1002/cite.330530323.

[8] Kapusta, Ł. J., Sutkowski, M., Rogóż, R., Zommara, M., and Teodorczyk, A. *Characteristics of water and urea-water solution sprays*. 2019. DOI: 10.3390/catal9090750.

[9] Lin, S. P. and Reitz, R. D. "Drop and spray formation from a liquid jet". In: *Annual Review of Fluid Mechanics* 30.1 (1998), pp. 85–105. DOI: 10.1146/annurev.fluid.30.1.85.

[10] Lefebvre, A. H. and McDonell, V. G. *Atomization and sprays*. Second. Boca Raton, FL: Press, CRC, 2017, pp. 1–284. DOI: 10.1201/9781315120911.

[11] Marsden, A. L., Vasilyev, O. V., and Moin, P. "Construction of commutative filters for LES on unstructured meshes". In: *Journal of Computational Physics* 175.2 (2002), pp. 584–603. DOI: 10.1006/jcph.2001.6958.

[12] Sun, X., Yan, H., and Chen, F. "Numerical investigation of atomization of swirling liquid sheets using transforming algorithm". In: *International Journal of Multiphase Flow* 152 (2022), p. 104084. DOI: 10.1016/j.ijmultiphaseflow.2022.104084.

[13] Duke, D. J., Kastengren, A. L., Matusik, K. E., Swantek, A. B., Powell, C. F., Payri, R., Vaquerizo, D., Itani, L., Bruneaux, G., Grover, R. O., Parrish, S., Markle, L., Schmidt, D., Manin, J., Skeen, S. A., and Pickett, L. M. "Internal and near nozzle measurements of Engine Combustion Network "Spray G" gasoline direct injectors". In: *Experimental Thermal and Fluid Science* 88 (2017), pp. 608–621. DOI: 10.1016/j.expthermflusci.2017.07.015.

[14] Bracho, G., Postrioti, L., Moreno, A., and Brizi, G. "Experimental study of the droplet characteristics of a SCR injector spray through optical techniques". In: *International Journal of Multiphase Flow* 135 (2021), p. 103531. DOI: 10.1016/j.ijmultiphaseflow.2020.103531.

[15] Weglarczyk, S. "Kernel density estimation and its application". In: *ITM Web of Conferences* 23 (2018). Ed. by W. Zielinski, L. Kuchar, A. Michalski, and B. Kazmierczak, p. 00037. DOI: 10.1051/itmconf/20182300037.

Chapter 6

Analysis of the UWS far-field spray

"One man's 'magic' is another man's engineering."
—Robert Heinlein

6.1 Introduction

Although having characterized the spray in the near-field region, there are several phenomena that take place in the regions far away from the injector tip position, that have other temporal and spatial scales. This chapter aims to analyze the spray behavior on the far-field regions by describing its morphology and its droplet characteristics, in addition to understand the evaporation event, and assess parameters such as the injection angle to improve the generation of the desired NH_3. To achieve these objectives, the validation of the chemical model will be performed, together with a methodology for fitting the spray droplet size distribution in the case that no previous VOF simulations were carried out. The VOF results obtained in Chapter 5 have not been introduced as initial conditions for the simulations as those were not generated when performed this analysis. Afterwards, a study on the spray optimum angle will be applied. The experimental data provided for the far-field validation is obtained from the DBI technique applied by Moreno [1]. The knowledge acquired during this step will be later applied together with the VOF-DDM coupling into the CC-SCR geometry described during Section 4.3.

6.2 Validation of the chemical model

Reproducing the phase change of the water content and the degradation of the urea through thermolysis and hydrolysis is critical to properly capture the behavior of the SCR systems. The chemistry model used for the subsequent simulations has been validated against the results obtained through the experimental facility from Kim et al. [2]. The experimental facility employed during that study has been computationally reproduced and the experimental conditions have been introduced. The geometry consists of a cylinder with a diameter-to-length ratio of 0.046, and a duct diameter of 0.3 m. The injector is not located at the duct wall but on the center of the cylinder, at a distance of 0.5 m from the duct inlet. The composition of the UWS is not the usual mixture, but of a mass fraction of 40% of urea and 60% of water. The injection pressure of the spray is set to 14 bar, and different gas conditions were set, which are described in Table 6.1.

Gas Temp.	**Gas Vel. 1**	**Gas Vel. 2**	**Gas Vel. 3**
673 K	$10.8\,\mathrm{m\,s^{-1}}$	$8.3\,\mathrm{m\,s^{-1}}$	$6.0\,\mathrm{m\,s^{-1}}$
623 K	$10.8\,\mathrm{m\,s^{-1}}$	$9.1\,\mathrm{m\,s^{-1}}$	$6.4\,\mathrm{m\,s^{-1}}$
573 K	-	$9.0\,\mathrm{m\,s^{-1}}$	$6.6\,\mathrm{m\,s^{-1}}$

Table 6.1: Gas temperature and velocity conditions used to validate the proposed chemical model [2].

A mesh independence study has been performed, resulting in an optimum base element size of 0.03 m, resulting in a mesh with an starting number of cells of 150000 due to the triggering of the AMR on the velocity and density gradients that rises the number of elements up to a peak of 1 Million. The simulations have been first initialized without considering the presence of the spray, and then the UWS has been injected. Three measuring sections have been considered, located at the tail-end of the duct, at distances of 3.0 m, 4.5 m and 6.0 m from the injection point, replicating the regions where the conversion efficiency was analyzed during the experimental study. A schematic view of the model setup is included in Figure 6.1.

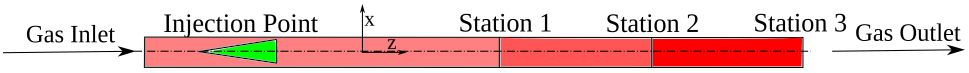

Figure 6.1: Schematic view of the validation geometry, and the corresponding ammonia measuring stations.

The results from the validation matrix have been included in Figure 6.2. In it, the NH_3 conversion efficiency (Section 4.5) is calculated at the three exhaust gas temperatures, and the three characteristic gas velocities. The x axis represents the residence time, which has been obtained based on the incoming gas velocity and the duct length, having an equivalent representation to the results shown by Kim et al. [2]. There is good agreement on the conversion efficiency at low gas temperatures, while on the high gas temperatures, deviations up to 20% can appear. The reason behind it might be the presence of both ammonia generation reactions at high temperatures, while at low gas temperatures only thermolysis is acting upon the droplets. Additionally, the Arrhenius expression that has been used for modeling the thermolysis does not consider any convective term, which could be affecting the results at high velocity conditions. Birkhold et al. [3] also showed deviations close to 25%, while other studies [4] showed discrepancies larger than 45% concerning Kim et al. data [2]. Based on these results, the model has been considered properly validated.

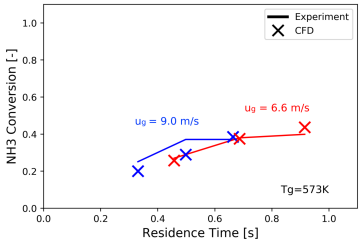

(a) 573 K.

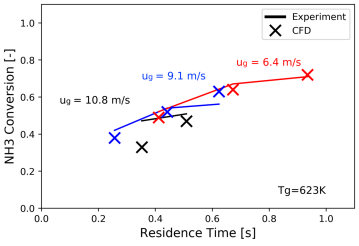

(b) 623 K.

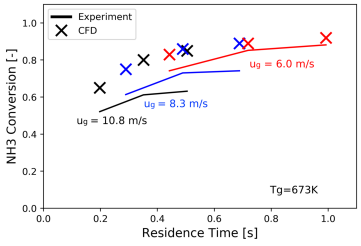

(c) 673 K.

Figure 6.2: Urea-to-ammonia conversion efficiencies for the conditions tested on Kim et al. work conditions [2].

Figure 6.3 shows the different transformations undergone by the UWS droplets on the validation simulations. Once the spray is injected into the do-

main, a sudden drop of gas temperature is expected due to the thermal energy transfer. The evaporation of water seen is faster at the pipe center, as the smaller droplets are the ones that suffer a faster phase change. On the spray outskirts, the evaporation of water takes larger times to occur. Figure 6.3b shows the production of HNCO, and allows locating the region where the thermolysis takes place, which is right after the injection point. Hydrolysis effects, on the other hand, can be seen in Figure 6.3c, which indicates the presence of NH_3. In that Figure, an increase in NH_3 content is seen where HNCO starts to appear (due to thermolysis), but a greater amount of NH_3 is observed at the end of the domain, indicating that the hydrolysis takes longer times to appear.

(a) Urea mass fraction.

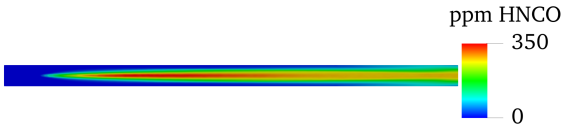

(b) Parts per million of HNCO.

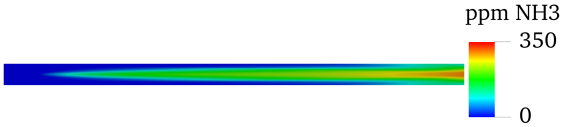

(c) Parts per million of NH_3.

Figure 6.3: Urea mass fraction, HNCO and NH_3 ppm contours for the 573 K and 6 m s^{-1} conditions.

6.3 Spray characteristics under cross-flow conditions

For the characterization of the far-field of the spray, the droplet characteristics used will not be related to the VOF simulations previously performed, but on data obtained at cross-flow conditions. To match the experimental

data obtained through DBI means [1], the parameters of a Rosin-Rammler distribution have been obtained.

Droplet characteristics have been obtained at three different windows of interest, P1, P2, and P3, as indicated in Figure 6.4. In that image the direction of the crossflow gases goes in the positive X direction.

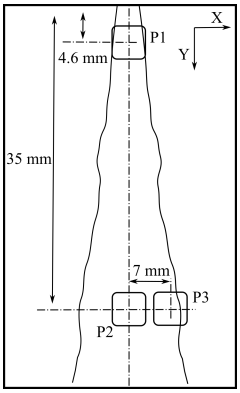

Figure 6.4: Location of the windows used for the droplet size and velocity calculations.

A Rosin-Rammler shape parameter of $k = 3$ has been chosen for the spray characterization campaign, as it is a common value on UWS studies [5]. The characteristic diameter values considered have been selected according to the injector orifice diameter d_0. From there, several simulations have been run considering the characteristic diameter as $0.6d_0$, $0.5d_0$, and $0.3d_0$ which corresponded to the distance between needle and seat, half the orifice diameter, and the narrowest gap within the injector. All three cases have been compared against experimental data in terms of drop size, and characteristic velocity in the cross-flow direction and injector axis. The corresponding results have been included in Figure 6.5, 6.6, and 6.7. These values have been obtained during the stabilized region of the injection curve for a specific injection pressure of 6 bar. The case of $0.5d_0$ shows the best agreement in terms of droplet sizing for P1, although for P2 and P3, the better agreement is obtained with $0.3d_n$. As observed during Section 5.3, the complete breakup of the liquid jet does not take place at the location of P1 (4.6 mm). Therefore, matching data at P1 is not accurate, as injected parcels will not undergo changes in their size characteristics, but experimental data will change when moving from P1 to P2. P2 is a more representative window for characterization of the spray as a completely atomized spray will be present there. With respect to P3, there is a general overestimation of small droplets, but the choosing of

the scale parameter has an effect, as the lower the parameter, the more the over-prediction of the small droplets. With respect to the droplet velocities, all conditions show considerable less velocity dispersion than experimental results. The peak velocity is captured at P1 and P2, while for P3, a bi-modal Y-velocity distribution is observed, though experimental data does not show that behavior. The reason for it lies in the over-representation of small droplets found in Figure 6.7a. These small droplets have transferred their initial momentum from the axial direction to the transverse direction thanks to the incoming hot gases. Hence, the axial velocity of those droplets is severely diminished. The largest droplets, on the other hand, are the most momentum-carrying particles, not losing so much momentum in the axial direction. The reason for the over-prediction of small droplets at P3 is due to the incapability of the experimental technique (DBI) [6] of detecting droplets smaller than 23 µm, and being capable of detecting only droplets present at the spray core due to the short camera-focused region. Due to the better agreement on a representative window as P2 on diameter and Y-velocity, the scale parameter $0.3d_n$ has been chosen.

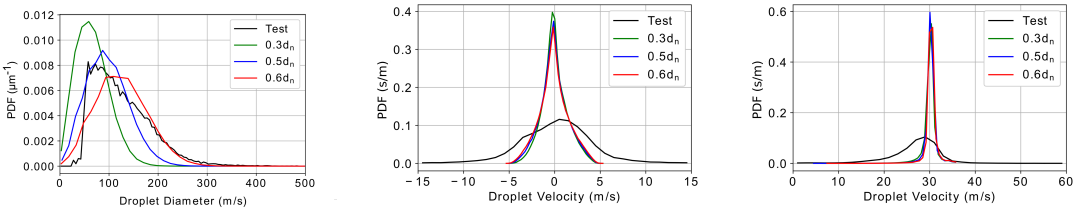

(a) Droplet diameter. (b) Spray transversal velocity. (c) Spray axial velocity.

Figure 6.5: Comparison of probabilities against experimental data for different RR scale parameters on P1.

6.3.1 Effect of the injection pressure

Three injection pressures have been tested, with values of 4, 6, and 8 barG. The comparison comprises the droplet size and velocity characteristics that were previously used to set up the DDM model. As P1 was shown not to be a representative window of the spray, the results have only been included for P2 and P3 regions.

The droplet diameters remain insensitive to injection pressure in the core region of the spray, P2, shown in Figure 6.8. This behavior was previously observed on the injection pressure study performed on the VOF simulations

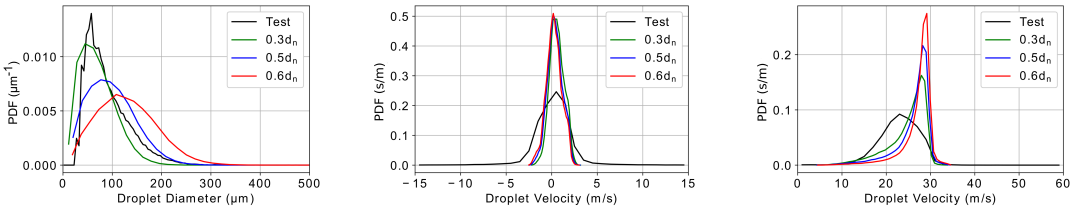

(a) Droplet diameter. (b) Spray transversal velocity. (c) Spray axial velocity.

Figure 6.6: Comparison of probabilities against experimental data for different RR scale parameters on P2.

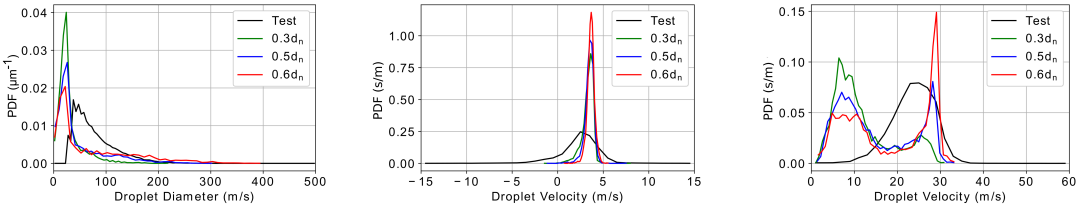

(a) Droplet diameter. (b) Spray transversal velocity. (c) Spray axial velocity.

Figure 6.7: Comparison of probabilities against experimental data for different RR scale parameters on P3.

(Section 5.3). Nonetheless, in the outskirts of the spray, P3, differences are observed. Lower injection presures produce a less pronounced probability peak. This implies the improvement in atomization of the spray with higher injection pressure. Effects on the axial velocity are observed on P2, similar to the velocity PDF plots observed with the VOF simulations (Figure 5.33b). Transversal velocities, on the other hand, show an increase in the dispersion of the curve with increasing pressures due to the larger velocity magnitude of the droplets, which implies a larger range of transversal component both in negative and positive velocities.

With respect to the PDF on the P3 window (Figure 6.9), the injection pressure affects the droplet size, increasing the injection pressure improves the droplet atomization, as the probability peak of small diameters is increased. Other differences are observed in the Y-velocity plot which, as expected, higher injection pressure implies higher maximum velocity in the axis direction.

The evolution of the spray droplet characteristic size has been done through a lateral projection of the spray, and interpolating the results into

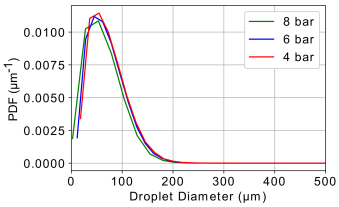

(a) Diameters.

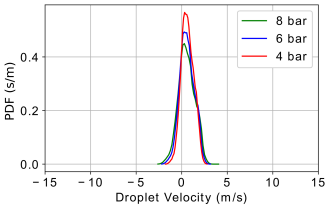

(b) Spray transversal velocity.

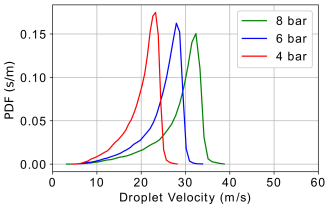

(c) Spray axial velocity.

Figure 6.8: PDF plots of the droplets diameters and velocities for three injection pressures, with air at 623 K and 40 kg/h of cross-flow, at the P2 window.

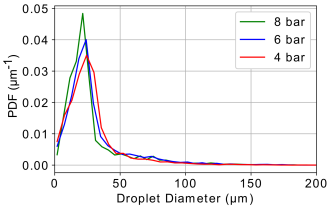

(a) Diameters.

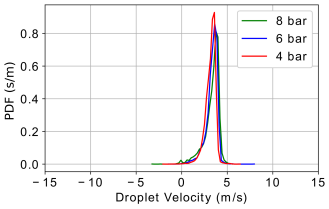

(b) Spray transversal velocity.

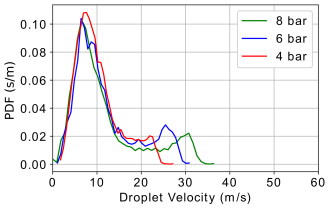

(c) Spray axial velocity.

Figure 6.9: PDF plots of the droplets diameters and velocities for three injection pressures, with air at 623 K and 40 kg/h of cross-flow, at the P3 window.

a uniform grid of 300x300 elements placed on the X-Y plane. In this mesh, the SMD has been obtained, and represented in Figure 6.10. Two main spray zones were detected, differentiated by their SMD. The spray core has SMD values larger than 120 µm, and it is linked with the injection pressure. At low injection pressure values, the droplets enter the domain with lower momentum, and acquire momentum toward the transversal direction driven by the cross-flow. That effect removes small droplets from within the core, increasing the SMD from that region. If the injection pressure is increased, the higher inertia of the droplets makes these small droplets to stay in the core region, decreasing its SMD. This is correlated to the amount of droplets that are found in the cross-flow direction, as with increasing injection pressure, less droplets can be found on the right side of the spray outskirts (P3) due to the higher momentum inferred in the injector.

The previously described effect can be confirmed by showing the dependency of the cross-flow velocity on the droplet diameter as done in Figure 6.11. In that representation, the dependency of the detected droplets

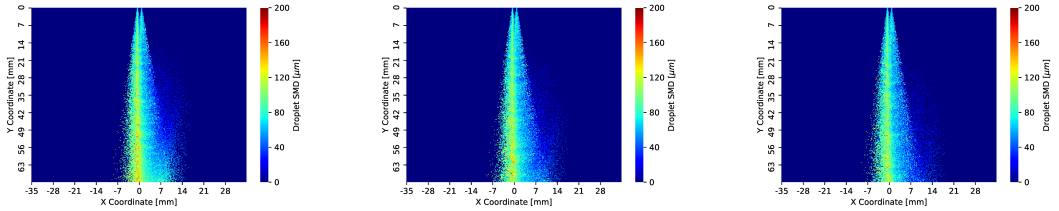

(a) 4 barG. (b) 6 barG. (c) 8 barG.

Figure 6.10: Two-dimensional SMD representation at three injection pressures and an exhaust gas temperature of 623 K and a gas mass flow rate of 40 kg/h .

on their transversal direction is shown. Based on the captured droplets, a regression curve that minimizes the error has been obtained and represented along the droplet cloud. The large droplets, which have higher inertia, almost do not acquire X-velocity values, while for smaller droplets (between 50 µm and 100 µm) the velocity range grows wider, more biased towards positive values of the spray transversal direction (in the cross-flow direction). With smaller diameters, the trend towards positive X-velocities grows stronger. On this data, an exponential decay regression has been applied. This allows to understand the greater SMD values located at the spray core, as the droplets located in here correspond to large-momentum-carrying particles.

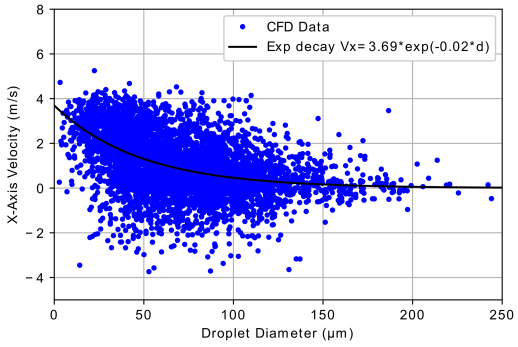

Figure 6.11: Droplet velocity on X-direction against the diameter, and the associated regression curve for 6 barG of injection pressure, 623 K and 40 kg/h .

6.3.2 Effect of the cross-flow velocity

Literature studies showed cross-flow velocities higher than the one introduced in the previous study [7]. It was of interest to analyse the influence of higher cross-flow velocities on the parameters studied. For it, a sole injection pressure was used (6 barG), and the air mass flow was increased to 200 kg/h and 400 kg/h .

As depicted in Figure 6.12, with respect to the PDF results on P2 location, the probability peak is translated toward larger diameters, with wider distribution as the cross-flow velocity increases. This is a consequence of the droplets being sweeped away from the spray axis due to the higher momentum transfer. Only the largest droplets, which carry the largest momentum tend to stay in the injector axis, implying that only large droplets will be found in this region. In P3 (Figure 6.13), the same trend is reproduced, as the smallest diameters have their trajectory bent in a more agressive way, skipping the P3 region.

When it comes to the velocity, the transversal velocity on the P2 window is shifted toward positive values, due to acquiring cross-flow momentum. The spray axial shows a bell-tightening trend with increasing cross-flow velocity. This is caused by the presence of large droplets in this region, while the small droplets, which would have lower spray axial velocities are out of the P2 window. Regarding the velocities at P3, the expected trend of increasing transversal velocity values is observed with higher air mass flow rates, and a relatable trend is found for the spray axial velocity with the trend found in P2.

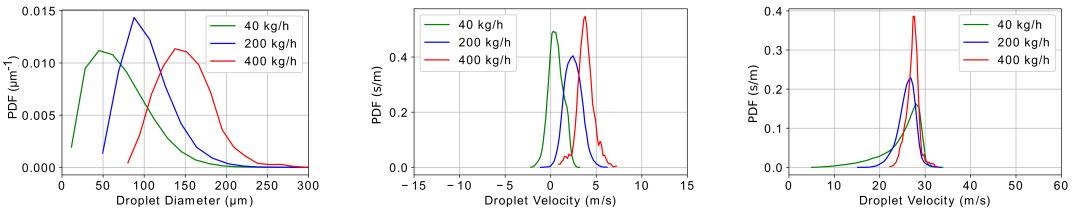

(a) Diameters. (b) Spray transversal velocity. (c) Spray axial velocity.

Figure 6.12: PDF plots of the droplets diameters and velocities for a injection pressure of 6 barG, with air at 623 K and three cross-flow velocities, at the P2 window.

This information has been complemented by the spatial depiction of the spray droplet sizes by means of the SMD representation in Figure 6.14. The

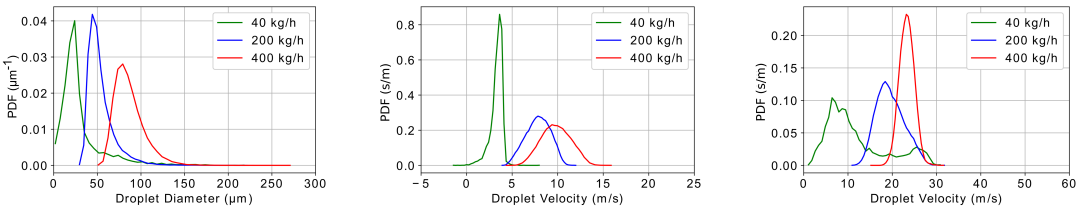

(a) Diameters. (b) Spray transversal velocity. (c) Spray axial velocity.

Figure 6.13: PDF plots of the droplets diameters and velocities for a injection pressure of 6 barG, with air at 623 K and three cross-flow velocities, at the P3 window.

SMD plots become more spatially discretized with higher cross-flow mass flow rates, as the largest droplets bend their direction less than the low-momentum carrying droplets. For the 200 kg/h case, the large droplets still remain on the injector axis location, but on the 400 kg/h case, they have been significantly bent as well. Nonetheless, the largest droplets still impact into the lower walls of the control volume.

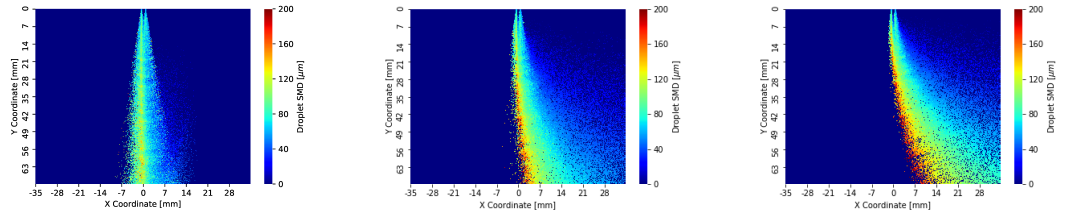

(a) 40 kg/h . (b) 200 kg/h . (c) 400 kg/h .

Figure 6.14: Projection of the SMD for 40 kg/h , 200 kg/h , and 400 kg/h for an injection pressure of 6 barG and air at 623 K.

6.4 Droplet evaporation dynamics

The water evaporation and urea degradation due to thermolysis have been proved to have little effect during the low residence times that the spray has in the test rig used during these simulations [8]. For that reason, a comparison between the PDF curves between inert and chemical models have not been included during this work. Nonetheless, it has been found useful to show the

droplet evaporation curves so to characterize the effect of the injection pressure at two different cross-flow temperatures, and to check that the evaporation profile follows the expected evolution from previous works [9].

6.4.1 Effect of the injection pressure

This approach has been carried out by tracking each droplet diameter throughout their lifetime, and the complete set of diameters has been averaged. The mean diameter has been normalized with the maximum mean diameter obtained in the simulation. The resulting temporal evolution is shown in Figure 6.15. Three specific regions can be detected from the temporal evolution of the simulation mean diameter. A rise of the droplet size is first observed, which is an effect of introducing a discrete distribution, which takes some time to become statistically representative. After reaching the maximum diameter value, a rapid decrease of the droplet size is observed, followed by a slower diameter reduction. These two slopes correspond to the water evaporation and the thermolysis reaction, respectively. The reaction enthalpy of water evaporation ($\approx$2300 kJ/kg) is lower than the thermolysis enthalpy ($\approx$3088 kJ/kg)[10], which explains the difference in droplet change rate. Additionally, when the water content of the UWS evaporates, the vapor pressure of the droplet decreases, leading to higher energy needed to achieve thermolysis. With respect to the effect of the injection pressure on the evaporation curve, although all three conditions show the same slopes, the 8 barG case starts its evaporation earlier than the other conditions. A faster penetration of the UWS spray increases the droplet Reynolds and Prandtl numbers, increasing the evaporation rate. On the low-temperature condition, the same conclusions can be extracted. Nonetheless, differences with respect to the 623 K case arises once the water has evaporated, as the slope of the curve is gentler for this low-temperature condition. This agrees with the outcomes from Yim et al. [11], which states that the complete decomposition of urea is only achieved at temperatures above 623 K.

The derivative of the previous curves has been computed to analyze the differences in evaporation rate of the droplets. The corresponding results are Figure 6.16. Although unnoticeable in the representation of the evaporation curves, the highest injection pressure shows a maximum absolute rate of diameter change for both temperatures. The rates found for the 623 K are consistently higher (in absolute terms) than the low temperature case (453 K).

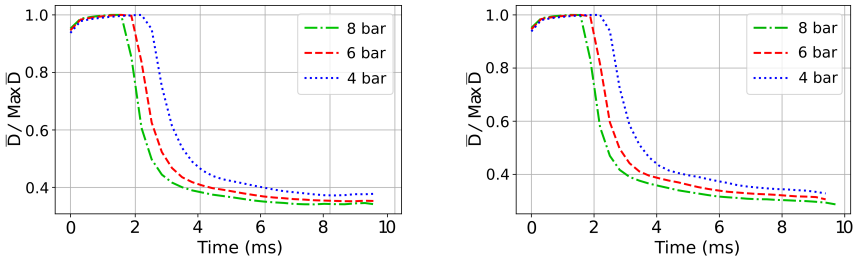

(a) 573 K. (b) 623 K.

Figure 6.15: Evolution of the mean droplet diameter with time at two gas temperatures.

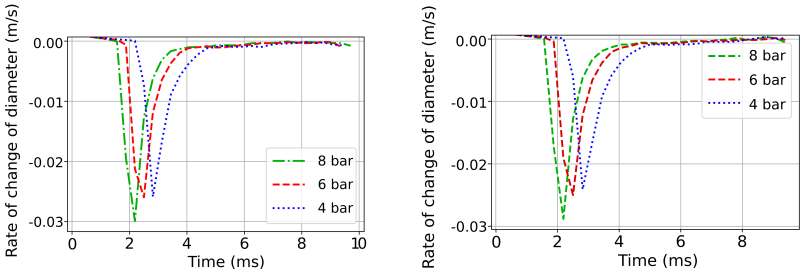

(a) 573 K. (b) 623 K.

Figure 6.16: Evolution of the rate of diameter variation with time at two gas temperatures.

6.4.2 Effect of the spray injection angle

Within SCR after-treatment, the inclination angle of the spray with respect to the exhaust gases has importance as it can promote o demote the generation of NH_3 from the UWS mixture [12]. With the objective of finding the relationship between the spray direction and the NH_3 generation, a computational campaign has been set up, ranging results from an angle of 90° (perpendicular to exhaust flow) to 30° (almost aligned with the flow direction). A visual representation of this approach has been included in Figure 6.17. In these simulations, no wall-impingement has been considered, but a vanishing condition is established.

First, a similar analysis to the one previously performed (Section 6.4) has been applied. In this case, two different injection angles have been considered

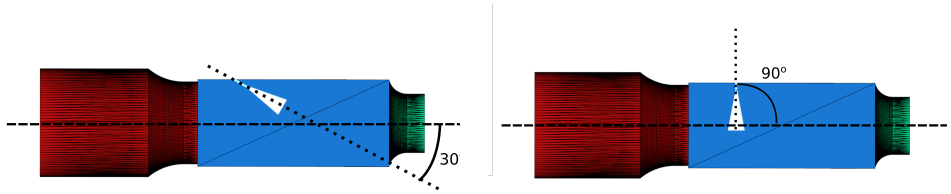

(a) 30°. (b) 90°.

Figure 6.17: Representation of the injector inclination angle.

(60° and 90°). Additionally, two ranges of droplet diameters have been considered to analyze differences between large and small droplets due to their different droplet surface areas. These results have been included in Figure 6.18. Three distinct slopes can be observed. At first, the droplet diameter diminishes due to the relatively fast water evaporation. The second slope is, as previously seen, where the urea starts to degradate. A later diameter reduction appears at 0.022 s due to the droplets leaving the computational domain. Higher injection pressures imply faster evaporation rates for all conditions due to the better atomization, specially when injecting at 90°. High injection angles represent a faster water evaporation for all cases due to largest convective effects. With respect to the discretization of the droplet diameters, larger droplets have a faster reduction in drop diameter than smaller droplets, which is caused by the larger exposed area of the high volume droplets. Once thermolysis starts, the evaporation slope becomes similar for both ranges. The faster evaporation with higher injector angles is due to the higher relative velocity in the cross-flow direction that enhances the convective evaporation effects.

The temporal evolution of the generated ammonia has been tracked along the simulation time to detect the effects of the injection conditions on the NH_3 generation. An initial analysis is performed by observing the NH_3 contours at several simulation times. Figure 6.19 depicts the location where the UWS droplets are present, and the concentration of NH_3. At t = 0.002 s the totality of the UWS parcels is present, while there is still no degradation of the urea content. At t = 0.010 s, a ñarge amount of the droplets has left the domain through the vanishing condition, while the droplets that remain in the injection chamber start decomposing and NH_3 starts to appear. At t = 0.018 s these droplets have largely decomposed. At further simulation times the amount of NH_3 will decay as it will rapidly leave the domain through the outlet boundary.

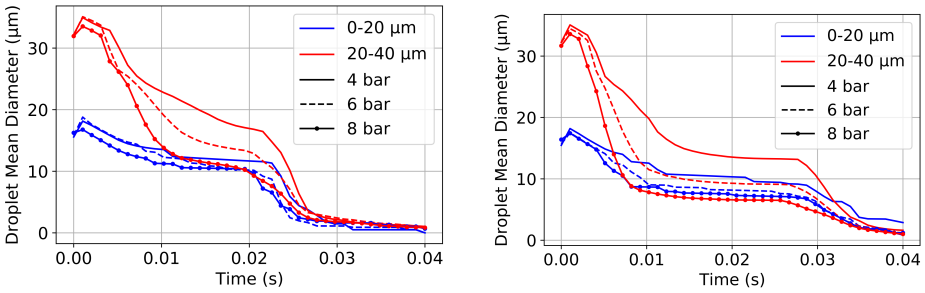

(a) 60°. (b) 90°.

Figure 6.18: Evolution of the droplet mean diameter for two characteristic sizes and for the two injector angles.

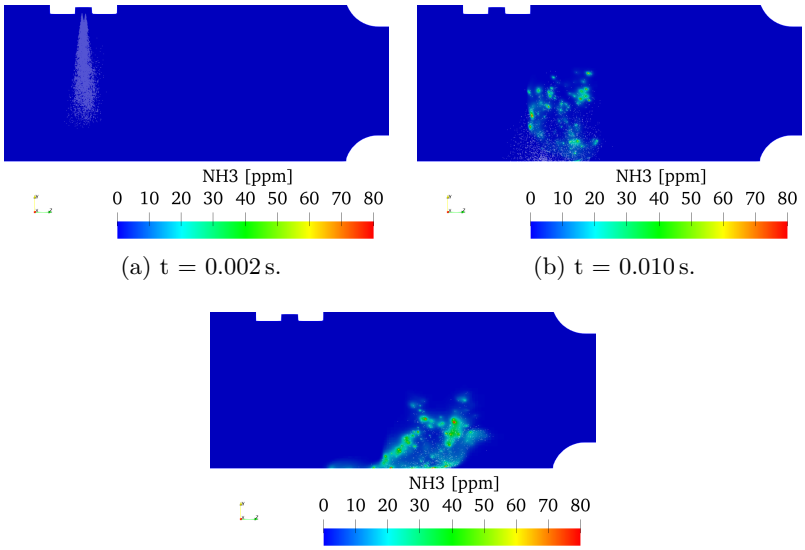

(a) t = 0.002 s. (b) t = 0.010 s.

(c) 0.018 s.

Figure 6.19: Evolution of the NH_3 ppm contours for different simulation times.

Figure 6.20 represents the NH_3 content within the domain. An increase in NH_3 content is observed with higher injection pressures. At the 90° case, the highest injection pressure shows lower NH_3 generated per injected mass than the 6 barG case. This is due to the spray reaching sooner the domain boundaries, leaving it and diminishing quicker the total NH_3 content. On the other hand, a higher generation rate is observed with higher injection pressures. With respect to the 60° case, a faster NH_3 growth is seen, although

the maximum value of NH_3 present during the simulation is lower than for the 90° case.

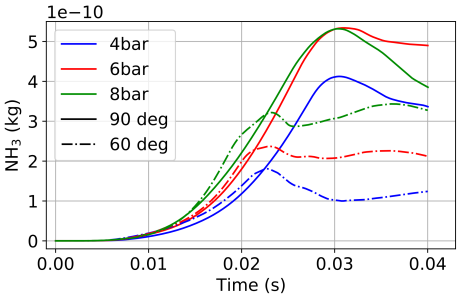

Figure 6.20: Temporal evolution of NH_3 content at different injection pressures and two injector angles, and a cross mass flow rate of 40 kg/h and a gas temperature of 623 K.

Figure 6.21 shows more clearly the effect of the injector angle on the NH_3 generation, for a given injection pressure. Two clear evolutions are observed. There is an increasing trend up to a maximum, and a decrease of NH_3 afterwards due to the droplets leaving the domain. No clear differences are observed in the slope of the NH_3 curves, but the disposition of the spray injector does affect the maximum NH_3 content found on the domain. Lower injection angles show the NH_3 peak earlier in time, although this effect is associated to the leaving of the UWS droplets through the outlet/boundaries. From 50° to 30°, the generation rates are reduced, indicating that the more coaxial the UWS is respect to the cross-flow gas direction, the higher the time the urea will need to decompose.

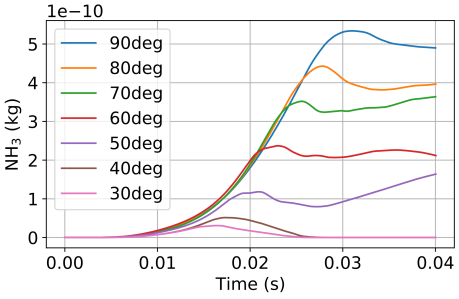

Figure 6.21: Temporal evolution of NH_3 content at different injector angles at a cross mass flow rate of 40 kg/h and a gas temperature of 623 K.

Lastly, the effect of the cross-flow velocity and gas temperature has been assessed. Due to the low urea decomposition occurring at a temperature of 623 K, a higher gas temperature has been included in the study (673 K). In Figure 6.22, a higher mass-flow rate (200 kg/h) and higher temperature case has been considered. For both mass flow rate cases, the amount of NH_3 increases with increasing the gas temperature to 673 K, both in the maximum value and the rate of generation. This rise in temperature decreases the density of the incoming air, augmenting the liquid-gas density ratio, speeding up the convective evaporation effects acting upon the droplets. This effect is seen on the location of NH_3 peak, which takes place earlier in time for the high temperature case. When it comes to the effect of the higher gas mass flow rate, a clear effect is seen, both in terms of the total amount of NH_3 in the domain and in the time needed for NH_3 generation. The increase in the relative velocity of the droplets respect to the gas accelerates the evaporation of water and the urea decomposition, although the total NH_3 is affected as the introduced droplets are washed away by the incoming flow.

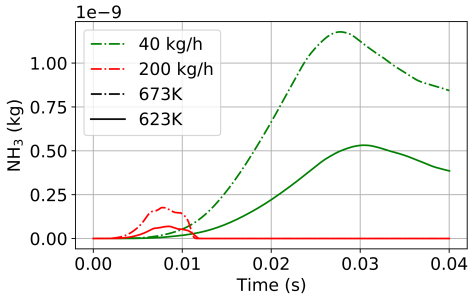

Figure 6.22: Temporal evolution of NH_3 content at different cross mass flow rates and gas temperatures, for an injector angle of 90°.

As the size of the computational domain limits the total amount of ammonia found within the domain, the rate of ammonia generation has been considered of greater use. In the region of ammonia increase of the domain, linearity has been assumed. A linear regression has been applied on the amount of NH_3 as function of time, and the slope of the curve is obtained. From each NH_3 curve, the largest region that provides an acceptable linear fitting (minimum fitting of >99%) has been considered. A visual example of the linearization procedure has been included in Figure 6.23. In order to avoid the effect of parcel vanishing through the domain outlet, the number of parcels present in the domain has been considered along the simulation time, determining that for the regions used for linearization, no significant creation/reduction of

parcels is taking place. The linear fitting shows a good overall determination coefficient (R^2), with a minimum value of 0.9917.

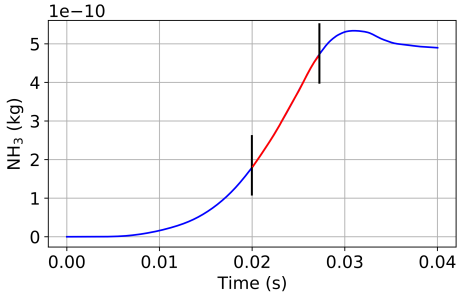

Figure 6.23: Snapshot of the linearization process of the NH_3 over time for a 90° injection angle, 40 kg/h of gas mass flow rate, and a gas temperature of 623 K. Region in red represents the linearized region.

Figure 6.24 shows the obtained NH_3 generation rate values for the different injection conditions used. For the low cross mass flow rate (Figure 6.24a), the maximum generation of NH_3 is achieved for the highest injection pressure condition, although the three injection pressures reach their maximum at an angle of 80°. The vanishing condition established on the geometry boundaries might be affecting the generation rate, as the spray in that situation would be highly oriented towards the lower chamber wall, leaving little time for the NH_3 to decompose in free-stream conditions. Orientating the injector towards the gas flow direction increases the residence time of the droplets in free-stream conditions, but due to the lower relative velocity between the droplet velocity and the one of the gas, the NH_3 generation rate is affected. At higher cross flow rates, the residence time of the injected droplets is diminished due to the higher momentum transfer and being dragged away. For low injector angles (30° and 40°), the NH_3 generation rate is higher than for the corresponding conditions at the 40 kg h^{-1}. For larger angle values, the NH_3 generation rates are lower than for the 40 kg/h case. This result, together with the evolution of the NH_3 content (Figure 6.22) indicates that the convective evaporation plays an important role in the urea degradation, although it gives the UWS droplets little time to evaporate and decompose. At high gas velocities, the effect of the injector angle becomes less critical. There is subtle generation enhancement up to an angle of 60°. For higher values, a uniform generation value is achieved. The effect observed at 90° for the 40 kg/h case is not observed as fewer droplets reach the bottom wall of the injection chamber.

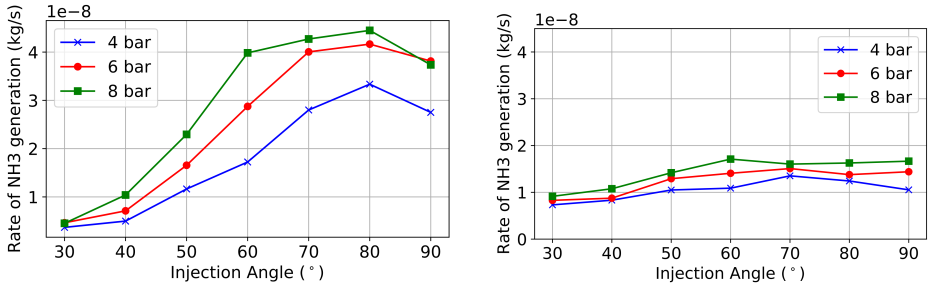

(a) 40 kg/h . (b) 200 kg/h .

Figure 6.24: Rate of NH_3 generation for the different injection angles at two characteristic gas mass flow rates.

Parameter	**Value**	
	623 K	**673 K**
K	$6.32 \times 10^{-5}\,K^{-1}\,Pa^{-1}$	$7.09 \times 10^{-4}\,K^{-1}\,Pa^{-1}$
α	0.542	0.496
β	1.23	1.04
γ	-0.48	-0.21

Table 6.2: Results from the correlation performed.

From these results, the dependency of the ammonia generation rate has been assessed through Equation 6.1 in order to obtain a semi-empirical expression for characterizing the NH_3 generation. In it, the exponential coefficients represent the dependency of the generation rate on that variable. The dimensional constant non-dimensionalizes the expression, hence acquiring the units of $K^{-1}\,Pa^{-1}$. The value of those coefficients was extracted by minimizing the Root Mean Square Error (RSME) obtained through the values of Equation 6.1. The results are presented in Table 6.2. The determination coefficient R^2 has been 0.84 and 0.705 for the 623 K and 673 K respectively, indicating that the correlation between these variables is not considerably strong. The NH_3 generation rate shows for both cases a linear relationship with the injection velocity ($u \propto \sqrt{P_{inj}}$). As expected, the injection angle shows the strongest relationship across both temperatures.

$$NH_{3,Rate} = f\left(P_{inj}, \theta, \dot{m}_f, T\right) = K P_{inj}^{\alpha} \theta^{\beta} \dot{m}_a^{\gamma} \tag{6.1}$$

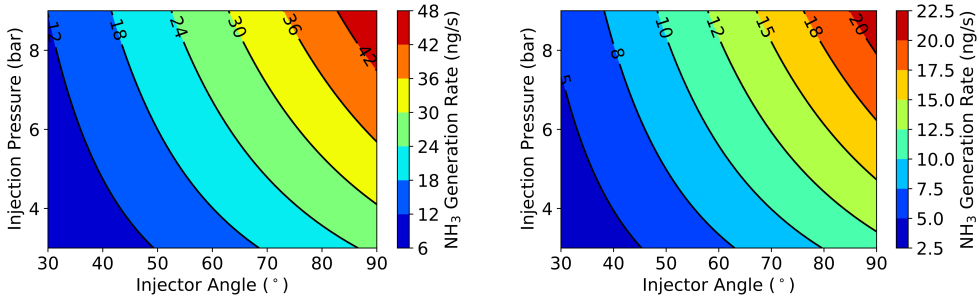

(a) 40 kg/h . (b) 200 kg/h .

Figure 6.25: Ammonia generation rate heatmaps obtained through the regression model.

Based on the previously obtained expression, a heatmap of ammonia generation rate was obtained as a function of the injection pressure and the injection angle. It allows to observe how the peak obtained at 80° is not captured by the regression model. Due to the negative dependency of the gas mass flow rate, the observed lower generation rates found for the 200 kg/h is captured by this semi-empirical expression.

6.5 Conclusions

During the present chapter, the far-field characteristics of UWS sprays have been assessed in different working conditions. The objective of the study was to obtain how the spray was affected by the exhaust and injector conditions.

First of all, a validation of the chemical model was performed against published experimental data. Good agreement in the conversion efficiency was obtained for low cross-flow velocities and low gas temperatures, while for increasing temperature and velocities, deviations were observed, matching conditions where both thermolysis and hydrolysis were present, achieving conversion efficiency values similar to other computational studies.

The velocity and size PDF were obtained at a certain distance from the injector location, and a Rosin Rammler distribution was introduced to match experimental data. Increasing the injection pressure showed trends similar to the ones obtained through the VOF method, with an almost unaffected number-weighted PDF and an increase of the injector axial velocity range with increasing injection pressure. Through an SMD analysis, two differentiated regions were detected. The spray core with a characteristic SMD larger

than 120 µm, and the outskirts, with smaller SMD values. Increasing the injection pressure diminishes the momentum transfer between the incoming cross-flow and the injected droplets, leading to a decrease the injector core SMD. Additionally, the effect on the SMD distribution was drastically modified by increasing the cross mass flow rate.

The water evaporation and urea thermolysis dynamics were analyzed, showing how using the *molten solid* approach, and according to experimentally obtained curves, the evaporation of water occurs at a faster rate than the thermolysis of the urea. Additionally, increasing the injection pressure, the water evaporation rate is increased for both gas temperatures tested.

The injector tilting angle has also been found to show an effect on the ammonia generation process. Several injector angles have been simulated, together with two cross air mass flow rates and gas temperatures to see their effect on the NH_3 generated. The injection angle showed effects on the droplet evaporation curve, being faster for the 90° case than for the 60° case. The largest droplets suffered a greater change in evaporation rate than the small injected droplets. The NH_3 generation rate was also affected by these parameters. The maximum rate was found for angles close to 80°, while for the high air mass flow rate case (200 kg/h), the maximum is obtained at 60°. Having a greater mass flow rate implied having an earlier generation of NH_3 and a higher generation rate of this compound at low injection angles, compared to the 40 kg/h case. From this data, a correlation was extracted, obtaining the influence of each one of the working condition parameters, indicating a linear dependency of the NH_3 generation rate with the spray injection velocity.

References

[1] Moreno, A. E. “Experimental Study of the Urea-Water Solution Injection Process”. PhD thesis. Valencia (Spain): Universitat Politècnica de València, 2022. DOI: 10.4995/Thesis/10251/181637.

[2] Kim, J. Y., Ryu, S. H., and Ha, J. S. “Numerical prediction on the characteristics of spray-induced mixing and thermal decomposition of urea solution in SCR system”. In: *Proceedings of the 2004 Fall Technical Conference of the ASME Internal Combustion Engine Division*. 2004, pp. 165–170. DOI: 10.1115/icef2004-0889.

[3] Birkhold, F., Meingast, U., Wassermann, P., and Deutschmann, O. “Modeling and simulation of the injection of urea-water-solution for automotive SCR DeNOx-systems”. In: *Applied Catalysis B: Environmental* 70.1-4 (2007), pp. 119–127. DOI: 10.1016/j.apcatb.2005.12.035.

[4] Raju, R., Chandran R, J., Salih, A., and Joseph, K. "Numerical analysis of mixing chamber non-uniformities and feed conditions for optimal performance of urea SCR". In: *Reaction Chemistry and Engineering* 5.12 (2020), pp. 2236–2249. DOI: 10.1039/d0re00269k.

[5] Varna, A., Spiteri, A. C., Wright, Y. M., Dimopoulos Eggenschwiler, P., and Boulouchos, K. "Experimental and numerical assessment of impingement and mixing of urea-water sprays for nitric oxide reduction in diesel exhaust". In: *Applied Energy* 157 (2015), pp. 824–837. DOI: 10.1016/j.apenergy.2015.03.015.

[6] Payri, R., Bracho, G., Gimeno, J., and Moreno, A. *Spray characterization of the urea-water solution (UWS) injected in a hot air stream analogous to SCR system operating conditions.* 2019. DOI: 10.4271/2019-01-0738.

[7] Rogóż, R., Kapusta, Ł. J., Bachanek, J., Vankan, J., and Teodorczyk, A. "Improved urea-water solution spray model for simulations of selective catalytic reduction systems". In: *Renewable and Sustainable Energy Reviews* 120 (2020), p. 109616. DOI: 10.1016/j.rser.2019.109616.

[8] Payri, R., Bracho, G., Martí-Aldaraví, P., and Marco-Gimeno, J. "Numerical Analysis of Urea to Ammonia Conversion in Automotive Selective Catalytic Reduction Realistic Conditions". In: *Industrial and Engineering Chemistry Research* 60.39 (2021), pp. 14329–14340. DOI: 10.1021/acs.iecr.1c02627.

[9] Wei, L., Youtong, Z., and Asif, M. "Investigation on UWS evaporation for vehicle SCR applications". In: *AIChE Journal* 62.3 (2016), pp. 880–890. DOI: 10.1002/aic.15078.

[10] Birkhold, F. *Selektive katalytische Reduktion von Stickoxiden in Kraftfahrzeugen: Untersuchung der Einspritzung von Harnstoffwasserlösung.* Aachen: Shaker Verlag, 2007.

[11] Yim, S. D., Kim, S. J., Baik, J. H., Nam, I. S., Mok, Y. S., Lee, J. H., Cho, B. K., and Oh, S. H. "Decomposition of urea into NH3 for the SCR process". In: *Industrial and Engineering Chemistry Research* 43.16 (2004), pp. 4856–4863. DOI: 10.1021/ie034052j.

[12] Prabhu S, S., Natesan, K., and Shivappa Nayak, N. "Effect of UWS spray angle and positioning of injector on ammonia concentration in Urea-SCR system". In: *Materials Today: Proceedings* 46 (2021), pp. 8051–8055. DOI: https://doi.org/10.1016/j.matpr.2021.03.026.

Chapter 7

Characterization of a CC-SCR

"Impossible is the word found only in a fool's dictionary. Wise people create opportunities for themselves and make everything possible..."
—Napoleon Bonaparte

7.1 Introduction

The models presented during the preceding chapters allowed to characterize the physical and chemical phenomena that a UWS jet undergoes from its injection point to its transformation into NH_3, without considering the effects of deposit formation. The knowledge acquired during these phases has been translated into a Close-Coupled (CC) SCR geometry, and the effect of the working conditions, together with the swirler typology is assessed. The impact of these variations has been analyzed. The simulations performed will cover a range of exhaust temperatures with a given exhaust mass flow rate. The spray droplet size distribution will be initialized from Volume-Of-Fluid data obtained at Section 5.3.

The study will start with the assessment of the LES index of quality for a specific working condition, and will be followed by the analysis of the effect of the temperature, the injection pressure and the swirler opacity on the variables of interest, which are the Uniformity Index (UI), the NH_3 conversion efficiency.

7.2 LES Index of quality

As it was performed during the study of the spray near-field, a preliminary study is performed to ensure that enough turbulent scales are solved during the LES approach with the generated mesh. Such indexes have been obtained once the flow solution has reached steady-state conditions. This steady-state has been assessed through the temporal evolution of the TKE, reaching an steady average value at t = 0.03 s. From there, the simulations have been run during 0.05 s. The definitions of Index of Quality introduced in Section 4.5 will be also employed in here, that is the criterion based on the resolved TKE [1], and the one based on the viscosity [2]. Three different sections of the geometry have been extracted to obtain the desired parameters. The first one is a plane that cuts the computational domain in a symmetrical way. The second one will be a cross-sectional plane right after the swirler geometry, where a large amount of turbulent structures are expected. The last one will be the entrance section to the catalyst. The parameters have been obtained at high temperature and high injection pressure conditions, with the baseline swirler (7 vanes).

When it comes to Pope's criteria, the Index of Quality contours are presented in Figure 7.1. With respect to the IQ in the symmetry section, there is an overall IQ value greater than 0.9 on the chosen planes. There is a low-quality region on the geometry inlet section, where no turbulence is expected. Regarding the section obtained after the swirler, again, there are enough turbulent structures solved along the section. On the wake region of the swirler, there are low-quality zones as the presence of the swirler would induce a large amount of small structures. This low-quality region is expected to grow in area in the most opaque swirler geometry (10 vanes). Nonetheless, these low-quality cells only account for the 5.5% of the cell count in each region. Finally, the outlet section of the computational domain shows high quality zones all along. Refining the swirler wake region would imply introducing a significant amount of cells that increase the computational cost of the simulations performed. Therefore, in general terms, the author considers the resolution of the proposed mesh to be sufficient for LES approaches.

The Index of Quality proposed by Celik has also been computed, and the results presented in Figure 7.2. As it happened for the previous quality index, the overall index of Quality matches Celik's criteria (0.75<IQ). The wake generated by the swirler geometry on Fig. 7.2b also drops the quality values, although they remain within acceptable limits.

Based on the presented quality contours, the introduced mesh to perform

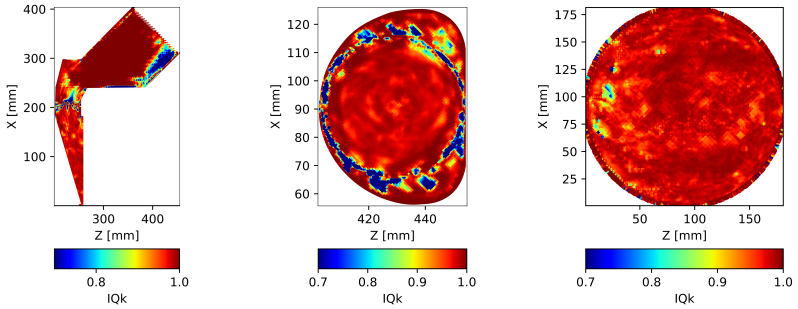

(a) Symmetry section. (b) After swirler section. (c) Catalyst entrance section.

Figure 7.1: Pope Index of Quality [1] contours obtained at three geometry sections at an exhaust temperature of 673 K, P_{inj}=8 barG, and a swirler with 7 vanes.

the subsequent analyses is considered to solve an enough portion of the turbulent energy generated, hence being acceptable for LES purposes.

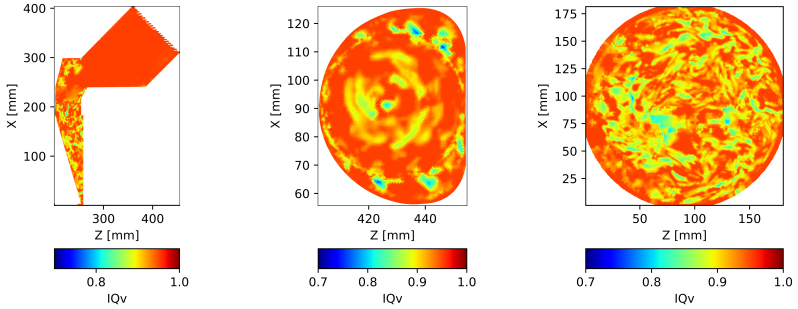

(a) Symmetry section. (b) After swirler section. (c) Catalyst entrance section.

Figure 7.2: Celik Index of Quality [2] contours obtained at three geometry sections at an exhaust temperature of 673 K, P_{inj}=8 barG, and a swirler with 7 vanes.

7.3 Analysis of the droplet size PDF

On SCR applications, the main reason for introducing a swirling element after the injection point and prior the entrance to the reduction catalyst is to trigger the secondary atomization of the injected UWS droplets and enhance the

evaporation of water and degradation of the urea into NH_3 through thermolysis. Additionally, its swirling vanes promotes turbulence after its location, which improves the mixing of the generated NH_3 with the exhaust gases [3, 4].

The first spray characteristic to be assessed during this chapter is the effect of the different working conditions set into the spray size distribution. A region of interest has been defined right after the location of the swirler geometry, as indicated in Figure 7.3. In it, the effect of the injection pressure, the exhaust temperature and the number of vanes of the swirler will be analyzed.

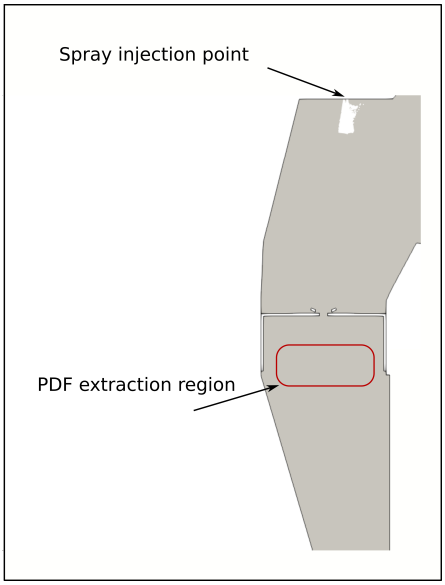

Figure 7.3: Definition of the region of interest for the extraction of droplet size PDF for the CC-SCR.

7.3.1 Effect of the injection pressure

The first analysis is performed on the effect of the injection pressure right after the swirler. The droplet size PDF results have been included in Figure 7.4. It is highlighted the differences between the PDF obtained at the injector exit on Section 5.3 (Figure 5.31), in which the peak PDF diameter was located at approximately 10 µm, while right going through the swirler geometry, the peak diameter is shifted to 0.4 µm. This represents a significant change in the size distribution, which highlights the performance of the swirler in further atomizing the injected droplets as secondary atomization was observed not to

happen due to the associated spray velocities. From the plot it can be deducted that when it comes to size PDF, the presence of the swirler homogenizes the shape of the curve for the simulated injection pressures, reaching all of them the same peak diameter, and the peak probability value.

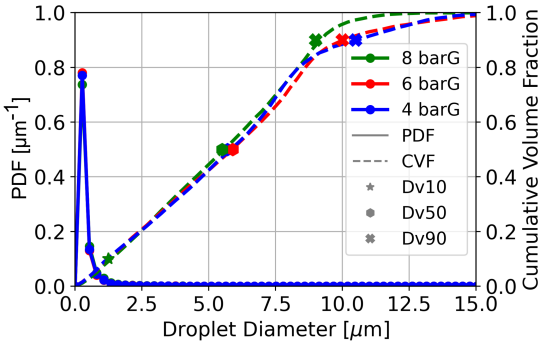

Figure 7.4: Droplet size PDF obtained for the three injection pressures of interest obtained at an exhaust temperature of 573 K, and a swirler composed of 7 blades for the CC-SCR.

7.3.2 Effect of the exhaust temperature

Temperature, on the other hand, does affect the size PDF distribution as observed in Figure 7.5 where the dependency of the number-based PDF results on the gas temperature is shown. The lowest exhaust temperature (473 K) shows differences in the distribution with respect to the highest temperature cases (573 K and 673 K). With increasing exhaust temperature, the most probable diameter remains unaltered for the three conditions tested, but the probability increases with the temperature. This indicates that further amount of urea content degrades when the temperature is increased, as expected. An additional reason for this behavior could be a different spray/wall interaction. At higher exhaust temperatures, the exhaust density decreases, and the spray accelerates. The higher We of the droplets could move its interaction regime from a partial deposition toward splash conditions, generating a set of smaller droplets. Differences are more visible in the volume distribution. While at 573 K and 673 K the CVF curves remain almost unaltered, it is at 473 K where the impingement regime with the swirler seems not to help as much with the secondary atomization.

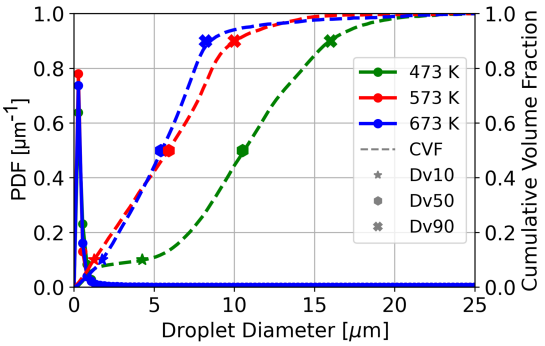

Figure 7.5: Droplet size PDF obtained for the three exhaust temperatures of interest obtained at an injection pressure of 6 barG, and a swirler composed of 7 blades.

7.3.3 Effect of the number of swirler blades

The last parameter to assess is the number of blades of the swirler geometry. The effects caused upon the PDF distribution are presented in Figure 7.6, where it can be observed that increasing the solidity (ratio of blade width and number of blades) increases the probability of finding small droplets in addition to locating a larger proportion of the spray volume in smaller diameters. A high-solidity swirler promotes the secondary atomization of the spray, as it rises the probability peak of the most common diameter, decreasing the probability of droplets larger than 1 µm of diameter. It is highlighted that for a swirler consisting of 7 blades and more, the differences between the spray droplet characteristics are negligible when it comes to the number PDF, while it still sees an improvement in the CVF curves.

7.4 Analysis of the ammonia generation

The following study performed based on the SCR simulations was to observe the differences in the NH_3 generation, in addition to the depicted differences within the droplet size PDF.

An initial analysis is done on the regiones where NH_3 is being generated, and to assess how the swirler helps in that purpose. Figure 7.7 shows the temporal evolution of the NH_3 contours for a specific working condition. It is highlighted the bending of the injected spray in the first milliseconds of injection caused by the flow coming from the DOC. This has an effect on the impacting region of the droplets which is displaced from the swirler center.

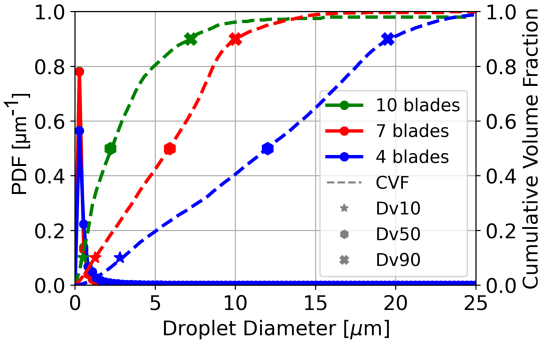

Figure 7.6: Droplet size PDF obtained for the three swirler geometries of interest obtained at an injection pressure of 6 barG, and a exhaust temperature of 573 K.

Once the spray has impinged with the swirler and domain walls, triggering secondary atomization events, NH_3 starts to appear in the computational domain. Largest NH_3 generation region takes place where tight spaces between the swirler and domain boundaries are located and highest gas speeds are found. At t = 0.0115 s, most of the droplets have gone through the swirler section already as not such uniform NH_3 contour is found after the swirler. Nonetheless, the regions in which droplets have impinged and formed liquid film keep decomposing their urea content.

Two different parameter will be analysed. The first will be the peak of NH_3 present in the domain compared to the potential NH_3 that would be present if all the urea would degrade through thermolysis, and the secondary NH_3 pathway (hydrolysis).

7.4.1 Amount of ammonia present within the domain

The results shown in Figure 7.8 correspond to the peak NH_3 value detected within the simulations compared to the potential NH_3 that would be present if complete thermolysis and hydrolysis were achieved. In it the effect of the gas exhaust temperature, the injection pressure and the number of vanes of the swirler can be observed. It is highlighted how the exhaust temperature plays an important role in the amount of NH_3 that is generated. Compared to the 673 K, the case with lowest gas exhaust temperature (473 K) shows little amount of NH_3. According to literature, urea melts and degrades when acquiring a temperature of 406 K [5], which is consistent with results obtained

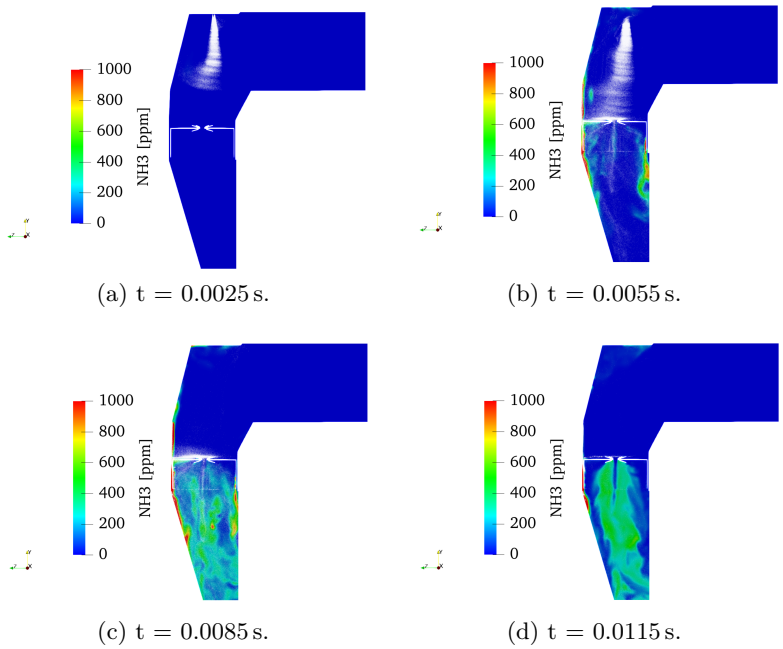

(a) t = 0.0025 s. (b) t = 0.0055 s.

(c) t = 0.0085 s. (d) t = 0.0115 s.

Figure 7.7: Temporal evolution of the NH_3 contour for an exhaust temperature of 673 K, an injection pressure of 6 barG and a 10-blade swirler.

at 473 K, although generating low amounts of NH_3. Increasing the exhaust temperature progressively increases the quantities of NH_3.

The second effect observed is of the injection pressure, which is not as evident as the effect of the gas exhaust temperature. There is not a clear trend in the generated NH_3, as in general terms, there is a decrease in NH_3 when moving from 4 barG to 6 barG, and a slight increase again when moving from 6 barG toward 8 barG. This is possibly due to effects in residence time of the injected droplets into the domain. Low injection pressures have associated low initial velocities and a larger residence time, hence larger possibilities of urea degrading. At high injection pressure, the convective effects play an important role in the water and urea phase change, increasing again the amount of NH_3 present.

At last, the effect of the number of blades of the swirler is assessed. A clear trend is seen, as for increasing the number of vanes, a higher amount of NH_3 is observed. This effect can be compared with the previous droplet size PDF results, in which an effect was observed from a swirler made of 4 blades to one of 7 blades, but no further effects were seen on a 10-blade swirler. Here,

moving to a 10-blade swirler changes the amount of NH_3. This trend takes place due to the change in NH_3 generation rate.

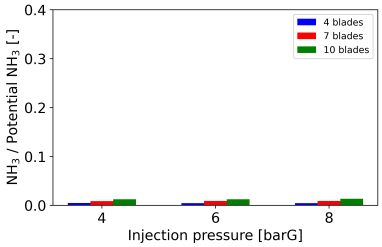

(a) 473 K.

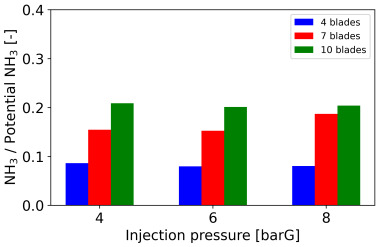

(b) 573 K.

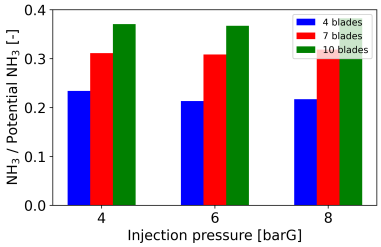

(c) 673 K.

Figure 7.8: Peak NH_3 amount during the SCR simulations for three injection pressures, three exhaust temperatures, and a swirler with different number of vanes.

7.4.2 Effect on the ammonia generation rate

The NH_3 generation rate is also assessed on the injection conditions previously depicted. The results are shown in Figure 7.9. Similar trends to the ones previously observed are obtained. The lowest gas exhaust temperature depicts the lowest generation rates from all the tested conditions. This contributes to the idea that, although at that temperature urea is degrading, it is doing so in a slow way. Once the exhaust gas temperature is increased, so it does the NH_3 generation rate.

Additionally, a clear tendency is captured with the injection pressure, as it continuously increases with higher values. This indicates that, although depicting similar droplet size PDF, the amount of droplets increases as the total injected mass increases with higher injection pressures (for a fixed injection time).

Finally, an increase on the NH_3 generation rate is achieved with a larger amount of swirler blades. A more solid swirler geometry makes the injected droplets more prone to impacting against it, and making the secondary atomization more plausible. Another effect of increasing the number of blades of the swirler is the enrichment of swirling motion inducted to the exhaust gas, which enhances the mixing of the gas phase with the atomized jet, which will have a beneficial effect on the degradation of the urea content of the droplets.

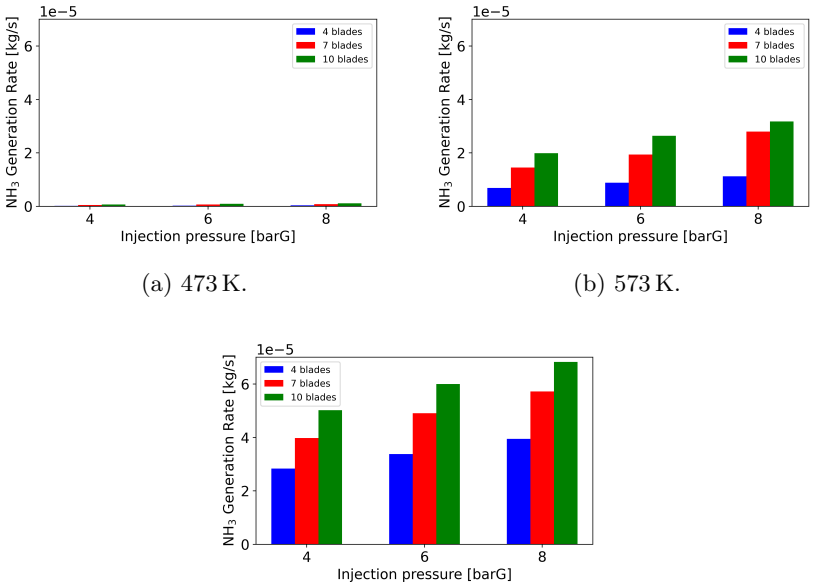

(a) 473 K.

(b) 573 K.

(c) 673 K.

Figure 7.9: NH_3 generation rate for three injection pressures, three exhaust temperatures, and a swirler with different number of vanes.

Increasing the number of blades of the swirler geometry does show a beneficial effect both in the total mass of NH_3 obtained and on the speed of its generation. Nonetheless, increasing the number of vanes will also act detrimentally on the exhaust pipe, as it will increase the counter-pressure on that section, and will increase its pressure drop [6]. Hence, that additional effect should be taken into account when designing deNOx after-treatment systems.

Additionally, increasing the number of blades in the swirler will also increase the area available for the incoming spray to impact into. Therefore, an increase in wall film mass is expected. As only one injection has been considered during this study, and the relative high temperatures of the swirler

surfaces, no deposition is expected to take place. Therefore, the total number of parcels that impacted into the surface was analyzed for a specific working condition. These results are shown in Table 7.1, and indicate that when increasing the number of blades of the swirler so it does the amount of liquid mass that impacts it along the injection event. On single injection events, liquid deposition does not imply deposition risks, due to the high temperature of the surface. But on multi-injection events, continuos impacting of the liquid particles into the swirler would subsequently decrease the wall temperature, making the system more prone to liquid deposition and hence, deposit generation.

Swirler	Total Impacted Mass
4 blades	2.99×10^{-6} kg
7 blades	3.767×10^{-6} kg
10 blades	3.92×10^{-6} kg

Table 7.1: Total impacted liquid mass into the swirler surfaces for an exhaust temperature of 573 K, and an injection pressure of 6 barG.

7.5 Analysis of the Uniformity Index

Achieving a uniform distribution of the desired NH_3 in the entrance into the reduction catalyst is of great importance, as it will ensure a better utilization of the entire monolith for reducing NOx. That is the reason why mixers are included in these systems, apart from triggering secondary atomization on the UWS jet.

For that reason, a measure of how well the generated NH_3 is distributed at the SCR has been included in the study. The Uniformity Index (UI) has been calculated for the detected NH_3 at the section that represents the entrance to the reduction catalyst.

Figure 7.10 shows the results of that calculation for all the conditions tested during the simulation campaign. All the conditions show a UI value close to the unity, indicating that independently on the number of vanes, placing a swirling structure allows having a significantly homogeneous NH_3 distribution. Increasing the number of swirler blades homogeneizes the NH_3 distribution along the domain as it has a better mixing performance than the swirlers with lower number of blades.

The effect of the injection pressure is almost negligible in the UI values, but the temperature seems to affect in some way the results. For example, at

higher temperatures, the UI of the 4-vane swirler seems to diminish from the lower temperature case. As observed, at the low-temperature, low-number-of-blades, the generation of NH_3 is really low, showing a NH_3 distribution very uniform at the SCR entrance (with close-to-zero values). At high temperatures, the NH_3 starts to appear in significant amounts, hence reducing the UI. In the cases with higher amount of blades, this effect is not as noticeable because, as observed, a higher amount of blades promotes the generation of NH_3 for all the cases.

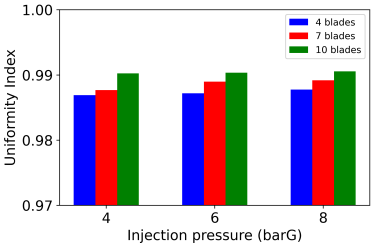

(a) 473 K.

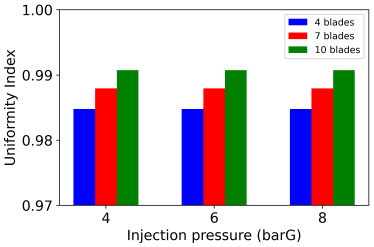

(b) 573 K.

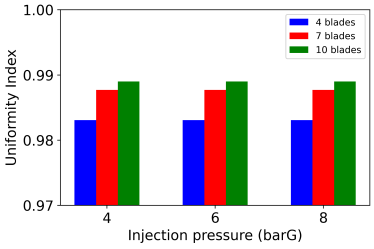

(c) 673 K.

Figure 7.10: Peak UI achieved during the SCR simulations for three injection pressures, three exhaust temperatures, and a swirler with different number of vanes.

7.6 Conclusions

During the present chapter of the thesis, the knowledge acquired during the previous chapters was applied to a realistic NOx after-treatment system. The associated geometry was recreated through computational means and introduced into the computational model. The aim of the study was to assess the effect of different working conditions on the NH_3 generation, and analyze the influence of the swirler into that process.

The spray characteristics obtained through VOF means were introduced into a DDM model in order to characterize sprays with injection pressures ranging from 4 barG to 8 barG. Different gas exhaust temperatures were introduced (473 K, 573 K and 673 K), and the number of blades the swirler was composed of was also varied, going from 4 blades, 7 blades and a geometry composed of 10 blades.

As a LES approach was carried out, the characteristic Index of Quality proposed during Chapter 4 was obtained at three different sections of the geometry. Both indexes returned acceptable results on all the critical regions, except for the wake of the swirler. In it, the index based on the TKE showed defficiencies that would require introducing a significant amount of cells to achieve high IQ values in a region where there is almost null velocity.

The first of the analyses assessed the effect of the working conditions on the droplet size distribution in a region located after the position of the swirler. The effect of the injection pressure was firstly obtained, which indicated that the swirler homogeneized the droplet size distribution to a single curve, independently of the injection pressure. Additionally, if compared to the droplet size PDF obtained at Chapter 5, the most common droplet is centered at droplet sizes lower than 1 µm, which is significantly lower than the outcomes obtained through VOF means. The exhaust gas temperature, on the other hand, did have an effect, shifting the PDF curve toward smaller diameters when increasing the gas temperature. This gave an insight about in which conditions did the urea start to decompose in a significant way. Finally, increasing the number of blades of the swirler promoted further secondary atomization of the injected spray as it increased its opacity, and the cross-sectional area available for the droplets to impact upon. Nonetheless, across all cases, the most probable diameter remained unaltered.

The second analysis was performed on the NH_3 content generated during the simulations. The maximum amount of NH_3 observed was associated to the high temperature, high injection pressure and high-solidity swirler geometry. For the low-temperature case almost no conversion of NH_3 is produced compared to the high-temperature case, indicating that at 473 K conditions, urea degradation happens, but not in a significant way. The rate of NH_3 generation was also analyzed, and relatable results to the peak NH_3 were achieved. The higher temperature, as expected, speeds up the degradation process, as expected. But it is highlighted how the larger impact surface of the 10-blade swirler also promotes the urea decomposition due to improved breakup and a better mixing of the liquid phase with the exhaust gas. As a downside of swirler geometries with high impact areas are the higher amount

of liquid phase that sticks to the swirler, which has a potential of forming solid deposits.

Lastly, the Uniformity Index (UI) was assessed for all the conditions depicted, showing a clear effect on increasing the number of blades of the swirler, which improved the homogeneity of the NH_3 present at the entrance of the SCR catalyst.

References

[1] Pope, S. B. "Ten questions concerning the large-eddy simulation of turbulent flows". In: *New Journal of Physics* 6 (2004), p. 35. DOI: 10.1088/1367-2630/6/1/035.

[2] Celik, I., Klein, M., and Janicka, J. "Assessment measures for engineering LES applications". In: *Journal of fluids engineering* 131.3 (2009).

[3] Tan, L., Feng, P., Yang, S., Guo, Y., Liu, S., and Li, Z. "CFD studies on effects of SCR mixers on the performance of urea conversion and mixing of the reducing agent". In: *Chemical Engineering and Processing-Process Intensification* 123 (2018), pp. 82–88.

[4] Mehdi, G., Zhou, S., Zhu, Y., Shah, A. H., and Chand, K. *Numerical Investigation of SCR Mixer Design Optimization for Improved Performance*. 2019. DOI: 10.3390/pr7030168.

[5] Börnhorst, M. and Deutschmann, O. "Advances and challenges of ammonia delivery by urea-water sprays in SCR systems". In: *Progress in Energy and Combustion Science* 87 (2021), p. 100949. DOI: 10.1016/j.pecs.2021.100949.

[6] Zhang, C., Sun, C., Wu, M., and Lu, K. "Optimisation design of SCR mixer for improving deposit performance at low temperatures". In: *Fuel* 237 (2019), pp. 465–474. DOI: 10.1016/j.fuel.2018.10.025.

Chapter 8

Maximum entropy principle applied to UWS sprays

"Science can amuse and fascinate us all, but it is engineering that changes the world."
—Isaac Asimov

8.1 Introduction

As introduced in previous chapters, computational studies applied to sprays commonly use Eulerian-Lagrangian frameworks to represent the dispersed liquid phase. Under this framework, breakup models represent the jet breakup under several conditions, without needing a pre-defined distribution or simulating the near-field spray to obtain the breakup characteristics. A second approach during this Thesis is VOF simulations, but they result in complex models that require considerable computational resources [1]. The DDM breakup models commonly used for Eulerian-Lagrangian spray applications (KH-RT [2], TAB [3]) do not perform well under low-velocity sprays, such as typical UWS jets [4]. Additionally, due to the low We associated with the droplets formed during the primary breakup phase, secondary breakup models do not depict any breakup. Therefore, a third approach can be employed, which uses pre-defined droplet size distributions obtained through previous experimental work carried out on characterizing the spray droplets [5]. This Chapter will introduce the Maximum Entropy Principle (MEP) as an alternative model

to generate an initial droplet distribution from initial injection data, detect subsequent droplet breakup and will apply it to UWS sprays to assess its performance.

8.2 Theoretical background of the MEP

The application of the MEP approach to atomization and sprays gained popularity in the mid-1980s and was initially applied to sprays by Xianguo and Tankin [6] and Sellens and Brzustowski [7]. It considers that the distribution that maximizes the system's entropy while satisfying a set of imposed conditions is the most probable joint distribution that describes the system. In that sense, it does not try to characterize the deformation and breakup instabilities but focuses on their possible outcomes by employing limited information regarding the spray of interest. Several work has been carried out by Sellens [7, 8], Li and Tankin [6, 9] in order to define the appropriate constraints that the MEP formulation needs to consider. The first author considered separate constraints for the kinetic energy and surface energy conservation, while Li and Tankin considered a unique energy conservation constraint. Both of them consider the joint size-velocity probability distribution. Some studies claimed that the prediction of the droplet size was independent of the velocity distribution [10], which has been classically adopted for simplification purposes. Experimentally, this assumption is proven wrong through Hsiang and Faeth's outcomes [11], which established a non-linear relationship between the formed droplet size and velocity. Guildenbecher et al. [12] also indicate that the velocity distribution shrinks with increasing droplet size. Some other work such as performed by Dumouchel [13, 14] was more based on information theory rather than not on thermodynamics. In them, a single constraint with two parameters were introduced, the value of the constraint diameter, and the value of its order. Later work from Dumouchel introduced a new formulation through which it was concluded that a minimum of three parameters are necessary to represent a spray droplet size distribution. The reader can refer to the work of Dumouchel [15] to acquire a general vision of the different MEP models used to predict drop size distributions. Due to the extensive use of the Li and Tankin approach, their approach has been adopted for this work.

In order to formulate the MEP equations, the stochastic nature of the breakup process needs to be understood, indicating that the outcomes from a specific breakup event are indeed random. Despite this random nature, the general conservation equations need to be satisfied. These equations are formulated based on the joint probability density function p_{ij}, representing the

probability of finding a droplet with volume V_i and velocity u_j. Mass, momentum, and energy conservation equations are given by Eq 8.1, Eq 8.2, and Eq 8.3, respectively. In addition to these equations, the sum of all probabilities should be the unit (Eq 8.4).

$$\sum_i \sum_j p_{ij}\, V_i\, \rho\, \dot{n} = \dot{m}_0 + S_m \tag{8.1}$$

$$\sum_i \sum_j p_{ij}\, V_i\, \rho\, \dot{n}\, u_j = \dot{J}_0 + S_{mom} \tag{8.2}$$

$$\sum_i \sum_j p_{ij}\, \dot{n}\, \left(V_i\, \rho\, u_j^2 + 2\sigma\, A_i\right) = \dot{E}_0 + S_e \tag{8.3}$$

$$\sum_i \sum_j p_{ij} = 1 \tag{8.4}$$

In them, $\dot{n}$ represents the droplet generation rate, $\dot{m}_0$ is the mass flow rate, while $\dot{J}_0$ and $\dot{E}_0$ are the momentum and energy entering the control volume. S_m, S_{mom}, and S_e are the mass, momentum, and energy equation source terms. Additionally, it has been assumed that the ambient velocity is null and that all droplets will be considered spherical, as the characteristic droplet We is expected to be lower than 12 [16]. From this point, in order to predict the droplet diameter distribution, a variable change is performed from volume to diameter ($V = \pi D^3/6$).

As stated, from the range of possible distributions that satisfy the previous conservation equations, the most probable would be the one that maximizes the entropy, that is, the one that maximizes Shannon entropy [17] defined in Equation 8.5.

$$S = -K \sum_i \sum_j p_{ij} \ln p_{ij} \tag{8.5}$$

The Shannon entropy is then maximized through the Lagrangian multiplier method [18], resulting in a continuous PDF with a shape indicated by Eq 8.6.

$$f = 3\bar{D}^2 \exp\left[-\lambda_0 - \lambda_1 \bar{D}^3 - \lambda_2 \bar{D}^3 \bar{u} - \lambda_3 \left(\frac{\bar{D}^3 \bar{u}^2}{H} + \frac{B\bar{D}^2}{H}\right)\right] \tag{8.6}$$

$$We = \frac{\rho U_0^2 D_{30}}{\sigma} \tag{8.7}$$

$$B = \frac{12}{We} \tag{8.8}$$

From the presented PDF, the unknowns to be assessed are the Lagrange coefficients (λ_i). The *overbar* variables are normalized with the characteristic diameter and velocity, while H represents a shape factor. Based on the PDF function, the conservation equations can be re-arranged in an integral way, with solution domains ranging from $\bar{D}_{min}$ to $\bar{D}_{max}$ and from $\bar{u}_{min}$ to $\bar{u}_{max}$.

Other studies start from already defined characteristics, in which the characteristic size and velocity is given by known PDF curves. In this case, the characteristic nozzle diameter and characteristic injection velocity will be used as starting points. In order to obtain the D_{30} value, a correlation shown by Kuo and Trujillo [19] has been included (Eq 8.9).

$$D_{30}^3 = D_{p,0}^3 \left(5.5392We^{2.2207}\right)^{-1} \tag{8.9}$$

The reader is informed that the previous correlation was obtained for a single droplet subjected to moderate We according to its original droplet diameter $D_{p,0}$. In this case, an initial *Blob* will be considered, whose breakup will be assessed. Additionally, the characteristic We of a droplet with the size of the orifice, subjected to the velocities of UWS applications, will return a relatively low We (<12). Nonetheless, the expression will be used to determine if it remains applicable to vibrational breakup regimes.

Regarding the source terms of the conservation equations, the mass source term has been neglected, assuming no evaporation is present. On the other hand, the momentum and energy terms need to be accounted for as they represent the drag forces and the energy losses. The approach followed by Kuo and Trujillo [19] has been followed to obtain the appropriate losses.

The system of equations proposed, consisting of the three conservation equations plus the probability equation, and four Lagrange multipliers; has been solved numerically through a Newton-Raphson iterative process [20]. Additionally, as Movahednejad et al. [21] pointed out, the integrals and the terms within the PDF function expression are exponential, which makes solving the system susceptible to the initial guesses provided.

Once the initial system of equations has been solved, further droplet breakup was considered based on the co-joined droplet size-velocity distribution. As the generated droplets (including the initial *Blob*) fall within the vibrational breakup regime, there is no clear threshold on the We value that determines if a droplet will further breakup. Little focus has been paid to this particular low We regime, and therefore, a user-input value has been introduced during this Thesis. Consequently, there will be combinations of droplet

size-velocity that will trigger an additional breakup event, generating a subsequent PDF. This has been done iteratively on the whole range of droplets provided by the initial *Blob* distribution. The global droplet size PDF has been updated in each iteration until no further breakup is expected. The flowchart followed for this procedure is shown in Figure 8.1.

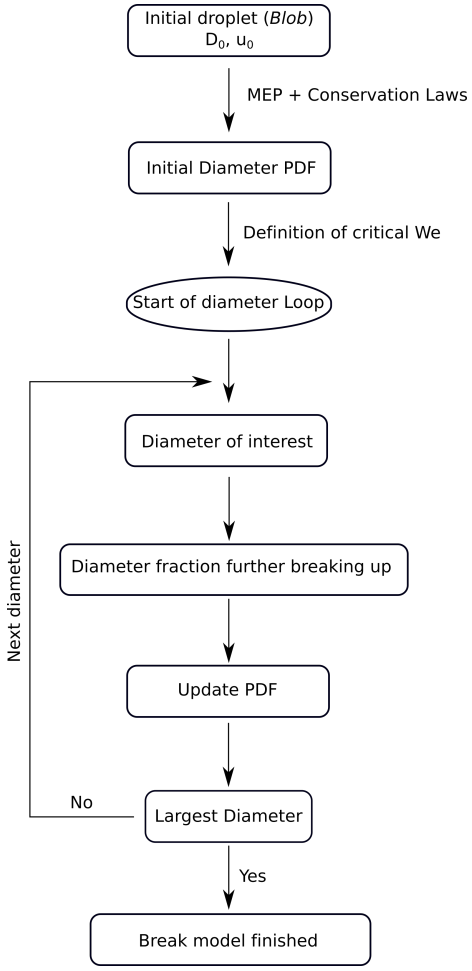

Figure 8.1: Flow chart of the MEP procedure applied to UWS sprays.

8.3 Application of the MEP approach to UWS sprays

The vibrational breakup of a droplet occurs when a formed droplet suffers an oscillatory behavior that eventually leads to breakup into smaller fragments. This breakup does not always occur and is slower than higher order modes, hence, most authors do not consider that regime. Nonetheless, some authors give an approximate range of critical We, which goes from $We_c \approx 0.5$ [22, 23] until the threshold value of the bag breakup $We_c \approx 12$.

From the initial *Blob* breakup, information could be extracted on the coupled diameter-velocity PDF distribution. This PDF has been obtained for an injection pressure of 8 barG, and the resulting probability contour is included in Figure 8.2. The maximum spread of diameter possibilities is obtained at a droplet velocity close to the characteristic U_0. Then, at higher and lower droplet velocities, the possible droplets that are more probable to appear are of a relatively small size. In agreement to the outcomes found by Guildenbencher et al. [12], with increasing droplet size, the velocity distribution becomes closely bounded, while at low diameters, the possible range of velocities increases. In this way, the experimental trends observed are reproduced by the MEP method.

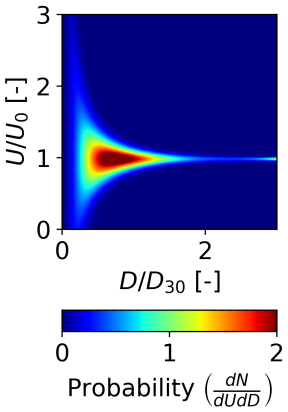

Figure 8.2: Predicted probability contour for a UWS injection pressure of 8 barG.

As explained, the MEP approach proposed needs of a critical We to determine if the velocity associated with each droplet diameter would trigger the further breakup of the generated droplets. Three different critical We have

been used to obtain the droplet size PDF for the three injection pressures used during this thesis. The value suggested by Hsiang et al. [11], and multiples of it are the selected values. The obtained results are included in Figure 8.4. As expected, reducing the critical We promotes further shifting of the PDF curve toward smaller diameters. At the same time, for the largest case $We_c = 2$, the distribution returned by MEP matches the initial PDF distribution obtained from the *Blob* droplet, as observed in Figure 8.3.

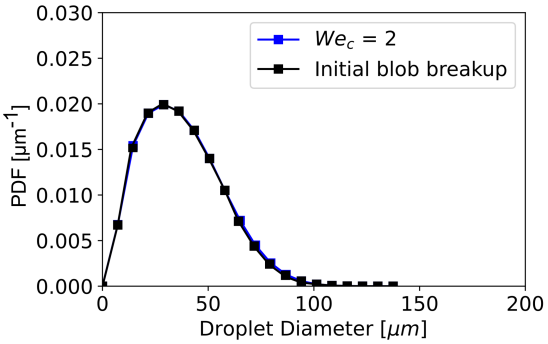

Figure 8.3: Comparison between the PDF outcomes of the breakup model and the initial blob breakup for an injection pressure of 4 barG, and a critical We=2.

That indicates that most of the droplets found within the initial PDF lie beneath the $We = 2$ limit, due to the small droplet sizes, the low velocities, the large density of the fluid, and the significant surface tension compared with typical fuel sprays. Additionally, the generated droplets are far away from suffering a *bag-shaped* breakup. These results also agree with the Re-We chart provided during the analysis of the near-field spray (Section 5.3), summarized in Figure 5.36, where almost the completeness of the generated droplets is located under the $We = 1$ limit. Many of them go down to a value of $We = 0.01$, indicating very stable droplets are present during typical UWS conditions. The effect of the injection pressure can also be observed from these results. A clear trend is observed with increasing the injection pressure value, as the droplet size distribution becomes more skewed toward smaller diameters, increasing the peak probability value. This effect is also observed through experimental means applied to UWS sprays, such as the work performed by Payri et al. [5]. The increase in injection velocity promotes atomization of the liquid jet, both producing a larger amount of low-diameter droplets, but also breaking up the momentum-carrying droplets, as for the

cases of $We_c = 2$, the largest droplet detected at 4 bar is of 100 µm, while for the largest injection pressure (8 bar), the largest droplet is of 65 µm.

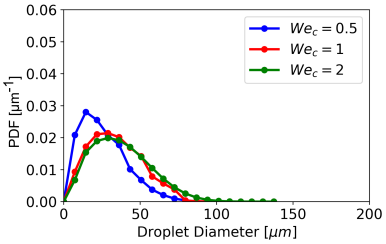

(a) 4 barG.

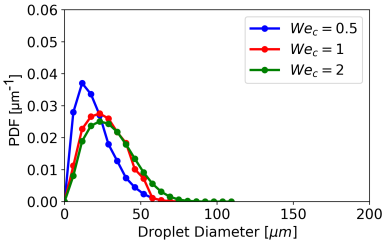

(b) 6 barG.

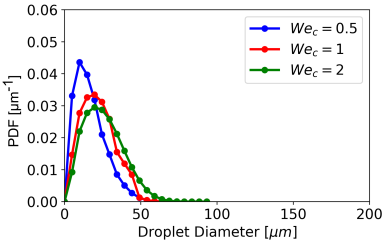

(c) 8 barG.

Figure 8.4: Droplet Size PDF results obtained based on the chosen We_c.

Based on the previous results and the determined threshold by experimental work, the value of $We_c = 0.5$ has been chosen to compare the model against the HRLBI results presented during Section 5.3. The reader is reminded that these experimental results were obtained at a distance of 30 mm from the orifice exit, therefore representing a snapshot of a completely developed spray. The results of the comparison are included in Figure 8.5. For the complete set of conditions, there is a general overprediction of tiny droplets compared to the HRLBI results. As a consequence, underprediction of droplets larger than 40 µm is obtained. On the other hand, the peak of maximum probability is close to the experimentally obtained. A quantification of these differences is included in Table 8.2. In it, with increasing injection pressure, the differences between the most probable diameter increase, as the reduction in that diameter with higher injection velocities is greater for the MEP than through experimental means. On the other hand, the peak probability value shows variations that decrease with injection pressure. The differences observed might be caused by the evaporation effects that could be seen on the

experimental procedure that on the MEP have been neglected ($S_m = 0$). The smallest droplets might evaporate at a distance of 30 mm, which is the region where measurements were taken, nonetheless, no information was available at a closer distance to the injector orifice. Additionally, HRLBI results could not detect droplets smaller than 17 µm through the mentioned experiments due to technical limitations. If compared against the DDM model initialized with the VOF droplet distributions (Subsubsection 5.3.5), there is an over-prediction of the probability of finding tiny droplets, although the deviation shown are considerably lower than with respect to HRLBI data. Again, the peak probability diameter shows a lower deviation for high injection pressures if compared to DDM with VOF results, while this deviation decreases with increasing jet velocities.

The results indicate that the critical Weber that determines the starting value for the vibrational breakup, which was obtained in previous studies, $We_c = 0.5$ provides an approximate diameter distribution close to the PDF obtained through HRLBI.

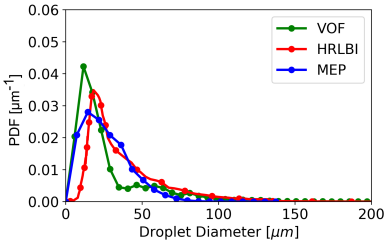

(a) 4 barG.

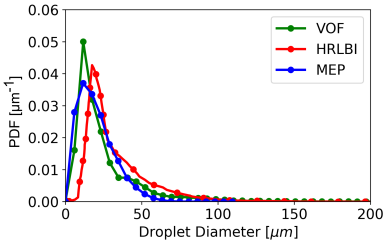

(b) 6 barG.

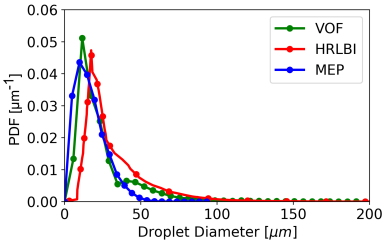

(c) 8 barG.

Figure 8.5: Comparison of the droplet size PDF between the MEP method and the HRLBI and DDM with VOF initialzed results.

Inj. Press.	Method	Peak Diam.	Peak Prob.	Max. Diam.
4 bar	HRLBI	19 µm	0.035	145 µm
	MEP	15 µm	0.028	82 µm
	DDM-VOF input	12 µm	0.042	120 µm
6 bar	HRLBI	18 µm	0.043	116 µm
	MEP	12 µm	0.037	68 µm
	DDM-VOF input	12 µm	0.050	125 µm
8 bar	HRLBI	17 µm	0.047	134 µm
	MEP	10 µm	0.043	57 µm
	DDM-VOF input	12 µm	0.051	105 µm

Table 8.1: Distribution parameters of the MEP method, HRLBI and DDM initialized with VOF results.

Inj. Press.	Method	Peak Diam. Var.	Peak Prob. Var.	Max. Diam. Var.
4 bar	HRLBI	21%	20%	43%
	VOF	25%	33%	32%
6 bar	HRLBI	33%	14%	46%
	VOF	5%	26%	15%
8 bar	HRLBI	41%	8.5%	57%
	VOF	16%	16%	46%

Table 8.2: Variations obtained from the PDF distribution results between the MEP and the HRLBI and VOF techniques.

8.4 Conclusions

During the present chapter, an alternative methodology has been presented to predict the droplet size PDF of general application sprays. Due to the lack of capabilities of commonly used breakup models on UWS applications, the Maximum Entropy Principle approach has been considered. The primary purpose of this chapter was to assess if, through the MEP, UWS sprays could be approximated.

Although some studies consider the velocity distribution and the droplet size distribution as independent variables, both have been found to be interdependent in literature. Therefore, the MEP approach has considered them

in this way. The procedure of the MEP has been described, including the appropriate equations.

A *Blob* approach employing the MEP has been proposed, in which an initial droplet with the size of the orifice is considered. From it, an initial PDF distribution is generated. From that distribution, each droplet diameter is assessed to check whether according to its We, further breakup should occur.

The results of the application of MEP show how droplet size and velocity distributions are coupled. Large droplet diameters show little dispersion of their associated size, while the most extensive range of possible velocities is associated with small droplet diameters.

The critical We has also been considered a critical parameter to check whether a specific droplet size should further breakup into smaller droplets. As expected, diminishing the critical We implies shifting the droplet distribution towards smaller sizes, while for a $We_c = 2$, the obtained size PDF is very similar to the initial distribution obtained from the *Blob* droplet.

A critical We of $We_c = 0.5$ has been used to compare the distributions with experimental results and VOF data, as previous studies indicated that value as the threshold We for vibrational breakup regimes, which is the regime to which these droplets will be subjected due to their velocity and the surface tension forces. Three injection pressures were considered, and acceptable results were obtained at a distance of 30 mm from the injector orifice. The most probable droplet was lower than through experimental results of approximately 8 µm for all conditions. However, the probability peak for both methods are similar between them. The results coming from the DDM model initialized with VOF data match in a better way the PDF results for high injection pressures.

Through the proposed method, it is possible to generate an approximated size PDF without the need of knowing beforehand the shape of such distribution, or employing computationally expensive methods such as VOF. This results in a useful way to initialize DDM models.

References

[1] Edelbauer, W., Birkhold, F., Rankel, T., Pavlović, Z., and Kolar, P. "Simulation of the liquid break-up at an AdBlue injector with the volume-of-fluid method followed by off-line coupled Lagrangian particle tracking". In: *Computers and Fluids* 157 (2017), pp. 294–311. DOI: 10.1016/j.compfluid.2017.09.003.

[2] Reitz, R. D. and Bracco, F. V. "Mechanism of atomization of a liquid jet". In: *Physics of Fluids* 25.10 (1982), pp. 1730–1742. DOI: 10.1063/1.863650.

[3] O'Rourke, P. J. and Amsden, A. A. "The tab method for numerical calculation of spray droplet breakup". In: *SAE Technical Papers*. 1987. DOI: 10.4271/872089.

[4] Lauer, T. "Preparation of Ammonia from Liquid AdBlue – Modeling Approaches and Future Challenges". In: *Chemie-Ingenieur-Technik* 90.6 (2018), pp. 783–794. DOI: 10.1002/cite.201700107.

[5] Bracho, G., Postrioti, L., Moreno, A., and Brizi, G. "Experimental study of the droplet characteristics of a SCR injector spray through optical techniques". In: *International Journal of Multiphase Flow* 135 (2021), p. 103531. DOI: 10.1016/j.ijmultiphaseflow.2020.103531.

[6] Li, X., Tankin, R. S., Sztal, B., and Most, J.-M. "Derivation of Droplet Size Distribution in Sprays By Using Information Theory". In: *Combustion Science and Technology* 60.4-6 (1988), pp. 345–357. DOI: 10.1080/00102208808923992.

[7] Sellens, R. W. and Brzustowski, T. A. "A prediction of the drop size distribution in a spray from first principles". In: *Atomisation Spray Technology* 1 (1985), pp. 89–102.

[8] Sellens, R. W. "Prediction of the Drop Size and Velocity Distribution in a Spray, Based on the maximum entropy formalism". In: *Particle & Particle Systems Characterization* 6.1-4 (1989), pp. 17–27. DOI: 10.1002/ppsc.19890060103.

[9] Li, X. and Tankin, R. S. "On the Prediction of Droplet Size and Velocity distributions in sprays through maximum entropy principle". In: *Particle & Particle Systems Characterization* 9.1-4 (1992), pp. 195–201. DOI: 10.1002/ppsc.19920090126.

[10] Ahmadi, M. S. and Sellens, R. W. "A SIMPLIFIED MAXIMUM-ENTROPY-BASED DROP SIZE DISTRIBUTION". In: *Atomization and Sprays* 3 (1993), pp. 291–310.

[11] Hsiang, L.-P. and Faeth, G. "Drop properties after secondary breakup". In: *International Journal of Multiphase Flow* 19.5 (1993), pp. 721–735. DOI: 10.1016/0301-9322(93)90039-W.

[12] Guildenbecher, D. R., Gao, J., Chen, J., and Sojka, P. E. "Characterization of drop aerodynamic fragmentation in the bag and sheet-thinning regimes by crossed-beam, two-view, digital in-line holography". In: *International Journal of Multiphase Flow* 94 (2017), pp. 107–122. DOI: 10.1016/j.ijmultiphaseflow.2017.04.011.

[13] Dumouchel, C. and Boyaval, S. "Use of the Maximum Entropy Formalism to Determine Drop Size Distribution Characteristics". In: *Particle & Particle Systems Characterization* 16.4 (1999), pp. 177–184. DOI: 10.1002/(SICI)1521-4117(199908)16:4<177::AID-PPSC177>3.0.CO;2-L.

[14] Dumouchel, C. and Malot, H. "Development of a Three-parameter Volume-based Spray Drop Size Distribution through the Application of the Maximum Entropy Formalism". In: *Particle & Particle Systems Characterization* 16.5 (1999), pp. 220–228. DOI: 10.1002/(SICI)1521-4117(199910)16:5<220::AID-PPSC220>3.0.CO;2-D.

[15] Dumouchel, C. "The Maximum Entropy Formalism and the Prediction of Liquid Spray Drop-Size Distribution". In: *Entropy* 11.4 (2009), pp. 713–747. DOI: 10.3390/e11040713.

[16] Helenbrook, B. and Edwards, C. "Quasi-steady deformation and drag of uncontaminated liquid drops". In: *International Journal of Multiphase Flow* 28.10 (2002), pp. 1631–1657. DOI: 10.1016/S0301-9322(02)00073-3.

[17] Shannon, C. E. and Weaver, W. *The Mathematical Theory of Communication*. Illini books v. 1. University of Illinois Press, 1949.

[18] Hoffmann, L. and Bradley, G. *Calculus for Business, Economics, and the Social and Life Sciences, Brief*. McGraw-Hill Companies,Incorporated, 2009.

[19] Kuo, C. W. and Trujillo, M. F. "A maximum entropy formalism model for the breakup of a droplet". In: *Physics of Fluids* 34.1 (2022). DOI: 10.1063/5.0076910.

[20] Dedieu, J.-P. "Newton-Raphson Method". In: *Encyclopedia of Applied and Computational Mathematics*. Berlin, Heidelberg: Springer Berlin Heidelberg, 2015, pp. 1023–1028. DOI: 10.1007/978-3-540-70529-1_374.

[21] Movahednejad, E., Ommi, F., Hosseinalipour, S. M., Chen, C. P., and Mahdavi, S. A. "Application of maximum entropy method for droplet size distribution prediction using instability analysis of liquid sheet". In: *Heat and Mass Transfer/Waerme- und Stoffuebertragung* 47.12 (2011), pp. 1591–1600. DOI: 10.1007/s00231-011-0797-5.

[22] Hsiang, L.-P. and Faeth, G. "Drop deformation and breakup due to shock wave and steady disturbances". In: *International Journal of Multiphase Flow* 21.4 (1995), pp. 545–560. DOI: 10.1016/0301-9322(94)00095-2.

[23] Habchi, C. "The Energy Spectrum Analogy Breakup (SAB) Modell for the Numerical Simulation of Sprays". In: *Atomization and Sprays* 21.12 (2011), pp. 1033–1057. DOI: 10.1615/AtomizSpr.2012004531.

Chapter 9

Conclusions and Future Work

"Without training, they lacked knowledge. Without knowledge, they lacked confidence. Without confidence, they lacked victory."
—Julius Caesar

9.1 Introduction

From the study performed throughout the present thesis, several conclusions have been drawn. As several techniques have been employed for the different studies (internal and external spray flow), the conclusions introduced in this chapter will be divided according to their objective and their approach. Hence, each chapter of results have associated a section in the present chapter, where the main objectives and achievements are synthesized. Lastly, a section containing the possible studies that could benefit from the present work and could be of interest for the industrial and research communities will be added under the name of *future work*.

9.2 Conclusions

The global trend toward zero-emission technologies for transportation purposes and the use of alternative fuels have provided enough motivation to generate this doctoral thesis in the field of Selective Catalytic Reduction (SCR) systems to improve the efficiency of this deNOx technology through the better understanding of the injection of Urea Water Solution (UWS) sprays and

its chemical decomposition to NH_3. More specifically, this thesis has tried to capture the physical dynamics that drive the jet breakup and atomization of UWS sprays. Additionally, the evaporation and chemical transformations undergone by the generated droplets are of great importance. For that, the dependency of such phenomenon on the engine working parameters was desired. To achieve these main goals, a computational framework capable of capturing the desired mechanics and chemical processes has been introduced. A validation of the presented models has followed, and a subsequent analysis of the physical and chemical dynamics has concluded the study. By introducing such computational methodology, an alternative is proposed to experimental techniques in order to cheapen the analysis performed on low-velocity sprays, as in UWS.

The strategy followed during the different chapters of the present document was to divide the domain of interest into the different characteristic length and time scales of the phenomena that take place, that is, internal and near-field region, and far-field region.

9.2.1 Near-field study

The results obtained for the near-field analysis were included in Chapter 5. In it, two Eulerian-Eulerian frameworks were proposed to characterize the hydraulic behavior of the UWS jet, and its breakup. A Mixture Model (MM) was applied to a first version of the inner geometry (*Generation 1*) of an UWS injector. The hydraulic characteristics were used to obtain the mesh characteristics needed for RANS applications, and indexes of quality based on turbulent characteristics were used for the LES approach. The results on the hydraulic performance of the UWS returned good agreement of the Rate Of Injection (ROI) values with experimental results, for the three injection pressures tested (4, 6 and 8 barG). The associated deviations where lower than 6% for RANS turbulent treatment, while LES showed errors lower than 4%. The Rate Of Momentum (ROM) results, on the other hand, show high deviations with respect to experimental techniques (as high as 35%) for all the tested conditions. These errors were first associated to the lack of needle lift dynamics during the simulations or a not accurate representation of the injector inner geometry. Flow coefficients were also obtained to assess where those differences came from. The discharge coefficient, as expected was consistent across all the working conditions, while the velocity and area coefficient differed from experimental values. The consistently lower velocity coefficients were compensated with the larger area coefficients, achieving proper discharge coefficients. Nonetheless, when it came to the momentum coefficient, the quadratic de-

pendence of the velocity leads to lower values. On the same study, it was found the influence of the orientation of cartesian meshes in the solution of Eulerian-Eulerian simulations. The decreasing of the breakup length value concluded that the injector was working within the first wind-induced regime for the LES results, but close to shifting to the second-wind breakup regime. Additionally, the location of jet breakup was found to be related to an increase in the Turbulent Kinetic Energy of the flow.

Further analysis on the near-field was carried out using a high-fidelity geometry (*Generation 2*) obtained through micro-CT scan, and a Volume-Of-Fluid (VOF) approach. The improvement in the fidelity of the inner geometry of the injector returned considerably better ROI and ROM results than the ones obtained through *Generation 1*, reducing the errors down to 7%, highlighting the need of properly capturing the orifice geometry. The VOF approach allowed to capture macroscopic characteristics such as the spray tip penetration and the spray angle. The spray tip velocity was properly captured for the three injection pressures of interest, although the spray angle did not show a specific trend, in agreement with the experimental results. Microscopic characteristics were extracted based on the injection of one out of the three injector orifices as the initial simulation performed on the complete geometry did not show jet-to-jet interaction. A validation study was carried out on the number-based and volume-based Probability Density Functions (PDFs). The Cumulative Volume Fraction (CVF) of these plots was also included. VOF simulations showed a distribution with the most common droplet diameter of 8 µm, whilst the experimental approach showed slightly larger droplets. The CVF curves on the other hand returned smaller characteristic diameters through the computational approach. This behavior can be partially explained through the limitation of the HRLBI technique to capture droplets smaller than 17 µm. Nonetheless, when it comes to characterizing the momentum-carrying droplets, good agreement was found between the volume-weighted PDF across both experimental and computational methodologies.

Once the validation of the VOF approach was carried out, the characterization of the spray dynamics were assessed. The spray achieved steady conditions at a time of 0.7 ms ASOI. The previous PDF and CVF curves were compared across the injection pressures that have been simulated. The number-based curves did not show significant changes when increasing the injection pressure (i.e. injection velocity). Though, CVF curves showed benefits from increasing the injection pressure as the volume located within large droplets was diminished in addition to a reduction of the characteristic diameters. Through an spatial analysis of the PDF curves it could be extracted that the most common droplet diameter was obtained at the region close to

the orifice (2-6 µm), while the largest droplets were formed in regions further away (6-10 µm). This meant that, although big ligaments detached from the main liquid structure at a certain distance from the injection point, a parallel atomization process with lower characteristic times and lengths takes place. Subsequent analyses captured the influence of the injection pressure also on the spray velocity distributions, showing that increasing the injection pressure spread the Y-Velocity and Z-Velocity PDFs. Additionally, characteristics of the droplet sphericity were obtained, showing that increasing the injection pressure generated more spherical droplets, increasing the possibility of finding low-diameter spherical particles, while for low injection pressures, the low-diameter particles could show a range of sphericities up to a value of $Sp = 5$.

Secondary atomization was found to be almost nonexistent as the detected droplets showed low We, significantly lower than the threshold We for it to happen, also lower than possible vibrational breakup regimes. This is introduced as an initial condition for Discrete Droplet Model (DDM) simulations, and returned good agreement with experimental data captured at longer distances from the injector orifice.

9.2.2 Far-field study

In order to characterize the far-field region of UWS sprays, Discrete Droplet Model (DDM) techniques were used. The first analysis done had as its objective generating a chemical model capable of reproducing the degradation of urea into NH_3 through thermolysis, and the transformation of HNCO to NH_3 through hydrolysis. The *molten solid* approach was followed, which considered a direct transformation of molten urea to NH_3, skipping the evaporation of the urea and its subsequent chemical transformation. The validation of these transformations returned good results for low-temperature and low gas velocity conditions, and deviations relatable to other computational studies of the literature.

The following study focused on representing the spray under inert conditions. The effect of increasing the injection pressure was similar to the one observed during VOF simulations, with little changes in the number-based distributions and an increase in the spread of the velocity PDF. Two different spray regions were detected based on the droplet Sauter Mean Diameter (SMD). The spray core was composed of a characteristic SMD larger than 120 µm, while the outskirt had a lower SMD value (approx 80 µm). If the injection pressure is increased, the momentum transfer between the gas cross-

flow and the droplets diminishes, decreasing the injector core SMD as the small droplets are not removed by the incoming gas.

The chemical model already validated was introduced into the simulations of practical applications. The evaporation curve of the droplets was assessed, depicting the so-called D^2 law for the water evaporation, which is considerably faster than the degradation rate of the urea. Although increasing the injection pressure does not show significant change in the urea thermolysis, it does speed up the water evaporation for the two temperatures simulated. Subsequent simulations were carried out to detect the influence of the spray injection angle on the NH_3 generation. The droplet evaporation curve showed a faster droplet reduction when injecting in a normal direction to the gas cross-flow if compared to an injection angle more co-axial with the direction of the gas cross-flow. From these results, the largest droplets showed the fastest diameter reduction due to the larger exposed surface. For low cross mass flow rates (40 kg/h), the maximum was found at injection angles close to 80°, while for high mass flow rates (200 kg/h) the maximum observed was found at 60°. Additionally, an increase in the gas mass flow rate made the thermolysis transformation to happen earlier in time, and to have a higher NH_3 generation rate. The correlation extracted out of it provided a correlation tool capable of quantitatively predicting the NH_3 generation rate based on the gas temperature and mass flow rate, and the liquid injection pressure and injection direction.

The knowledge acquired during these studies was later applied to a Close-Coupled SCR system, as it was desired to analyze the effect of the swirler geometry within the exhaust line. Three exhaust gas temperatures, three injection pressures and three swirler geometries (differing in the number of vanes) were simulated through DDM approach. This simulations were coupled with the spray breakup outcomes obtained through the VOF approach. The swirler geometry located downstream further atomized the injected spray into smaller droplets (<1 µm), independently of the injection pressure, the exhaust temperature and the number of blades of the swirler, as the most probable diameter is located at the same diameter for all conditions. Nonetheless, it does affect the probability of finding such droplets. The amount of NH_3 found and the NH_3 generation rate does see greater variations. This parameters were most affected by the exhaust gas temperature. While all temperatures show degradation of urea, it is not until a temperature of 573 K where significant amounts of NH_3 are found. The injection pressure did not show significant changes in NH_3 content, but increasing the amount of swirlers increased as well the NH_3 found in the domain. Relatable results were found for the NH_3 generation rate. This indicated that the swirler with more vanes, although

producing a similar droplet size PDF, generated a highly turbulent field and improved the mixing of the injected droplets with the exhaust gas flow. On the other hand, it significantly increased the surface are in which the droplets could impact upon, generating a deposit formation risk on situations where multiple injections were present.

Lastly, to comply with one of the objectives of the thesis, an alternative breakup model was generated to use with UWS sprays. Available breakup models to use with DDM approach are created to high-order breakup modes not valid for the low We of UWS droplets. For it, the Maximum Entropy Principle (MEP) technique has been adopted, and modified to act upon a *blob* model in which its primary atomization is considered, in addition to the secondary vibrational breakup of the subsequently generated droplets. A critical We = 0.5 was set to determine in which conditions the secondary breakup through vibrational mechanisms should take place. The generated MEP model worked reasonably well for the three injection pressures tested, showing acceptable results on the probability peak value when compared with experimental results and the results from the DDM model initialized with VOF data. Certain deviations were observed when capturing the most probable diameter value, as MEP returned smaller droplet diameters. Nonetheless, these deviations could be explained due to limitations in the experimental technique to capture such small droplets. This tool provided the possibility of generating an realistic UWS PDF distribution without the need of previous experimental of VOF characterization, reducing the associated costs of these techniques.

9.3 Future work

The injection of UWS sprays is a field that deals with a large amount of both physical and chemical processes that need to be carefully individually understood, in addition to their interaction when considered as a whole. This doctoral Thesis has aimed to provide a better understanding of these phenomena and tried to broaden the knowledge of the scientific community through it. Nonetheless, the field of after-treatment sprays will continue to grow in the future with the introduction of carbon-free fuels (such as H_2 and NH_3) which, although not producing CO_2, will continue to produce NOx compounds. For that reason, further effort should be placed toward an optimization of the deNOx systems. Several questions have arisen during the development of this Thesis that remain unanswered and should be further reviewed to push forward the SCR technology.

- *Determination of the UWS injector needle lift.* The ROI and ROM results presented in this Thesis have been validated against the mean value of the curves obtained from literature. These curves show transient behavior at the start and at the end of the injection process. As the lift and wobbling of the needle are responsible for this behavior, the needle lift profile should be taken into account for future VOF simulations. By considering them, the initial breakup phenomenon could differ from the one captured using the steady state ROI and ROM values.
- *Usage of the Eulerian-Lagrangian Spray Atomization (ELSA) model.* In the approach followed during this Thesis, the near-field and far-field simulations were done independently from each other, but with an offline coupling procedure. The ELSA model allows for a direct transition of the generated droplets from the VOF approach to DDM parcels, all within the same simulation. This process would not only introduce the droplet size characteristics, but their corresponding velocity and properties. Following studies could benefit from it, given that enough computational resources are available.
- *Experimental characterization of the urea degradation.* The validation of the chemical model was done using literature data provided almost 20 years ago on single point measurements. Additional experimental work on the evaporation of the urea could be carried out using *Schlieren* techniques. This could provide additional data useful for the validation of the *molten solid* approach on the same working conditions.
- *Characterization of the formation of solid deposits.* Although including a droplet/wall interaction model (Kuhnke) in Chapter 7, no wall film was created due to the simulation of single injection events at high wall temperatures. Multiple injection events, together with Conjugate Heat Transfer (CHT) models could be employed to recreate the wall film formation, the solid phase temperature evolution and the deposit formation assessment through *fixed flow* techniques.
- *Consideration of the deNOx behavior.* The SCR monolith could also be included in further studies to consider the reduction of the harmful NOx. To do so, it would be needed to experimentally capture a typical engine exhaust flow composition, in addition to characterize the presence of the monolith in the exhaust line through *porous media* approach together with a DDM treatment of the liquid droplets.
- *Assessment of spray characteristics under different injector geometries.* For UWS applications, not only pressure atomizers with plain orifices are

used (as in the present study), but pressure-swirl (simplex) geometries can generate different spray topologies that could benefit the droplet size PDF, and improving the atomization of the jet. For that, it is proposed applying the same micro-CT scan to an injector using such internal geometry, and apply the VOF approach to it.

- *Consideration of alternative swirler geometries.* The helix-type swirler is one of the several swirler types that state-of-the-art SCR employ. A comparison of the effectiveness of the different typologies could provide a better understanding of their behavior and could push forward the generation of geometries capable of enhancing the secondary atomization and prevent the deposit formation on its surfaces.
- *To obtain a experimental correlation of the droplet breakup outcomes for low breakup regimes.* During the MEP chapter, a correlation to assess the characteristic droplet size of a breakup events was extracted from the literature. Such correlation was intended to be used at bag-breakup regimes and higher order breakup modes. For this purpose, it could be assessed a correlation for vibrational breakup regimes.
- *Implementation of the MEP approach to initialize simulations.* The MEP technique has proven certain accuracy when representing UWS sprays. Nonetheless, during this Thesis has only been employed for validating against already generated droplet size PDF. The very same DDM simulations could be carried out using this technique as initialization of those sprays, and the results could be further compared against VOF-initialized and experimentally-initialized UWS jets.

Global Bibliography

Abu-Ramadan, E., Saha, K., and Li, X. "Modeling of the injection and decomposition processes of urea-water-solution spray in automotive SCR systems". In: *SAE 2011 World Congress and Exhibition* 2011-01-13.x (2011). DOI: 10.4271/2011-01-1317 (cited on pages 5, 62, 63).

Ahmadi, M. S. and Sellens, R. W. "A SIMPLIFIED MAXIMUM-ENTROPY-BASED DROP SIZE DISTRIBUTION". In: *Atomization and Sprays* 3 (1993), pp. 291–310 (cited on page 214).

Ai, W., Wang, J., Wen, J., Wang, S., Tan, W., Zhang, Z., Liang, K., Zhang, R., and Li, W. "Research landscape and hotspots of selective catalytic reduction (SCR) for NOx removal: insights from a comprehensive bibliometric analysis". In: *Environmental Science and Pollution Research* 30.24 (2023), pp. 65482–65499. DOI: 10.1007/s11356-023-26993-4 (cited on page 3).

Alagumalai, A., Jodat, A., Mahian, O., and Ashok, B. "NOx formation chemical kinetics in IC engines". In: *NOx Emission Control Technologies in Stationary and Automotive Internal Combustion Engines: Approaches Toward NOx Free Automobiles* (2021), pp. 39–68. DOI: 10.1016/B978-0-12-823955-1.00002-4 (cited on page 19).

Aldhaidhawi, M., Chiriac, R., Bădescu, V., Descombes, G., and Podevin, P. "Investigation on the mixture formation, combustion characteristics and performance of a Diesel engine fueled with Diesel, Biodiesel B20 and hydrogen addition". In: *International Journal of Hydrogen Energy* 42.26 (2017), pp. 16793–16807. DOI: 10.1016/j.ijhydene.2017.01.222 (cited on page 21).

Amsden, A. A., O'Rourke, P. J., and Butler, T. D. *KIVA-II: A computer program for chemically reactive flows with sprays*. Tech. rep. Los Alamos, NM (United States): Los Alamos National Laboratory (LANL), 1989. DOI: 10.2172/6228444 (cited on page 93).

Araneo, L., Coghe, A., Brunello, G., and Cossali, G. E. "Experimental investigation of gas density effects on diesel spray penetration and entrainment". In: *SAE Technical Papers* (1999), pp. 679–693. DOI: 10.4271/1999-01-0525 (cited on page 54).

Ashgriz, N. and Givi, P. "Binary collision dynamics of fuel droplets". In: *International Journal of Heat and Fluid Flow* 8.3 (1987), pp. 205–210. DOI: 10.1016/0142-727X(87)90029-4 (cited on page 35).

Bai, C. and Gosman, A. D. "Development of methodology for spray impingement simulation". In: *SAE Technical Papers* 412 (1995). DOI: 10.4271/950283 (cited on page 44).

Balachandar, S. "A scaling analysis for point–particle approaches to turbulent multiphase flows". In: *International Journal of Multiphase Flow* 35.9 (2009), pp. 801–810. DOI: https://doi.org/10.1016/j.ijmultiphaseflow.2009.02.013 (cited on page 90).

Baldwin, B. and Lomax, H. "Thin-layer approximation and algebraic model for separated turbulentflows". In: *16th aerospace sciences meeting*. 1978, p. 257. DOI: https://doi.org/10.2514/6.1978-257 (cited on page 82).

Baleta, J., Vujanović, M., Pachler, K., and Duić, N. "Numerical modeling of urea water based selective catalytic reduction for mitigation of NOx from transport sector". In: *Journal of Cleaner Production* 88 (2015), pp. 280–288. DOI: 10.1016/j.jclepro.2014.06.042 (cited on page 54).

Balland, J., Parmentier, M., and Schmitt, J. "Control of a Combined SCR on Filter and Under-Floor SCR System for Low Emission Passenger Cars". In: *SAE International Journal of Engines* 7.3 (2014), pp. 1252–1261. DOI: 10.4271/2014-01-1522 (cited on page 4).

Bardi, M., Payri, R., Malbec, L. M., Bruneaux, G., Pickett, L. M., Manin, J., Bazyn, T., and Genzale, C. "Engine Combustion Network: Comparison Of Spray Development, Vaporization, and Combustion in Different Combustion Vessels". In: *Atomization and Sprays* 22.10 (2012), pp. 807–842. DOI: 10.1615/AtomizSpr.2013005837 (cited on page 125).

Bautista Rodriguez, A. "Study of the Gasoline direct injection process under novel operating conditions". PhD thesis. Valencia (Spain): Universitat Politècnica de València, 2021. DOI: 10.4995/Thesis/10251/167809 (cited on page 6).

Bayer, T., Samuelsen, D., Bareiss, S., and Chaineux, M. "Double injection SCR – Bosch's development for future emission regulations". In: ed. by M. Bargende, H.-C. Reuss, and J. Wiedemann. Wiesbaden: Springer Fachmedien Wiesbaden, 2018, pp. 579–593. DOI: 10.1007/978-3-658-21194-3_45 (cited on page 4).

Bender, E. "Numerical heat transfer and fluid flow. VonS. V. Patankar. Hemisphere Publishing Corporation, Washington - New York - London. McGraw Hill Book Company, New York 1980. 1. Aufl., 197 S., 76 Abb., geb., DM 71,90". In: *Chemie Ingenieur Technik* 53.3 (1981), pp. 225–225. DOI: 10.1002/cite.330530323 (cited on page 140).

Bernhard, A. M., Peitz, D., Elsener, M., and Kröcher, O. "Quantification of gaseous urea by FT-IR spectroscopy and its application in catalytic urea thermolysis". In: *Topics in Catalysis* 56.1-8 (2013), pp. 130–133. DOI: 10.1007/s11244-013-9941-4 (cited on page 59).

Birkhold, F. *Selektive katalytische Reduktion von Stickoxiden in Kraftfahrzeugen: Untersuchung der Einspritzung von Harnstoffwasserlösung*. Aachen: Shaker Verlag, 2007 (cited on pages 5, 61, 62, 66, 188).

Birkhold, F., Meingast, U., Wassermann, P., and Deutschmann, O. "Modeling and simulation of the injection of urea-water-solution for automotive SCR DeNOx-systems". In: *Applied Catalysis B: Environmental* 70.1-4 (2007), pp. 119–127. DOI: 10.1016/j.apcatb.2005.12.035 (cited on pages 54, 62, 63, 179).

Börnhorst, M., Kuntz, C., Tischer, S., and Deutschmann, O. "Urea derived deposits in diesel exhaust gas after-treatment: Integration of urea decomposition kinetics into a CFD simulation". In: *Chemical Engineering Science* 211 (2020), p. 115319. DOI: https://doi.org/10.1016/j.ces.2019.115319 (cited on page 65).

Börnhorst, M. and Deutschmann, O. "Single droplet impingement of urea water solution on a heated substrate". In: *International Journal of Heat and Fluid Flow* 69 (2018), pp. 55–61. DOI: 10.1016/j.ijheatfluidflow.2017.10.007 (cited on page 59).

Börnhorst, M. and Deutschmann, O. "Advances and challenges of ammonia delivery by urea-water sprays in SCR systems". In: *Progress in Energy and Combustion Science* 87 (2021), p. 100949. DOI: 10.1016/j.pecs.2021.100949 (cited on pages 21, 67, 205).

Börnhorst, M., Langheck, S., Weickenmeier, H., Dem, C., Suntz, R., and Deutschmann, O. "Characterization of solid deposits from urea water solution injected into a hot gas test rig". In: *Chemical Engineering Journal* 377 (2019), p. 119855. DOI: 10.1016/j.cej.2018.09.016 (cited on page 59).

Boussinesq, J. *Essai sur la théorie des eaux courantes*. Impr. nationale, 1877 (cited on page 83).

Bracho, G., Postrioti, L., Moreno, A., and Brizi, G. "Experimental study of the droplet characteristics of a SCR injector spray through optical techniques". In: *International Journal of Multiphase Flow* 135 (2021), p. 103531. DOI: 10.1016/j.ijmultiphaseflow.2020.103531 (cited on pages 4, 213, 219).

Bracho, G., Postrioti, L., Moreno, A., and Brizi, G. "Experimental study of the droplet characteristics of a SCR injector spray through optical techniques". In: *International Journal of Multiphase Flow* 135 (2021), p. 103531. DOI: 10.1016/j.ijmultiphaseflow.2020.103531 (cited on page 162).

Bracho, G., Postrioti, L., Moreno, A., and Brizi, G. "Experimental study of the droplet characteristics of a SCR injector spray through optical techniques". In: *International Journal of Multiphase Flow* 135 (2021), p. 103531. DOI: 10.1016/j.ijmultiphaseflow.2020.103531 (cited on pages 135, 172).

Brack, W., Heine, B., Birkhold, F., Kruse, M., Schoch, G., Tischer, S., and Deutschmann, O. "Kinetic modeling of urea decomposition based on systematic thermogravimetric analyses of urea and its most important by-products". In: *Chemical Engineering Science* 106 (2014), pp. 1–8. DOI: 10.1016/j.ces.2013.11.013 (cited on pages 64, 65).

Brackbill, J. U., Kothe, D. B., and Zemach, C. "A continuum method for modeling surface tension". In: *Journal of Computational Physics* 100.2 (1992), pp. 335–354. DOI: 10.1016/0021-9991(92)90240-Y (cited on page 89).

Bröer, S. and Hammer, T. "Selective catalytic reduction of nitrogen oxides by combining a non-thermal plasma and a V2O5-WO3/TiO2 catalyst". In: *Applied Catalysis B: Environmental* 28.2 (2000), pp. 101–111. DOI: 10.1016/S0926-3373(00)00166-1 (cited on page 22).

Budziankou, U., Quissek, M., and Lauer, T. "A Fast Modeling Approach for the Numerical Prediction of Urea Deposit Formation". In: 2020. DOI: 10.4271/2020-01-0358 (cited on page 3).

Canyurt, T. G., Ergin, S., Zeren, H. B., and Savcı, İ. H. "Experimental and numerical investigation on the urea-deposit formation at different severities in selective catalytic reduction systems". In: *Applied Thermal Engineering* 214 (2022), p. 118884. DOI: 10.1016/j.applthermaleng.2022.118884 (cited on page 55).

Carslaw, D. C. and Rhys-Tyler, G. "New insights from comprehensive on-road measurements of NOx, NO2 and NH3 from vehicle emission remote sensing in London, UK". In: *Atmospheric Environment* 81 (2013), pp. 339–347. DOI: 10.1016/j.atmosenv.2013.09.026 (cited on page 18).

Celik, I., Klein, M., and Janicka, J. "Assessment measures for engineering LES applications". In: *Journal of fluids engineering* 131.3 (2009) (cited on pages 122, 136, 200, 201).

Celik, I. B., Cehreli, Z. N., and Yavuz, I. "Index of resolution quality for large eddy simulations". In: *Journal of Fluids Engineering, Transactions of the ASME* 127.5 (2005), pp. 949–958. DOI: 10.1115/1.1990201 (cited on page 122).

Chavez, M. d. J. "Modelado CFD Euleriano-Lagrangiano del Chorro Diesel y evaluacion de su combinacion con modelos fenomenologicos y unidimensionales." PhD thesis. Valencia (Spain): Universitat Politècnica de València, 2013, p. 203. DOI: 10.4995/Thesis/10251/32954 (cited on page 6).

Chin, J. S. and Lefebvre, A. H. "Some comments on the characterization of drop-size distribution in sprays". In: *IN: ICLASS-85; Proceedings of the Third International Conference on Liquid Atomisation and Spray Systems.* Vol. 2. 1986 (cited on page 34).

Cichanowicz, J. E. and Muzio, L. J. "Twenty-Five Years of SCR Evolution: Implications For US Application And Operation". In: 2006 (cited on pages 15, 16).

Clift, R., Grace, J. R., and Weber, M. E. "Bubbles, drops, and particles". In: (2005) (cited on page 37).

Cobb, D., Glatch, L., Ruud, J., and Snyder, S. "Application of selective catalytic reduction (SCR) technology for NOx reduction from refinery combustion sources". In: *Environmental Progress* 10.1 (1991), pp. 49–59. DOI: 10.1002/ep.670100116 (cited on page 15).

Commission, E. "Questions and Answers : Commission proposal on the new Euro 7 standards". In: November (2022) (cited on page 2).

Convergent Science, ed. *CONVERGE 3.0 Manual*. Middleton, 2019 (cited on page 8).

Dedieu, J.-P. “Newton-Raphson Method”. In: *Encyclopedia of Applied and Computational Mathematics*. Berlin, Heidelberg: Springer Berlin Heidelberg, 2015, pp. 1023–1028. DOI: 10.1007/978-3-540-70529-1_374 (cited on page 216).

Desantes, J. M., Garcia-Oliver, J. M., Pastor, J. M., and Pandal, A. “A Comparison of Diesel Sprays CFD Modeling Approaches: DDM Versus E-Y Eulerian Atomization Model”. In: *Atomization and Sprays* 26.7 (2016), pp. 713–737. DOI: 10.1615/AtomizSpr.2015013285 (cited on page 82).

Devadas, M., Kröcher, O., Elsener, M., Wokaun, A., Söger, N., Pfeifer, M., Demel, Y., and Mussmann, L. “Influence of NO2 on the selective catalytic reduction of NO with ammonia over Fe-ZSM5”. In: *Applied Catalysis B: Environmental* 67.3-4 (2006), pp. 187–196. DOI: 10.1016/j.apcatb.2006.04.015 (cited on page 22).

Dinesh, M. H., Pandey, J. K., and Kumar, G. N. “Study of performance, combustion, and NOx emission behavior of an SI engine fuelled with ammonia/hydrogen blends at various compression ratio”. In: *International Journal of Hydrogen Energy* 47.60 (2022), pp. 25391–25403. DOI: 10.1016/j.ijhydene.2022.05.287 (cited on page 2).

Dörnhöfer, J., Börnhorst, M., Ates, C., Samkhaniani, N., Pfeil, J., Wörner, M., Koch, R., Bauer, H.-J., Deutschmann, O., Frohnapfel, B., and Koch, T. “A Holistic View on Urea Injection for NOx Emission Control: Impingement, Re-atomization, and Deposit Formation”. In: *Emission Control Science and Technology* 6.2 (2020), pp. 228–243. DOI: 10.1007/s40825-019-00151-0 (cited on page 4).

Duke, D. J., Kastengren, A. L., Matusik, K. E., Swantek, A. B., Powell, C. F., Payri, R., Vaquerizo, D., Itani, L., Bruneaux, G., Grover, R. O., Parrish, S., Markle, L., Schmidt, D., Manin, J., Skeen, S. A., and Pickett, L. M. “Internal and near nozzle measurements of Engine Combustion Network “Spray G” gasoline direct injectors”. In: *Experimental Thermal and Fluid Science* 88 (2017), pp. 608–621. DOI: 10.1016/j.expthermflusci.2017.07.015 (cited on page 153).

Dumouchel, C. “The Maximum Entropy Formalism and the Prediction of Liquid Spray Drop-Size Distribution”. In: *Entropy* 11.4 (2009), pp. 713–747. DOI: 10.3390/e11040713 (cited on page 214).

Dumouchel, C. and Boyaval, S. "Use of the Maximum Entropy Formalism to Determine Drop Size Distribution Characteristics". In: *Particle & Particle Systems Characterization* 16.4 (1999), pp. 177–184. DOI: 10.1002/(SICI)1521-4117(199908)16:4<177::AID-PPSC177>3.0.CO;2-L (cited on page 214).

Dumouchel, C. and Malot, H. "Development of a Three-parameter Volume-based Spray Drop Size Distribution through the Application of the Maximum Entropy Formalism". In: *Particle & Particle Systems Characterization* 16.5 (1999), pp. 220–228. DOI: 10.1002/(SICI)1521-4117(199910)16:5<220::AID-PPSC220>3.0.CO;2-D (cited on page 214).

Eaton, J. K. "Two-way coupled turbulence simulations of gas-particle flows using point-particle tracking". In: *International Journal of Multiphase Flow* 35.9 (2009), pp. 792–800. DOI: https://doi.org/10.1016/j.ijmultiphaseflow.2009.02.009 (cited on page 90).

Ebrahimian, V., Nicolle, A., and Habchi, C. "Detailed modeling of the evaporation and thermal decomposition of urea-water solution in SCR systems". In: *AIChE Journal* 58.7 (2012), pp. 1998–2009. DOI: 10.1002/aic.12736 (cited on pages 5, 63).

Edelbauer, W., Birkhold, F., Rankel, T., Pavlović, Z., and Kolar, P. "Simulation of the liquid break-up at an AdBlue injector with the volume-of-fluid method followed by off-line coupled Lagrangian particle tracking". In: *Computers and Fluids* 157 (2017), pp. 294–311. DOI: 10.1016/j.compfluid.2017.09.003 (cited on pages 67, 213).

Edelbauer, W., Kolar, P., Schellander, D., Pavlovic, Z., and Almbauer, R. "Numerical simulation of spray break-up from cavitating nozzle flow by combined Eulerian–Eulerian and volume-of-fluid methods". In: *International Journal of Computational Methods and Experimental Measurements* 6.2 (2017), pp. 314–325. DOI: 10.2495/CMEM-V6-N2-314-325 (cited on page 67).

EEA Relevance. *REGULATION (EU) No 167/2013 OF THE EUROPEAN PARLIAMENT AND OF THE COUNCIL of 5 February 2013 on The Approval and Market Surveillance of Agricultural and Forestry Vehicles.* 2013 (cited on page 19).

Elmøe, T. D., Sørensen, R. Z., Quaade, U., Christensen, C. H., Nørskov, J. K., and Johannessen, T. "A high-density ammonia storage/delivery system based on Mg(NH 3)6Cl2 for SCR-DeNOx in vehicles". In: *Chemical Engineering Science* 61.8 (2006), pp. 2618–2625. DOI: 10.1016/j.ces.2005.11.038 (cited on page 24).

Emelyanenko, V. N., Kabo, G. J., and Verevkin, S. P. "Measurement and Prediction of Thermochemical Properties: Improved Increments for the Estimation of Enthalpies of Sublimation and Standard Enthalpies of Formation of Alkyl Derivatives of Urea". In: *Journal of Chemical & Engineering Data* 51.1 (2006), pp. 79–87. DOI: 10.1021/je050230z (cited on page 63).

EU Commission. *Tracking EU Citizens' Interest in EC Priorities Using Online Search Data: The European Green Deal*. Publications Office, 2021. DOI: doi/10.2760/18216 (cited on page 1).

European Council. *Directive 88/77/EEC on the approximation of the laws of the Mermber States relating to the measures to be taken against the emission of gaseous pollutants from diesel engines for use in vehicles*. 1987 (cited on page 19).

Fang, H. L. and DaCosta, H. F. "Urea thermolysis and NOx reduction with and without SCR catalysts". In: *Applied Catalysis B: Environmental* 46.1 (2003), pp. 17–34. DOI: 10.1016/S0926-3373(03)00177-2 (cited on pages 59, 63).

Fenimore, C. P. "Formation of nitric oxide in premixed hydrocarbon flames". In: *Symposium (International) on Combustion* 13.1 (1971), pp. 373–380. DOI: 10.1016/S0082-0784(71)80040-1 (cited on page 17).

Fischer, S. "Simulation of the Urea-water-solution Preparation and Ammonia-homogenization with a Validated CFD-model for the Optimization of Automotive SCR-systems". PhD thesis. Technische Universität Wien, 2012 (cited on pages 62, 64).

Fischer, S., Bitto, R., Lauer, T., Krenn, C., Tauer, J., and Pessl, G. "Impact of the Turbulence Model and Numerical Approach on the Prediction of the Ammonia Homogenization in an Automotive SCR System". In: *SAE International Journal of Engines* 5.3 (2012), pp. 1443–1458. DOI: https://doi.org/10.4271/2012-01-1291UI-2012-01-1291 (cited on page 66).

Forzatti, P. "Present status and perspectives in de-NOx SCR catalysis". In: *Applied Catalysis A: General* 222.1-2 (2001), pp. 221–236. DOI: 10.1016/S0926-860X(01)00832-8 (cited on page 22).

Fritzsche, L., Schwarze, R., Junghans, F., and Bauer, K. "Toward unraveling the mechanisms of aerosol generation during phonation". In: *Physics of Fluids* 34.12 (2022), p. 121904. DOI: 10.1063/5.0124944 (cited on page 34).

Frössling, N. "Über die verdunstung fallender tropfen". In: *Gerlands Beiträge zur Geophysik* 52.1 (1938), pp. 170–216 (cited on page 93).

Garcia, A. “Estudio de los efectos de la Post Inyeccion sobre el Proceso de Combustion y la Formacion de Hollin en Motores Diesel”. PhD thesis. Universitat Politecnica de Valencia, 2009, p. 237 (cited on page 6).

Germano, M., Piomelli, U., Moin, P., and Cabot, W. H. “A dynamic subgrid-scale eddy viscosity model”. In: *Physics of Fluids A* 3.7 (1991), pp. 1760–1765. DOI: 10.1063/1.857955 (cited on page 86).

Gimeno, J. “Desarrollo y aplicacion de la medida del flujo de cantidad de movimiento de un chorro diesel”. PhD thesis. Valencia (Spain): Universitat Politècnica de València, 2008. DOI: 10.4995/Thesis/10251/8306 (cited on page 27).

Gimeno, J. “Desarrollo y aplicacion de la medida del flujo de cantidad de movimiento de un chorro diesel”. PhD thesis. 2008 (cited on page 6).

González Montero, L. A. “Computational and Experimental Study of the Primary Atomisation Process under Different Injection Conditions”. PhD thesis. Valencia (Spain): Universitat Politècnica de València, 2022. DOI: 10.4995/Thesis/10251/190635 (cited on page 6).

GÓRKA, K., KAŹMIERSKI, B., and KAPUSTA, Ł. “Numerical analysis of the flow rig for UWS spray examination in exhaust system-relevant conditions”. In: *Combustion Engines* 186.3 (2021), pp. 103–112. DOI: 10.19206/ce-141182 (cited on page 5).

Gottfried, B. S., Lee, C. J., and Bell, K. J. “The leidenfrost phenomenon: film boiling of liquid droplets on a flat plate”. In: *International Journal of Heat and Mass Transfer* 9.11 (1966), pp. 1167–1188. DOI: 10.1016/0017-9310(66)90112-8 (cited on page 43).

Grant, R. P. and Middleman, S. “Newtonian jet stability”. In: *AIChE Journal* 12.4 (1966), pp. 669–678. DOI: 10.1002/aic.690120411 (cited on page 40).

Guildenbecher, D. R., Gao, J., Chen, J., and Sojka, P. E. “Characterization of drop aerodynamic fragmentation in the bag and sheet-thinning regimes by crossed-beam, two-view, digital in-line holography”. In: *International Journal of Multiphase Flow* 94 (2017), pp. 107–122. DOI: 10.1016/j.ijmultiphaseflow.2017.04.011 (cited on pages 214, 218).

Habchi, C., Nicolle, A., and Gillet, N. “Numerical study of deposits formation in SCR systems using urea-water solution injection”. In: *J Mater Sci Nanotechnol* 6.2 (2018), p. 201 (cited on page 66).

Habchi, C. “The Energy Spectrum Analogy Breakup (SAB) Modell for the Numerical Simulation of Sprays”. In: *Atomization and Sprays* 21.12 (2011), pp. 1033–1057. DOI: 10.1615/AtomizSpr.2012004531 (cited on page 218).

Halonen, S., Pitkäaho, S., Pääkkönen, T. M., Väisänen, E., and Haataja, M. "A novel method for automated SCR catalyst uniformity measurement". In: *Chemical Engineering Journal* 425 (2021), p. 130257. DOI: https://doi.org/10.1016/j.cej.2021.130257 (cited on page 127).

Han, Z. and Reitz, R. D. "Turbulence Modeling of Internal Combustion Engines Using RNG κ-ϵ Models". In: *Combustion Science and Technology* 106.4-6 (1995), pp. 267–295. DOI: 10.1080/00102209508907782 (cited on page 82).

Harlow, F. H. and Welch, J. E. "Numerical calculation of time-dependent viscous incompressible flow of fluid with free surface". In: *Physics of Fluids* 8.12 (1965), pp. 2182–2189. DOI: 10.1063/1.1761178 (cited on page 87).

Hasan Shahariar, G. M., Jo, H., and Lim, O. "Analysis of the spray wall impingement of urea-water solution for automotive SCR De-NOx systems". In: *Energy Procedia* 158 (2019), pp. 1936–1941. DOI: 10.1016/j.egypro.2019.01.448 (cited on pages 59, 60, 64).

Held, W., König, A., Richter, T., and Puppe, L. "Catalytic NOx Reduction in Net Oxidizing Exhaust Gas". In: *SAE Technical Papers*. SAE International, 1990. DOI: 10.4271/900496 (cited on page 54).

Helenbrook, B. and Edwards, C. "Quasi-steady deformation and drag of uncontaminated liquid drops". In: *International Journal of Multiphase Flow* 28.10 (2002), pp. 1631–1657. DOI: 10.1016/S0301-9322(02)00073-3 (cited on page 215).

Hirt, C. W. and Nichols, B. D. "Volume of fluid (VOF) method for the dynamics of free boundaries". In: *Journal of Computational Physics* 39.1 (1981), pp. 201–225. DOI: 10.1016/0021-9991(81)90145-5 (cited on page 67).

Hoffmann, L. and Bradley, G. *Calculus for Business, Economics, and the Social and Life Sciences, Brief*. McGraw-Hill Companies,Incorporated, 2009 (cited on page 215).

Hsiang, L.-P. and Faeth, G. "Drop properties after secondary breakup". In: *International Journal of Multiphase Flow* 19.5 (1993), pp. 721–735. DOI: 10.1016/0301-9322(93)90039-W (cited on pages 214, 219).

Hsiang, L.-P. and Faeth, G. "Drop deformation and breakup due to shock wave and steady disturbances". In: *International Journal of Multiphase Flow* 21.4 (1995), pp. 545–560. DOI: 10.1016/0301-9322(94)00095-2 (cited on pages 32, 218).

Hua, L., Zhao, Y. G., Hu, J., Tao, T., and Shuai, S. J. "Comparison between air-assisted and airless urea spray for diesel SCR System by PDA and CFD". In: *SAE Technical Papers* x (2012). DOI: 10.4271/2012-01-1081 (cited on page 4).

Ishimoto, J., Sato, F., and Sato, G. "Computational prediction of the effect of microcavitation on an atomization mechanism in a gasoline injector nozzle". In: *Journal of Engineering for Gas Turbines and Power* 132.8 (2010). DOI: 10.1115/1.4000264 (cited on page 67).

Issa, R. I. "Solution of the implicitly discretised fluid flow equations by operator-splitting". In: *Journal of Computational Physics* 62.1 (1986), pp. 40–65. DOI: 10.1016/0021-9991(86)90099-9 (cited on page 99).

Jacob, A., Ashok, B., Vignesh, R., Balusamy, S., and Alagumalai, A. "NOx and PM trade-off in IC engines". In: *NOx Emission Control Technologies in Stationary and Automotive Internal Combustion Engines: Approaches Toward NOx Free Automobiles*. Ed. by B. B. T. N. E. C. T. i. S. Ashok and A. I. C. Engines. Elsevier, 2021, pp. 69–93. DOI: 10.1016/B978-0-12-823955-1.00003-6 (cited on page 20).

Kaario, O., Larmi, M., and Tanner, F. "Relating integral length scale to turbulent time scale and comparing k-ϵ and RNG k-ϵ turbulence models in diesel combustion simulation". In: *SAE Transactions* (2002), pp. 1886–1900 (cited on page 82).

Kaario, O. T., Vuorinen, V., Zhu, L., Larmi, M., and Liu, R. "Mixing and evaporation analysis of a high-pressure SCR system using a hybrid LES-RANS approach". In: *Energy* 120 (2017), pp. 827–841. DOI: 10.1016/j.energy.2016.11.138 (cited on page 66).

Kalghatgi, G. "Is it really the end of internal combustion engines and petroleum in transport?" In: *Applied Energy* 225 (2018), pp. 965–974. DOI: 10.1016/j.apenergy.2018.05.076 (cited on page 1).

Kapusta, Ł. J. "LIF/Mie Droplet Sizing of Water Sprays from SCR System Injector using Structured Illumination". In: *Proceedings ILASS–Europe 2017. 28th Conference on Liquid Atomization and Spray Systems*. Valencia: Universitat Politècnica València, 2017. DOI: 10.4995/ilass2017.2017.5031 (cited on pages 4, 57).

Kapusta, Ł. J., Sutkowski, M., Rogóż, R., Zommara, M., and Teodorczyk, A. *Characteristics of water and urea-water solution sprays*. 2019. DOI: 10.3390/catal9090750 (cited on pages 30, 32, 145).

Kapusta, Ł. J., Sutkowski, M., Rogóż, R., Zommara, M., and Teodorczyk, A. "Characteristics of water and urea-water solution sprays". In: *Catalysts* 9.9 (2019). DOI: 10.3390/catal9090750 (cited on pages 23, 38, 54, 58).

Kapusta, L. J. and Teodorczyk, A. "Laser diagnostics for urea-water solution spray characterization". In: *MATEC Web of Conferences* 118 (2017), p. 00029. DOI: 10.1051/matecconf/201711800029 (cited on page 57).

Kaźmierski, B., Górka, K., and Kapusta, Ł. "A conceptual design and numerical analysis of the mixerless urea-SCR system". In: *Combustion Engines* 60.4 (2021). DOI: 10.19206/CE-140539 (cited on page 66).

Kaźmierski, B. and Kapusta, Ł. J. "The importance of individual spray properties in performance improvement of a urea-SCR system employing flash-boiling injection". In: *Applied Energy* 329 (2023), p. 120217. DOI: 10.1016/j.apenergy.2022.120217 (cited on page 43).

Kaźmierski, B. and Kapusta, Ł. J. "The importance of individual spray properties in performance improvement of a urea-SCR system employing flash-boiling injection". In: *Applied Energy* 329 (2023), p. 120217. DOI: 10.1016/j.apenergy.2022.120217 (cited on page 4).

Khan, D., Bjernemose, J. H., and Lund, I. "Confidence interval analysis of urea water solution spray measurement data from Phase Doppler Anemometry using numerical validations from a commercial CFD code". In: *ILASS-Americas 32nd Annual Conference on Liquid Atomization and Spray Systems,* 2022 (cited on page 4).

Khan, D., Bjernemose, J. H., and Lund, I. "Experimental Characterization and Numerical Modelling of Urea Water Solution Spray in High-Temperature Crossflow for Selective Catalytic Reduction Applications". In: *SAE International Journal of Sustainable Transportation, Energy, Environment, & Policy* 3.2 (2022), pp. 139–153. DOI: https://doi.org/10.4271/13-03-02-0012UI-13-03-02-0012 (cited on pages 65, 79).

Khristamto Aditya Wardana, M. and Lim, O. "Investigation of ammonia homogenization and NOx reduction quantity by remodeling urea injector shapes in heavy-duty diesel engines". In: *Applied Energy* 323 (2022), p. 119586. DOI: https://doi.org/10.1016/j.apenergy.2022.119586 (cited on page 66).

Kieke, M. L., Schoppelrei, J. W., and Brill, T. B. "Spectroscopy of hydrothermal reactions. 1. The CO2-H2O system and kinetics of urea decomposition in an FTIR spectroscopy flow reactor cell operable to 725 K and 335 bar". In: *Journal of Physical Chemistry* 100.18 (1996), pp. 7455–7462. DOI: 10.1021/JP950964Q/ASSET/IMAGES/LARGE/JP950964QF00010.JPEG (cited on page 63).

Kim, J. Y., Ryu, S. H., and Ha, J. S. "Numerical prediction on the characteristics of spray-induced mixing and thermal decomposition of urea solution in SCR system". In: *Proceedings of the 2004 Fall Technical Conference of the ASME Internal Combustion Engine Division*. 2004, pp. 165–170. DOI: 10.1115/icef2004-0889 (cited on pages 5, 178, 179).

Kneer, R., Schneider, M., Noll, B., and Wittig, S. "Diffusion controlled evaporation of a multicomponent droplet: theoretical studies on the importance of variable liquid properties". In: *International Journal of Heat and Mass Transfer* 36.9 (1993), pp. 2403–2415. DOI: 10.1016/S0017-9310(05)80124-3 (cited on page 42).

Koebel, M., Elsener, M., and Kleemann, M. "Urea-SCR: a promising technique to reduce NOx emissions from automotive diesel engines". In: *Catalysis Today* 59.3 (2000), pp. 335–345. DOI: 10.1016/S0920-5861(00)00299-6 (cited on page 59).

Koebel, M., Madia, G., and Elsener, M. "Selective catalytic reduction of NO and NO2 at low temperatures". In: *Catalysis Today* 73.3-4 (2002), pp. 239–247. DOI: 10.1016/S0920-5861(02)00006-8 (cited on page 22).

Koebel, M. and Strutz, E. O. "Thermal and hydrolytic decomposition of urea for automotive selective catalytic reduction systems: Thermochemical and practical aspects". In: *Industrial and Engineering Chemistry Research* 42.10 (2003), pp. 2093–2100. DOI: 10.1021/ie020950o (cited on page 59).

Kröcher, O., Elsener, M., and Jacob, E. "New reducing agents for the low-NOx SCR technology". In: *5th International Exhaust Gas and Particulate Emissions Forum*. 2008, pp. 19–20 (cited on pages 3, 23).

Kropotova, S. and Strizhak, P. "Collisions of Liquid Droplets in a Gaseous Medium under Conditions of Intense Phase Transformations: Review". In: *Energies* 14.19 (2021), p. 6150. DOI: 10.3390/en14196150 (cited on page 36).

Kuhn, C., Schweigert, D., Kuntz, C., and Börnhorst, M. "Single droplet impingement of urea water solution on heated porous surfaces". In: *International Journal of Heat and Mass Transfer* 181 (2021), p. 121836. DOI: 10.1016/j.ijheatmasstransfer.2021.121836 (cited on page 59).

Kuhnke, D. *Spray/Wall-Interaction Modelling by Dimensionless Data Analysis*. Berichte aus der Strömungstechnik. Shaker, 2004 (cited on pages 43, 44, 95).

Kumar, A., Muddapur, A., and Sahu, S. "Experimental investigation of Urea-water solution (UWS) spray impingement on a heated flat surface". In: *Proceeding of Proceedings of the 26thNational and 4th International ISHMT-ASTFE Heat and Mass Transfer Conference December 17-20, 2021, IIT Madras, Chennai-600036, Tamil Nadu, India*. Connecticut: Begellhouse, 2022, pp. 609–615. DOI: 10.1615/IHMTC-2021.910 (cited on page 59).

Kuo, C. W. and Trujillo, M. F. "A maximum entropy formalism model for the breakup of a droplet". In: *Physics of Fluids* 34.1 (2022). DOI: 10.1063/5.0076910 (cited on page 216).

Lauer, T. "Preparation of Ammonia from Liquid AdBlue – Modeling Approaches and Future Challenges". In: *Chemie-Ingenieur-Technik* 90.6 (2018), pp. 783–794. DOI: 10.1002/cite.201700107 (cited on pages 3, 33, 213).

Launder, B. E. and Spalding, D. B. "The numerical computation of turbulent flows". In: *Computer Methods in Applied Mechanics and Engineering* 3.2 (1974), pp. 269–289. DOI: https://doi.org/10.1016/0045-7825(74)90029-2 (cited on page 82).

Lavoie, G. A. and Blumberg, P. N. "A Fundamental Model for Predicting Fuel Consumption, NOx and HC Emissions of the Conventional Spark-Ignited Engine". In: *Combustion Science and Technology* 21.5-6 (1980), pp. 225–258. DOI: 10.1080/00102208008946939 (cited on page 17).

Lavole, G. A., Heywood, J. B., and Keck, J. C. "Experimental and theoretical study of nitric oxide formation in internal combustion engines". In: *Combustion Science and Technology* 1.4 (1970), pp. 313–326. DOI: 10.1080/00102206908952211 (cited on page 17).

Lee, S. I. and Park, S. Y. "Numerical analysis of internal flow characteristics of urea injectors for SCR dosing system". In: *Fuel* 129 (2014), pp. 54–60. DOI: 10.1016/j.fuel.2014.03.031 (cited on pages 4, 26).

Lefebvre, A. H. and McDonell, V. G. *Atomization and sprays*. Second. Boca Raton, FL: Press, CRC, 2017, pp. 1–284. DOI: 10.1201/9781315120911 (cited on pages 31, 39, 40, 146, 170).

Li, X., Tankin, R. S., Sztal, B., and Most, J.-M. "Derivation of Droplet Size Distribution in Sprays By Using Information Theory". In: *Combustion Science and Technology* 60.4-6 (1988), pp. 345–357. DOI: 10.1080/00102208808923992 (cited on page 214).

Li, X. and Tankin, R. S. "On the Prediction of Droplet Size and Velocity distributions in sprays through maximum entropy principle". In: *Particle & Particle Systems Characterization* 9.1-4 (1992), pp. 195–201. DOI: 10.1002/ppsc.19920090126 (cited on page 214).

Liao, Y., Dimopoulos Eggenschwiler, P., Rentsch, D., Curto, F., and Boulouchos, K. "Characterization of the urea-water spray impingement in diesel selective catalytic reduction systems". In: *Applied Energy* 205 (2017), pp. 964–975. DOI: 10.1016/J.APENERGY.2017.08.088 (cited on pages 60, 66).

Liao, Y., Dimopoulos Eggenschwiler, P., Spiteri, A., Nocivelli, L., Montenegro, G., and Boulouchos, K. "Fluid Dynamic Comparison of AdBlue Injectors for SCR Applications". In: *SAE International Journal of Engines* 8.5 (2015), pp. 2303–2311. DOI: 10.4271/2015-24-2502 (cited on pages 56, 57).

Lieber, C., Koch, R., and Bauer, H. J. "Spray evaporation of urea–water solution: Experiments and modelling". In: *Experimental Thermal and Fluid Science* 116.February (2020), p. 110108. DOI: 10.1016/j.expthermflusci.2020.110108 (cited on page 4).

Lilly, D. K. "The representation of small-scale turbulence in numerical simulation experiments". In: *IBM Form* (1967), pp. 195–210 (cited on page 85).

Lilly, D. K. "A proposed modification of the Germano subgrid-scale closure method". In: *Physics of Fluids A: Fluid Dynamics* 4.3 (1992), pp. 633–635. DOI: 10.1063/1.858280 (cited on page 86).

Lin, S. P. and Reitz, R. D. "Drop and spray formation from a liquid jet". In: *Annual Review of Fluid Mechanics* 30.1 (1998), pp. 85–105. DOI: 10.1146/annurev.fluid.30.1.85 (cited on page 145).

Ling, Y., Zaleski, S., and Scardovelli, R. "Multiscale simulation of atomization with small droplets represented by a Lagrangian point-particle model". In: *International Journal of Multiphase Flow* 76 (2015), pp. 122–143. DOI: 10.1016/j.ijmultiphaseflow.2015.07.002 (cited on page 91).

Liu, A. B., Mather, D., and Reitz, R. D. "Modeling the effects of drop drag and breakup on fuel sprays". In: *SAE Technical Papers*. Vol. 298. 1993, pp. 1–6. DOI: 10.4271/930072 (cited on pages 37, 91).

Liu, G. and Gao, P. X. "A review of NOx storage/reduction catalysts: Mechanism, materials and degradation studies". In: *Catalysis Science and Technology* 1.4 (2011), pp. 552–568. DOI: 10.1039/c1cy00007a (cited on page 22).

Lundströml, A., Waldheim, B., Ström, H., and Westerberg, B. "Modelling of urea gas phase thermolysis and theoretical details on urea evaporation". In: *Proceedings of the Institution of Mechanical Engineers, Part D: Journal of Automobile Engineering* 225.10 (2011), pp. 1392–1398. DOI: 10.1177/0954407011406048 (cited on pages 5, 63).

Mao, T., Kuhn, D. C. S., and Tran, H. "Spread and rebound of liquid droplets upon impact on flat surfaces". In: *AIChE Journal* 43.9 (1997), pp. 2169–2179. DOI: 10.1002/aic.690430903 (cited on page 43).

Marsden, A. L., Vasilyev, O. V., and Moin, P. "Construction of commutative filters for LES on unstructured meshes". In: *Journal of Computational Physics* 175.2 (2002), pp. 584–603. DOI: 10.1006/jcph.2001.6958 (cited on page 150).

Martí Gómez-Aldaraví, P. "Development of a Computational Model for a Simultaneous Simulation of Internal Flow and Spray Break-Up of the Diesel Injection Process". PhD thesis. Valencia (Spain): Universitat Politècnica de València, 2014. DOI: 10.4995/Thesis/10251/43719 (cited on page 6).

Martínez García, M. "Computational Study of the Injection Process in Gasoline Direct Injection (GDI) Engines". PhD thesis. Valencia (Spain): Universitat Politècnica de València, 2022. DOI: 10.4995/Thesis/10251/185180 (cited on page 6).

Matusik, K. E., Duke, D. J., Kastengren, A. L., Sovis, N., Swantek, A. B., and Powell, C. F. "High-resolution X-ray tomography of Engine Combustion Network diesel injectors". In: *International Journal of Engine Research* 19.9 (2018), pp. 963–976. DOI: 10.1177/1468087417736985 (cited on page 101).

Mehdi, G., Zhou, S., Zhu, Y., Shah, A. H., and Chand, K. *Numerical Investigation of SCR Mixer Design Optimization for Improved Performance.* 2019. DOI: 10.3390/pr7030168 (cited on page 202).

Miesse, C. C. "Correlation of Experimental Data on the Disintegration of Liquid Jets". In: *Industrial & Engineering Chemistry* 47.9 (1955), pp. 1690–1701. DOI: 10.1021/ie50549a013 (cited on page 30).

MohamedMusthafa, M., Sivapirakasam, S. P., and Udayakumar, M. "Comparative studies on fly ash coated low heat rejection diesel engine on performance and emission characteristics fueled by rice bran and pongamia methyl ester and their blend with diesel". In: *Energy* 36.5 (2011), pp. 2343–2351. DOI: 10.1016/j.energy.2010.12.047 (cited on page 21).

Mohapatra, C. K., Schmidt, D. P., Sforozo, B. A., Matusik, K. E., Yue, Z., Powell, C. F., Som, S., Mohan, B., Im, H. G., Badra, J., Bode, M., Pitsch, H., Papoulias, D., Neroorkar, K., Muzaferija, S., Martí-Aldaraví, P., and Martínez, M. "Collaborative investigation of the internal flow and near-nozzle flow of an eight-hole gasoline injector (Engine Combustion Network Spray G)". In: *International Journal of Engine Research* (2020), p. 1468087420918449. DOI: 10.1177/1468087420918449 (cited on page 138).

Mojtabi, M., Chadwick, N., Wigley, G., and Helie, J. "The effect of flash boiling on break up and atomization in GDI sprays". In: *22nd European Conference on Liquid Atomization and Spray Systems*. 2008, pp. 8–10 (cited on page 43).

Monin, A. S. "On the nature of turbulence". In: *Soviet Physics Uspekhi* 21.5 (1978), p. 429 (cited on page 80).

Moore, C., Brown, S., MacDonald, P., Ewen, M., and Broadbent, H. "European Electricity Review 2022". In: *Ember* February (2022), p. 34 (cited on page 2).

Moreno, A. E. "Experimental Study of the Urea-Water Solution Injection Process". PhD thesis. Valencia (Spain): Universitat Politècnica de València, 2022. DOI: 10.4995/Thesis/10251/181637 (cited on pages 6, 55, 56, 108, 111, 135, 138, 139, 151, 153, 157–159, 164, 165, 177, 181).

Movahednejad, E., Ommi, F., Hosseinalipour, S. M., Chen, C. P., and Mahdavi, S. A. "Application of maximum entropy method for droplet size distribution prediction using instability analysis of liquid sheet". In: *Heat and Mass Transfer/Waerme- und Stoffuebertragung* 47.12 (2011), pp. 1591–1600. DOI: 10.1007/s00231-011-0797-5 (cited on page 216).

Mugele, R. A. and Evans, H. D. "Droplet Size Distribution in Sprays". In: *Industrial & Engineering Chemistry* 43.6 (1951), pp. 1317–1324. DOI: 10.1021/ie50498a023 (cited on page 35).

Musa, S. N. A., Saito, M., Furuhata, T., and Arai, M. "Evaporation characteristics of a single aqueous urea solution droplet". In: *10th International Conference on Liquid Atomization and Spray Systems, ICLASS 2006*. 2006 (cited on page 58).

N/N. *Proposal for Regulation of the European Parliament and of the Council on Type-Approval of Motor Vehicles and Engine of such Systems, Components and Separate Technical Units Intended for Such Vehicles, with Respect to thir Emissione and Battery Durability*. 2022 (cited on page 20).

Naber, J. D. and Siebers, D. L. *Effects of gas density and vaporization on penetration and dispersion of diesel sprays*. 1996. DOI: 10.4271/960034 (cited on page 38).

Nishad, K., Ries, F., Janicka, J., and Sadiki, A. "Analysis of spray dynamics of urea–water-solution jets in a SCR-DeNOx system: An LES based study". In: *International Journal of Heat and Fluid Flow* 70 (2018), pp. 247–258. DOI: 10.1016/j.ijheatfluidflow.2018.02.017 (cited on page 66).

Nocivelli, L., Montenegro, G., and Dimopoulos Eggenschwiler, P. "Low pressure-driven injection characterization for SCR applications". In: *SAE Technical Papers* 2019-April.April (2019), pp. 1–12. DOI: 10.4271/2019-01-0994 (cited on page 5).

Nocivelli, L., Montenegro, G., Onorati, A., Curto, F., Dimopoulos Eggenschwiler, P., Liao, Y., and Vogel, A. *Quantitative Analysis of Low Pressure-Driven Spray Mass Distribution and Liquid Entrainment for SCR Application through a Mechanical Patternator*. Tech. rep. March. 2017. DOI: 10.4271/2017-01-0965 (cited on pages 4, 65).

O'Rourke, P. J. "Collective Drop Effects on Vaporizing Liquid Sprays". PhD thesis. Princeton University, 1981 (cited on page 91).

O'Rourke, P. J. and Amsden, A. A. "The tab method for numerical calculation of spray droplet breakup". In: *SAE Technical Papers*. 1987. DOI: 10.4271/872089 (cited on pages 91, 213).

Ohnesorge, W. "Formation of Drops by nozzles and the breakup of liquid jets". In: *Z. Angew. Math. Mech.* 16 (1936), pp. 355–358 (cited on page 29).

P., S. and Allmaras, S. "A one-equation turbulence model for aerodynamic flows". In: *30th Aerospace Sciences Meeting and Exhibit*. Reston, Virigina: American Institute of Aeronautics and Astronautics, 1992. DOI: 10.2514/6.1992-439 (cited on page 82).

Panigrahi, T. H., Sahoo, S. R., Murmu, G., Maity, D., and Saha, S. "Current challenges and developments of inorganic/organic materials for the abatement of toxic nitrogen oxides (NOx) – A critical review". In: *Progress in Solid State Chemistry* 68 (2022), p. 100380. DOI: 10.1016/j.progsolidstchem.2022.100380 (cited on page 2).

Park, T., Sung, Y., Kim, T., Lee, I., Choi, G., and Kim, D. "Effect of static mixer geometry on flow mixing and pressure drop in marine SCR applications". In: *International Journal of Naval Architecture and Ocean Engineering* 6.1 (2014), pp. 27–38. DOI: 10.2478/IJNAOE-2013-0161 (cited on page 24).

Patterson, M. A. *Modeling the effects of fuel injection characteristics on diesel combustion and emissions*. The University of Wisconsin-Madison, 1997 (cited on page 92).

Payri, R., Bracho, G., Gimeno, J., and Moreno, A. "Spray Characterization of the Urea-Water Solution (UWS) Injected in a Hot Air Stream Analogous to SCR System Operating Conditions". In: *SAE Technical Papers*. Vol. 2019-April. April. 2019. DOI: 10.4271/2019-01-0738 (cited on page 107).

Payri, R., Bracho, G., Gimeno, J., and Moreno, A. *Spray characterization of the urea-water solution (UWS) injected in a hot air stream analogous to SCR system operating conditions*. 2019. DOI: 10.4271/2019-01-0738 (cited on pages 4, 54, 55, 107, 182).

Payri, R., Salvador, F. J., Martí-Aldaraví, P., and Vaquerizo, D. "ECN Spray G external spray visualization and spray collapse description through penetration and morphology analysis". In: *Applied Thermal Engineering* 112 (2017), pp. 304–316. DOI: https://doi.org/10.1016/j.applthermaleng.2016.10.023 (cited on page 125).

Payri, R., Bracho, G., Martí-Aldaraví, P., and Marco-Gimeno, J. "Numerical Analysis of Urea to Ammonia Conversion in Automotive Selective Catalytic Reduction Realistic Conditions". In: *Industrial and Engineering Chemistry Research* 60.39 (2021), pp. 14329–14340. DOI: 10.1021/acs.iecr.1c02627 (cited on page 187).

Payri, R., Bracho, G., Martí-Aldaraví, P., and Moreno, A. "Using momentum flux measurements to determine the injection rate of a commercial Urea Water Solution injector". In: *Flow Measurement and Instrumentation* 80 (2021). DOI: 10.1016/j.flowmeasinst.2021.101999 (cited on pages 57, 58, 123, 138).

Pilch, M. and Erdman, C. A. "Use of breakup time data and velocity history data to predict the maximum size of stable fragments for acceleration-induced breakup of a liquid drop". In: *International Journal of Multiphase Flow* 13.6 (1987), pp. 741–757. DOI: 10.1016/0301-9322(87)90063-2 (cited on pages 31, 32).

Pisupadti, S. V. “Fuel Chemistry”. In: *Encyclopedia of Physical Science and Technology*. Elsevier, 2003, pp. 253–274. DOI: 10.1016/B0-12-227410-5/00933-9 (cited on page 16).

Plewa, T., Linde, T., and Weirs, V. G. “Adaptive mesh refinement-theory and applications”. In: (2005) (cited on page 8).

Pomraning, E. “Development of Large Eddy Simulation Turbulence Models Development of Large Eddy Simulation Turbulence Models By the requirements for the degree of Doctor of Philosophy (Mechanical Engineering) At the University of Wisconsin–Madison”. PhD thesis. University of Wisconsin, 2000 (cited on page 114).

Pope, S. B. “Ten questions concerning the large-eddy simulation of turbulent flows”. In: *New Journal of Physics* 6 (2004), p. 35. DOI: 10.1088/1367-2630/6/1/035 (cited on pages 122, 136, 150, 200, 201).

Postrioti, L., Brizi, G., Ungaro, C., Mosser, M., and Bianconi, F. “A methodology to investigate the behaviour of urea-water sprays in high temperature air flow for SCR de-NOx applications”. In: *Fuel* 150.x (2015), pp. 548–557. DOI: 10.1016/j.fuel.2015.02.067 (cited on pages 4, 56).

Prabhu S, S., Natesan, K., and Shivappa Nayak, N. “Effect of UWS spray angle and positioning of injector on ammonia concentration in Urea-SCR system”. In: *Materials Today: Proceedings* 46 (2021), pp. 8051–8055. DOI: https://doi.org/10.1016/j.matpr.2021.03.026 (cited on page 189).

Prather, M. J., Hsu, J., DeLuca, N. M., Jackman, C. H., Oman, L. D., Douglass, A. R., Fleming, E. L., Strahan, S. E., Steenrod, S. D., Søvde, O. A., Isaksen, I. S., Froidevaux, L., and Funke, B. “Measuring and modeling the lifetime of nitrous oxide including its variability”. In: *Journal of Geophysical Research* 120.11 (2015), pp. 5693–5705. DOI: 10.1002/2015JD023267 (cited on page 22).

Putnam, A. *Integratable form of droplet drag coefficient*. 1961 (cited on page 37).

Qian, F., Lü, L., and Yang, D. “Simulation of Deposit Formation Inside the Exhaust Pipe on a Diesel Engine with SCR”. In: *Neiranji Xuebao/Transactions of CSICE (Chinese Society for Internal Combustion Engines)* 36.2 (2018), pp. 144–152. DOI: 10.16236/j.cnki.nrjxb.201802019 (cited on page 38).

Qian, J. and Law, C. K. “Regimes of coalescence and separation in droplet collision”. In: *Journal of Fluid Mechanics* 331 (1997), pp. 59–80. DOI: 10.1017/S0022112096003722 (cited on page 36).

Raju, R., Chandran R, J., Salih, A., and Joseph, K. "Numerical analysis of mixing chamber non-uniformities and feed conditions for optimal performance of urea SCR". In: *Reaction Chemistry and Engineering* 5.12 (2020), pp. 2236–2249. DOI: 10.1039/d0re00269k (cited on page 179).

Ranz, W. E. and Marshall, W. R. "Evaporation from drops: Part II". In: *Chemical Engineering Progress* 48 (1952), pp. 141–146 (cited on page 93).

Ranz, W. E. "Some experiments on orifice sprays". In: *The Canadian Journal of Chemical Engineering* 36.4 (1958), pp. 175–181. DOI: 10.1002/cjce.5450360405 (cited on page 30).

Reitz, R. D. "Atomization and other breakup regimes of a liquid jet". PhD thesis. AA(Princeton University, New Jersey), 1978 (cited on page 29).

Reitz, R. D. and Bracco, F. V. "Mechanism of atomization of a liquid jet". In: *Physics of Fluids* 25.10 (1982), pp. 1730–1742. DOI: 10.1063/1.863650 (cited on pages 92, 213).

Rhie, C. M. and Chow, W. L. "Numerical study of the turbulent flow past an airfoil with trailing edge separation". In: *AIAA Journal* 21.11 (1983), pp. 1525–1532. DOI: 10.2514/3.8284 (cited on page 100).

Rizk N.K. and Lefebvre A.H. "Prediction of Velocity Coefficient and Spray Cone Angle for Simplex Swirl Atomizers". In: International Journal of Turbo and Jet Engines 4.1-2 (1987), pp. 65–74. DOI: 10.1515/TJJ.1987.4.1-2.65 (cited on page 39).

Rogóż, R., Kapusta, Ł. J., Bachanek, J., Vankan, J., and Teodorczyk, A. "Improved urea-water solution spray model for simulations of selective catalytic reduction systems". In: *Renewable and Sustainable Energy Reviews* 120 (2020), p. 109616. DOI: 10.1016/j.rser.2019.109616 (cited on pages 65, 112, 186).

Rosin, P. and Rammler, E. "The laws governing the fineness of powdered coal". In: *Journal of the Institute of Fuel*. Vol. 7. 1933, pp. 29–36 (cited on page 33).

Saad, Y. *Iterative Methods for Sparse Linear Systems*. Second. Society for Industrial and Applied Mathematics, 2003. DOI: 10.1137/1.9780898718003 (cited on page 118).

Sagaut, P. *Large eddy simulation for incompressible flows: an introduction*. Springer Science & Business Media, 2006 (cited on page 123).

Saiteja, P., Ashok, B., Saiteja, P., and Vignesh, R. "NOX reduction through various low temperature combustion technologies". In: *NOx Emission Control Technologies in Stationary and Automotive Internal Combustion Engines: Approaches Toward NOx Free Automobiles* (2021), pp. 423–459. DOI: 10.1016/B978-0-12-823955-1.00014-0 (cited on page 21).

Sala, R., Bielaczyc, P., and Brzezanski, M. *Concept of vaporized urea dosing in selective catalytic reduction*. 2017. DOI: 10.3390/catal7100307 (cited on page 4).

Salvador, F. J. *Influencia de la cavitación sobre el desarrollo del chorro Diesel*. Reverté, 2007 (cited on page 6).

Sapio, F., Millo, F., Fino, D., Monteverde, A., Sartoretti, E., Bianco, A., Postrioti, L., Tarabocchia, A., Buitoni, G., and Brizi, G. "Experimental and Numerical Analysis of Latest Generation Diesel Aftertreatment Systems". In: *SAE Technical Papers*. Vol. 2019-Septe. September. SAE International, 2019. DOI: 10.4271/2019-24-0142 (cited on pages 38, 54).

Schaber, P. M., Colson, J., Higgins, S., Thielen, D., Anspach, B., and Brauer, J. "Thermal decomposition (pyrolysis) of urea in an open reaction vessel". In: *Thermochimica Acta* 424.1-2 (2004), pp. 131–142. DOI: 10.1016/j.tca.2004.05.018 (cited on pages 25, 63).

Schiffmann, P., Lecompte, M., and Laget, O. "Experimental Investigation of Novel Ammonia Mixer Designs for SCR Systems". In: *SAE Technical Papers* 2018-April (2018), pp. 1–13. DOI: 10.4271/2018-01-0343 (cited on page 4).

Schmidt, D. P. and Rutland, C. J. "A New Droplet Collision Algorithm". In: *Journal of Computational Physics* 164.1 (2000), pp. 62–80. DOI: 10.1006/jcph.2000.6568 (cited on page 91).

Schweigert, D., Damson, B., Lüders, H., Becker, C., and Deutschmann, O. "New experimental insights in AdBlue-spray/wall interaction and its impacts on EGT system design BT - 19. Internationales Stuttgarter Symposium". In: ed. by M. Bargende, H.-C. Reuss, A. Wagner, and J. Wiedemann. Wiesbaden: Springer Fachmedien Wiesbaden, 2019, pp. 142–154 (cited on page 60).

Sellens, R. W. and Brzustowski, T. A. "A prediction of the drop size distribution in a spray from first principles". In: *Atomisation Spray Technology* 1 (1985), pp. 89–102 (cited on page 214).

Sellens, R. W. "Prediction of the Drop Size and Velocity Distribution in a Spray, Based on the maximum entropy formalism". In: *Particle & Particle Systems Characterization* 6.1-4 (1989), pp. 17–27. DOI: 10.1002/ppsc.19890060103 (cited on page 214).

Semakula, M. and Inambao, P. F. "The Formation, Effects and Control of Oxides of Nitrogen in Diesel Engines". In: *International Journal of Applied Engineering Research* 13.6 (2018), pp. 3200–3209 (cited on page 18).

Senecal, P. K., Pomraning, E., Richards, K. J., Briggs, T. E., Choi, C. Y., McDavid, R. M., and Patterson, M. A. "Multi-dimensional modeling of direct-injection diesel spray liquid length and flame lift-off length using cfd and parallel detailed chemistry". In: *SAE Technical Papers*. 2003, p. 23. DOI: 10.4271/2003-01-1043 (cited on page 95).

Shahariar, G. M. H., Wardana, M. K. A., and Lim, O. T. "A study on post impingement effects of urea-water solution spray on the heated wall of automotive SCR systems". In: *IOP Conference Series: Earth and Environmental Science* 133 (2018), p. 012025. DOI: 10.1088/1755-1315/133/1/012025 (cited on page 64).

Shannon, C. E. and Weaver, W. *The Mathematical Theory of Communication*. Illini books v. 1. University of Illinois Press, 1949 (cited on page 215).

Shi, X., Deng, J., Wu, Z., and Li, L. "Effect of injection parameters on spray characteristics of urea-SCR system". In: *SAE International Journal of Engines* 6.2 (2013), pp. 873–881. DOI: 10.4271/2013-01-1067 (cited on page 60).

Shi, Y., Li, Z., Cao, W., and Dong, Q. "Investigation on Internal Flow Characteristics of a Pressure-Driven Swirling Injector for Urea-SCR System BT - Proceedings of the International Conference of Fluid Power and Mechatronic Control Engineering (ICFPMCE 2022)". In: Atlantis Press, 2022, pp. 376–392. DOI: https://doi.org/10.2991/978-94-6463-022-0_32 (cited on page 26).

Sirignano, W. A. "Fuel droplet vaporization and spray combustion theory". In: *Progress in Energy and Combustion Science* 9.4 (1983), pp. 291–322. DOI: 10.1016/0360-1285(83)90011-4 (cited on page 42).

Smagorinsky, J. "General Circulation Experiments With the Primitive Equations". English. In: *Monthly Weather Review* 91.3 (1963), pp. 99–164. DOI: 10.1175/1520-0493(1963)091<0099:gcewtp>2.3.co;2 (cited on page 85).

Smith, A. M. and Cebeci, T. *Numerical solution of the turbulent-boundary-layer equations*. Tech. rep. 1967 (cited on page 82).

Smith, H., Lauer, T., Mayer, M., and Pierson, S. "Optical and Numerical Investigations on the Mechanisms of Deposit Formation in SCR Systems". In: *SAE International Journal of Fuels and Lubricants* 7.2 (2014), pp. 525–542. DOI: https://doi.org/10.4271/2014-01-1563UI-2014-01-1563 (cited on page 64).

Solla, A., Westerholm, M., Söderström, C., Tormonen, K., Härmä, T., Nissinen, T., and Kukkonen, J. "Effect of ammonium formate and mixtures of urea and ammonium formate on low temperature activity of SCR systems". In: *SAE Technical Papers* (2005). DOI: 10.4271/2005-01-1856 (cited on pages 3, 24).

Spiteri, A. and Dimopoulos Eggenschwiler, P. "Experimental fluid dynamic investigation of urea-water sprays for diesel selective catalytic reduction-denox applications". In: *Industrial and Engineering Chemistry Research* 53.8 (2014), pp. 3047–3055. DOI: 10.1021/ie404037h (cited on pages 4, 54, 55, 57, 65).

Spiteri, A., Dimopoulos Eggenschwiler, P., Varna, A., Boulouchos, K., and Wright, Y. M. "Numerical Modelling and Experimental Characterization of a Pressure-Assisted Multi-Stream Injector for SCR Exhaust Gas After-Treatment". In: *SAE International Journal of Engines* 7.4 (2014), pp. 2012–2021. DOI: https://doi.org/10.4271/2014-01-2822UI-2014-01-2822 (cited on page 65).

Spiteri, A. C., Srna, A., and Dimopoulos Eggenschwiler, P. "Characterization of Sprays of Water and Urea-Water Solution from a Commercial Injector for SCR DeNOx Applications". In: *Proceedings 13. Internationales Stuttgarter Symposium* (2013), pp. 193–201 (cited on page 57).

Stein, M., Bykov, V., Bertótiné Abai, A., Janzer, C., Maas, U., Deutschmann, O., and Olzmann, M. "A reduced model for the evaporation and decomposition of urea–water solution droplets". In: *International Journal of Heat and Fluid Flow* 70 (2018), pp. 216–225. DOI: 10.1016/j.ijheatfluidflow.2018.02.005 (cited on page 41).

Sterling, A. M. and Sleicher, C. A. "The instability of capillary jets". In: *Journal of Fluid Mechanics* 68.3 (1975), pp. 477–495. DOI: 10.1017/S0022112075001772 (cited on page 30).

Ström, H., Lundström, A., and Andersson, B. "Choice of urea-spray models in CFD simulations of urea-SCR systems". In: *Chemical Engineering Journal* 150.1 (2009), pp. 69–82. DOI: https://doi.org/10.1016/j.cej.2008.12.003 (cited on pages 61, 65).

Su, C. "Commercial Vehicle Post-processing system of Urea Crystallization Problem Research". In: *Automob. Appl. Technol* (2016), pp. 10–223 (cited on page 38).

Suite of Nonlinear and Differential Algebraic equation Solvers. 2008. DOI: 10.1002/0471686786.ebd0076 (cited on page 95).

Sun, X., Yan, H., and Chen, F. "Numerical investigation of atomization of swirling liquid sheets using transforming algorithm". In: *International Journal of Multiphase Flow* 152 (2022), p. 104084. DOI: 10.1016/j.ijmultiphaseflow.2022.104084 (cited on pages 123, 152).

Surendran, M., Anand, T. N., and Bakshi, S. "Experimental investigation of the evaporation behavior of urea-water-solution droplets exposed to a hot air stream". In: *AIChE Journal* 66.2 (2020), e16845. DOI: 10.1002/aic.16845 (cited on page 4).

Tan, L., Feng, P., Yang, S., Guo, Y., Liu, S., and Li, Z. "CFD studies on effects of SCR mixers on the performance of urea conversion and mixing of the reducing agent". In: *Chemical Engineering and Processing-Process Intensification* 123 (2018), pp. 82–88 (cited on page 202).

Taskinen, P. "Modeling of spray turbulence with the modified rng k-epsilon model". In: *Energy and Process Engineering, Tampere University of Tehnology* (2004) (cited on page 82).

Tian, H., Xu, R., Canadell, J. G., Thompson, R. L., Winiwarter, W., Suntharalingam, P., Davidson, E. A., Ciais, P., Jackson, R. B., Janssens-Maenhout, G., Prather, M. J., Regnier, P., Pan, N., Pan, S., Peters, G. P., Shi, H., Tubiello, F. N., Zaehle, S., Zhou, F., Arneth, A., Battaglia, G., Berthet, S., Bopp, L., Bouwman, A. F., Buitenhuis, E. T., Chang, J., Chipperfield, M. P., Dangal, S. R., Dlugokencky, E., Elkins, J. W., Eyre, B. D., Fu, B., Hall, B., Ito, A., Joos, F., Krummel, P. B., Landolfi, A., Laruelle, G. G., Lauerwald, R., Li, W., Lienert, S., Maavara, T., MacLeod, M., Millet, D. B., Olin, S., Patra, P. K., Prinn, R. G., Raymond, P. A., Ruiz, D. J., Werf, G. R. van der, Vuichard, N., Wang, J., Weiss, R. F., Wells, K. C., Wilson, C., Yang, J., and Yao, Y. "A comprehensive quantification of global nitrous oxide sources and sinks". In: *Nature* 586.7828 (2020), pp. 248–256. DOI: 10.1038/s41586-020-2780-0 (cited on page 22).

Trinh, H. P. and Chen, C. P. "Modeling of turbulence effects on liquid jet atomization and breakup". In: *43rd AIAA Aerospace Sciences Meeting and Exhibit - Meeting Papers*. Aerospace Sciences Meetings. American Institute of Aeronautics and Astronautics, 2005, pp. 5781–5801. DOI: 10.2514/6.2005-154 (cited on page 30).

Tu, J., Yeoh, G. H., Liu, C., and Tao, Y. *Computational fluid dynamics: a practical approach*. Elsevier, 2023 (cited on page 5).

Turns, S. R. "An introduction to combustion: concepts and applications". In: *System* 499 (2000), p. 411. DOI: 10.1016/j.ijhydene.2008.07.121 (cited on page 18).

Uludamar, E. "Effect of hydroxy and hydrogen gas addition on diesel engine fuelled with microalgae biodiesel". In: *International Journal of Hydrogen Energy* 43.38 (2018), pp. 18028–18036. DOI: 10.1016/j.ijhydene.2018.01.075 (cited on page 21).

Van Vuuren, N., Brizi, G., Buitoni, G., Postrioti, L., and Ungaro, C. "AUS-32 Injector Spray Imaging on Hot Air Flow Bench". In: *SAE Technical Papers* 2015-April.April (2015). DOI: 10.4271/2015-01-1031 (cited on page 55).

Van Vuuren, N., Brizi, G., Buitoni, G., Postrioti, L., and Ungaro, C. "Experimental analysis of the urea-water solution temperature effect on the spray characteristics in SCR systems". In: *SAE Technical Papers* 24.2500 (2015). DOI: 10.4271/2015-24-2500 (cited on page 56).

Van Vuuren, N. and Sayar, H. "High speed video measurements of a heated tip urea injector spray". In: *SAE Technical Papers* 9 (2012). DOI: 10.4271/2012-01-1747 (cited on page 55).

Varna, A., Boulouchos, K., Spiteri, A., Dimopoulos Eggenschwiler, P., and Wright, Y. M. "Numerical Modelling and Experimental Characterization of a Pressure-Assisted Multi-Stream Injector for SCR Exhaust Gas After-Treatment". In: *SAE International Journal of Engines* 7.4 (2014), pp. 2012–2021. DOI: 10.4271/2014-01-2822 (cited on pages 5, 82).

Varna, A., Spiteri, A. C., Wright, Y. M., Dimopoulos Eggenschwiler, P., and Boulouchos, K. "Experimental and numerical assessment of impingement and mixing of urea–water sprays for nitric oxide reduction in diesel exhaust". In: *Applied Energy* 157 (2015), pp. 824–837. DOI: https://doi.org/10.1016/j.apenergy.2015.03.015 (cited on pages 65, 116).

Varna, A., Spiteri, A. C., Wright, Y. M., Dimopoulos Eggenschwiler, P., and Boulouchos, K. "Experimental and numerical assessment of impingement and mixing of urea-water sprays for nitric oxide reduction in diesel exhaust". In: *Applied Energy* 157 (2015), pp. 824–837. DOI: 10.1016/j.apenergy.2015.03.015 (cited on pages 5, 82, 181).

Venkatachalam, P., Sahu, S., and Anupindi, K. "Investigation of cross-stream spray injection and wall impingement in a circular channel for SCR application". In: *Thermal Science and Engineering Progress* 32 (2022), p. 101229. DOI: 10.1016/j.tsep.2022.101229 (cited on page 4).

Versteeg, H. K. (K. *An introduction to computational fluid dynamics : the finite volume method*. Harlow, Essex, England ; Longman Scientific Technical : New York : Wiley, 1995., 1995 (cited on page 79).

Versteeg, H. K. and Malalasekera, W. *An introduction to computational fluid dynamics: the finite volume method*. Pearson education, 2007 (cited on pages 79, 84).

Waclawczyk, T. and Koronowicz, T. "Modeling of the wave breaking with CICSAM and HRIC high resolution schemes". In: *European Conference on Computational Fluid Dynamics*. 2006, pp. 1–19 (cited on page 88).

Wacławczyk, T. and Koronowicz, T. "Modeling of the flow in systems of immiscible fluids using volume of fluid method with cicsam scheme". In: *Modelling of Multiphase Flows in Thermo-Chemical Systems Advanced Measurement Techniques* 8 (2005), pp. 267–276 (cited on page 88).

Wang, M., Liu, X., Bao, J., Li, Z., and Hu, J. "Simulation Study on Prediction of Urea Crystallization of a Diesel Engine Integrated after-Treatment Device". In: *ACS Omega* 6.10 (2021), pp. 6747–6756. DOI: 10.1021/acsomega.0c05785 (cited on page 54).

Wang, T. J., Baek, S. W., Lee, S. Y., Kang, D. H., and Yeo, G. K. "Experimental investigation on evaporation of urea-water-solution droplet for SCR applications". In: *AIChE Journal* 55.12 (2009), pp. 3267–3276. DOI: 10.1002/aic.11939 (cited on page 58).

Wang, Y. Y., Zhang, H., and Wang, J. "NOx Sensor Reading Correction in Diesel Engine Selective Catalytic Reduction System Applications". In: *IEEE/ASME Transactions on Mechatronics* 21.1 (2016), pp. 460–471. DOI: 10.1109/TMECH.2015.2434846 (cited on page 23).

Wardana, M. K. and Lim, O. *Investigation of Solid Deposit Inside L-Type Urea Injector and NOx Conversion in a Heavy-Duty Diesel Engine*. 2021. DOI: 10.3390/catal11050595 (cited on page 66).

Weglarczyk, S. "Kernel density estimation and its application". In: *ITM Web of Conferences* 23 (2018). Ed. by W. Zielinski, L. Kuchar, A. Michalski, and B. Kazmierczak, p. 00037. DOI: 10.1051/itmconf/20182300037 (cited on page 169).

Wegner, B., Maltsev, A., Schneider, C., Sadiki, A., Dreizler, A., and Janicka, J. "Assessment of unsteady RANS in predicting swirl flow instability based on LES and experiments". In: *International Journal of Heat and Fluid Flow* 25.3 (2004), pp. 528–536. DOI: https://doi.org/10.1016/j.ijheatfluidflow.2004.02.019 (cited on page 81).

Wei, L., Youtong, Z., and Asif, M. "Investigation on UWS evaporation for vehicle SCR applications". In: *AIChE Journal* 62.3 (2016), pp. 880–890. DOI: 10.1002/aic.15078 (cited on pages 41, 59, 188).

Wilcox, D. C. "Reassessment of the scale-determining equation for advanced turbulence models". In: *AIAA Journal* 26.11 (1988), pp. 1299–1310. DOI: 10.2514/3.10041 (cited on page 82).

Wilcox, D. C. *Turbulence modeling for CFD*. Vol. 2. DCW industries La Canada, CA, 1998 (cited on page 82).

Wu, P. K., Kirkendall, K. A., Fulle, R. P., and Nejad, A. S. "Breakup processes of liquid jets in subsonic crossflows". In: *Journal of Propulsion and Power* 13.1 (1997), pp. 64–73. DOI: 10.2514/2.5151 (cited on page 40).

Wu, Y., Mei, J., Cai, T., Wang, W., Zhu, H., Sun, T. L., and Liu, D. "Reducing the NOx emissions during NH3 oxidation with Nickel modified Fe2O3-a promising cost-effective and environmentally friendly catalyst for NH3 combustion". In: *Combustion and Flame* 237 (2022), p. 111845. DOI: 10.1016/j.combustflame.2021.111845 (cited on page 2).

Yakhot, V., Orszag, S. A., Thangam, S., Gatski, T. B., and Speziale, C. G. "Development of turbulence models for shear flows by a double expansion technique". In: *Physics of Fluids A* 4.7 (1992), pp. 1510–1520. DOI: 10.1063/1.858424 (cited on page 83).

Yang, H. C., Ryou, H. S., Hong, K. B., Kim, H. S., and Park, S. K. "Application of the RNG k-ϵ Model to the Analysis of Flows and Spray Characteristics". In: *Atomization and Sprays* 7.6 (1997), pp. 581–601. DOI: 10.1615/AtomizSpr.v7.i6.20 (cited on page 82).

Yim, S. D., Kim, S. J., Baik, J. H., Nam, I. S., Mok, Y. S., Lee, J. H., Cho, B. K., and Oh, S. H. "Decomposition of urea into NH3 for the SCR process". In: *Industrial and Engineering Chemistry Research* 43.16 (2004), pp. 4856–4863. DOI: 10.1021/ie034052j (cited on pages 59, 188).

Yue, Z., Battistoni, M., and Som, S. "Spray characterization for engine combustion network Spray G injector using high-fidelity simulation with detailed injector geometry". In: *International Journal of Engine Research* 21.1 (2020), pp. 226–238. DOI: 10.1177/1468087419872398 (cited on page 105).

Zel'dovich, Y., Sadonikov, P., and Frank-Kamenetskii, D. A. *Oxidation of Nitrogen in Combustion (Okislenie azota pri gorenii)*. Publishing House of the Acad of Sciences of USSR, 1947 (cited on page 17).

Zhang, C., Sun, C., Wu, M., and Lu, K. "Optimisation design of SCR mixer for improving deposit performance at low temperatures". In: *Fuel* 237 (2019), pp. 465–474. DOI: 10.1016/j.fuel.2018.10.025 (cited on pages 24, 208).

Zuzio, D. "Direct numerical simulation of two phase flows with adaptive mesh refinement". PhD thesis. ONERA - The French Aerospace Lab, 2010 (cited on page 89).